Forschungsbericht 2012-06

Multiple-Input Multiple-Output Synthetic Aperture Radar for Multimodal Operation

Jung-Hyo Kim

Deutsches Zentrum für Luft- und Raumfahrt
Institut für Hochfrequenztechnik und
Radarsysteme
Oberpfaffenhofen

Deutsches Zentrum
DLR für Luft- und Raumfahrt e.V.
in der Helmholtz-Gemeinschaft

ISRN DLR-FB--2012-06

J.-H. Kim

Forschungsbericht 2012-06

Multiple-Input Multiple-Output Synthetic Aperture Radar for Multimodal Operation

Jung-Hyo Kim

Deutsches Zentrum für Luft- und Raumfahrt
Institut für Hochfrequenztechnik und Radarsysteme
Oberpfaffenhofen

**Deutsches Zentrum
für Luft- und Raumfahrt** e.V.
in der Helmholtz-Gemeinschaft

Multiple-Input Multiple-Output Synthetic Aperture Radar for Multimodal Operation

Zur Erlangung des akademischen Grades einer

DOKTOR-INGENIEURS

der Fakultät für
Elektrotechnik und Informationstechnik
des Karlsruher Institut für Technologie (KIT)

genehmigte

DISSERTATION

von

M. Sc. Jung-Hyo Kim
aus Seoul, Südkorea

Vorwort

Contents

Acronyms and Symbols

Acronyms

Italic letters indicate that the acronym is also used as a variable.

AASR	Azimuth Ambiguity-to-Signal Ratio
ADC	Analog-to-Digital Converter
AGC	Automatic Gain Control
AoA	Angle of Arrival
ATI	Along-Track Interferometry
AWG	Arbitrary Waveform Generator
AWGN	Additive White Gaussian Noise
BPF	Band Pass Filter
CP	Cyclic Prefix
DAC	Digital-to-Analog Converter
DBF	Digital Beamforming
DDS	Direct Digital Synthesis
DEM	Digital Elevation Model
DFC	Discrete Frequency Coding
DFT	Discrete Fourier Transform
DLR	German Aerospace Center (Deutsches Zentrum für Luft- und Raumfahrt)
DPCA	Displaced Phase Center Antenna
FFT	Fast Fourier Transform
FM	Frequency Modulation
FMCW	Frequency Modulated Continuous Wave
FPGA	Field Programmable Gate Array
GB	Ground-Based
GCPW	Grounded Coplanar Waveguide
GMTI	Ground Moving Target Indication
GUI	Graphic User Interface
HPA	High Power Amplifier
HPBW	Half Power Beam Width
HRTI	High Resolution Terrain Information
HRWS	High-Resolution Wide-Swath
ICI	Inter-Carrier Interference
IDFT	Inverse Discrete Fourier Transform
IF	Intermediate Frequency
IFFT	Inverse Fast Fourier Transform
InSAR	SAR Interferometry
IRF	Impulse Response Function
ISI	Inter-Symbol-Interference
ISLR	Integrated Side Lobe Ratio
LO	Local Oscillator
LPF	Low Pass Filter

LS	Least Square
LTCC	Low Temperature Co-fired Ceramic
MIMO	Multiple-Input Multiple-Output
MISO	Multiple-Input Single-Output
ML	Maximum Likelihood
MMIC	Monolithic Microwave Integrated Circuit
MMSE	Minimum Mean Square Error
MVDR	Minimum Variance Distortionless Response
NESZ	Noise Equivalent Sigma Zero
NF	Noise Figure
OFDM	Orthogonal Frequency Division Multiplexing
PAPR	Peak-to-Average Power Ratio
PDF	Probability Density Function
PGA	Phase Gradient Autofocus
PN	Pseudo-Noise
PRF	Pulse Repetition Frequency
PRI	Pulse Repetition Interval
Pol-InSAR	Polarimetric SAR Interferometry
PolSAR	Polarimetric SAR
PSLR	Peak Side Lobe Ratio
RAM	Random Access Memory
RASR	Range Ambiguity-to-Signal Ratio
RCM	Range Cell Migration
RCS	Radar Cross Section
RF	Radio Frequency
SAR	Synthetic Aperture Radar
SCORE	SCan-On-REceive
SFC	Space-Frequency Coding
SFDR	Spurious Free Dynamic Range
SIR	Signal-to-Interference (or Image) Ratio
SIMO	Single-Input Multiple-Output
SISO	Single-Input Single-Output
SLPR	Signal-to-Leakage Power Ratio
SNR	Signal-to-Noise Ratio
SP5T	Single-Pole-5-Through
SPECAN	SPECtral ANalysis
SRTM	Shuttle Radar Topography Mission
STAP	Space-Time Adaptive Processing
STC	Space-Time Coding
T/R	Transmit/Receive
TTL	Transistor-Transistor Logic
TWT	Traveling Wave Tube
UAV	Unmanned Aerial Vehicle
ULA	Uniform Linear Array
VGA	Variable Gain Amplifier
1-D	One Dimensional
2-D	Two Dimensional
3-D	Three Dimensional

Mathematical Symbols and Operations

$ceil[\cdot]$	Rounding towards plus infinity
$\mathbf{A}^H$	Hermitian transpose (complex conjugate transpose) of matrix $\mathbf{A}$
$\mathbf{A}^T$	Transpose of matrix $\mathbf{A}$
$diag(\cdot)$	Diagonal matrix with components in blank
Σ	Summation operator
$\int$	Integral
$E\{\cdot\}$	Expected value
$*$	Convolution
$\ln$	Natural logarithm
$\text{Im}\{\cdot\}$	Imaginary part of a complex number
∇f	Gradient of the function f
$\mathcal{F}\{\cdot\}$	Fourier Transform
$\mathcal{F}^{-1}\{\cdot\}$	Inverse Fourier Transform
$\overline{f(x)}$	Mean of the function $f(x)$
$\angle s(t)$	Angle of the complex signal $s(t)$
$\lvert \cdot \rvert$	Absolute value
$arg\{\cdot\}$	Argument of a complex variable (number)
$\min\limits_{x}$	Minimum value of x for given conditions
x^*	Complex conjugate of x
$\mathbf{I}_n$	$n \times n$ Identity matrix
$\text{rect}[\cdot]$	Rectangular window function
$\mathcal{L}$	Lagrangian function
$\langle n \rangle_m$	Arithmetic modulo operation, n modulo m
x'	Derivative of x
$\widetilde{x}$	Estimation of x

Greek Symbols

ΔA	Gain imbalance in I-Q demodulator
$\Delta \phi$	Phase imbalance in I-Q demodulator
Δd	Travel distance during a pulse repetition interval
Δf	Subcarrier spacing
ΔL_{rs}	Separation between array elements
$\Delta \theta_{rx}$	Main lobe beam width
$\Delta \theta_{side}$	Angular range of side lobes
$\Delta \tau$	Delay spread
ΔR	Range difference
$\Delta \varphi(i)$	Steering angle of ith Rx channel
Ψ	Phase of Doppler spectrum
Ψ_e	Higher order phase error in Doppler domain
α	Over-sampling ratio
β	Order of PRF, order of aliasing
λ	Wave length
δR	Range resolution
δA	Azimuth resolution
δ	Kronecker delta function

ϵ_r	Relative dielectric constant
ξ	Lagrange multiplier
ζ	Scaling parameter
η	Order of grating lobes
σ^2	Variance of a random signal
θ	Elevation angle
θ_{3dB}	Half power beam width of antenna
θ_{inc}	Incident angle
θ_c	Look angle at the center of a target scene
θ_l	Look angle of the lth Rx beam (spatial filter beam)
θ_{un}	Elevation angle at where unambiguous echoes arrive
$\Delta\theta_{rx}$	Main lobe width of spatial filter (receive array)
φ	Phase variable
$\varphi_{e,i}$	Constant phase offset of ith receive channel
ρ	Interferometric coherence
ρ_H	Influence of different processing filters on interferometric coherence
ρ_a	Influence of temporal decorrelation on interferometric coherence
ρ_{SNR}	Influence of finite SNR on interferometric coherence
ϱ	Ratio between spatial sampling distance and total receive array length
τ	Time delay of echo signal
σ	Radar Cross Section (RCS)
σ_{ij}	Covariance of the ith and jth channel
ψ	Azimuth angle
ω	Angular frequency
ω_o	Angular frequency corresponding to signal bandwidth f_o
ξ_e	Flare angle in E-plane
ξ_h	Flare angle in H-plane

Latin Symbols

A_{ant}	Antenna area
$A_{ant,min}$	Minimum antenna area
A_{2way}	2-way amplitude pattern in Doppler domain
A_{ij}	Amplitude of channel transfer function H_{ij}
$\mathbf{A}$	Steering matrix in Doppler domain
B_p	Doppler processing bandwidth
C_{tx}	Transmit antenna pattern
C_{rx}	Receive array pattern
C_{2way}	Two-way antenna pattern
$\mathbf{F}$	DFT matrix
$F_w(k_a)$	Fourier transform of the function $f_w(y)$
$\mathbf{H}$	Channel transfer function matrix
$\mathbf{I}$	Identity matrix (or vector)
$\mathbf{N}$	Spectral noise vector (matrix)
$\mathbf{S}$	Input data sequence for the OFDM
G_T	Transmit antenna gain
G_R	Receive antenna gain
$I(t)$	In-phase component of an IF-band signal

$I_b(t)$	In-phase component of a baseband signal
K	Total number of targets in a received signal
$K_{1,2}$	I-Q channel imbalance factor
K_r	Chirp rate (FM rate)
L_a	Length of a pyramidal horn antenna aperture
L_{ant}	Loss due to antenna feed network
L_c	Compression loss
L_{mono}	Length of a monostatic SAR antenna
L_{tx}	Length of transmit antenna
L_{rx}	Length of receive array
L_{rs}	Length of single receive antenna or subarray
L_p	Length of rectangular patch element
M	Number of azimuth samples of single channel
$M_e(f, f_d)$	Matched filter function for the Doppler effect compensation
M_E	Number of Rx subarrays in elevation
M_T	Number of transmit antennas
M_R	Number of receive panels in azimuth
N	Number of subcarriers, time samples, lengths of FFT or IFFT
N_o	Noise power
N_{sub}	Number of subswathes
$N_{n,f}$	Number of ambiguities in the near and far range
P_e	Radial length from the apex to the base of a pyramidal horn in E-palne
$\vec{\mathbf{P}}_{e,ij}$	Position vector of the effective phase center of the ith receive and jth transmit antenna
P_h	Radial length from the apex to the base of a pyramidal horn in H-plane
$Q(t)$	Quadrature component of the an IF-band signal
$Q_b(t)$	Quadrature component of a baseband signal
$R_{rx,i}$	Slant range from a target to the ith receive antenna
R_s	Slant range in the boresight direction
$R_{tx,j}$	Slant range from the jth transmit antenna to a target
$R(\omega)$	Spectrum of a received signal
$\mathbf{R}_{rr}$	Covariance matrix of received signals
$\mathbf{S}$	Multiple waveform vector, input vector of a MIMO system
$S_j(f)$	Spectrum of the jth waveform $s_j(t)$
$S_d(f, u)$	Desired signal in frequency-azimuth domain
S_o	Signal power
S_w	Swath width
S_{sub}	Subswath width
SL	A desired side lobe level
T	Absolute temperature
T_p	Pulse duration
T_s	Sampling time(interval)
$\vec{\mathbf{T}}\mathbf{x}_j$	Position vector of jth transmit antenna
$\vec{\mathbf{R}}\mathbf{x}_i$	Position vector of ith receive antenna
V_p	Velocity of platform
W_a	Height of a pyramidal horn antenna aperture
W_{rs}	Height of a single element in an elevation receive array
W_{rx}	Total receive array height

W_{tx}	Transmit antenna height
$\mathbf{W}$	Beamforming weight matrix in Doppler domain
$\mathbf{W}_{rec}$	Reconstruction filter matrix
$\mathbf{W}_{mvdr}$	Beamforming weight matrix of MVDR method
Y_c	Azimuth center in a SAR image
Y_w	The length of an azimuth window used in PGA algorithm
$\mathbf{a}$	Steering vector in time domain
b_{HP}	Beam broadening factor
f	Frequency
f_{IF}	Intermediate frequency
f_{LO}	Local signal frequency
$f(x, y)$	Complex SAR image function in 2-D Cartesian coordinate, x-y
f_d	Doppler frequency
f_o	Signal bandwidth
f_s	Sampling frequency in fast-time
$f_w(y)$	Windowed version of function $f(y)$
g_i	Amplitude correction factor for ith channel
h_o	Altitude of SAR sensor
$h(t)$	Channel impulse response function
$i(t)$	Image band signal
k_a	Azimuth (Doppler) wavenumber
k_r	Range wavenumber
k_s	Wavenumber corresponding a spatial sampling frequency (PRF)
k_u	Spatial frequency (wavenumber) in u-axis
l_b	Width of a rectangular waveguide
$\mathbf{n}$	Gaussian noise vector (or matrix)
$\mathbf{r}$	Received signal vector(or matrix) in time domain
$r(t)$	Received signal in time domain
$r_l(t)$	Received signal from the lth subswath
$s(t)$	Transmitted waveform(signal) in time domain
$s_b(t)$	Baseband signal in time domain
$s_d(t)$	Desired signal
t	Fast-time
$\mathbf{w}$	Beamforming weight vector (or matrix) in time domain
$\mathbf{w}_{mvdr}$	Weight matrix of the MVDR beam former in time domain
w_a	Height of a rectangular waveguide
$x_{IF}(t)$	Complex IF local signal
$x_{LO}(t)$	Complex RF local signal
x_n	The nearest ground range in a subswath
x_f	The furthest ground range in a subswath

Constants

c_o	Speed of light, $2.997925 \times 10^8 m/sec$
k_{bol}	Boltzmann's constant, $1.3807 \times 10^{23} J K^{-1}$
R_E	Local Earth radius

1. Introduction

Microwave remote sensing is a powerful technique used to sense an object and deliver information about that object without physical contact. It has been successfully contributing to the understanding of the Earth system and to the monitoring of our natural resources. Spaceborne *Synthetic Aperture Radar* (SAR) has been playing an essential role in these contributions. It consists of an imaging radar sensor on a moving platform, which collects back-scattered signals during its movement and coherently synthesizes the signal in order to construct a large aperture, leading to a high resolution image. Since the idea of aperture synthesis proposed by Carl Wiley [132] in 1951 was first demonstrated, its high potential promoted intensive research activities on the SAR techniques. As a result, in 1978, the first civilian SAR satellite, SEASAT [68], was launched and opened a new era of Earth observation from space. Spaceborne SAR provided weather-independent radar images over a wide area, which airborne systems could not cover. In the 1990s, increasing awareness of the prominence of SAR led to several spaceborne SAR missions: the first European spaceborne SAR mission ERS-1 (1991), the following mission ERS-2 (1995) [2], the Shuttle Imaging Radar SIR-C/X-SAR (1994) [1], and Radarsat-1 (1995) [98, 5] have consecutively acquired plenty of data over the Earth. Thanks to the revolutionary improvement of observation capability, modern spaceborne SAR expands its utility into a wide spectrum of applications.

1.1. State-of-the-Art SAR System

A spaceborne SAR system is an aggregation of cutting-edge technologies which provide outstanding imaging capability and high performance. In this sense, state-of-the-art SAR has been leading revolutionary progress in microwave technology. The low-cost, high-efficiency *Monolithic Microwave Integrated Circuit* (MMIC) technology dramatically reduces the profile of *Transmit/Receive* (T/R) modules and the multilayer circuit technique improves the signal distribution of complex electronics. Above all, one of the most important technologies in the modern SAR system is the phased-array antenna, which can electrically steer the antenna beam and realize multiple data acquisition modes. Its beam-steering capability is exploited to enhance the swath width or the azimuth resolution. Those operation modes are commonly introduced in most modern SAR systems along with the standard stripmap data acquisition mode. Figure 1.1 shows the multiple modes based on the phased array antenna. In the spotlight mode shown in Figure 1.1 (b), the antenna beam continuously tracks a target area during the movement of satellite in a range of azimuth steering angles. Thus the signal integration time over the target area of interest is lengthened in comparison to the stripmap mode in Figure 1.1 (a). Thereby a fine azimuth resolution image can be achieved [126, 113, 20].

The scanSAR mode is specialized to substantially improve the swath width in the spaceborne SAR. The data acquisition of the scanSAR mode is illustrated in Figure 1.1 (c). In the scanSAR mode, the wide area of terrain is divided into multiple subswaths. The antenna beam illuminates each subswath during a specific period. Following this, the beam is steered to the next subswath and acquires the data in the same manner. A continuous SAR image over the wide area is reconstructed by stitching the subswath images, however with poor azimuth resolution

(a) Stripmap mode

(b) Spotlight mode

(c) ScanSAR mode
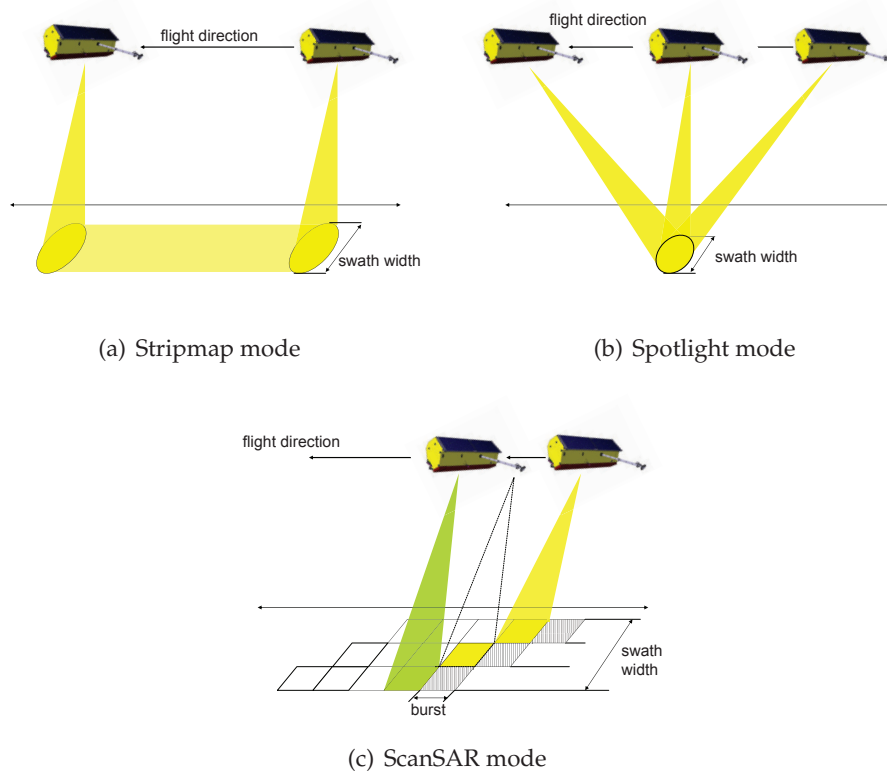
Figure 1.1.: Multiple SAR operation modes implemented by the phased array antenna in the state-of-the-art SAR system.

[90, 29]. The single-channel SAR images present the 2-D intensity maps of a target scene. However, the intensity information of targets may be insufficient for the classification and the identification of the targets and their properties. Therefore along with the single-channel modes, the modern SAR also employs multiple data acquisition channels in space, time or polarization. The use of dual orthogonal polarizations, typically horizontal and vertical, on transmission and reception allows the measuring of full scattering coefficients. More detailed information about geophysical properties and electromagnetic scattering process can be obtained by the polarization synthesize techniques, which is called *polarimetry* [144, 17]. Hence *Polarimetric SAR* (PolSAR) is an indispensable tool in modern airborne and spaceborne SAR remote sensing. Figure 1.2 (a) shows a fully polarimetric SAR image obtained by DLR's airborne SAR system, E-SAR [3]. The first full polarimetry in a SAR satellite was demonstrated by Japanese Earth Observation Satellite ALOS at L-band (1.27GHz) [108]. Recent spaceborne SAR missions, such as TerraSAR-X, COSMO-SkyMed, and Radarsat-2, also adopt the fully polarimetric data acquisition mode for a wide scope of applications.

A further benefit of the multichannel data acquisition in the modern spaceborne SAR is also found in its global 3-D imaging, motion estimation and change detection capabilities. *SAR Interferometry* (InSAR) is a radar technique to extract such information using the data acquired at different positions or times. The InSAR produces an interferogram by coherently processing differences in phase between multiple complex SAR images, and provides several measures of geophysical quantities, such as topography, deformation and ocean currents on a global scale [12]. As an example, Figure 1.2 (b) shows an interferogram produced by the *Shuttle Radar Topog-*
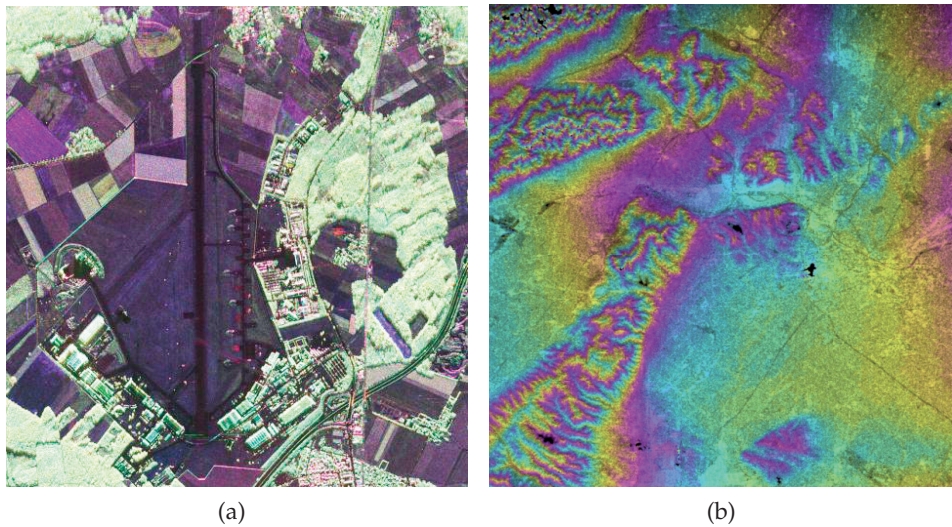
Figure 1.2.: Examples of multichannel SAR images: (a) fully polarimetric SAR image at C-band, German Aerospace Center (DLR), Oberpfaffenhofen, Germany and (b) SRTM C-band SAR interferogram, Los Angeles, California, USA (©JPL/NASA).

raphy Mission (SRTM) in the year 2000, which has proved the capability of topographic mapping from space and has generated nearly global topographic data.

In summary, the contribution of the spaceborne SAR to scientific and technological progress, environment monitoring and understanding our planet is beyond doubt. Additionally, it is expected that the commercial use of the spaceborne SAR data will be increasingly popular in future. The German TerraSAR-X satellite built in public-private partnership may be a representative example. From a technical point of view, the modern SAR has been making technical progress on the basis of a monostatic system configuration, combined with analog beam steering capacity, however has not been able to overcome inherent restrictions in SAR performance. Therefore there are increasing demands for a new paradigm for the next generation spaceborne SAR.

1.2. Motivation and Contributions of this Work

Expanding utilities of SAR data in various fields, capabilities of frequent monitoring, wide coverage and high geometric resolution are becoming issues of greater and greater importance in spaceborne SAR missions. In particular, the observation of a wide area with fine resolution is of great interest for various applications, such as the surveillance of geological formations, biomass and other dynamic features. However, the state-of-the-art SAR sensors do not simultaneously satisfy these demands. This work aims to establish a novel SAR system concept and techniques based on a digital multichannel radar concept, in order to overcome the modern SAR performance and satisfy the demands in a wide range of applications. Through this, the work seeks to open up a new perspective to approaching the ultimate goal of an adaptive high-performance SAR system. Figure 1.3 displays the background and the contributions of this work in diagram form.

Figure 1.3 presents the challenges in the modern SAR in ❶, a new digital system approach as a transition from the current SAR to a future SAR concept in ❷, and the final goal pursued
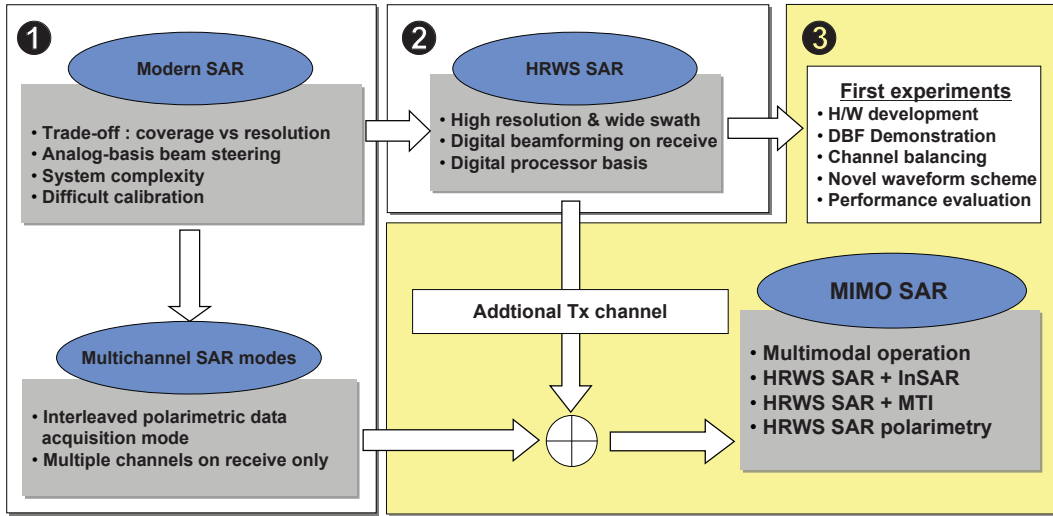
Figure 1.3.: Motivation and new contributions of this work.

in the present work in ❸. Based on Figure 1.3, the following sections concretely address the motivation and the contributions of this work.

1.2.1. Challenges in Modern SAR

Challenges facing the modern SAR are inherent limitations originating in the SAR operation principles or difficulties emerging from technological issues. This section addresses several important challenging topics in the modern SAR, stated in Figure 1.3 ❶.

Trade-off between Azimuth Resolution and Swath Width

The performance of modern SAR systems is limited by a strict rule regarding the antenna area to avoid ambiguities, a so-called minimum antenna area constraint [122]. The relationship is derived by considering the antenna pattern, *Pulse Repetition Frequency* (PRF) and the SAR geometric parameters. It is given by

$$A_{ant} > \frac{PRF}{PRF_{low}} \cdot \frac{4 \cdot V_p \cdot \lambda \cdot R_s}{c_o} \cdot \tan\theta_{inc} \tag{1.1}$$

where c_o denotes the speed of light; V_p is the sensor velocity; λ is the wavelength of carrier frequency; R_s and θ_{inc} denote the slant range at the boresight of antenna and the incident angle respectively; and PRF_{low} is the PRF lower bound for a desired azimuth resolution. For the given geometric parameters, the antenna area A_{ant} is determined by only the ratio between *PRF* and the lower limit PRF_{low}. The theoretical minimum antenna size is hence found when the ratio is equal to unity[1]:

---

[1]In practical system design, the ratio near unity is undesirable since it allows no design margins.

$$A_{ant,min} = \frac{4 \cdot V_p \cdot \lambda \cdot R_s}{c_o} \cdot \tan \theta_{inc}. \tag{1.2}$$

It means the minimum antenna area is determined by the geometric parameters. To increase the swath width, the antenna height must be reduced according to the reciprocal proportion between the antenna height and elevation beam width. Therefore the total antenna area becomes smaller but is limited by the lower bound of PRF. If the antenna height is reduced for further increment of the swath width, *PRF* must be set lower than its lower bound, and consequently, it leads to azimuth ambiguities in SAR images. On the other hand, for the improvement of the azimuth resolution, the lower bound of PRF must be increased, since it corresponds to the spatial sampling frequency in along-track. As a result of this, the swath width is reduced. In conclusion, the azimuth resolution can be improved at the cost of the swath width and vice versa [122, 30, 31].

As aforementioned, a time-multiplex imaging mode, such as the scanSAR mode, improves the swath width but deteriorates the azimuth resolution due to limited data acquisition time for each subswath [90]. In contrast, the spotlight mode dramatically improves the azimuth resolution only on a confined narrow area. Therefore the current SAR operation modes, based on the analog beam steering, cannot enhance both the swath width and the azimuth resolution at the same time.

Interleaved Polarimetric Data Acquisition

A SAR system employing an orthogonal dual-polarized antenna on both transmission and reception can acquire the complete scattering matrix, which accounts for polarimetric scattering characteristics of targets. The modern SAR systems transmit the orthogonally polarized pulses alternatively, so that only two scattering components for each transmitted polarization are acquired. In consequence, the entire scattering matrix is measured through two successive pulse transmissions, as shown in Figure 1.4.
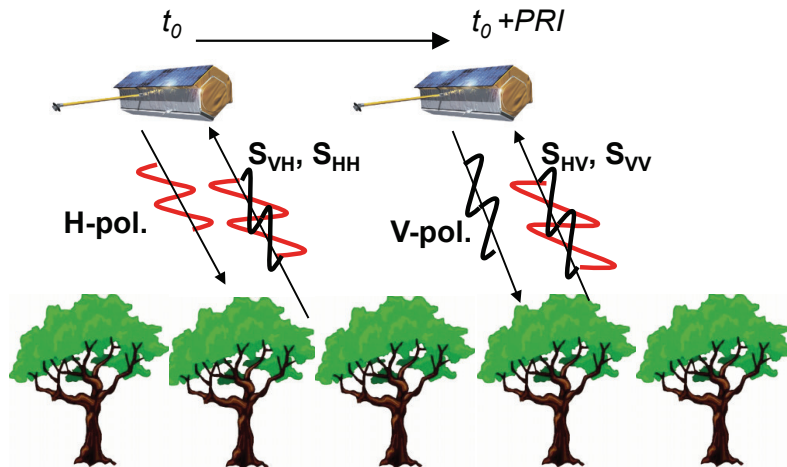
Figure 1.4.: Conventional mode for the fully polarimetric data acquisition.

Since the inter-pulse interval corresponds to the *Pulse Repetition Interval* (PRI), which is the reciprocal of PRF, a shorter interval leads to a narrower coverage, according to (1.1). As a

result, the current interleaved acquisition mode requires either a twofold increase of the PRF or the azimuth resolution reduction [144, 17, 64]. This trade-off can be more severe, when the polarimetry is combined with the interferometry, a so-called *Polarimetric SAR Interferometry* (Pol-InSAR) [24]. In this emerging technique, the PRF must be increased fourfold to achieve the maximum baseline between two sensors[2].

System Complexity and Calibration

Modern SAR systems employ the phased array antenna composed of hundreds of radiating elements and *Radio Frequency* (RF) electronics. Phase shifters and *Variable Gain Amplifiers* (VGAs) integrated in the T/R modules make electrical beam steering possible. Thanks to *Low Temperature Cofired Ceramic* (LTCC) and MMIC technologies, a compact and low-loss T/R module is available [114]. Nevertheless, the phased array remains the most complicated and the heaviest subsystem among spaceborne SAR subsystems. In addition, the complex feed networks with many cables and connectors introduce the loss, which degrades receiver sensitivity [103].

Regarding the system calibration, the SAR antenna can be a major source of calibration error. The SAR electronic is characterized by the internal calibration process using inserted known reference signals, called calibration pulses. However, the major difficulty of the phase array calibration lies in the characterization of the performance of each array element. This is because signals from the hundreds of array elements and T/R modules are combined before digitization and storage devices [30]. This makes it difficult to measure the individual performance.

Another calibration issue is the correction of dynamic errors occurring in operation, such as phase drift or gain variation. For this calibration, each T/R module monitors temperature variations in flight and adjusts a control voltage of the phase shifter, according to the look-up table which accounts for the pre-measured thermal behavior of the phase shifter. Unfortunately, a difficult problem arises from the fact that the relationship between the phase shifter behavior and the control voltage is slightly time-variant. It will result in an additional source of error [134, 23].

In future SAR systems, it is desired to improve the calibration quality and also reduce the calibration efforts. A digital array system allows a sophisticated error estimation and correction by signal processing either on-board or on-ground [130]. Therefore the current phased-array antenna system may be replaced by a software-defined adaptive digital systems in the future.

1.2.2. HRWS SAR Concept

An innovative SAR concept, called a *High-Resolution Wide-Swath* (HRWS) SAR, was proposed in order to resolve the fundamental trade-off between the coverage and the azimuth resolution [117, 119]. As stated in Figure 1.3 ❷, this system enables the production of high resolution SAR images over a wide area with the aid of *Digital Beamforming* (DBF). Its operation and an example configuration are illustrated in Figure 1.5.

The system operates with a low PRF in order to increase the swath width. According to its operation principles, this system is equipped with a small transmit antenna and the broad beam of this transmit antenna in both elevation and azimuth illuminates a wide area. On the other

---

[2]This acquisition mode is called ping-pong mode [71].

hand, a large array is employed on receive. The low signal gain resulting from the small transmit antenna is compensated by high-gain beam scanning on receive [117, 119]. The receive array consists of multiple independent receive channels in along-track, as shown in Figure 1.5. Data acquired by these channels are combined for increasing the spatial sampling rate, and thereby the azimuth resolution can be improved as well.
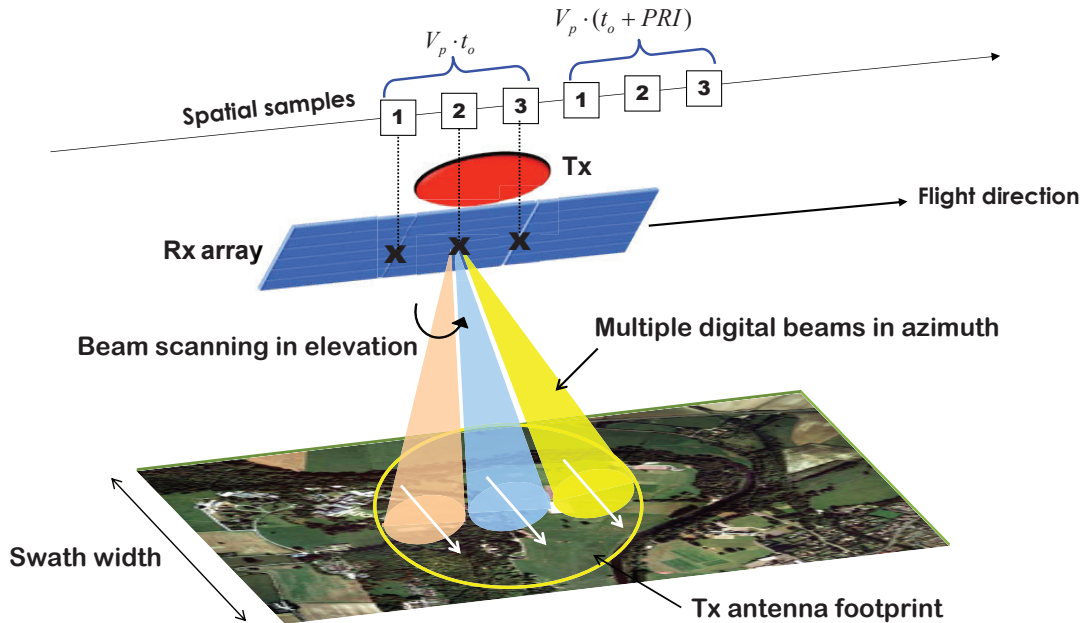
Figure 1.5.: Illustration of the HRWS SAR imaging system and its conceptual operation.

If the multiple receive channel data are simply interleaved in along-track, the azimuth samples can be increased. However, it causes additional azimuth ambiguities in the case of non-uniform azimuth sampling [139, 58]. To put it simply, only using a specific PRF, one can achieve the optimal imaging performance. DBF algorithms presented in [69, 79] make it possible to suppress the azimuth ambiguities and increase the effective PRF, even using the non-uniformly sampled data.

This system provides more stability and flexibility in hardware design and implementation, since the system consists of mostly digital hardware. The separated and independent multiple receive channels allow real-time adaptive calibration using image signals by means of digital signal processing techniques. Investigations of the HRWS SAR do not just remain at conceptual studies, but also continue towards the implementation of the system. For instance, a digital array antenna and RF breadboards are developed and used to verify this advanced system concept and the DBF technique [42].

1.2.3. Contributions and Outline of this Work

As introduced up to this point, the challenges and the desired performance in spaceborne SAR systems motivate a novel system approach, which enables the multimodal operation and the high performance imaging simultaneously. To build a new SAR system concept satisfying this demand, this work encompasses with a wide range of technical topics from hardware to digital signal processing. The main contributions of the present work are as follows:

- Establishment of a novel multimodal SAR system concept

- Development of a novel waveform scheme and processing algorithms

- Development of a laboratory measurement system

- Experimental validation of novel techniques

The need of multi-functionality in future SAR systems is emphasized when it is intended to combine multichannel acquisition modes with the HRWS SAR imaging mode[3]. In the case of single-pass interferometry, a secondary large receive array will be required for producing hybrid HRWS SAR images. If these large arrays must be carried on a single satellite, it can be problematic in the system implementation. Furthermore, the conventional interleaved mode (see section 1.2.1) costs either the coverage or the resolution in the fully polarimetric data acquisition in any case. Therefore the full HRWS SAR imaging performance cannot be achieved in such combinational modes.

This work adopts multiple antennas both on receive and transmit in order to realize the multimodal operation and outperform the modern SAR, as shown in Figure 1.3 ❸. Such systems are known as *Multiple-Input Multiple-Output* (MIMO) systems. This work establishes a novel MIMO SAR concept, combined with DBF and orthogonal waveform scheme, and develops the operational principles of the MIMO SAR. Although the term *MIMO SAR* was previously used in literatures [128, 37, 78, 107, 65], the MIMO SAR system presented in this work will be distinguished from previous system approaches in regard to the system purpose, operation and technique.

A vital issue in the MIMO SAR system is multiple waveform design. The MIMO SAR system needs new waveforms that must be separable from each other, and SAR images reconstructed from the waveforms should be sufficiently coherent for the interferometric and the polarimetric post-processing. In other words, the new waveform should fulfill the requirement of the orthogonality and the high coherence. The present work develops a novel waveform scheme and relevant processing algorithms inspired by the *Orthogonal Frequency Division Multiplexing* (OFDM) principle. Uniqueness of the novel waveform scheme is the fact that it still uses a chirp signal as a basic waveform function, but it is highly orthogonal in frequency domain. It implies that the multiple orthogonal waveforms can be produced from the same frequency band, and focused SAR images from these waveforms are highly coherent. This work intensively investigates the orthogonality and the coherency of the developed waveforms regarding a typical distributed target scenario.

The scope of this work is not limited to develop the new technique and evaluate performances, but also expanded by experimental verification for the MIMO SAR techniques. As one of core techniques in the MIMO SAR, the digital beamforming plays an essential role in selective data acquisition and ambiguity suppression. This work presents the first experiment for the digital beamforming in along-track and also demonstrates its capability. For this purpose, a laboratory experimental system is developed and is dedicated to the demonstration. This work addresses hardware design issues for successful demonstration and hardware system aspects, as well as experimental results. This dissertation is composed of two main parts. One part copes with the theory and principle of the MIMO SAR system operation and techniques, and the other part focuses on the subject of experiments and verification.

---

[3]The term "*HRWS SAR imaging*" is used to indicate an imaging mode to overcome the inherent trade-off between the swath width and the azimuth resolution, but does not name a specific system in this dissertation.

Chapter 2 presents an overall MIMO system concept and operational principles. Starting with the description of a generic system configuration, this chapter introduces the main functionality of each subsystem and technical issues regarding its implementation. In this chapter, some example modes are presented in order to show exploitation of increased degrees of freedom of this system for the multimodal operation. Based on those modes, a general MIMO SAR processing strategy is established. Before coming to detailed signal processing, this chapter briefly points out challenging topics in MIMO SAR and in current approaches. Through this, the next chapters will highlight the uniqueness of this work.

Chapter 3 deals with the basic principles and theories of MIMO SAR techniques. First of all, a MIMO SAR signal model is developed in Cartesian coordinates and used to describe the principle of digital beamforming, plus its cooperative roles in the MIMO SAR system. This chapter also introduces principles of the classical OFDM technique, which was originally developed to counteract a frequency selective channel in wireless communications, and addresses the key idea exploited in this work for the multiple OFDM waveform generation. In addition, a schematic implementation model of the OFDM technique is presented and certain issues regarding the system realization are discussed.

Chapter 4 focuses on a MIMO SAR transmission strategy and novel waveform technique, based on the OFDM principle introduced in Chapter 3. Starting with reinterpreting the conventional chirp waveform, this chapter derives the novel orthogonal waveform scheme for dual transmit antennas. In particular, this chapter develops an analytic signal model for the OFDM waveform and describes the detailed modulation and demodulation algorithm combined with spatial filtering using this model. The rest of the chapter is dedicated to the intensive evaluation of the waveform performance and feasibility in regard to real SAR target scenarios through simulations and experiments.

Chapter 5 introduces several important system design parameters, particularly antenna parameters regarding the digital beamforming and the OFDM demodulation performance. This chapter also presents an example system design and evaluates the performance of the designed system in terms of the system sensitivity and image quality.

Chapter 6 and 7 cope intensively with the theme of *Ground-Based* (GB) SAR experiments. To begin with, in a short range radar scenario, system parameters are specified, and thereby a GB multichannel SAR system is built for the demonstration of the MIMO SAR techniques. The system is composed of several subsystems, such as Tx/Rx antennas, RF front-end subsystem, digital instruments and a moving platform including a precise stepper motor and its controller. Chapter 6 describes the design, development and characterization of each subsystem in detail. The developed GB SAR demonstrator is used to carry out several multichannel SAR experiments in side-looking SAR geometries. Specific geometries and data acquisition methods in the measurements are presented in Chapter 7. This chapter starts with introducing an experimental MIMO SAR processor which is implemented for the experiments. The $\omega-k$ SAR processing algorithm is adopted and combined with the digital beamformer algorithm and the OFDM demodulator. The experiment addresses a channel imbalance effect on the digital beamforming performance. In this work, a digital channel balancing algorithm is implemented for the correction of the channel imbalance in phase and amplitude. This chapter introduces every processing step and corresponding result, and finally reveals the first experimental results of DBF in SAR. Furthermore, an equivalent experiment for the developed OFDM waveform scheme is carried out using the measured GB SAR data.

Finally, Chapter 8 summarizes the contributions of this work with a conclusion and emphasizes the benefits of the system and techniques developed in this work. This chapter also includes a discussion about potential techniques that are expected to boost the MIMO SAR imaging capabilities as well as challenges to be investigated, and encourages them for future research.

2. Novel MIMO SAR Approach

In the early 1990s, for the purpose of increasing channel capacity, Paulraj and Kailath have proposed the use of multiple antennas for both the transmission and the reception in wireless communications [99]. This multiple antenna concept has been showing great potential for various applications not only for wireless communications, but also for radar sensors. It has triggered active research works on the multiple antenna systems. Consequently, a radar system with multiple antennas, called *MIMO radar*, is currently one of the most popular topics in radar communities [43].

An early idea behind the MIMO concept for radar was to realize a large co-array by combining multiple transmit and receive antennas. The co-array principle was widely applicable for both coherent and incoherent sources with M_T transmit and M_R receive antennas. If the MIMO radar transmits multiple independent waveforms through spatially uncorrelated antennas, each receiver acquires multiple angular responses from a target delivered by the independent waveforms. The angular responses provide $M_T \times M_R$ independent phase centers, and thereby a large equivalent array is constructed [53]. The array elements must be arranged to avoid angular ambiguities within the angular range of interest. Adjusting the antenna constellations, the MIMO radar brings astonishing improvements to the angular resolution [13, 14, 6, 106, 137, 109]. In addition, the MIMO radar permits the use of spatial or angular diversity techniques to improve the detection capability. For example, the independence of the multiple channel data is exploited in order to compensate the fluctuation of *Radar Cross Section* (RCS) or the angular spread. As a result, the probability of detection can be substantially improved [14, 43, 110, 76].

Approaches for MIMO SAR imaging can be different from the MIMO radar, which is mostly dedicated to detect certain target objects. The present work suggests to utilize the MIMO antennas for multimodal operation and improving SAR image quality. Depending on the MIMO antenna constellation, multiple complex SAR images can be simultaneously produced and used for the coherence post-processing. Furthermore, suppressing ambiguities using the multichannel data contributes to SAR image quality enhancement synchronistically. To make use of the potentials and the advantages provided by the MIMO SAR concept, proper multiple waveforms and involved processing techniques must be developed.

Prior to dealing with concrete MIMO SAR techniques, this chapter presents a novel MIMO SAR system concept, a generic system configuration, and operational principles in a wider sense. In particular, the multimodal operation principles show the uniqueness of this approach to overcome the limitations of current systems and achieve the multi-functionality required. This chapter concludes by giving an overview of existing approaches and addresses an important technical issue on the present MIMO SAR approach. The MIMO SAR is not only based on a single platform system but multiple platforms as well. This chapter draws the system concept, data acquisition strategies, and multimodal operation principles for a single platform case for simplicity. However it must be emphasized that the theoretical background is the same for multistatic configurations as well.

2.1. System Configuration

Figure 2.1 depicts a conceptual system block diagram. The proposed MIMO SAR system consists of the transceiver subsystems with multiple antennas, the digital waveform modulator and demodulator block, and the multiple HRWS SAR processing units.
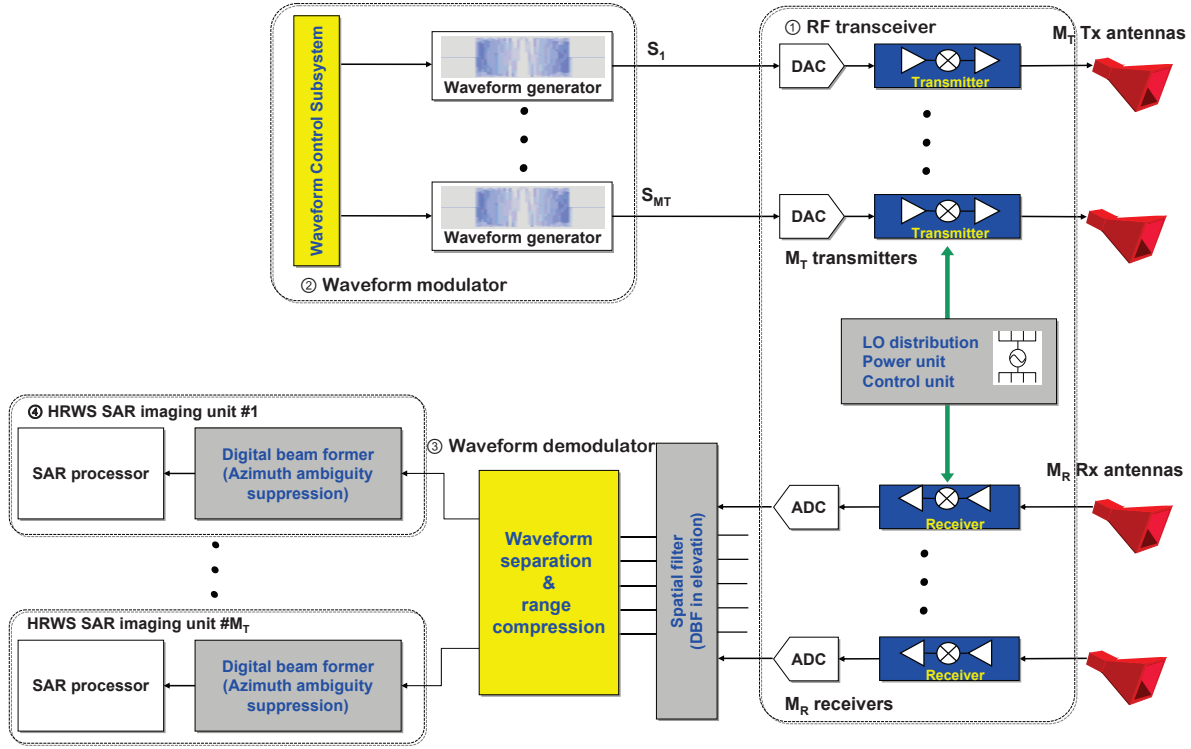
Figure 2.1.: Generic MIMO SAR system block diagram.

2.1.1. Transmit and Receive Antennas

The antenna block is composed of dual-polarized M_R receive subarrays displaced in azimuth and M_T transmit antennas. According to the HRWS SAR imaging principle, each receive subarray consists of a number of array elements in elevation, so the whole receive antenna becomes a 2-D array. Each element within the subarray is connected to an independent receiver containing its own *Analog-to-Digital Converter* (ADC). Considering the large number of antenna elements, a low-profile and low-cost antenna technology would be essential. For instance, the microstrip patch antenna could be considered as a good candidate due to its light weight and easy integration with other RF components, such as the *Low Noise Amplifier* (LNA) [42]. The multiple transmit antennas can be independently accommodated or likewise, a part of the receive subarrays can also be used for the transmission.

The transmit antenna is combined with an independent transmitter and *Digital-to-Analog Converter* (DAC) unit, most likely the receive antenna. An important requirement would be a highly efficient transmit antenna since each transmit antenna should illuminate a wide area. Thus, the low antenna gain due to a small antenna size should be taken into account. Trav-

eling wave antennas such as horn antennas can be adequate for the MIMO SAR. Moreover, a rapid progress of antenna technology leads to highly efficient deployable reflector antennas, which are available for lower frequency bands as well [45, 84]. The reflector antenna, combined with a digital feed array, offers the important benefit to generate a broad beam by activating all feed elements [141]. Further issues regarding the antenna block are the polarization purity, which is a common topic in modern polarimetric radars, and the homogeneous characteristic of receive array elements to mitigate calibration efforts and optimize the digital beamforming performance.

2.1.2. Transceiver Subsystem

The basic function of the transceiver (see Figure 2.1 ①) is not too dissimilar to that of conventional SAR systems. It basically amplifies signals and converts them to the baseband on receive, or similarly converts them to a RF band on transmit. Compared to RF frontend modules of the conventional SAR, the main aspect is the independent transmit and receive channels, including individual DAC and ADC units for each channel. This is a typical configuration of the digital radar concept, and leads to simpler optimization and higher integration than the conventional system [130]. Unlike the conventional PolSAR mode, the present MIMO system aims at simultaneous polarimetric data acquisition. For this purpose, each polarization channel needs its own transceiver subsystem instead of the polarization switch of the conventional SAR. Therefore, the number of transceiver subsystems increases. Concerning mass, power consumption, and cost of the transceivers for all subarray elements, the digital-IF receiver topology can be eligible for this system, since it reduces the number of analog devices by performing the I-Q demodulation in digital domain [42]. Regarding the wide coverage, highly efficient *Traveling Wave Tubes* (TWTs) can be used for high power amplifiers. For the coherent detection, this subsystem contains a local signal distribution network, either with a single local oscillator or multiple local oscillators which are synchronized to each other. In any case, the distribution network must be designed to minimize the leakage of the local signal and to achieve a sufficient isolation level. Furthermore, stable power generators will be included in this subsystem.

2.1.3. Digital Waveform Modulator and Demodulator

The main function of these parts is to generate multiple waveforms for the transmitters and to separate those waveforms on receive. Figure 2.1 ② and ③ show the waveform modulator and demodulator block, respectively. According to operation commands, the waveform control subsystem adjusts waveform parameters and assigns them to individual waveform generators. The waveform generator is based on a *Direct Digital Synthesis* (DDS) technique, which enables numerical determination and digital tuning of the frequency and phase of sinusoidal signals to produce various waveforms [120, 8]. The waveforms are then stored in fast *Random Access Memory* (RAM) and reused or modified by software, even in flight.

On receive, the spatial filter block (DBF in elevation) preliminarily processes received signals and afterwards the demodulator separates the transmitted waveforms. This block includes *Fast Fourier Transform* (FFT) and *inverse* FFT (IFFT) blocks, digital correlation filters (matched filters), and other digital signal processing units that may be needed for the demodulation. To effectively handle a large volume of data from multiple receive channels, the demodulator consists of parallel on-board processors, which are supposed to be highly reliable, cost-efficient,

and adaptable. It could be achievable by intensive use of *Field Programmable Gate Array* (FPGA) based solutions [55].

2.1.4. HRWS SAR Processing Unit

The HRWS SAR processing unit in Figure 2.1 ④ consists of two main parts. One is the digital beamforming unit for the azimuth ambiguity suppression, and the other is the conventional SAR processor. Since the DBF is a linear processing, the digital beam former can be modularized and integrated with the SAR processor. Therefore, a significant modification of the conventional SAR processor is not required. The HRWS SAR processing unit consists of a bank of M_T parallel processors and each unit reconstructs a HRWS SAR image. The reconstructed multiple SAR images will be used for post-processing. As a rule, this block is not deployed on the flight system but is implemented on the ground segment.

2.2. System Operation

A large digital array forms separate multiple phase centers, which can be regarded as spatial samples. The present MIMO SAR operation is closely associated with strategies to acquire such multiple spatial samples and exploit them for mission objectives. This section describes the data acquisition mode for standard SAR imaging and the multimodal operation principles.

2.2.1. Data Acquisition

The data acquisition of the present MIMO SAR system is divided into fast-time[1] and slow-time[2] domain. In both domains, the digital beamforming plays a key role in data acquisition and enhances the system imaging performance.

Fast-Time Data Acquisition

First, the data acquisition in fast-time domain is discussed. This data acquisition is closely associated with the digital beamforming in elevation. Each element of the receive array in elevation illuminates a target scene with a broad beam and captures back-scattered signals from the target simultaneously. The digital beam former at the end of the elevation channels coherently sums the signals and realizes a high gain beam in elevation. Figure 2.2 illustrates two DBF approaches in fast-time.

The first approach shown in Figure 2.2 (a) divides a long echo signal into multiple data subsets, depending on *Angle of Arrival* (AoA). In this case, the multiple digital beams are regarded as multiple spatial filters. Each beam collects signals only from an angular range of interest and suppresses signals outside of the angular range. This functionality will play a vital role in MIMO SAR imaging and details regarding that shall be dealt in Chapter 4.

The second approach in Figure 2.2 (b) is to continuously steer a high gain digital beam over the whole swath, the so-called *SCan-On-REceive* (SCORE) technique [117, 119]. This technique

---

[1]The fast-time is the commonly used definition of time in terms of range processing.
[2]The slow-time is the temporal domain representation of SAR sensor positions in along-track.
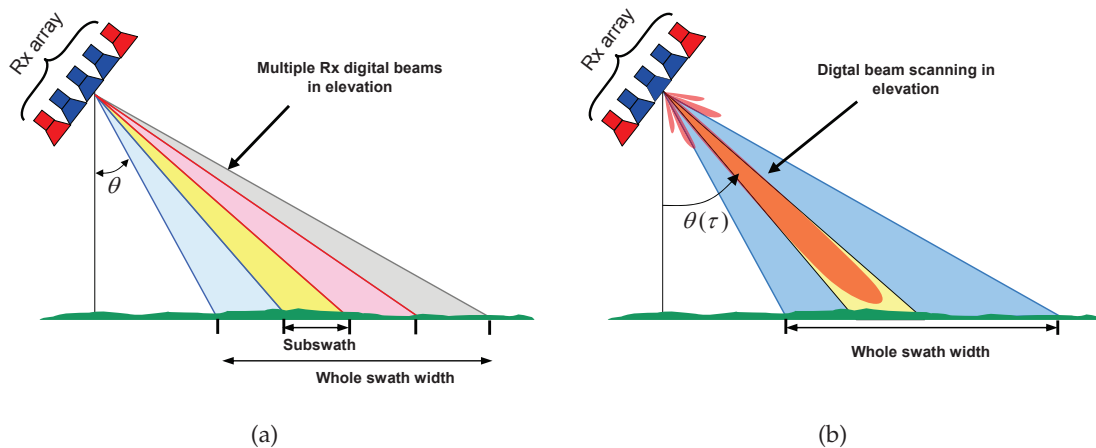
Figure 2.2.: Spatial filtering in elevation angle via (a) simultaneous multiple digital beams and (b) continuous digital beam scanning (SCORE).

changes the steering angle at each time instant from SAR geometries, so that the digital beam traces the ground pulse over the whole swath continuously.

Those beamforming functions can be incorporated into a real-time processor with the aid of a parallel signal processing. It would be of important merit to handle a burden of data acquired from the wide area [70]. Additionally, the DBF in elevation improves the *Signal-to-Noise Ratio* (SNR) and suppresses the range ambiguities by forming nulls.

Slow-Time Data Acquisition

The data acquisition in slow-time is carried out by the separate multiple receive channels with low PRFs, which allow a wide area observation. However this either deteriorates the azimuth resolution or results in the azimuth ambiguities [139, 49].

Figure 2.3 illustrates the spatial sampling in along-track with the four receive subarrays. The transmit antenna is positioned in the middle of the whole receive array. The sensor transmits a pulse and the four receive subarrays collect signals simultaneously. According to the *Displaced Phase Center Antenna* (DPCA) principle (see Appendix A), each transmit and receive antenna pair can be regarded as an equivalent monostatic antenna and its effective phase center is situated in the middle between the phase centers of the transmit and receive antennas [94]. In fact, the spatial sample positions are coincident with the effective phase centers of every bistatic pair. Every transmission event produces a set of multiple spatial samples in along-track. Thereby the effective spatial sampling rate[3] increases. In Figure 2.3, the effective phase centers in along-track are indicated by different symbols.

The multiple phase centers provide the optimum performance in the case of a uniform sampling in along-track. However uniform sampling leads to the strict requirement which demands that the travel distance Δd within successive pulses, must be equal to half of the receive array length [139, 137]:

$$\Delta d = \frac{V_p}{PRF} = \frac{M_R \cdot L_{rs}}{2} \tag{2.1}$$

---

[3]The spatial sampling rate or frequency corresponds to PRF in a side-looking SAR system.

where M_R is the number of receive subarrays and L_{rs} is the length of a single subarray. It means that the uniform sampling can be achievable only with a particular PRF, called uniform PRF. Otherwise, the spatial sampling becomes non-uniform and the performance is degraded. Robust digital beamforming algorithms in [69, 79] overcome the rigid uniform sampling requirement and provide steady performance for various PRFs. Therefore, a possible PRF selection range is expanded.

Figure 2.3.: Slow-time data acquisition via the multiple receive antennas and the spatial sampling representation by the effective phase centers between transmit and receive antennas. For clarity, a single transmit antenna is assumed.

2.2.2. Spatial Sampling Criteria

This section describes detailed spatial sampling rules based on a uniform receive array of a single platform system. As shown in Figure 2.3, the spatial samples are acquired at the effective phase center positions and are distributed in along track. The spacing between receive subarrays is described as the following:

$$\Delta L_{rs} = \zeta \cdot L_{rs} \tag{2.2}$$

where ζ is the scaling factor indicating the relative separation with respect to the subarray length L_{rs}. For example, if ζ is equal to one, then there are no gaps between the subarrays ($\Delta L_{rs} = L_{rs}$). This is typical array geometry of a single platform case. A very large ζ may mean a uniform multistatic constellation[4]. In the same manner, (2.1) is generalized as

$$\Delta d = \varrho \cdot \frac{M_R \cdot L_{rs}}{2} \tag{2.3}$$

where ϱ is the spatial sampling scaling factor and dependent on PRF. Although the multiple subarrays in along-track increase the number of spatial samples, the travel distance Δd must

---

[4]A more general formulation regarding antenna position and the sampling is derived in [69]

satisfy the Nyquist sampling criteria. Therefore, ϱ must fulfill the following condition:

$$\varrho = \frac{2 \cdot \Delta d}{M_R \cdot L_{rs}} \leq 1 \tag{2.4}$$

Using (2.2) and (2.3) the spatial sample position u is formulated as follows:

$$u = \varrho \cdot \frac{M_R \cdot L_{rs} \cdot (m-1)}{2} + 0.5 \cdot (i-1) \cdot \Delta L_{rs} \tag{2.5}$$

where m denotes the sensor position in along-track and i is the receive subarray index. ($i = 1, 2, 3, \cdots, M_R$)
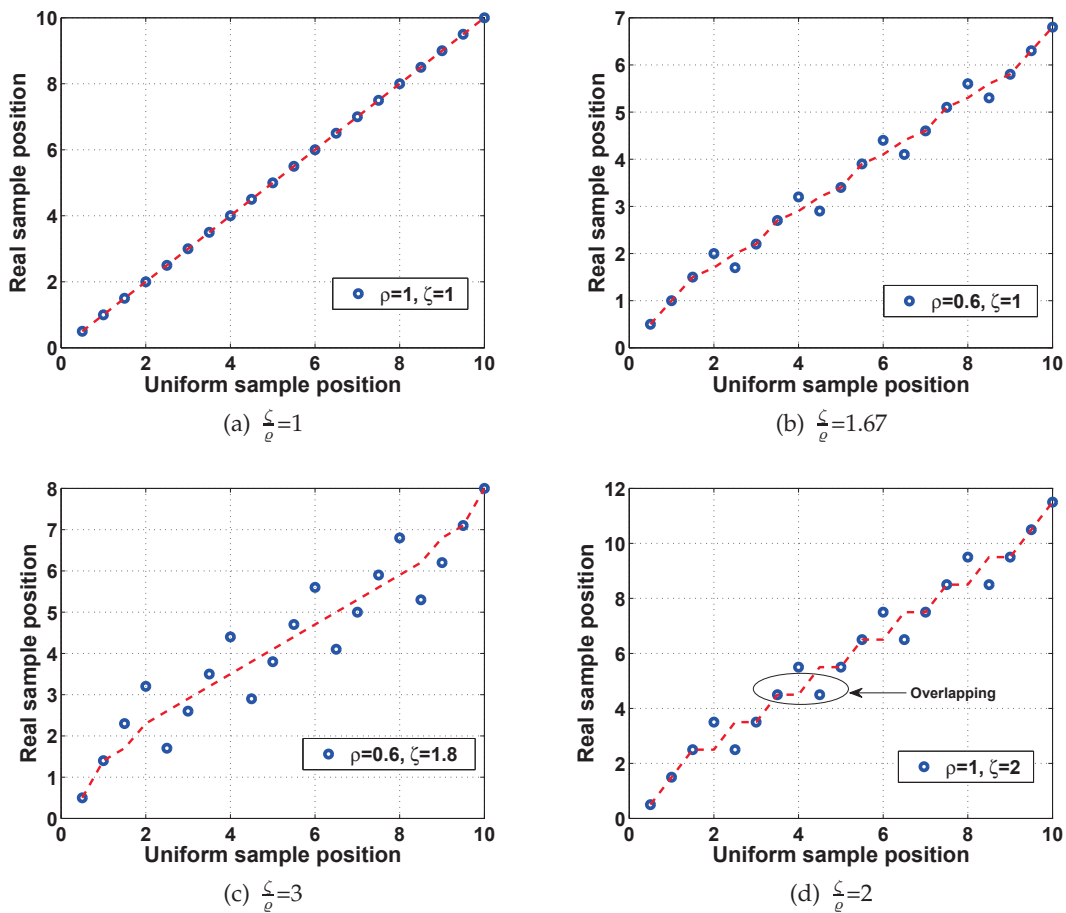
Figure 2.4.: Examples of the spatial sample distribution according to the sampling criteria: (a),(c) uniform sampling, (b) non-uniform sampling, and (d) uniform-overlapping sampling.

From (2.5) and (2.2), sampling criteria can be built for the non-overlapping uniform spatial sampling. First of all, $\frac{\zeta}{\varrho}$ must be positive odd numbers

$$\frac{\zeta}{\varrho} = 1, 3, 5, \cdots \tag{2.6}$$

and not be even numbers:

$$\frac{\zeta}{\varrho} \neq 2, 4, 6, \cdots \tag{2.7}$$

Only if the above conditions are satisfied, the spatial samples will be uniform and will not overlap. In some cases, the intention is to form several overlapping spatial samples at different instances. The criteria offer an easy determination of PRF for various sampling requirements.

Several examples are plotted in Figure 2.4 in the case of four receive subarrays (M_R=4), where the circles indicate the effective phase centers of the array. The vertical axis is the real spatial sample position in the along-track direction, and the horizontal axis is the sample position in the case of uniform sampling. Both axes are normalized by the single subarray length L_{rs}. If the real spatial samples are uniform, then their projection (dashed line) in along-track increases linearly versus the ideal sample position, as shown in Figure 2.4 (a). In contrast, if the spatial sampling violates the first criterion (2.6), the projection loses the linearity, which means a non-uniform sampling, like that shown in Figure 2.4 (b). Figure 2.4 (c) shows the spatial sample distribution in the case of a large separated array. $\frac{\zeta}{\varrho}$ meets both criteria (2.6) and (2.7), so that the spatial samples are uniformly distributed, except the outermost samples, due to a larger antenna separation than L_{rs} ($\zeta > 1$). Figure (d) is a typical case of a uniform distribution of overlapping samples. This occurs since the sampling meets only the criterion (2.6) and not (2.7).

2.2.3. Multimodal Operation Principles

Increased phase centers in the MIMO configuration provide a great opportunity to merge two or more advanced multichannel modes into a single system. The basic idea behind the multimodal operation is to adjust the phase center distributions by reconfiguring antenna constellations for multiple modes. This principle is only realizable if multiple waveforms are available for a parallel transmission through multiple antennas. On the premise that such orthogonal waveforms are available, the following sections describe operation principles for several example modes.

HRWS SAR Across-Track Interferometry

SAR interferometry considered here, is the across-track interferometry[5] for topography. A conventional InSAR mode can be problematic if it is combined with a system utilizing M_R receive antennas for another purpose, such as the HRWS SAR imaging. An example of this would be a multichannel SAR system with M_R receive subarrays, which must have at least total $2M_R$ receive channels in order to implement the InSAR mode without any performance loss, such as the azimuth resolution and the coverage. Such a large number of receive channels are impractical with regard to the system weight and size.

The present MIMO SAR uses the second transmit antenna instead of an additional large receive array and deploys it at an exact baseline in across-track. Figure 2.5 draws the combination of the HRWS SAR imaging and the InSAR operation modes in the MIMO SAR, which in

---

[5]For convenience, the term "InSAR" in this section means the across-track SAR interferometry.
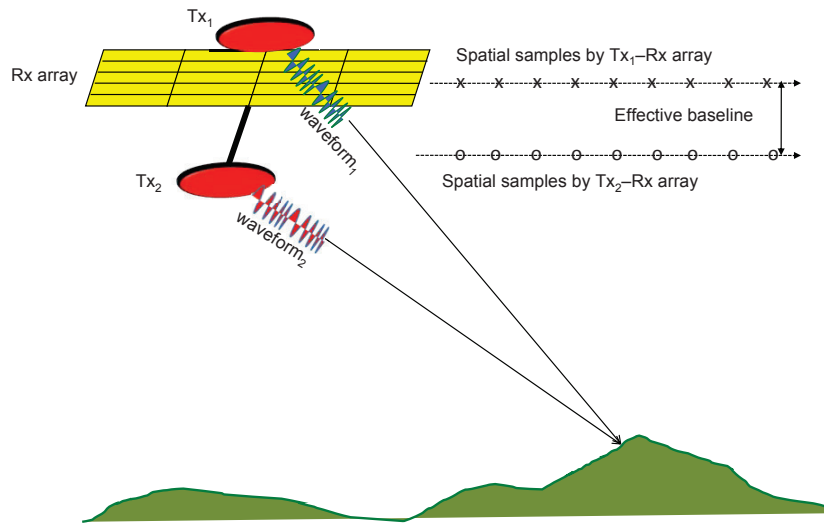
Figure 2.5.: Antenna constellation and the spatial sample distribution in the combination of the HRWS SAR imaging, and the across-track SAR interferometry. The effective baseline is defined as a distance between spatial samples in across-track.

a word, is HRWS InSAR mode. A parallel orthogonal pulse transmission produces two separated phase center arrays denoted by the symbols "x" and "o" in Figure 2.5 respectively. Each spatial sample array contributes to the HRWS SAR imaging mode independently and thereby two SAR images are reconstructed. In this case, the total $M_R + 2$ antennas are needed in the HRWS InSAR mode, whereas in the conventional approach, $2M_R$ antennas are necessary to give out the same performance. Consequently, the presented MIMO configuration facilitates the effective combination of both advanced modes.

HRWS SAR Imaging for GMTI

In a similar way, when the second transmit antenna is arranged with a certain baseline in along-track, M_R additional phase centers are produced between the second Tx antenna and the receive array, as shown in Figure 2.6. Their positions depend on the baseline. At the time instance, t_o, both transmit antennas send pulses simultaneously and thereby two phase center arrays marked by "x" and "o" are formed in along-track. In the next transmission at $t_o + $PRI, the other phase centers are formed consecutively. Thus, $2M_R$ samples in along-track are obtained by every single pulse transmission event. The increased number of spatial samples improves *Ground Moving Target Indication* (GMTI) performance and also relieves the conflict between PRF and coverage.

To give an example, the M_R samples are used for the HRWS SAR imaging, so that two high resolution SAR images are produced over a wide area. Due to the along-track baseline, the two images contain different information for non-stationary objects. Therefore, using the *Along-Track Interferometry* (ATI) or the DPCA technique, the moving objects can be distinguished from the stationary clutter. This operation mode can be very fascinating for applications, such as ship
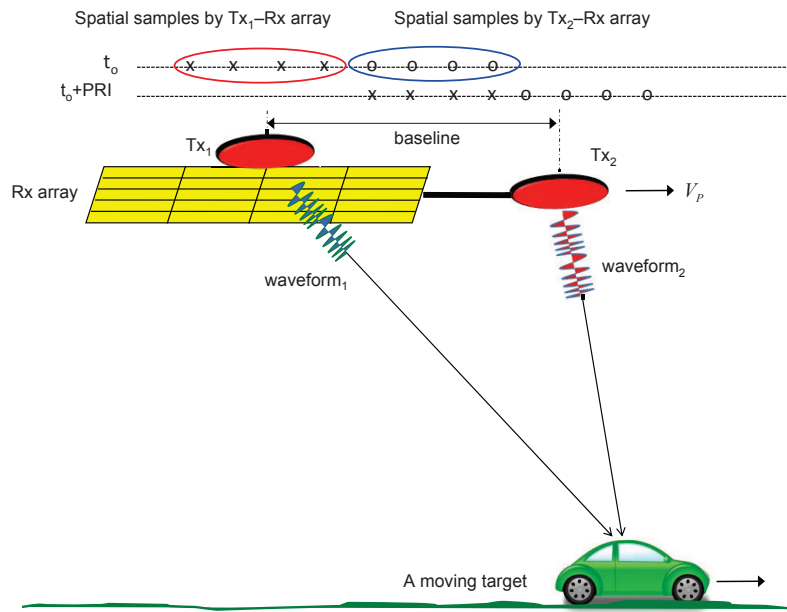
Figure 2.6.: Antenna constellation and the spatial sample distribution for GMTI.

surveillance and ocean surface current monitoring. Another example is the motion parameter estimation of moving targets and the ground clutter suppression, which may require more than two channels to improve performance [38]. In the case of a system with M_R receive channels only, a high PRF is mandatory in order to reconstruct M_R SAR images from every single channel. Therefore, the high PRF limits the swath width. Use of a second Tx channel relaxes the high PRF requirement by increasing the number of spatial samples by a factor of 2. By combining two successive channels for the HRWS SAR imaging, the same M_R images can be obtained with half of the PRF that would have been required for the single Tx system. The MIMO SAR presents a great opportunity to improve both the GMTI performance and the coverage of SAR imaging simultaneously.

HRWS PolSAR

As introduced in section 1.2.1, in the conventional PolSAR mode, each vertically and horizontally polarized signal is radiated by an alternative transmission mode, and two scattering components are acquired by each transmission event. Hence, a full scattering matrix can be obtained through the interleaved data acquisition. In the MIMO SAR, orthogonal waveforms assigned to each polarization allow a simultaneous acquisition of fully polarimetric data [61] and thereby the present system overcomes the restriction of the conventional PolSAR data acquisition. Figure 2.7 depicts the operation principle.

The orthogonal waveforms are radiated through both polarization channels of transmitter. Depending on target properties, the polarization state of a reflected signal is transformed, and the receive array collects two orthogonally polarized signals from each waveform. Unlike the conventional scattering matrix in the polarization and slow-time domain, the scattering matrix is built in the polarization and waveform domain in the MIMO SAR, as shown in Figure 2.7. The vertical and horizontal polarization channels of each receive array acquire $h_{1,VV}$ and $h_{2,VH}$,
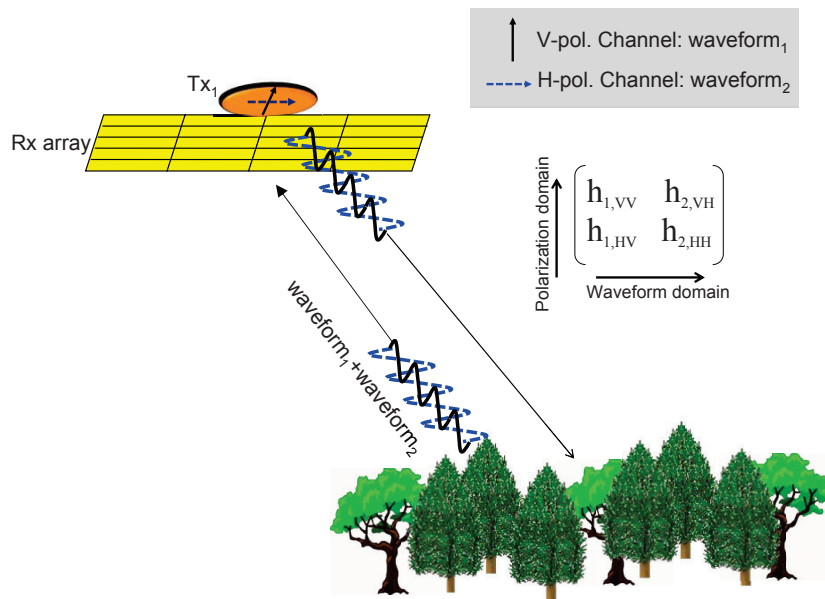
Figure 2.7.: Fully polarimetric data acquisition based on orthogonal waveforms in the HRWS PolSAR mode. For clarity, a single transmit antenna with dual-polarizations is assumed.

and $h_{1,HV}$ and $h_{2,HH}$, respectively. Each polarization channel signal is composed of both the waveforms, which can then be separated by the waveform demodulator. As a result, a complete scattering matrix is obtained by every single acquisition.

2.3. Generic MIMO SAR Processing

The primary objectives of the MIMO SAR processing are the successful demodulation of multiple waveforms and the reconstruction of multiple HRWS SAR images from the waveforms. Figure 2.8 draws the generic MIMO SAR processor schematic diagram. In the figure, the number of Tx and Rx antennas are denoted by M_T and M_R, respectively. The MIMO SAR processor is conjunctively formed up of multiple parallel SAR processors and MIMO processing blocks: digital beam formers and a waveform demodulator. In fact, each block may contain a number of subunits carrying out common functions, such as FFT/IFFT and switching. However for simplicity's sake, these are skipped in the schematic. The main functionalities of the processor are summarized as follows:

- Digital beamforming in elevation and Doppler domain

- Multiple waveform demodulation and separation prior to the conventional SAR processor

- SAR processing, based on M_T parallel multiple processors

The first step is the spatial filtering, performed by digital beamforming in elevation. As introduced before, the digital beamforming is an inseparable option for wide swath imaging in order to achieve a predefined SNR. The DBF divides a large amount of data into N_{sub} data
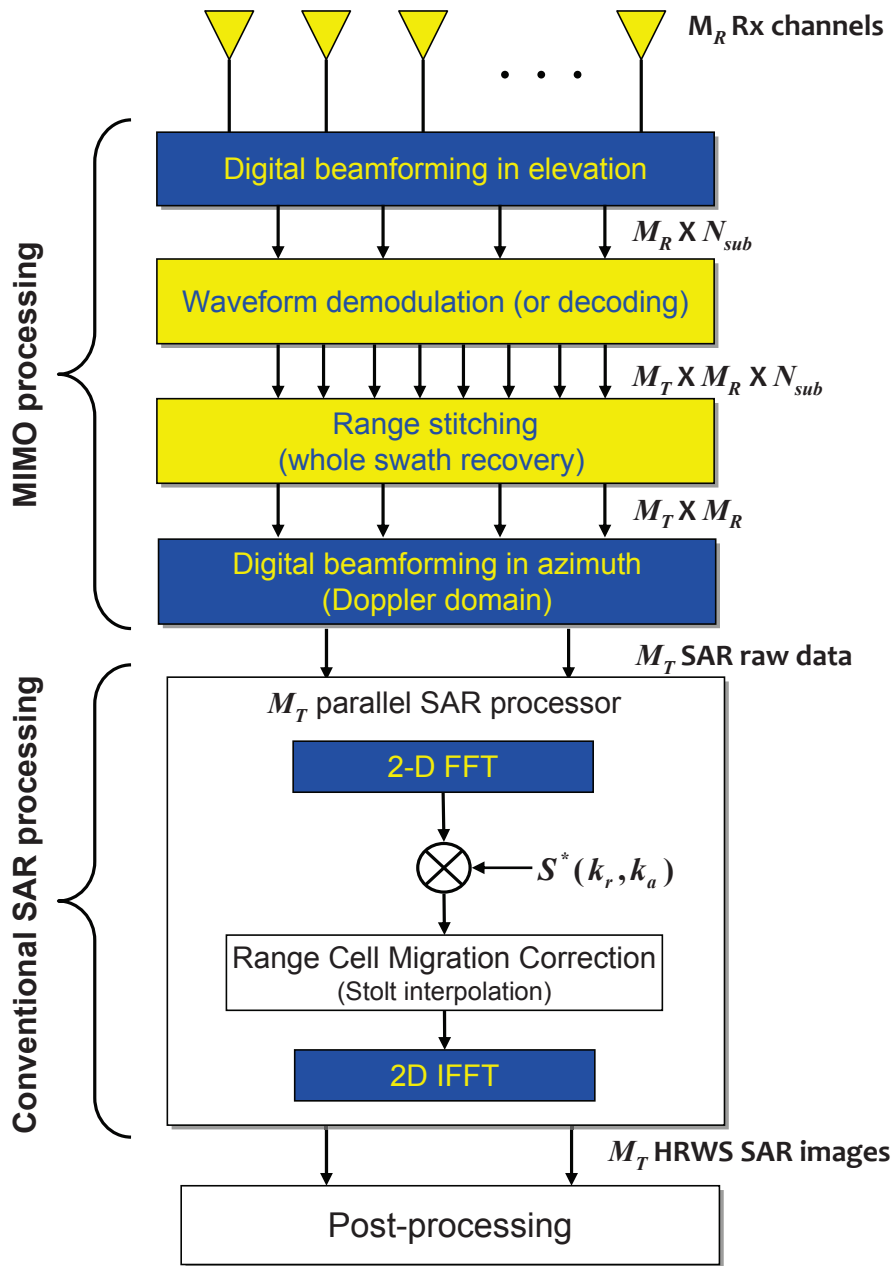
Figure 2.8.: Generic MIMO SAR processing schematic. Two major functions of the generic MIMO SAR processor are the MIMO signal processing and the conventional SAR processing. In this figure, the ω-k algorithm is considered as an example, so that the range cell migration correction is performed by the Stolt interpolation [29].

subsets (N_{sub} subswaths) for the purpose of effective parallel processing and for the waveform demodulation. Thus, $M_R \times N_{sub}$ data subsets are constructed.

Each subset signal contains multiple waveforms, delivering individual channel impulse responses. The second step is to demodulate and separate those waveforms without the loss of channel impulse responses. Generally, an orthogonal waveform scheme requires a very good

aperiodic auto-correlation property. In this case, the waveform separation process can be directly completed by range focusing, which in turn is done by a correlation filter, i.e. matched filter. In this schematic, it is assumed that the waveform demodulation block is separated from the range processing for clarity. From this point onwards, the whole swath is divided into the N_{sub} data subsets of each waveform. Therefore, the demodulator output becomes a $M_T \times M_R \times N_{sub}$ data cube.

The N_{sub} blocks can be stitched at this stage or after the range compression. It can even be stitched after the full image focusing, in order to recover the whole coverage. This section assumes the N_{sub} divisions are concatenated before SAR processing. So, the data dimension is reduced to $M_T \times M_R$ but the total amount of data remains unchanged.

The next step is the digital beamforming in Doppler domain. In principle, this digital beamforming can be carried out at any stage of the processing, since it is a linear operation[6] [79, 69, 139]. The beam former block is therefore linearly combined with the SAR processor. Detailed DBF processing will be introduced in section 3.3. The DBF coherently combines M_R azimuth channel signals and reconstructs a wide Doppler spectrum from those by suppressing the aliasing of Doppler spectrum. This procedure should be carried out for each waveform, so that M_T data sets are processed by a set of parallel SAR processors. Finally, M_T SAR images are reconstructed independently. At the post-processing stage, the multiple images or data can be exploited to retrieve geometric and physical information of interest.

In summary, the MIMO SAR processor consists of the digital signal processors for the MIMO techniques and the M_T parallel multiple conventional SAR processors. This implies the fact that the digital processors for the MIMO techniques can be independently developed and verified, and afterwards can be integrated to the SAR processors. It may also be worth noting that details of a practical MIMO SAR processor may differ from the generic schematic shown in this section. However the basic functionalities and frameworks of processing will be based on this schematic.

2.4. Challenge in MIMO SAR Implementation

One of the most critical issues in the MIMO SAR is a design of multiple waveforms and development of related processing algorithms. In particular, the orthogonality of waveforms is a premise in the MIMO SAR. If there are two waveforms $s_i(t)$ and $s_j(t)$, the orthogonal condition[7] is then given as [40]:

$$\int_{-\infty}^{\infty} s_i(t) \cdot s_j^*(t + \tau) \mathrm{d}t = \delta_{ij} \quad \text{if } \tau = 0 \tag{2.8}$$

where τ is the time shift and δ_{ij} is the Kronecker delta function defined by

$$\delta_{ij} = \begin{cases} 1 & \text{if } i = j \\ 0 & \text{if } i \neq j \end{cases} \tag{2.9}$$

---

[6]This beamforming can be performed either before or after the range focusing. However considering SNR, the range compression prior to the beamforming would be recommended.

[7]This is actually the orthonormal function since the amplitude of the correlation is normalized. The term "orthonormal" originates from the combination of "**ortho**gonal" and "**normal**ize".

(2.8) implies the ideal aperiodic autocorrelation condition. The reason for such rigorous conditioning required for the MIMO SAR is the distributed targets. The following simple simulation shows the importance of the orthogonality in the MIMO SAR.

| (a) | (b) |
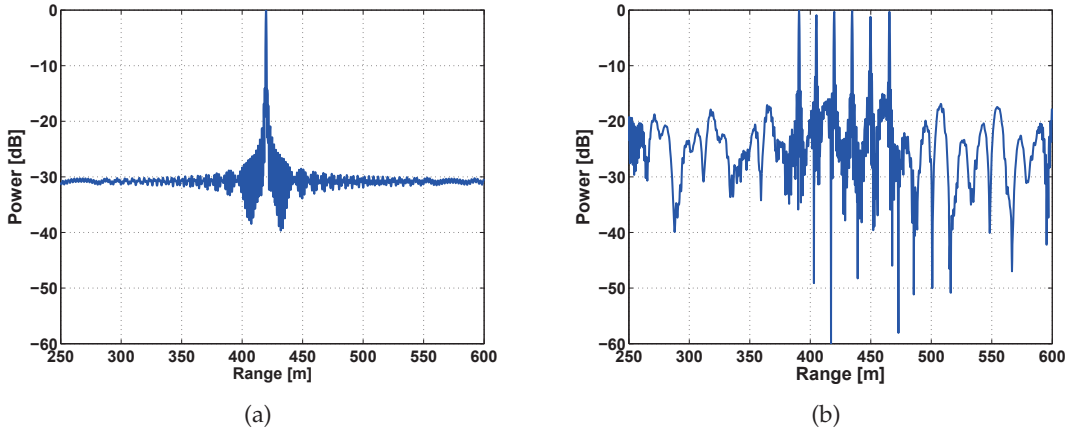
Figure 2.9.: Impulse responses produced by matched filtering with respect to the up-chirp for (a) a single target and (b) 6 point targets. The peaks correspond to the autocorrelation functions of the up-chirp for point targets. The cross-correlation functions between the up- and down-chirp are spread over range.

By using the up- and down-chirp, their correlation property is evaluated. Figure 2.9 plots the correlation between them. Firstly, a single point target scenario is considered. Echoes of the waveforms from the target are superposed in the received signal. When the correlation filtering is performed for the up-chirp, the target response from the up-chirp is focused on the corresponding delay time instance and the cross-correlation is suppressed up to -30dB, as shown in Figure 2.9 (a). The same operation is carried out with 6 point targets and the result is shown in Figure 2.9 (b). The target responses are significantly deteriorated due to the high noise floor, since the cross-correlation responses are only spread over the range and *not* eliminated. It is straightforward to anticipate that this phenomenon will be even more significant for distributed targets in a real SAR. Therefore, the orthogonality of waveforms is the most critical property for SAR applications.

2.4.1. Overview of Current Approaches

Most of the current orthogonal waveform schemes are based on multi-dimensional modulation techniques. Before dealing with a novel waveform technique, this section gives an overview of the current MIMO transmission schemes using orthogonal waveforms. This overview will clarify a difference between the existing approaches and the novel approach presented in this work.

- *Space-Time Modulation*: This scheme assigns respective waveforms to separated Tx antennas and transmits them at different time instances. Figure 2.10 shows an example modulation.

  Recently, an InSAR system employing a MIMO array on an *Unmanned Aerial Vehicle* (UAV) was presented in [66, 65]. The system builds a virtual array in across-track by using a
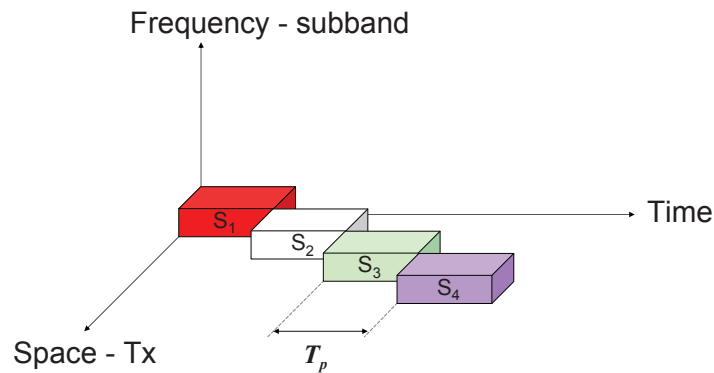
Figure 2.10.: An example of space-time modulation.

switching mode, and reconstructs a high resolution 3-D topographic map. The space-time modulation scheme is also beneficial for detecting and recognizing a particular target, such as a ground moving target or difficult targets in complex environments [38]. However this approach yields an increase in PRF or a reduction of azimuth resolution in order to avoid azimuth ambiguities. A combination of the spatiotemporal encoding and the DBF on receive in elevation is provided as a solution to avoiding the increase of PRF [70], but it is only possible if DBF in elevation is available.

• *Space-Frequency Modulation*: The frequency diversity technique in radar improves the target detection performance and reduces the RCS fluctuation of target [145, 9, 41, 9]. Multiple frequency bands, called subbands, can easily be created by splitting a whole system bandwidth into several non-overlapping subbands. This scheme allows a simultaneous pulse transmission based on the orthogonality of the subbands, as shown in Figure 2.11.
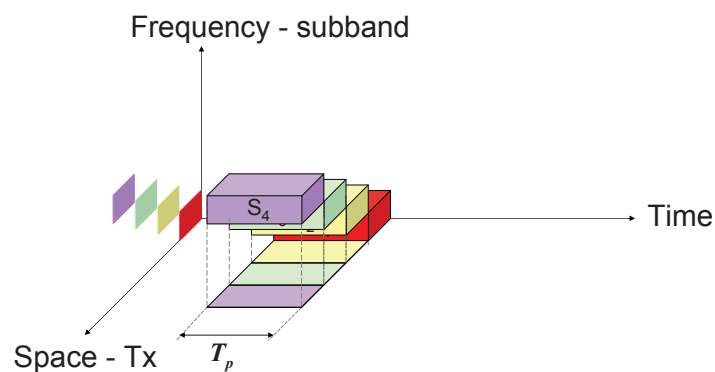
Figure 2.11.: An example of space-frequency modulation.

A significant drawback of this scheme is the spectral incoherence between the subbands. This modulation scheme may however only be suitable for permanent scatterers and inappropriate for distributed targets. Thus, the coherent multichannel measurements, such as the interferometry and polarimetry, are limited. Additionally, the range resolution of each subband image is deteriorated in case the whole bandwidth is sectioned. A wide subband for each transmitter improves the range resolution but requires the system bandwidth to be expanded by a factor of the number of Tx antennas on receive. With the aid

of frequency-dependent beamforming on both transmit and receive, the subband signals can be coherently combined, and the whole bandwidth can be recovered [41]. However in practice, non-ideal band pass filter characteristics cause a spectral overlap or gap between the subbands. Hence, the recovered spectrum can contain some discontinuities, which in turn increase the side lobe level in target range responses.

- *Space-Time-Frequency Modulation*: The technique introduced here merges the previous two modulation schemes in order to maximize the diversity effect between waveforms. As shown in Figure 2.12, each transmit antenna radiates an individual subband signal in turns. This switching mode leads to an decreased SNR by a factor of the number of Tx antennas, since only one antenna is activated and the others are silent [37]. This approach can be improved by a cyclic shift in the space-frequency modulation, i.e. frequency multiplexing. In this case, the subband assigned to each transmit antenna is rotationally changed from pulse to pulse, so that the whole bandwidth is used at every transmission event. This scheme maximizes its robustness in combination with *Space-Time Adaptive Processing* (STAP) [36, 37]. This technique focuses on the performance enhancement of GMTI, but at the cost of a high PRF and low spectral coherence.
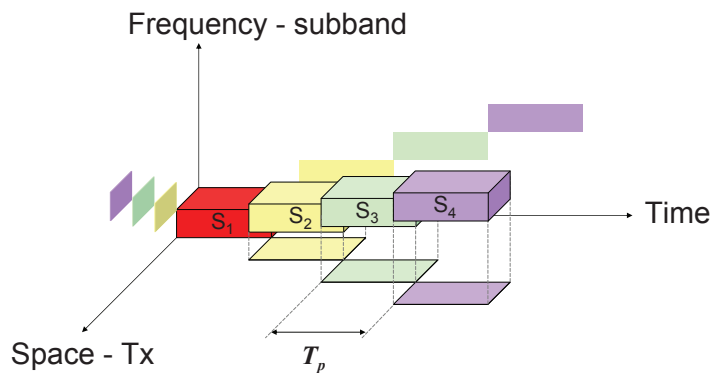
Figure 2.12.: Space-time-frequency modulation without rotational subband transmission.

- *Orthogonal Code Modulation*: Orthogonal coding techniques have been intensively investigated in MIMO radar, whereas it is barely considered in MIMO SAR due to its non-ideal autocorrelation property.

  There are several approaches that attempt to optimize the autocorrelation property using a cyclic phase coding, such as *Pseudo-Noise* (PN) sequences or constant modulus signals based on the cyclic algorithm [57, 78]. Another interesting approach is to apply the phase coding to multiple discrete frequency [93, 77, 32]. Those schemes still suffer from a degradation of SNR in a distributed target scenario. In addition, these schemes mostly yield a complicated optimal receive filter design for SAR imaging, which means that the conventional SAR processor may be inapplicable for those types of signal.

In summary, the current orthogonal waveform approaches are based on the multiple dimensional modulation techniques and allow the use of multiple transmitters for enhanced SAR imaging or target detection. However those approaches cost either a high PRF, or coherence between multiple images. It restricts the degrees of freedom of the MIMO SAR system and possible application areas. The maximum degree of freedom can be achieved by a simultaneous pulse transmission and the coherence can be further improved by generating multiple and
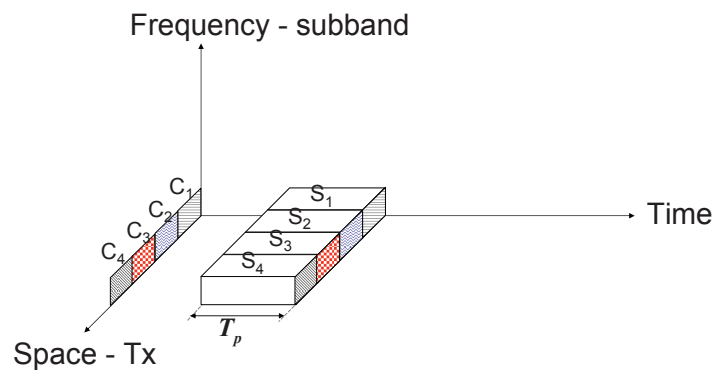
Figure 2.13.: Orthogonal code modulation: C_1-C_4 denote orthogonal codes assigned to the transmit antennas.

separable waveforms within a common frequency band. Regarding the present MIMO SAR, this work pursues both goals.

3. Principles of MIMO SAR Techniques

This chapter presents the principles of the core techniques, the digital beamforming and the orthogonal waveform scheme. The chapter starts by defining a MIMO scenario in Cartesian coordinates under the flat Earth assumption for simplicity. First of all, in order to develop a MIMO SAR signal model, a MIMO Radar signal model is developed and then extended to a side-looking SAR scenario. The digital beamforming algorithms introduced in [79, 69] will be described using this signal model in a 2-D wavenumber domain.

When it comes to the orthogonal waveform, this work focuses on the principles of a multiple subcarrier technique, called *Orthogonal Frequency Division Multiplexing* (OFDM), so as to derive a novel orthogonal waveform scheme. Specific theories and investigations about the new waveform scheme will be intensively presented in Chapter 4. This chapter gives an overview of the classical OFDM principle and the system schematic.

3.1. MIMO SAR Signal Model

This section describes a MIMO SAR signal model. The MIMO signal model is composed of the input data, propagation channel, and output signals. It ought to be noted that the input and output are defined with respect to the MIMO channel.

3.1.1. MIMO Geometry

A MIMO geometry is considered within the Cartesian coordinate, like shown in Figure 3.1. The multiple transmit and receive antennas are situated at arbitrary positions and illuminate a target area. Taking a simple propagation channel into consideration, the signal transmitted by the jth Tx antenna $(x_{t,j}, y_{t,j}, z_{t,j})$ reaches a target (x, y, z) and is scattered back to the ith Rx antenna $(x_{r,i}, y_{r,i}, z_{r,i})$.

The distance between the jth Tx antenna and the target, and between the target and the ith Rx antenna are denoted by $R_{tx,j}$ and $R_{rx,j}$, respectively:

$$R_{tx,j} = \sqrt{(x_{t,j} - x)^2 + (y_{t,j} - y)^2 + (z_{t,j} - z)^2}, \tag{3.1}$$

$$R_{rx,i} = \sqrt{(x_{r,i} - x)^2 + (y_{r,i} - y)^2 + (z_{r,i} - z)^2}. \tag{3.2}$$

In a side-looking scenario, the antennas move along the u-axis, which is parallel to the y-axis.
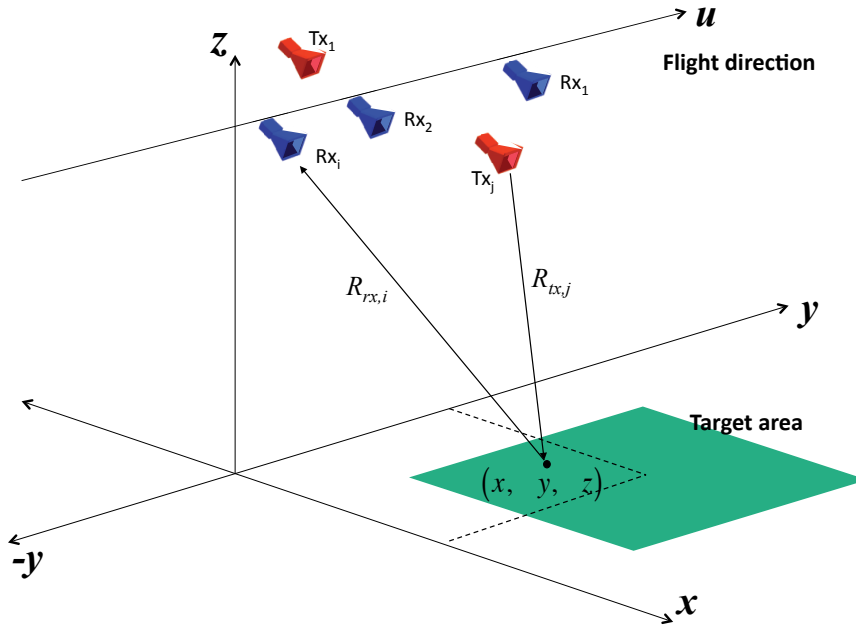
Figure 3.1.: Geometry of a generic MIMO antenna constellation.

3.1.2. MIMO Radar Signal Model

A simplified MIMO radar system model with M_T transmitters and M_R receivers is portrayed in Figure 3.2. In this case, the MIMO radar model consists of the M_T input and M_R output, which are defined with respect to the MIMO channel.

For simplicity, it is assumed that the transmitters and the receivers have a gain of unity without any phase change, and the channel impulse response $h_{ij}(t)$ accounts for only the reflectivity and the phase information of the round-trip path between the jth Tx and ith Rx antennas, for a point-like target at (x, y, z):

$$h_{ij}(t) = a_{ij} \cdot \delta(t - \tau) \tag{3.3}$$

where a_{ij} denotes the complex coefficient representing the scattering and the path loss. $\delta(t)$ is the Kronecker delta function and τ is the round-trip delay time, which depends on the distance between the antennas and the target position:

$$\tau(i, j, x, y, z) = \frac{R_{tx,j}(x, y, z) + R_{rx,i}(x, y, z)}{c_o}. \tag{3.4}$$

The received signal at the ith receiver is represented as a convolution of the channel impulse response and the transmitted signal. Since all transmitters in the MIMO data acquisition are simultaneously activated, the received signal contains all of the transmitted waveforms and the channel impulse responses:

$$r_i(t) = \sum_{j=1}^{M_T} [s_j(t) * h_{ij}(t)] + n_i(t) \tag{3.5}$$
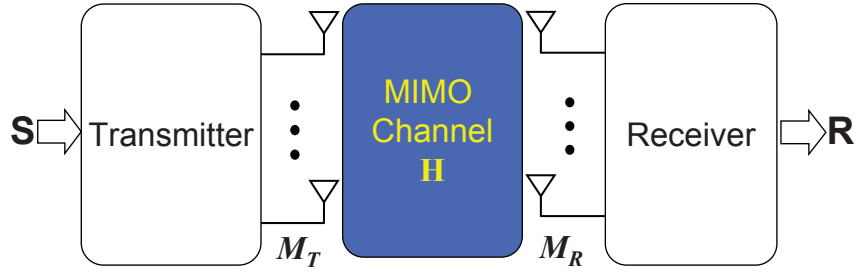
Figure 3.2.: Simplified MIMO radar system model.

where $s_j(t)$ is the waveform transmitted by the jth Tx antenna. The asterisk $*$ is the convolution operator and $n_i(t)$ is the *Additive White Gaussian Noise* (AWGN) at the ith receiver. By applying the Fourier transform, one obtains the frequency domain representation of (3.5):

$$\mathcal{F}\{r_i(t)\} = \sum_{j=1}^{M_T} [\mathcal{F}\{s_j(t)\} \cdot \mathcal{F}\{h_{ij}(t)\}] + N_i(f) \tag{3.6}$$

where $\mathcal{F}\{\cdot\}$ stands for the Fourier transform operator and $N_i(f)$ is the Fourier transform of the noise term in (3.5). The Fourier transform of the channel impulse response for a point target leads to the channel transfer function $H_{ij}(f)$:

$$\begin{aligned} \mathcal{F}\{h_{ij}(t)\} &= H_{ij}(f) \\ &= A_{ij} \cdot \exp\left(-j(2\pi f \tau + \varphi)\right) \\ &= A_{ij} \cdot \exp\left(-j\left(\frac{2\pi}{\lambda}(R_{tx,j} + R_{rx,i}) + \varphi\right)\right) \end{aligned} \tag{3.7}$$

where A_{ij} denotes the amplitude of the channel transfer function and the exponential term represents the phase history of the $i-j$ channel. φ is a constant phase of the complex coefficient a_{ij}, and is omitted in further developments.

In radar imaging, the target is generally specified as an area of interest. Assuming a flat surface ($z = 0$), the channel transfer function is represented by an integral of the overall target area, as follows:

$$H_{ij}(f) = \iint A_{ij}(x,y) \cdot \exp\left(-j\frac{2\pi}{\lambda}(R_{tx,j}(x,y) + R_{rx,i}(x,y))\right) \mathrm{d}x\mathrm{d}y. \tag{3.8}$$

Let $S_j(f) = \mathcal{F}\{s_j(t)\}$ and subsequently the spectrum of the receive signal $R_i(f)$ is given by

$$R_i(f) = \sum_{j=1}^{M_T} [S_j(f) \cdot H_{ij}(f)] + N_i(f). \tag{3.9}$$

3.1.3. Expansion to the MIMO SAR Signal Model

In a side-looking SAR geometry, the SAR system moves and acquires data at every position in along-track. The SAR operation at any given position in along-track can be regarded as the radar operation. In this sense, a MIMO SAR model can be represented by an array of the MIMO radar models in along-track. Figure 3.3 illustrates the expansion of the MIMO radar model to a MIMO SAR model. The number of spatial samples, denoted by M, is decided by a spatial sampling distance and a synthetic aperture length.
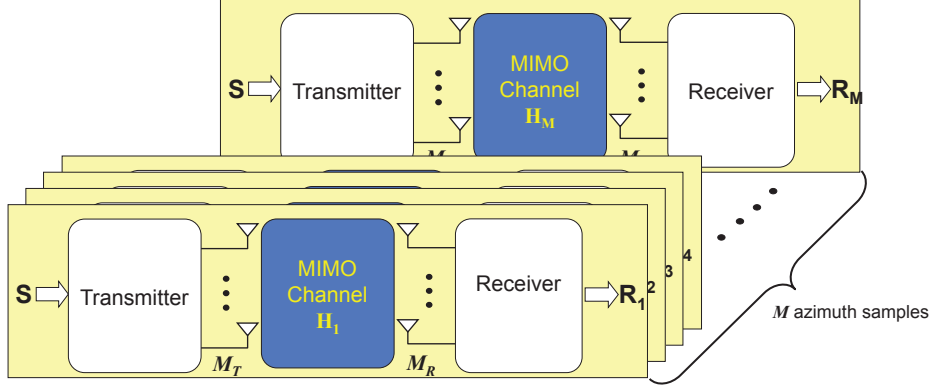
Figure 3.3.: MIMO SAR model expanded from the MIMO radar model.

In the case of a MIMO SAR on a single platform, whereby both transmit and receive antennas are moving along the u-axis with the same velocity, and recalling (3.9), the received signal spectrum can be rewritten in the frequency-space domain:

$$R_i(f, u) = \sum_{j=1}^{M_T} S_j(f) \cdot H_{ij}(f, u) + N_i(f, u) \tag{3.10}$$

where u represents the sensor position in the flight track. The effective phase center position of the $i - j$ pair is then given by $u = (y_{t,j} + y_{r,i})/2$, according to the DPCA principle (see Appendix A). Following this, (3.10) is transformed into the Doppler wavenumber domain k_u:

$$R_i(f, k_u) = \int_{-\infty}^{\infty} \left[\sum_{j=1}^{M_T} S_j(f) \cdot H_{ij}(f, u) + N_i(f, u) \right] \cdot e^{-j \cdot k_u \cdot u} \mathrm{d}u. \tag{3.11}$$

Since the integral is a linear operator and the waveform $S_j(f)$ is constant with respect to u, (3.11) can be rearranged as follows:

$$R_i(f, k_u) = \sum_{j=1}^{M_T} S_j(f) \underbrace{\int_{-\infty}^{\infty} H_{ij}(f, u) \cdot e^{-j \cdot k_u \cdot u} \mathrm{d}u}_{H_{ij}(f, k_u)} + N_i(f, k_u). \tag{3.12}$$

Using the principle of stationary phase, the 2-D spectrum of the channel transfer function $H_{ij}(f, k_u)$ can be derived in a closed form [113, 29, 30]:

$$H_{ij}(f, k_u) = A_{ij}(f, k_u) \cdot \exp\left(-j\sqrt{4\left(\frac{2\pi}{\lambda}\right)^2 - k_u^2} \cdot X_{s,ij} - jk_u\left(y - \frac{y_{t,j} + y_{r,i}}{2}\right)\right) \quad (3.13)$$

where $A_{ij}(f, k_u)$ represents the amplitude of the 2-D spectral channel transfer function and $X_{s,ij}$ is the minimum slant range of the $i-j$ bistatic pair, which is given by

$$X_{s,ij} = \sqrt{\left(\frac{x_{t,j} + x_{r,i}}{2} - x\right)^2 + \left(\frac{z_{t,j} + z_{r,i}}{2} - z\right)^2}. \quad (3.14)$$

Finally, the 2-D signal spectrum of the ith receiver is derived as:

$$R_i(f, k_u) = \sum_{j=1}^{M_T} A_{ij}(f, k_u) \cdot S_j(f) \cdot \exp\left(-j\sqrt{4\left(\frac{2\pi}{\lambda}\right)^2 - k_u^2} \cdot X_{s,ij} - jk_u\left(y - \frac{y_{t,j} + y_{r,i}}{2}\right)\right)$$
$$+ N_i(f, k_u). \quad (3.15)$$

In the next step, (3.15) is rewritten in the 2-D wavenumber domain, which is defined for both the range and the azimuth, as follows:

$$k_r = \sqrt{4\left(\frac{2\pi}{\lambda}\right)^2 - k_u} \quad (3.16)$$

and

$$k_a = k_u \quad (3.17)$$

where k_r is the range wavenumber, accounting for the *Range Cell Migration* (RCM) in the SAR data. The azimuth wavenumber k_a is identical to k_u, due to the linear movement of the sensor along the u-axis. Using (3.16) and (3.17), (3.15) is rewritten as:

$$R_i(k_r, k_a) = \sum_{j=1}^{M_T} S_j(f) \cdot H_{ij}(k_r, k_a) + N_i(k_r, k_a) \quad (3.18)$$

where the 2-D channel transfer function is

$$H_{ij}(k_r, k_a) = A_{ij}(k_r, k_a) \cdot \exp\left(-jk_r \cdot X_{s,ij} - jk_a\left(y - \frac{y_{t,j} + y_{r,i}}{2}\right)\right). \quad (3.19)$$

Due to the periodicity of *Discrete Fourier Transform* (DFT), the Doppler spectrum of SAR signal repeats at each order of PRF and the higher ordered spectra partially overlap the original baseband spectrum. It causes azimuth ambiguities in SAR images, depending on the azimuth
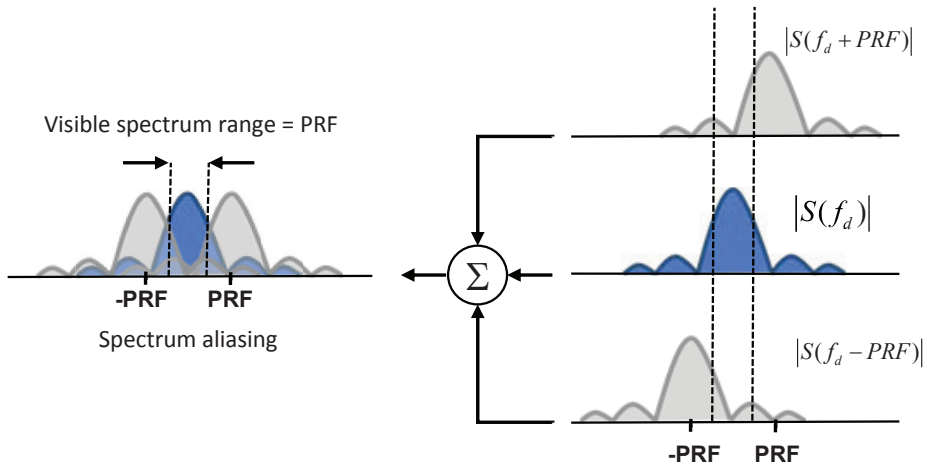
Figure 3.4.: Aliasing of the sub-sampled single channel data. The first repetition of the original baseband signal is considered.

antenna pattern and PRF [30]. Figure 3.4 illustrates the spectral aliasing in Doppler frequency domain.

The spectral aliasing is introduced in this signal model. Firstly, the PRF is represented by the wavenumber k_s, which is defined as

$$k_s = \frac{2\pi}{V_p} \cdot PRF = \frac{2\pi}{\Delta d} \tag{3.20}$$

where V_p is the sensor velocity and Δd is the travel distance for the pulse repetition interval. Let β denote the order of aliasing, and consequently the spectrum in 2-D wavenumber domain is expressed as

$$R_i(k_r, k_a) = \sum_{j=1}^{M_T} S_j(f) \cdot \left(\sum_{\beta=-\infty}^{\infty} H_{ij}(k_r, k_a + \beta k_s) \right) + N_i(k_r, k_a) \tag{3.21}$$

The array signal can simply be described using vector and matrix notations. The inner summation in (3.21) of each receiver is expressed by a $M_R \times 1$ vector:

$$\mathbf{H}_j = \begin{bmatrix} H_{1j}(k_r, k_a) & H_{1j}(k_r, k_a + k_s) & \dots & H_{1j}(k_r, k_a + \beta \cdot k_s) \\ H_{2j}(k_r, k_a) & H_{2j}(k_r, k_a + k_s) & \dots & H_{2j}(k_r, k_a + \beta \cdot k_s) \\ \vdots & \vdots & \ddots & \vdots \\ H_{M_Rj}(k_r, k_a) & H_{M_Rj}(k_r, k_a + k_s) & \dots & H_{M_Rj}(k_r, k_a + \beta \cdot k_s) \end{bmatrix} \cdot \mathbf{I} \tag{3.22}$$

where $\mathbf{I}$ is a $M_R \times 1$ vector of unity. This vector is arranged for M_T waveforms ($j = 1, 2, \cdots, M_T$). One obtains a $M_R \times M_T$ channel transfer function matrix in the wavenumber domain:

$$\mathbf{H}(k_r, k_a) = [\mathbf{H}_1 \quad \mathbf{H}_2 \quad \cdots \quad \mathbf{H}_{M_T}] \tag{3.23}$$

The transmitted waveforms, received signal spectra, and noise are given in a matrix form shown as follows:

$$\mathbf{S} = [S_1 \quad S_2 \quad \cdots \quad S_{M_T}]^T \tag{3.24}$$

$$\mathbf{R} = [R_1 \quad R_2 \quad \cdots \quad R_{M_R}]^T \tag{3.25}$$

$$\mathbf{N} = [N_1 \quad N_2 \quad \cdots \quad N_{M_R}]^T \tag{3.26}$$

where the superscript $[\cdot]^T$ denotes the vector transpose. Finally a linear equation of the received signal spectrum is established:

$$\mathbf{R}(k_r, k_a) = \mathbf{H} \cdot \mathbf{S} + \mathbf{N} \tag{3.27}$$

The signal model in the wavenumber domain is used in ground-based SAR experiments in which a sensor velocity is not defined.

3.2. Digital Beamforming in Elevation

The beamforming can be classified into two different categories in regard to implementation: the analog beamforming and the digital beamforming. The latter technique, digital beamforming, has been a subject of great interest in many applications, since it provides a flexible and adaptive filtering capability, such as adaptive null steering for the jammer rejection, direction finding, and multiple spatial filtering [123, 142, 56, 89].

In the present MIMO SAR, the digital beamforming contributes to both elevation and azimuth processing. The DBF in elevation aims to fulfill the following two objectives. The first is to compensate for a low SNR resulting from the increase of a swath width and a small Tx antenna. The other is to divide a long echo signal into multiple data sets for parallel signal processing. In the present MIMO SAR, two DBF strategies are considered. One is multiple spatial filtering and the other is continuous beam scanning. This section introduces the basic principles of DBF using an elevation array and presents the two DBF approaches in a side-looking SAR scenario.

3.2.1. Fundamentals

The DBF differs from the analog beamforming in its implementation, yet the basic principles are the same. When M_E receive array elements are assumed in the elevation array, the time delay in (3.4) at the gth array element can be given by a relative value, with respect to the first Rx array element:

$$\tau_g = \frac{R_{tx} + R_{rx,1} + \Delta R_{rx,g}}{c_o}$$

$$= \tau_1 + \frac{\Delta R_{rx,g}}{c_o} \tag{3.28}$$

where $\Delta R_{rx,g}$ is the range difference between the gth element and the reference element, and depends on the separation of elements and the impinging angle ($g = 1, 2, 3, \cdots, M_E$). In the

case of the *Uniform Linear Array* (ULA) as shown in Figure 3.5, the range difference between the receiving element is represented in a phase:

$$\Delta\varphi_g(\theta) = \frac{f}{c_o}\cdot\Delta R_{rx,g} = \frac{2\pi}{\lambda}\cdot W_{rs}\cdot(g-1)\cdot\sin\theta \tag{3.29}$$

where W_{rs} is the separation between the array elements, and θ is the elevation angle where the signal originates.
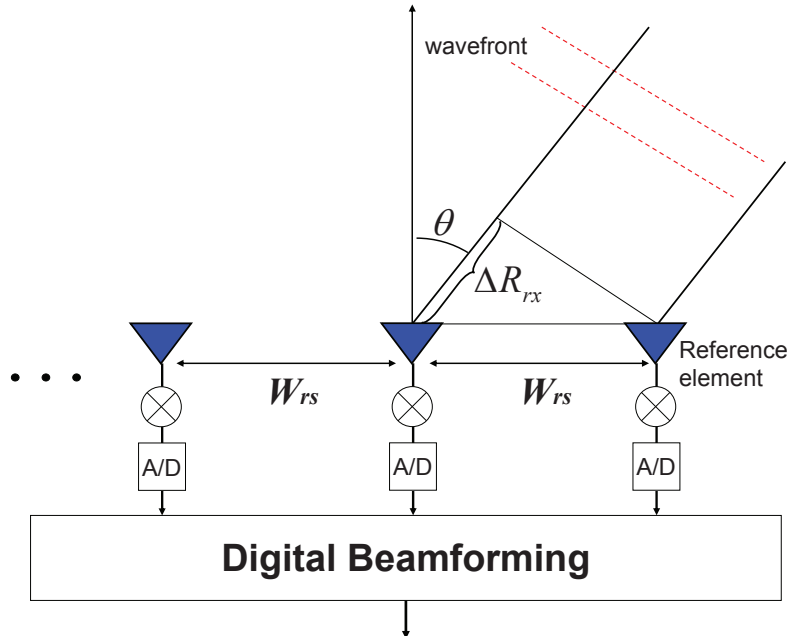
Figure 3.5.: Uniform linear array geometry receiving a plane wave from the direction θ.

If the signal bandwidth is comparable to the carrier frequency, the beamforming is frequency-dependent. Thus the broadband beamforming is commonly performed in the frequency domain [89, 56]. In the case of a narrow band signal, the signal at the gth array element in the ULA is described by

$$r_g(t) = s(t)\cdot\exp(j2\pi f(t-\tau_1) - j\Delta\varphi_g(\theta)) + n_g(t) \tag{3.30}$$

where $n_g(t)$ is the Gaussian noise at the gth receiver and $s(t)$ is the transmitted pulse. The phase differences between the array elements are represented by a $M_E \times 1$ vector, called the steering vector [52]:

$$\mathbf{a} = [\exp(-j\Delta\varphi_1(\theta)), \exp(-j\Delta\varphi_2(\theta)), \cdots, \exp(-j\Delta\varphi_{M_E}(\theta))]^T. \tag{3.31}$$

The received signal is a product of the reference channel signal and the steering vector:

$$\mathbf{r} = s(t)\cdot\exp(j2\pi f(t-\tau_1))\cdot\mathbf{a} + \mathbf{n}(t) \tag{3.32}$$

where $\mathbf{n}$ denotes the $M_E \times 1$ Gaussian noise vector.

A basic antenna synthesis step is the compensation of the phase difference by the multiplication of its complex conjugate [11]. Therefore, the beam former weight vector is given by

$$\mathbf{w} = [\exp(j\Delta\varphi_1(\theta)), \exp(j\Delta\varphi_2(\theta)), \cdots, \exp(j\Delta\varphi_{M_E}(\theta))] \tag{3.33}$$

$$= \mathbf{a}^H$$

where $[\cdot]^H$ denotes the Hermitian transpose. The beam former output $y(t)$ is then given by

$$y(t) = \mathbf{w} \cdot \mathbf{r} \qquad (3.34)$$

$$= \mathbf{a}^H \cdot (s(t) \cdot \exp(j2\pi f(t - \tau_1)) \cdot \mathbf{a} + \mathbf{n}(t))$$

$$= s(t) \cdot \exp(j2\pi f(t - \tau_1)) \cdot \mathbf{a}^H \cdot \mathbf{a} + \mathbf{a}^H \cdot \mathbf{n}$$

$$= M_E \cdot s(t) \cdot \exp(j2\pi f(t - \tau_1)) + \mathbf{a}^H \cdot \mathbf{n},$$

where

$$\mathbf{a}^H \cdot \mathbf{a} = M_E. \qquad (3.35)$$

The output signal power is calculated by taking the expected value of the output power as:

$$E\{y \cdot y^H\} = E\{(M_E \cdot s(t) \cdot \exp(j2\pi f(t - \tau_1)) + \mathbf{a}^H \cdot \mathbf{n}) \qquad (3.36)$$

$$\cdot (M_E \cdot s(t) \cdot \exp(j2\pi f(t - \tau_1)) + \mathbf{a}^H \cdot \mathbf{n})^H\}.$$

Since the noise is spatially white and orthogonal to the signal $s(t)$, (3.36) is simplified as:

$$E\{y \cdot y^H\} = E\{|M_E \cdot s(t)|^2\} + E\{\mathbf{a}^H \cdot \mathbf{n} \cdot \mathbf{n}^H \cdot \mathbf{a}\} \qquad (3.37)$$

$$= M_E \cdot S_o + N_o$$

where S_o and N_o denote the signal power $|s_j(t)|^2$ and the noise power $|n|^2$, respectively. If the SNR of a single receiver is given by

$$SNR_{in} = \frac{S_o}{N_o}, \qquad (3.38)$$

then in turn, the output SNR of the beam former becomes

$$SNR_{out} = M_E \cdot \frac{S_o}{N_o} = M_E \cdot SNR_{in}. \qquad (3.39)$$

Consequently, the beamforming enhances the SNR in the optimal case by a factor of M_E.

3.2.2. Multiple Spatial Filtering

In the MIMO SAR, and as a spatial filter, the digital beam former simultaneously generates multiple beams in elevation and collects echo signals from each angular segment independently. The multiple spatial filtering concept is illustrated in Figure 3.6, in the scenario that three beams cover the whole swath.

The dashed line denotes a broad Tx antenna beam and the solid lines denote multiple digital Rx beams, which are fixed at each look angle and time-invariant. This operation permits the division of a long echo into several subsets depending on the elevation angle, and thereby parallel processing becomes feasible. It is important to note that the echo signal length of each beam is limited by the angular range, i.e. the beam width. In Figure 3.6, the length of a horizontal slice at any angle corresponds to the transmitted pulse length. A total echo length of a single beam
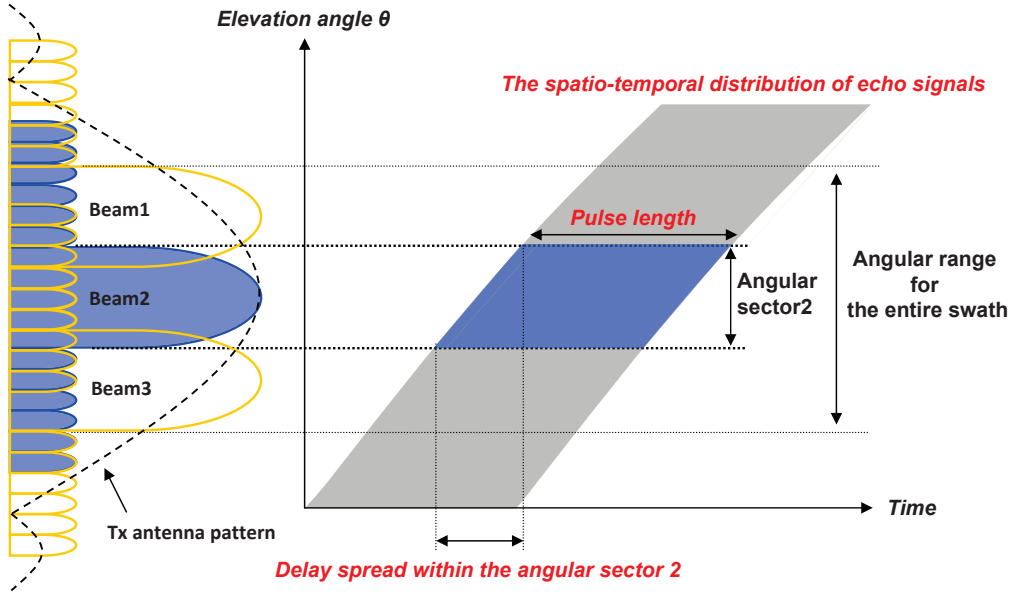
Figure 3.6.: Spatial filtering by three digital beams simultaneously collecting echoes within individual angular sectors. For example, the angular sector2 covered by the beam2 is highlighted. The received signal length within the angular sector2 is a sum of the delay spread and the transmitted pulse length.

is the sum of the length of delay spread[1] and the pulse length, so that it is always longer than the latter.

If an entire swath is specified by the *Half Power Beam Width* (HPBW) of Tx antenna, $\theta_{3dB,Tx}$, the angular scope of the echo signal is then

$$\theta \in [\theta_c - \theta_{3dB,Tx}/2, \quad \theta_c + \theta_{3dB,Tx}/2] \tag{3.40}$$

where θ_c is the look angle at the scene center. The phase of each receiver for the lth beam is given by

$$\Delta\varphi_g(\theta_l) = \frac{2\pi}{\lambda} \cdot W_{rs} \cdot (g-1) \cdot \sin\theta_l \tag{3.41}$$

where θ_l is the steering angle of the lth beam. The corresponding steering vector for the lth beam is obtained in the same manner:

$$\mathbf{a}_l = [\exp(-j\Delta\varphi_1(\theta_l)), \exp(-j\Delta\varphi_2(\theta_l)), \cdots, \exp(-j\Delta\varphi_{M_E}(\theta_l))]^T. \tag{3.42}$$

If a total of N_{sub} Rx beams cover the entire swath, the beamforming weight is composed of N_{sub} steering vectors, in order to form N_{sub} beams, so that it becomes a $N_{sub} \times M_E$ matrix:

$$\mathbf{w} = [\mathbf{a}_1, \quad \mathbf{a}_2, \quad \mathbf{a}_3, \quad \cdots, \quad \mathbf{a}_{N_{sub}}]^H. \tag{3.43}$$

The output signal of the spatial filters, $\mathbf{y}$, is a $N_{sub} \times 1$ vector as follows:

$$\mathbf{y} = \mathbf{w} \cdot \mathbf{r}. \tag{3.44}$$
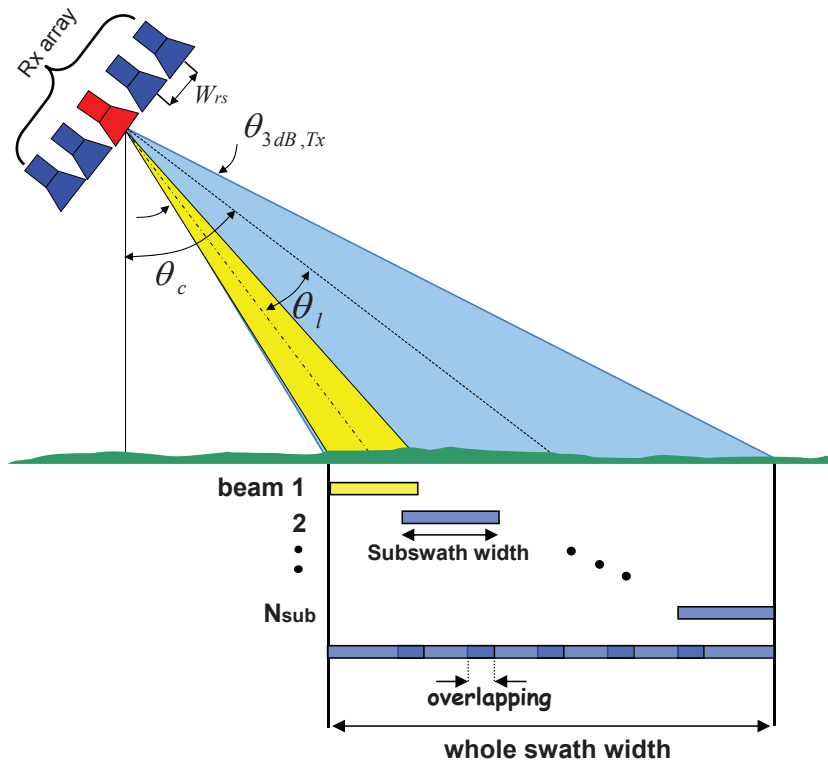
Figure 3.7.: Geometric parameters of multiple spatial filtering concept. Each subswath is overlapping the adjacent subswaths. Thereby, the spatial filter pattern effect can be compensated in images.

For the enhancement of the spatial filtering, an amplitude tapering can be applied to the array. Typical tapering techniques suppress the side lobes at the cost of the broadening of a main beam. For example, a Dolph-Chebyshev windowing is considered in order to generate the narrowest possible main lobe for a specific uniform side lobe level [33].

When the Dolph-Chebyshev window matrix is denoted by $\mathbf{w}_{cheb}$, which is a $M_E \times M_E$ diagonal matrix, the resulting output signal is

$$\mathbf{y} = \mathbf{w} \cdot \mathbf{w}_{cheb} \cdot \mathbf{r} \tag{3.45}$$

In practice, the multiple subswaths are set to slightly overlap, in order to compensate for a signal intensity variation due to the spatial filter pattern. As shown in Figure 3.7, the subswaths are partially overlapping each other. The overlapping regions are doubly illuminated by adjacent spatial filter beams. The processed signal of those regions can be exploited to compensate for the narrow array pattern effect. For example, if five beams cover a whole area and are separated by the HPBW of the Rx array beam, by synthesizing the multi-beam data, one can obtain a quasi-uniform amplitude pattern on receive, as shown in Figure 3.8.

---

[1]The delay spread is defined as the delay time difference between the first and the last echo signal.
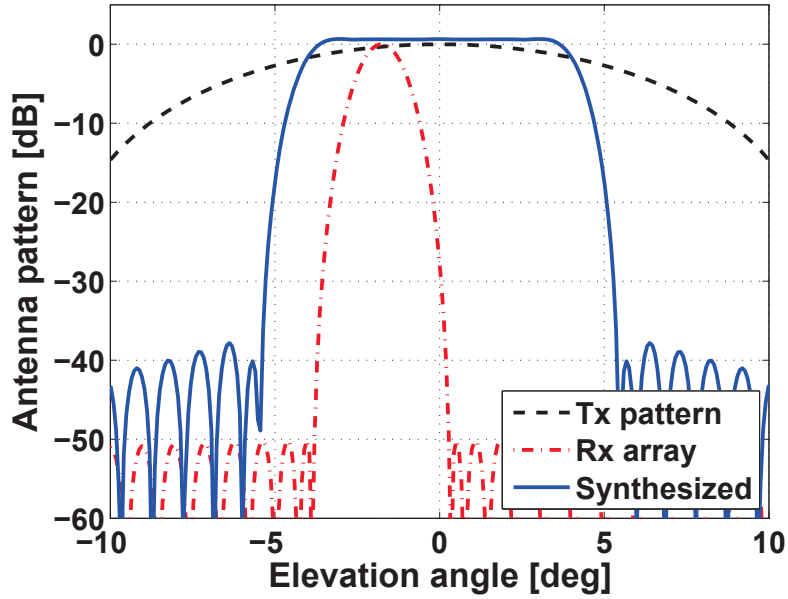
Figure 3.8.: Synthesized amplitude pattern of the spatial filters (solid line), a single Rx array pattern (dash-dot line), and Tx pattern (dashed line). Dolph-Chebyshev amplitude taper for the side lobe level of -50dB is applied.

3.2.3. SCORE Technique

Alternatively, the digital beamforming in elevation can be performed by the SCORE technique presented in [119, 117]. The main idea of the SCORE is to form a time-varying array beam and continuously track the pulse echo on the ground. The primary goal of this technique is data acquisition using a full array gain over a wide area.

The array beam sweeps the elevation angle, which is then directly related to the delay time. On a spherical Earth model without topographic height, there is a one-to-one correspondence between the scan angle and the echo delay time, as follows [117]:

$$\theta(\tau) = \cos^{-1}\left(\frac{4(h_o + R_E)^2 - 4R_E^2 + (c_o \cdot \tau)^2}{4(h_o + R_E) \cdot c_o \cdot \tau}\right) \tag{3.46}$$

where R_E denotes the local radius of Earth, with the SAR geometry sketched in Figure 3.9. It is noted that the scan angle range is determined by a Tx antenna beam.

In the case of a chirp waveform being used, the SCORE beam boresight looks at the middle of chirp and pursues it at every time instant, as depicted in Figure 3.10. If the pulse extension on ground is larger than the array beam, only a part of the pulse receives the full array gain, and pulse extension loss occurs [140]. Exploiting the linear time-frequency relationship of chirp signal, the SCORE compensates for this effect by adding a frequency-variant phase in the frequency domain. Thereby the whole pulse is processed utilizing the full gain of the array beam. In addition to this, the range ambiguity can be suppressed by the SCORE beam. Detailed formulations and the SAR performance associated with the SCORE are specifically presented in [117, 140, 15].
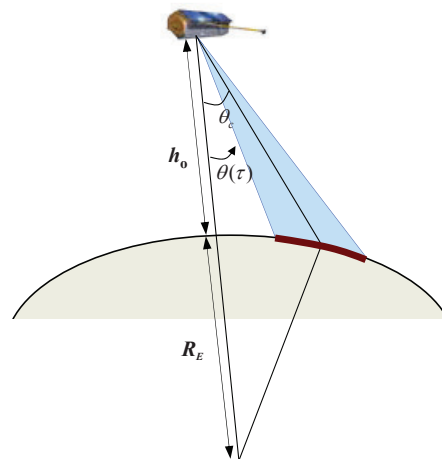
Figure 3.9.: Spherical SAR geometry in the vertical slant range plane. θ_c is the elevation angle from the nadir direction to the center of the swath.

Using the multiple spatial filtering approach, several high gain beams can be generated for parallel data acquisition in the SCORE mode as well. In this case, each beam scans the received signal within a specific angular sector (or echo delay range). The main difference between the SCORE and the spatial filtering is that the SCORE beam is time-variant, whereas the spatial filters are fixed consistently over time. If a beam is sufficiently narrow, then the SCORE beam can be used for an angle-dependent decomposition of the echo signal.
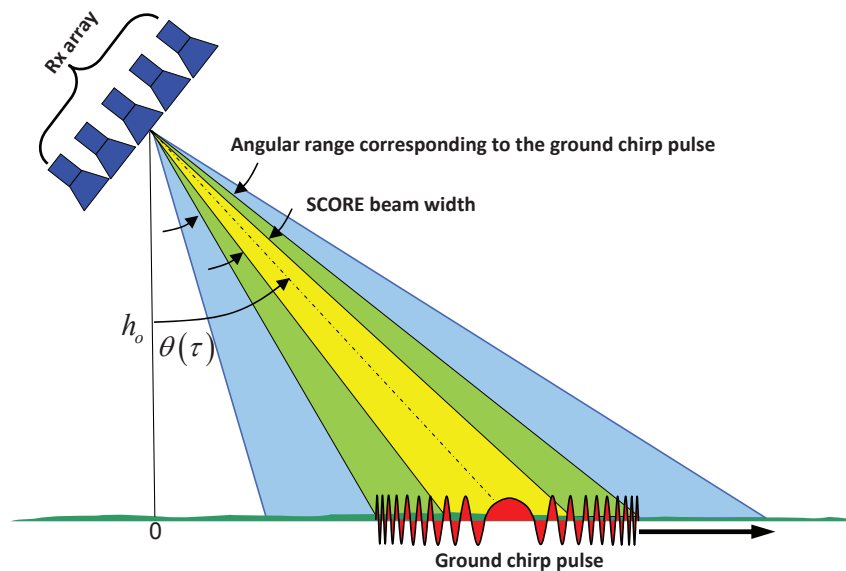
Figure 3.10.: Principle of beam scanning by the SCORE technique. The multiple frequency signals arriving at the same time instance from different angles form a linearly frequency-modulated signal (chirp) on ground. The SCORE beam chases this ground chirp pulse at the delay time instance. The SCORE beam narrower than the ground pulse extension requires the frequency-variant phase compensation.

41

3.3. Digital Beamforming in Azimuth

Multiple receive apertures, which are deployed in along-track, produce more spatial samples than a single channel system. By rearranging those spatial samples, PRF can be increased effectively [31]. However, a simple interleaving of the increased spatial samples leads to a rigid uniform sampling requirement [139]. Advanced signal processing techniques based on the beamforming theory overcome the severe sampling criterion, and widen the range of PRF selection available [69, 79]. This section describes the major role of DBF in azimuth and formulates the DBF algorithms in [69, 79], in a 2-D wavenumber domain.

3.3.1. Principle of Azimuth Ambiguity Suppression

The azimuth ambiguities are caused by the Doppler spectral aliasing of spatially sampled signal, and they become more significant if the sampling rate (PRF in side-looking SAR) is lower than the Nyquist sampling rate. In the HRWS SAR imaging mode, the SAR data is acquired using a lower PRF than the optimum rate, so that the Doppler spectrum of a single channel is severely distorted by aliasing. This section describes the theoretical background of the azimuth ambiguity in side-looking SAR, and derives the principle of a Doppler spectrum reconstruction from the spectral aliasing.
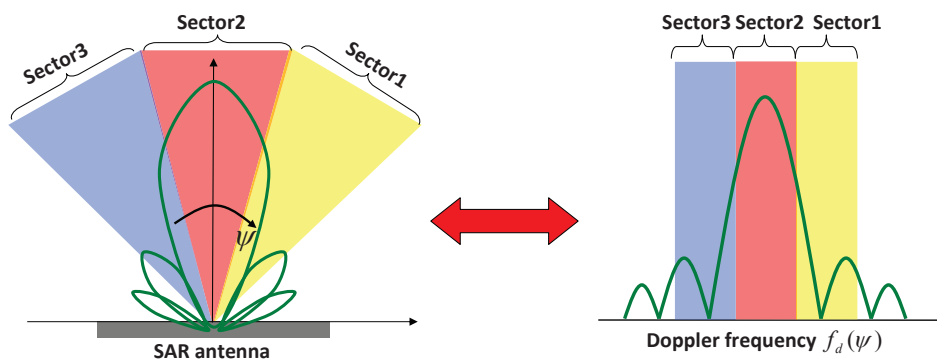
Figure 3.11.: Correspondence between the azimuth angle and the Doppler frequency.

In a side-looking SAR geometry, the azimuth angle ψ and the Doppler frequency are in the one-to-one correspondence relationship. Figure 3.11 depicts the angle-dependency of the Doppler spectrum. Each angular sector yields the individual subbands in the Doppler spectrum, as shown in Figure 3.11. For example, the spectral aliasing occurs if the subband by angular sector 1 folds back into the subband by angular sector 2, due to sub-sampling. This implies that the overlapping subbands originate from different azimuth angles and have a difference in the phase. Therefore, the aliasing is decomposable in the azimuth angle domain[2].

DBF techniques, which are presented in the following sections, exploit the angle dependency of Doppler frequency. They create multiple beams, only tracing signals from desired azimuth angles and suppressing interferences (aliasing). This operation is equivalent to a parallel filter-
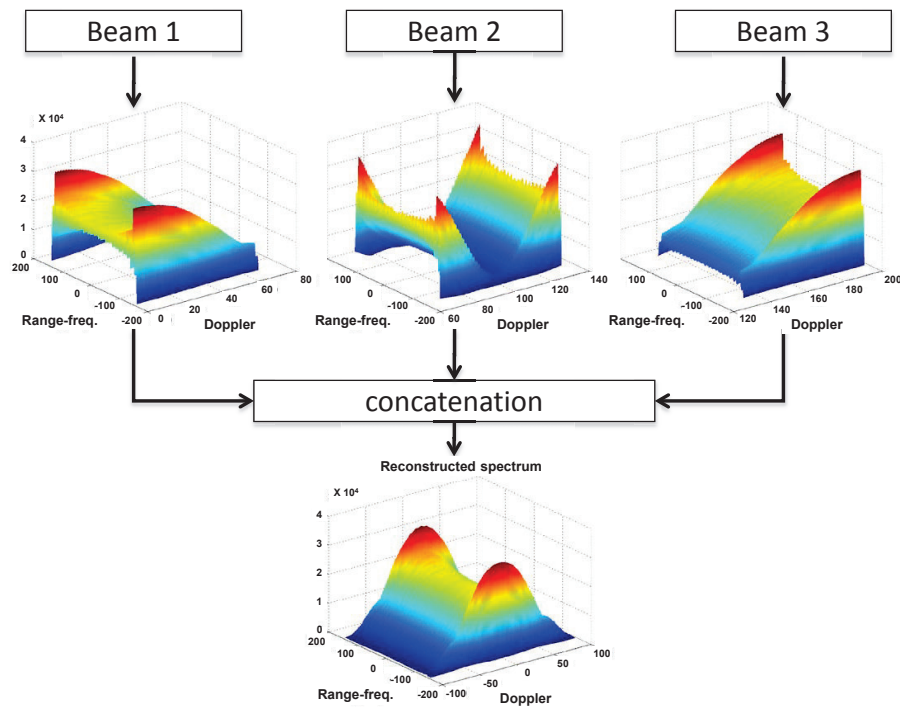
Figure 3.12.: Concatenation of the Doppler subbands to reconstruct a wide Doppler spectrum. Each beam recovers the individual subband (top) and the beam former reconstructs the wide Doppler spectrum using the concatenation of the subbands (bottom).

ing for each subband with the bandwidth of PRF. The extracted subbands are concatenated to reconstruct a wide Doppler spectrum, as in Figure 3.12.

3.3.2. Multichannel Reconstruction Algorithm

The multichannel sampling technique in [18] divides a band-limited baseband signal into multiple independent subbands, and samples each subband signal with a lower frequency than the sampling rate required for the entire bandwidth. The original signal is then reconstructed from the sub-sampled subband signals using a reconstruction filter bank. A beam former introduced in [69] was inspired by the subband sampling technique. This method regards the sub-sampled SAR data as pre-processed data by a bank of multiple filters, and thereby attempts to find reconstruction filter coefficients through solving a linear system equation for the pre-filtered data. This technique is therefore called a *Multichannel Reconstruction Algorithm* [69, 49]. This algorithm considers a general antenna constellation, which can be on single or multiple platforms. In this section, the algorithm is derived in the 2-D wavenumber domain using the developed signal model in the case of a uniform linear array system.

In section 3.1.3, the channel transfer function of the MIMO SAR signal has already been de-

---

[2]According to this theoretical background, azimuth ambiguity suppression techniques using multiple antennas are called "beamforming".

rived in the wavenumber domain. From (3.19) and (3.21), the channel transfer function[3], including the spectral aliasing, is given by

$$H_{ij}(k_r, k_a + \beta \cdot k_s) = \sum_{\beta=0}^{M_R-1} A_{ij} \cdot \exp\left(-jk_r \cdot X_{s,ij} - j(k_a + \beta \cdot k_s)\left(y - \frac{y_{t,j} + y_{r,i}}{2}\right)\right) \qquad (3.47)$$

where β is the order of aliasing and M_R is the number of receive subarrays in azimuth. $X_{s,ij}$ is the minimum slant range, which is identical for all receive apertures in a uniform linear array. The channel transfer function can be reformulated in relation to the first antenna. The receive antenna position in azimuth is described by

$$\frac{y_{t,j} + y_{r,i}}{2} = \frac{y_{t,j} + y_{r,1}}{2} - \frac{(i-1) \cdot \Delta L_{rs}}{2} \qquad (3.48)$$

where ΔL_{rs} is the spacing between the antenna phase centers. (3.47) can be rewritten by using a multiplication of the first Rx channel transfer function and a phase shift term, due to the separation of the antenna. For simplicity, when the range wavenumber k_r is omitted, the channel transfer function becomes:

$$H_{ij}(k_a + \beta \cdot k_s) = \sum_{\beta=0}^{M_R-1} H_{1j}(k_a + \beta \cdot k_s) \cdot \exp\left(-j(k_a + \beta \cdot k_s)\frac{(i-1) \cdot \Delta L_{rs}}{2}\right) \qquad (3.49)$$

where the exponential term accounts for the phase difference between the reference channel and the rest. This term is regarded as the distortion filter (pre-filter) coefficient of the ith receive channel:

$$H_{dist,i\beta} = \exp\left(-j(k_a + \beta \cdot k_s)\frac{(i-1) \cdot \Delta L_{rs}}{2}\right). \qquad (3.50)$$

Similarly, the reference channel H_{1j} is denoted by $H_{o,j}$, and then the ith receive channel transfer function is expressed as

$$H_{ij}(k_r, k_a) = \sum_{\beta=0}^{M_R-1} H_{o,j}(k_r, k_a + \beta \cdot k_s) \cdot H_{dist,i\beta}(k_r, k_a + \beta \cdot k_s). \qquad (3.51)$$

Now all receive channel transfer functions are rewritten in a matrix form. A column vector $\mathbf{H}_{o,j}$ consists of M_R components:

$$\mathbf{H}_{o,j}(k_a) = [H_{o,j}(k_a), H_{o,j}(k_a + k_s), \cdots, H_{o,j}(k_a + (M_R - 1) \cdot k_s)]^T. \qquad (3.52)$$

This vector is extended to M_T waveforms, so that one obtains the reference channel matrix:

$$\mathbf{H}_o = [\mathbf{H}_{o,1}, \quad \mathbf{H}_{o,2}, \quad \cdots, \quad \mathbf{H}_{o,M_T}]. \qquad (3.53)$$

---

[3]This function is an approximation of full channel transfer function including antenna patterns and slant range terms [69]. However, this approximation is sufficient to use, since those terms can be negligible in the case of a single platform system.

In the same manner, (3.50) is used to derive the $M_R \times M_R$ distortion channel matrix as follows:

$$\mathbf{H}_{dist} = \begin{bmatrix} H_{dist,11}(k_a) & H_{dist,12}(k_a+k_s) & \dots & H_{dist,1M_R}(k_a+(M_R-1)\cdot k_s) \\ H_{dist,21}(k_a) & H_{dist,22}(k_a+k_s) & \dots & H_{dist,2M_R}(k_a+(M_R-1)\cdot k_s) \\ \vdots & \vdots & \ddots & \vdots \\ H_{dist,M_R1}(k_a) & H_{dist,M_R2}(k_a+k_s) & \dots & H_{dist,M_RM_R}(k_a+(M_R-1)\cdot k_s) \end{bmatrix} \quad (3.54)$$

where its column and row represent the aliasing and the receive channel. The whole channel transfer function matrix $\mathbf{H}$ is given by a matrix product of the reference channel and the distortion filter matrix. From the above formulation, a linear system equation is established:

$$\mathbf{H} = \mathbf{H}_{dist} \cdot \mathbf{H}_o. \quad (3.55)$$

The reconstruction algorithm attempts to recover the reference channel matrix from the entire channel matrix by multiplying a reconstruction filter matrix $\mathbf{W}_{rec}$. So in principle, one should find a solution for

$$\mathbf{H}_o = \mathbf{W}_{rec} \cdot \mathbf{H} = \mathbf{W}_{rec} \cdot (\mathbf{H}_{dist} \cdot \mathbf{H}_o). \quad (3.56)$$

Fortunately, the distortion matrix has a full rank as long as the effective phase centers are *not* collocated. Therefore, the solution for (3.56) is the inverse of the distortion filter matrix [69]:

$$\mathbf{W}_{rec} = \mathbf{H}_{dist}^{-1}. \quad (3.57)$$

3.3.3. Minimum Variance Distortionless Response Method

J. Capon has proposed a high resolution spectral analysis method, which is called *Minimum Variance Distortionless Response* (MVDR) method [19]. This method provides robust AoA estimation performance, so that this is also well-known as Capon's beam former [56]. This beam former determines a weight vector to keep unit gain on a desired direction (angle), yet remaining orthogonal to other directions. Thereby the beam former considerably improves the angular resolution [19, 56, 89].

This technique is applied to the azimuth ambiguity suppression in SAR images [79]. In the azimuth ambiguity suppression, a weight function for a desired azimuth angle is derived in the Doppler frequency domain. This method attempts to find a weight preserving the signal energy of the desired Doppler component and aims to minimize the interference energy of other Doppler components [79]. The beamforming weight is then obtained by solving the following optimization problem, with respect to a desired angle ψ_o:

$$\min_{\mathbf{W}} \mathbf{W}^H \cdot \mathbf{R}_{rr} \cdot \mathbf{W} \quad \text{subject to} \quad \mathbf{W} \cdot \mathbf{A}(\psi_o) = 1 \quad (3.58)$$

where $\mathbf{R}_{rr}$ is the covariance matrix of the received signals including noise. In this work, the covariance matrix is generated in a 2-D wavenumber domain. Under the assumption of a narrow band signal[4], the frequency-independent weight of the MVDR beam former is obtained:

$$\mathbf{W}_{mvdr} = \frac{\mathbf{R}_{rr}^{-1} \cdot \mathbf{A}(\psi)}{\mathbf{A}^H(\psi) \cdot \mathbf{R}_{rr}^{-1} \cdot \mathbf{A}(\psi)}. \quad (3.59)$$

---

[4]This dissertation describes all formulas for a narrow band signal.

This solution is derived using the Lagrange method, which is described in detail in Appendix B. The MVDR beam former weight provides the optimum solution for the desired angle ψ_o:

$$\mathbf{W}_{mvdr} = \mathbf{A}^{-1}(\psi_o). \tag{3.60}$$

The steering vector for an azimuth angle ψ_o is derived from a corresponding Doppler frequency, using

$$f_d = \frac{2V_p}{\lambda} \cdot \sin \psi. \tag{3.61}$$

The Doppler wavenumber is defined as a ratio of the Doppler angular frequency and the platform velocity:

$$k_a = \frac{2\pi f_d}{V_p} = 2 \cdot \frac{2\pi}{\lambda} \cdot \sin \psi. \tag{3.62}$$

By introducing the spectral aliasing to (3.62), the Doppler wavenumber is rewritten as follows:

$$k_a + \beta \cdot k_s = 2k \cdot \sin \psi \tag{3.63}$$

where $\beta = 0, 1, 2, \cdots, M_R-1$. The azimuth angle corresponding to the given Doppler wavenumber is obtained from (3.63):

$$\sin \psi \approx \psi = \frac{k_a + \beta \cdot k_s}{2k}. \tag{3.64}$$

The above approximation is valid if the divergence azimuth angle is much smaller than the unit radian ($\psi \ll 1$ [rad]). The azimuth angle ψ is a function of β, and is therefore replaced by $\psi(\beta)$. Using (3.64), the weight for the ith antenna is given by

$$a_i(\beta) = \exp\left(-j\frac{2\pi}{\lambda} \cdot \Delta L_{rs}(i-1) \cdot \sin \psi(\beta)\right) \tag{3.65}$$

$$= \exp\left(-j(k_a + \beta \cdot k_s) \cdot \frac{\Delta L_{rs} \cdot (i-1)}{2}\right).$$

The steering vector is an array of each antenna weight:

$$\mathbf{a}(\beta) = [a_1(\beta), \quad a_2(\beta), \quad \cdots, \quad a_{M_R}(\beta)]^T. \tag{3.66}$$

In order to suppress the M_R spectrum repetition, M_R beams are required. Taking this into account, a steering matrix is built in a $M_R \times M_R$ matrix form as follows:

$$\mathbf{A} = [\mathbf{a}(0), \mathbf{a}(1), \quad \cdots, \quad \mathbf{a}(M_R - 1)]. \tag{3.67}$$

Comparing the resulting steering vector in (3.65) with the distortion filter coefficient in (3.50), it is noticeable that both algorithms result in the identical beam former weight in the case of a uniform linear array, although they are derived from different points of view. For multiple platform systems (sparse arrays), a large antenna separation and antenna patterns must be taken into account, like a full version of the reconstruction filter [49].

3.4. Multiple Subcarrier Technique: OFDM

In a typical multipath scenario, a wide band signal is strongly distorted by the frequency-selective fading channel. A possible solution to negate this effect is to divide a wide band channel into multiple subbands (subchannels), and transfer data through these multiple subchannels in parallel. This is the basic idea behind the OFDM technique. This technique is implemented effectively within digital systems, and is widely used in modern digital communications.

3.4.1. Principle of OFDM

The OFDM scheme was proposed and patented in the mid 1960s [22]. Figure 3.13 illustrates a schematic view of the basic multiple subcarrier modulation scheme.
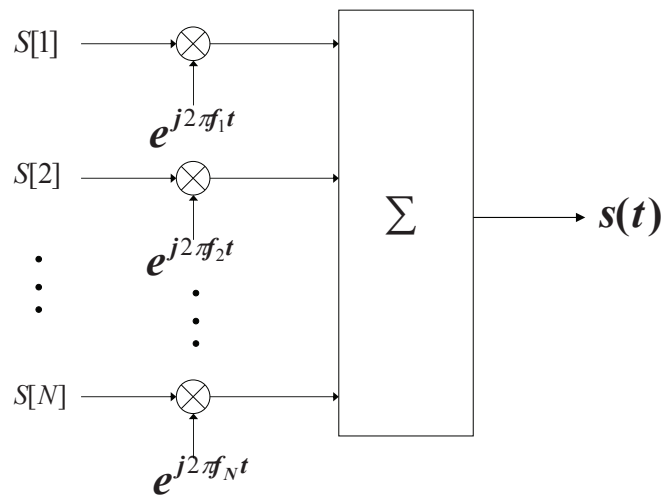
Figure 3.13.: Basic configuration of the multiple subcarrier modulation.

Within an available signal bandwidth, N input data, $S[p](p = 1, 2, \cdots, N)$, are modulated by independent subcarriers and summed up. Each subchannel bandwidth is specified to be narrower than the channel coherence bandwidth, in order to avoid the frequency-selective channel effect [100, 39]. The modulated output signal $s(t)$ is given by

$$s(t) = \sum_{p=1}^{N} S[p] \cdot \exp(j2\pi f_p t) \cdot \text{rect}\left[\frac{t}{T_p}\right] \tag{3.68}$$

where T_p is the symbol duration and rect $[\cdot]$ denotes the rectangular window function. In order to demodulate all of the input data, each subchannel must fulfill the orthogonal condition of

$$\int_{-\infty}^{\infty} \exp\left(j2\pi f_l t\right) \cdot \exp\left(-j2\pi f_p t\right) \mathrm{d}t = \delta_{lp} \tag{3.69}$$

where

$$\delta_{lp} = \begin{cases} 1 & \text{if } l = p, \\ 0 & \text{if } l \neq p. \end{cases} \tag{3.70}$$

Under the assumption of an ideal system, the receiver demodulates the OFDM signal and recovers the transmitted data using the orthogonality of the subcarriers, which is defined in (3.69). The OFDM demodulation is accomplished by a bank of correlation filters for each subcarrier. Therefore, The demodulation process is equivalent to the Fourier transform of the input signal (3.68):

$$\mathcal{F}\{s(t)\} = \int_{-T_p/2}^{T_p/2} s(t) \cdot \exp\left(-j2\pi f_p t\right) \mathrm{d}t \tag{3.71}$$

$$= \frac{T_p}{2} \sum_{p=1}^{N} [S[p] * \text{sinc}((f - f_p)T_p]$$

where $\text{sinc}(\cdot)$ denotes the sinc function ($\text{sinc}(x) = \frac{\sin(\pi x)}{\pi x}$). The Fourier transform of $s(t)$ is represented by a convolution sum of the transmitted data $S[p]$ and the sinc function, which result from the Fourier transform of the rectangular time window in (3.68). Let Δf denote the subcarrier spacing. If the symbol period T_p is set to be the reciprocal of the subcarrier spacing ($1/\Delta f$), then the different subcarriers do not interfere with each other at every subcarrier frequency, as shown in Figure 3.14. Indeed, they are orthogonal.
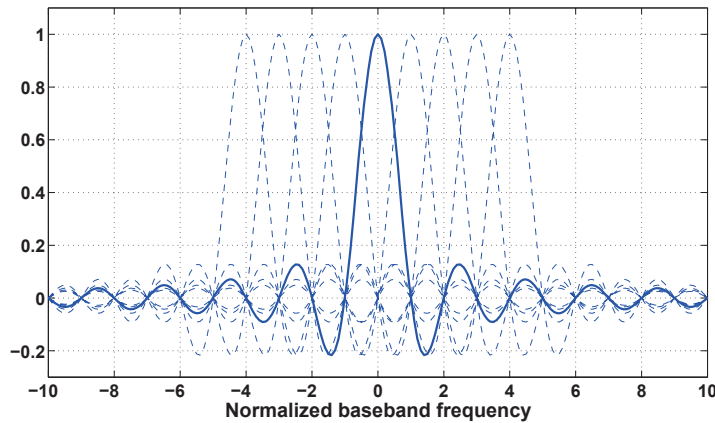
Figure 3.14.: Orthogonality between the subcarriers in frequency normalized by the subcarrier distance Δf. For example, all the zero-crossings of a reference subcarrier (solid line) occur at the peaks of adjacent subcarriers (dashed lines).

OFDM wireless communication systems prefix the data symbol with a repetition at the end in order to counteract time-dispersive channels. The redundant addition is called *Cyclic Prefix* (CP)[5], and its length must be longer than the delay spread of the channel [101, 100]. This gives a guard interval between successive data symbols. The CP is discarded at the receiver before

---

[5]In the first proposal, this redundant addition was called "cyclic extension" by authors, since it increases the symbol length.

the demodulation, in order to remove interferences between the data symbols, a so-called *Inter-Symbol Interference* (ISI). In the present MIMO SAR, the CP is not applied at the transmission, but the principle of the CP is used. This present work exploits the orthogonality of subcarriers, in order to produce multiple orthogonal waveforms. As long as the orthogonality is maintained, the multiple waveforms can be distinguished from one another.

3.4.2. Implementation of OFDM Systems

It can be intuitively figured out that the implementation of an OFDM system requires a number of oscillators and integrators for multiple subcarriers. In 1971, Weinstein and Ebert proved that the *Fast Fourier Transform* (FFT) and its *inverse FFT* (IFFT) could replace such complex system configurations and implement the OFDM system in digital [129]. In order to improve the computation efficiency of FFT/IFFT, the number of subcarriers is chosen to be a power of 2 as a rule. Under the assumption of the synchronization between transmitters and receivers, in terms of the sampling frequency and the length of FFT/IFFT, a generic schematic of OFDM systems is drawn in Figure 3.15. It is noted that DFT/IDFT are used in the following formulations.
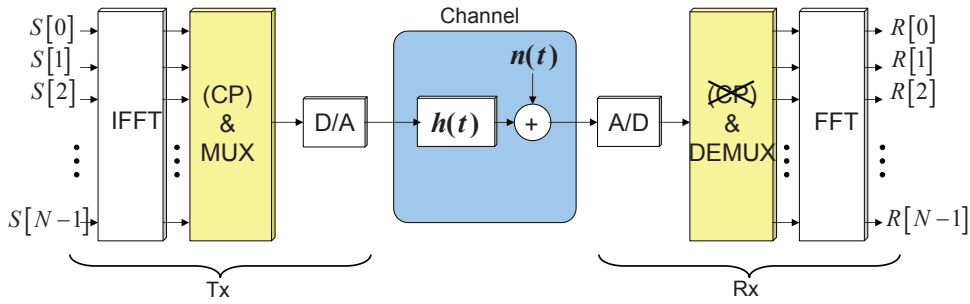
Figure 3.15.: A generic implementation model of an OFDM system using FFT/IFFT.

The input data $S[p]$ is modulated by N-point IDFT:

$$s[n] = \sum_{p=0}^{N-1} S[p] \cdot \exp\left(j\frac{2\pi}{N}np\right) \tag{3.72}$$

where n and p denote the discrete time and the subcarrier index, respectively ($n, p = 0, 1, 2, \cdots, N-1$). After the modulation, the CP is added to the modulated symbol, so that the symbol length is increased. For instance, if the CP length is L, then the symbol length becomes $N + L$. Through the multiplexer and DAC, the data symbol is converted into an analog data signal, which travels into the channel $h(t)$. The implementation of demodulation is an inverse of the modulator. ADC converts the analog input signal into a digital sequence and the CP is discarded from the digitized receive sequence. The symbol length once again becomes N without a loss of information. The final data retrieval is completed by DFT with the length N.

As aforementioned, the CP in SAR is not an applicable technique, due to echo delay spread much longer than the pulse length. To apply the OFDM principle to SAR systems, a remarkably long received signal must be partitioned to fit the N-point DFT in any case. The present MIMO

SAR resolves this issue via digital beamforming in elevation or using the deramping[6] technique followed by low-pass filtering, which is widely used in spotlight SAR signal processing [87]. In this section, an ideal partition is assumed. It is now straightforward to show the demodulation using DFT. The demodulated signal is henceforth given by

$$R\left[p\right] = \sum_{n=0}^{N-1} \left[h\left[n\right] * s\left[n\right]\right] \cdot \exp\left(-\frac{j2\pi}{N}np\right) + N\left[p\right]$$

(3.73)

where $N\left[p\right]$ is the noise spectrum. Substituting (3.72) for $s\left[n\right]$, (3.73) is rewritten as

$$R\left[p\right] = \sum_{n=1}^{N} \left[h\left[n\right] * \sum_{p=0}^{N-1} S\left[p\right] \cdot \exp\left(\frac{j2\pi}{N}np\right)\right] \cdot \exp\left(-\frac{j2\pi}{N}np\right) + N\left[p\right].$$

(3.74)

According to the convolution theorem, the Fourier transform of the convolution between the channel and signal becomes a multiplication. From the MIMO signal model, the received signal can be denoted in matrix form:

$$\mathbf{R}\left[p\right] = \mathbf{H}\left[p\right] \cdot \mathbf{S}\left[p\right] + \mathbf{N}\left[p\right]$$

(3.75)

where $\mathbf{H}\left[p\right]$ is the channel transfer function given in (3.19) inside section 3.1.3. In this case, the range wavenumber k_r, in (3.16), is written using the discrete subcarriers.

$$k_r = \sqrt{4\left(\frac{2\pi(p \cdot \Delta f - f_o/2)}{c_o}\right)^2 - k_u^2}$$

(3.76)

where f_o denotes the signal bandwidth. Note that the range frequency in the square root is shifted by $f_o/2$, in order to describe the baseband ($p \cdot \Delta f \in [-f_o/2, f_o/2,]$). If the channel transfer function is known, then the data sequence $\mathbf{S}\left[p\right]$ is estimated by compensating the channel transfer function:

$$\tilde{\mathbf{S}}\left[p\right] = \mathbf{H}^{-1}\left[p\right] \cdot (\mathbf{H}\left[p\right] \cdot \mathbf{S}\left[p\right] + \mathbf{N}\left[p\right])$$

(3.77)

where $\mathbf{H}^{-1}\left[p\right]$ is inverse of the channel transfer function matrix.

Unlike communication systems, radar systems exploit the knowledge of transmitted waveforms, in order to obtain target information, which is delivered by the channel transfer function. The channel transfer function can be estimated in the same manner. Generally, the waveform and the channel are complex, so this processing is achieved via the multiplication of the complex conjugate of the input sequence. The process is equivalent to the range focusing by matched filtering:

$$\tilde{\mathbf{H}}\left[p\right] = (\mathbf{H}\left[p\right] \cdot \mathbf{S}\left[p\right] + \mathbf{N}\left[p\right]) \cdot \mathbf{S}^H\left[p\right]$$

(3.78)

$$= |S\left[p\right]|^2 \cdot \mathbf{H}\left[p\right] + \tilde{\mathbf{N}}\left[p\right].$$

An important aspect of this is that the OFDM processing is independent of the input sequence $S[p]$. In other words, any type of waveforms can be applied to this technique as the input sequence. The orthogonality is provided by the subcarriers, not the input sequence. In addition,

---

[6]This is relevant only to in the case that a chirp waveform is used.

the modulation and the demodulation are linear processes, so that they can be implemented separate from conventional SAR processing. In the next chapter, the orthogonality of subcarriers is exploited in order to generate multiple orthogonal waveforms for this present MIMO SAR system, and a relevant processing algorithm is developed.

4. Novel Waveform for MIMO SAR

In 2007, several spaceborne SAR missions, TerraSAR-X, COSMO-SkyMed, and Radarsat-2, were launched and thus opened a new era of spaceborne SAR remote sensing [71, 51, 81]. The TerraSAR-X in particular is flying with a second satellite in a closely controlled formation for the purpose of a consistent global DEM generation, so the mission was therefore named as TanDEM-X(**T**erraSAR-X **a**dd-o**n** for **D**igital **E**levation **M**easurement). Despite the need for multiple spacecrafts and sophisticated orbit control, its benefits overwhelm its costs. For instance, the *High Resolution Terrain Information* (HRTI)-3 specification is then achievable [71]. An interesting point is that both the TerraSAR-X and the TanDEM-X implement a 2×4 MIMO configuration, since each satellite carries dual receive antennas. It may well be regarded as the first spaceborne MIMO SAR. However, uncolored waveform transmission forces the innovative mission to pursue the conventional data acquisition modes. Hence, the inherent problems of the conventional SAR system still remain. The waveform design is the most important and also the most critical issue in realizing the multimodal high-performance imaging capability in the present MIMO concept. Besides the orthogonality between waveforms for simultaneous multiple pulse transmissions, a new waveform should provide easy implementation and integration for a conventional SAR processor. In addition to this, a constant envelope of the waveform is desired considering the *High Power Amplifier* (HPA) in transmitters. The HPAs in spaceborne SAR systems operate in saturation in order to generate the maximum available power and ensure a stable power level for variations in the input signal [30]. A significant envelop variation therefore yields a clipping effect, and thereby the orthogonality can be broken.

This chapter presents a novel waveform which satisfies the above requirements. The idea behind the new waveform is to combine the chirp waveform and the OFDM technique. A major problem of the typical OFDM signal is the fast variation of the signal envelope [77]. The present work resolves the problem through the application of the OFDM principle to the chirp waveform. Thereby, one can exploit the orthogonality of multiple subcarriers and achieve the constant envelope of waveforms at the same time. For a dual transmit antenna scenario, this chapter derives the novel waveform scheme consisting of the modulation and demodulation algorithm, based on the conventional OFDM processing algorithm, and validates its potential in regard to distributed target scenarios. Special attention has to be paid to the demodulation, since the classical OFDM demodulation assumes that the delay spread of received signal is shorter than the length of cyclic prefix (see section 3.4), but a SAR echo signal is generally much longer than the transmitted pulse length. A demodulation strategy of such a long SAR signal is to divide it into several angle-dependent subsets and apply the classical demodulation scheme to these subsets. For this purpose, the present work uses the digital beamforming in elevation in order to implement spatial filtering, as introduced in Chapter 3.

In spotlight SAR processing, the dechirp-on-receive technique combined with low-pass filtering performs the angular decomposition of received signals [87, 88, 20]. Every single echo after the dechirp process is converted to a sinusoidal signal with a frequency dependent on its delay time. The low-pass filtering selects signals within a specific range of the delay. As shown in Chapter 3, according to the one-to-one correspondence between the delay and the AoA, this low pass filtering is equivalent to the spatial filtering. However, this approach is valid only for a chirp waveform used for both demodulators. In order to provide a framework for the demod-

ulation process, this work is concerned with general scenarios. Therefore this chapter derives a demodulation algorithm based on the DBF function of the MIMO SAR.

4.1. Orthogonal OFDM Waveforms using Chirp Signals

The development of novel waveforms starts with a derivation of the combination of the chirp waveform and the OFDM technique to achieve the design goal. In the following section, it is shown that a conventional chirp signal can be interpreted as an OFDM signal. From this, the principle and aspects of this waveform scheme are explained.

4.1.1. Reinterpretation of Chirp Signal

Under the assumption that a chirp waveform is generated in frequency domain, this section draws the waveform generation step-by-step and points out an analogy within the traditional OFDM modulation.

The instantaneous frequency of a chirp signal is linearly increasing or decreasing with time, a so-called up-chirp or down-chirp signal. In the case of an up-chirp signal, the spectrum is given by

$$S(f) = \exp\left(-j\frac{\pi f^2}{K_r}\right) \tag{4.1}$$

where f_o is the signal bandwidth ($f \in \left[-\frac{f_o}{2}, \frac{f_o}{2}, \right]$), and K_r is the chirp rate[1] defined as $K_r = \frac{f_o}{T_p}$

where T_p is the chirp signal length. The chirp spectrum is inversely Fourier transformed to give a time domain signal:

$$s(t) = \mathcal{F}^{-1}\{S(f)\} \tag{4.2}$$

$$= \exp\left(j\pi K_r t^2\right) \cdot \text{rect}\left[\frac{t}{T_p}\right]$$

where $\mathcal{F}^{-1}\{\cdot\}$ denotes the inverse Fourier transform. In practical implementation using digital instruments, the spectrum $S(f)$ is replaced by a $1 \times N$ complex data sequence $\mathbf{S}$:

$$\mathbf{S} = [S(f_0), S(f_1), \cdots, S(f_{N-1})]. \tag{4.3}$$

As mentioned in Chapter 3, the OFDM modulation and demodulation can be effectively implemented by using IDFT and DFT [129]. Thus the inverse Fourier transform of the complex sequence $\mathbf{S}$ is equivalent to the OFDM modulation using IDFT:

$$\mathbf{s} = \mathbf{F}^{-1} \cdot \mathbf{S}^T(f) \tag{4.4}$$

where $\mathbf{F}$ is the DFT matrix and its inverse matrix is multiplied by the input sequence. The superscript $\{\cdot\}^T$ denotes the vector transpose, which can be understood to be the serial-to-parallel conversion[2] of $\mathbf{S}$ in this case. The output vector $\mathbf{s}$ is recovered to a serial data sequence and converted to an analog signal at the end. As depicted in Figure 4.1, the above procedure is
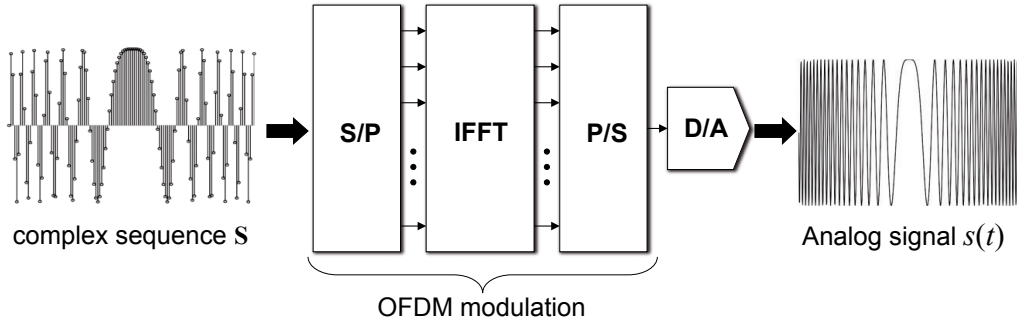
Figure 4.1.: Chirp generation schematic in frequency domain, interpreted as the OFDM modulation.

identical to the classical OFDM modulation process, except for the cyclic prefix (see also Figure 3.15).

In a signal model, the same conclusion is derived. The OFDM signal is the sum of the input sequence modulated by N orthogonal subcarriers:

$$s(t) = \sum_{p=0}^{N-1} \underbrace{S(f_p)}_{\text{data}} \cdot \underbrace{\exp(j2\pi \cdot (p \cdot \Delta f) \cdot t)}_{\text{orthogonal subcarriers}} \tag{4.5}$$

where the exponential term accounts for the orthogonal subcarriers. Using the relationship $t = nT_s$ and $\Delta f = 1/NT_s$ where T_s is a sampling interval, (4.5) is rewritten in a discrete signal form:

$$s[n] = \sum_{p=0}^{N-1} S[p] \cdot \exp\left(j\frac{2\pi}{N}pn\right) \tag{4.6}$$

which is the general expression of DFT, except for the amplitude scaling term, $\frac{1}{N}$. (4.6) is accordance with the OFDM implementation model in (3.72). Consequently, the chirp waveform can be regarded as an OFDM signal.

The *Peak-to-Average Power Ratio* (PAPR) is the ratio between the maximum power and the average power of an OFDM signal for a pulse duration,[3] and indicates flatness of the OFDM signal envelop [121, 127]. OFDM's primary drawback is a high PAPR caused by wild amplitude fluctuations. The chirp waveform as an OFDM signal, by contrast, has a constant envelop. The waveform of an OFDM signal depends on the ***input data sequence***, while the orthogonality is provided by the ***orthogonal subcarriers***. This is the most important concept of the present novel OFDM waveform scheme.

On this basis, multiple orthogonal waveforms can be produced by modulating an input sequence with different subcarriers, and the constant envelop can be achieved by employing a chirp spectrum as the input data sequence. In the following section, two OFDM waveforms for the present MIMO SAR are derived.

---

[1] This is also called *Frequency Modulation* (FM) rate in literatures.

[2] The row vector is converted to a column vector.

[3] In OFDM communications, this parameter is generally defined as a symbol duration.

4.1.2. OFDM Modulation using Chirp for Dual Tx Antennas

In this section, the modulation principle of new waveform scheme is described from the OFDM principle viewpoint. Let us take into account two OFDM modulators containing the same number of orthogonal subcarriers. The subcarriers of each modulator are separated by $2\Delta f$, and both sets are mutually shifted by Δf, as shown in Figure 4.2. Since those subcarriers are orthogonal, although the same input data sequence **S** is modulated by both OFDM modulators, the output signals, $s_1(t)$ and $s_2(t)$, are separable on receive after the demodulation.
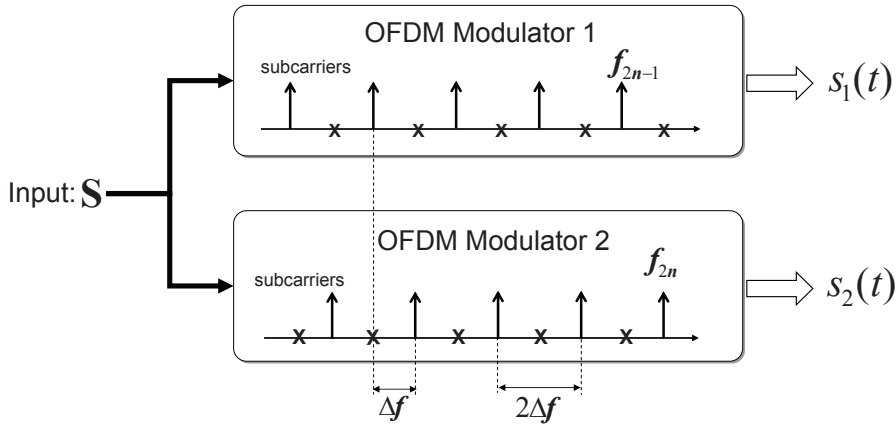
Figure 4.2.: OFDM modulation of a single input sequence with two non-overlapping subcarrier sets.

For a successful demodulation on receive, a total number of subcarriers should be taken into account. If the length of the input data **S** is N, in principle, N subcarriers are required for the OFDM modulation. However, the two OFDM waveform signals are superposed and therefore return to a receiver. In this case, the received signal contains total $2N$ subcarrier components from both waveforms, so that DFT with the length N fails to demodulate the signal. Thus the modulator (IDFT) and the demodulator (DFT) should both have the same length of $2N$. The number of subcarriers is increased by interleaving zeros indicated by the symbol "x" in Figure 4.2. Thereby both modulators have the length of $2N$ but use only N subcarriers to carry the input data. In the same manner, the input sequence **S** is modified to also have the length $2N$ in order to fit the length of IDFT/DFT. The input sequence is interleaved by zeros and shifted by the subcarrier difference Δf, as shown in Figure 4.3.

As aforementioned, a chirp signal spectrum is used in the present work to achieve the constant envelop. In the case of a up-chirp waveform, two orthogonal spectra produced by the zero-interleaving and the frequency shift are formulated as follows:

$$S_1[p] = \begin{cases} S_o[p] = \exp\left(-j\pi\dfrac{(p\cdot\Delta f)^2}{K_r}\right) & \text{if } \dfrac{p}{2} \text{ is integer} \\ 0 & \text{otherwise} \end{cases} \tag{4.7}$$
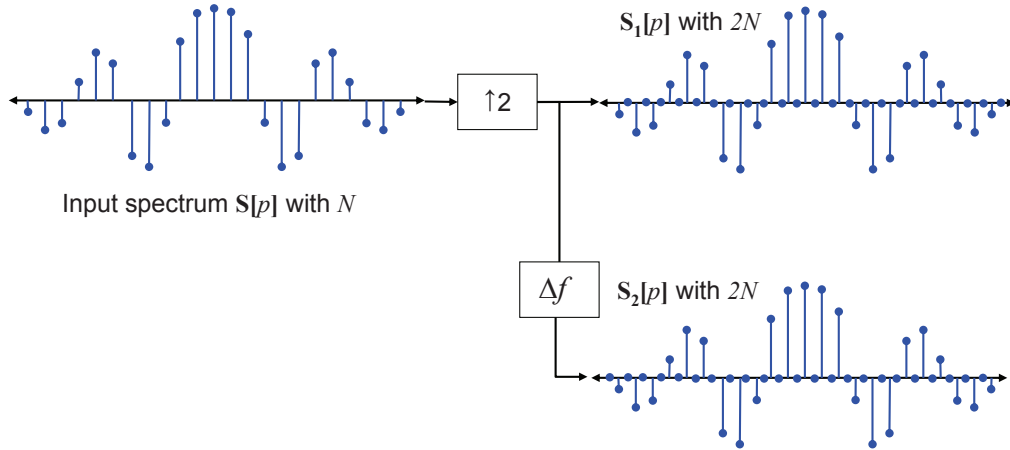
Figure 4.3.: Preprocessing of the input sequence **S**, in order to produce two orthogonal inputs for each OFDM demodulator with the length of $2N$.

and

$$
S_2[p] = \begin{cases} S_e[p] = \exp\left(-j\pi\dfrac{((p-1)\cdot\Delta f)^2}{K_r}\right) & \text{if } \dfrac{p+1}{2} \text{ is integer} \\ 0 & \text{otherwise} \end{cases} \tag{4.8}
$$

where $p = 0, 1, 2, \cdots, 2N - 1$. $S_o[p]$ and $S_e[p]$ are odd and even components of $S_1[p]$ and $S_2[p]$, respectively. Time domain signals are obtained by IDFT:

$$
s_1[n] = \mathcal{F}^{-1}\{S_1[p]\}, \tag{4.9}
$$
$$
s_2[n] = \mathcal{F}^{-1}\{S_2[p]\}. \tag{4.10}
$$

According to the Cooley-Tukey algorithm [54], the DFT/IDFT can be performed by separate transforms with respect to the odd and even components of the input. Since the even components in S_1 are zeros, the inverse Fourier transform of $S_1[p]$ is equivalent to that of $S_o[p]$. Substituting $\bar{p}$ for $\frac{p}{2}$, the modulated waveform s_1 is given by

$$
s_1[n] = \mathcal{F}^{-1}\{S_o[p]\}
$$
$$
= \sum_{\bar{p}=0}^{N-1} S_o[\bar{p}]\cdot\exp\left(j\frac{2\pi}{N}\bar{p}n\right), \tag{4.11}
$$

and in the same way, using $\frac{p+1}{2} = \bar{p} + \frac{1}{2}$, the other modulated waveform s_2 is derived as

$$
s_2[n] = \mathcal{F}^{-1}\{S_e[p]\}
$$
$$
= \sum_{\bar{p}=0}^{N-1} S_e[\bar{p}]\cdot\exp\left(j\frac{2\pi}{N}\bar{p}n\right)\cdot\exp\left(j\frac{\pi}{N}n\right) \tag{4.12}
$$

where $\bar{p} = 0, 1, 2, \cdots, N - 1$ and $n = 0, 1, 2, \cdots, 2N - 1$. The extra exponential term in (4.12) accounts for the subcarrier offset between the two OFDM waveforms. According to the repetitive

property of DFT (see Appendix C.2), $s_1[n]$ and $s_2[n]$ are expressed by a repetition of the inverse Fourier transform of $S_o[p]$ and $S_e[p]$, respectively:

$$s_1 = s_o[n] \cdot \mathrm{rect} \left[\frac{n}{N} \right] + s_o[n - N] \cdot \mathrm{rect} \left[\frac{n - N}{N} \right] \tag{4.13}$$

and

$$s_2 = \left(s_e[n] \cdot \mathrm{rect} \left[\frac{n}{N} \right] + s_e[n - N] \cdot \mathrm{rect} \left[\frac{n - N}{N} \right] \right) \cdot \exp \left(j \frac{\pi}{N} n \right). \tag{4.14}$$

These modulated OFDM waveforms are converted to analog forms by DAC. The OFDM waveforms in time domain are plotted in Figure 4.4.

(a) $s_1(t)$ (b) $s_2(t)$
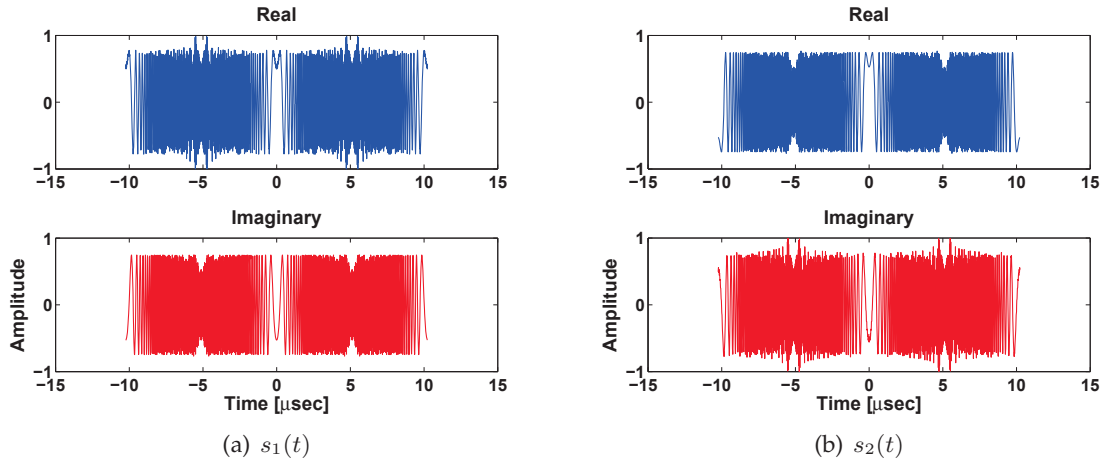
Figure 4.4.: Complex baseband OFDM waveforms with 50MHz bandwidth and N=1024. The overshoots due to a limited signal bandwidth are observed in the real part of $s_1(t)$ and the imaginary part of s_2(t).

Using the signal model above, the OFDM waveforms can be directly produced in time domain. The time domain generation is valuable, since a band-limited input sequence can cause an overshoot in time domain waveforms, as shown in Figure 4.4 [97].

4.1.3. Time Domain Generation

Based on the relationship $\Delta f = \frac{1}{2NT_s}$, (4.13) and (4.14) can be rewritten in analog forms:

$$s_1(t) = s_o(t) \cdot \mathrm{rect} \left[\frac{t}{T_p} \right] + s_o(t - T_p) \cdot \mathrm{rect} \left[\frac{t - T_p}{T_p} \right] \tag{4.15}$$

and

$$s_2(t) = \left(s_e(t) \cdot \mathrm{rect} \left[\frac{t}{T_p} \right] + s_e(t - T_p) \cdot \mathrm{rect} \left[\frac{t - T_p}{T_p} \right] \right) \cdot \exp \left(j 2\pi \cdot \Delta f \cdot t \right). \tag{4.16}$$

Since $s(t) = s_o(t) = s_e(t) = \exp\left(j\pi K_r t^2\right)$, (4.15) and (4.16) are rewritten as follows:

$$s_1(t) = \exp\left(j\pi K_r t^2\right)\cdot\text{rect}\left[\frac{t}{T_p}\right] + \exp\left(j\pi K_r (t - T_p)^2\right)\cdot\text{rect}\left[\frac{t - T_p}{T_p}\right] \tag{4.17}$$

and

$$s_2(t) = \left(\exp\left(j\pi K_r t^2\right)\cdot\text{rect}\left[\frac{t}{T_p}\right] + \exp\left(j\pi K_r (t - T_p)^2\right)\cdot\text{rect}\left[\frac{t - T_p}{T_p}\right]\right)\cdot\exp\left(j2\pi\cdot\Delta f\cdot t\right) \tag{4.18}$$

$$= s_1(t)\cdot\exp\left(j2\pi\cdot\Delta f\cdot t\right).$$

From (4.17) and (4.18), $s_1(t)$ and $s_2(t)$ are directly generated in time domain. Figure 4.5 depicts the time domain generation schematic, which is the graphical expression of (4.17) and (4.18).

(a)

(b)
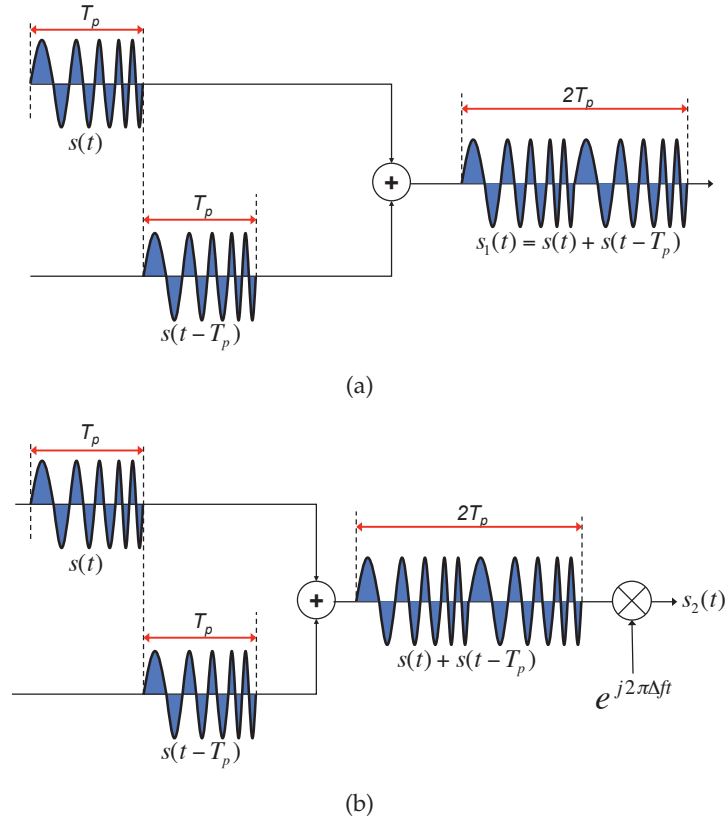
Figure 4.5.: Schematic of the time domain generation for two OFDM chirp waveforms: (a) $s_1(t)$ and (b) $s_2(t)$.

It may be notable that the subcarrier offset Δf in $s_2(t)$ should be multiplied after the serial connection of two chirps, as shown in Figure 4.5 (b). In the time domain generation, a phase discontinuity at the junction of successive chirps is considered. This discontinuity can be avoided by selecting N to meet the following condition:

$$\pi K_r t^2|_{t=T_p} \overset{!}{=} \pi K_r (t - T_p)^2|_{t=T_p}. \tag{4.19}$$

The above condition means that the preceding and the succeeding chirp phases of an OFDM signal are equal at the time instance T_p. Substituting f_o/T_p for K_r, one obtains

$$f_o \cdot T_p \overset{!}{=} \text{even integer,} \tag{4.20}$$

and, using $f_o = 2N \cdot \Delta f$ and $\Delta f = 1/2T_p$, the final requirement is derived as:

$$N \overset{!}{=} \text{even integer.} \tag{4.21}$$

4.1.4. Signal Power Consideration

Since the IDFT is a linear operation, the input power of each OFDM modulator must remain unchanged after the modulation. However, due to the increment of the spectral components ($N \rightarrow 2N$), the OFDM chirp waveform generation, with the zero-interleaving in frequency domain, yields a change in the signal peak power. This section is dedicated to the description of the relationship between the peak power and the total energy of the OFDM waveform. In the Fourier analysis, *Parseval's theorem* states that the average power of a periodic signal is equal to the sum of the average powers in all of its harmonic components [97]:

$$\sum_{p=0}^{N-1} |S[p]|^2 = \frac{1}{N} \cdot \sum_{n=0}^{N-1} |s[n]|^2 \tag{4.22}$$

where $s[n]$ is the discrete time signal and $S[p]$ is its Fourier transform pair. The average power of $s[n]$ is given by

$$\frac{1}{N} \cdot \sum_{n=0}^{N-1} |s[n]|^2 = \frac{1}{N} N \cdot A^2 = A^2 \tag{4.23}$$

where A denotes the signal amplitude. According to Parseval's theorem (4.22), this average power is conserved in frequency domain as well:

$$\sum_{p=0}^{N-1} |S[p]|^2 = A^2. \tag{4.24}$$

If two OFDM chirp waveforms, $S_1[p]$ and $S_2[p]$, are produced from $S[p]$ and their Fourier transform pairs are denoted by $s_1[n]$ and $s_2[n]$, each OFDM spectrum consists of N non-zero subcarrier components and N zeros. The sum of the average power $|S_1[p]|^2$ is hence calculated by

$$\sum_{p=0}^{2N-1} |S_1[p]|^2 = \sum_{\bar{p}=0}^{N-1} |S_1[\bar{p}]|^2 = \bar{A}^2 \tag{4.25}$$

where $\bar{A}$ is the amplitude and $\bar{p} = 0, 1, 2, \cdots, N-1$. Its time domain signal $s_1[n]$ conserves the same energy:

$$\frac{1}{2N} \cdot \sum_{n=0}^{2N-1} |s_1[n]|^2 = \bar{A}^2. \tag{4.26}$$

The N harmonic components in $S_1[p]$ are zeros. Therefore, although the zero-interleaving in frequency domain increases the signal length in time domain, the total energy of $s[n]$ and $s_1[n]$ must remain unchanged:

$$2T_p \cdot \bar{A}^2 \overset{!}{=} T_p \cdot A^2. \tag{4.27}$$

Finally the amplitude of the modulated waveform is found:

$$\bar{A} = \frac{A}{\sqrt{2}}. \tag{4.28}$$

Without loss of generality, the same rule is applied to $S_2[p]$ and its pair $s_2[n]$. Therefore its signal amplitude is also equal to $A/\sqrt{2}$. All these relationships are depicted in Figure 4.6.
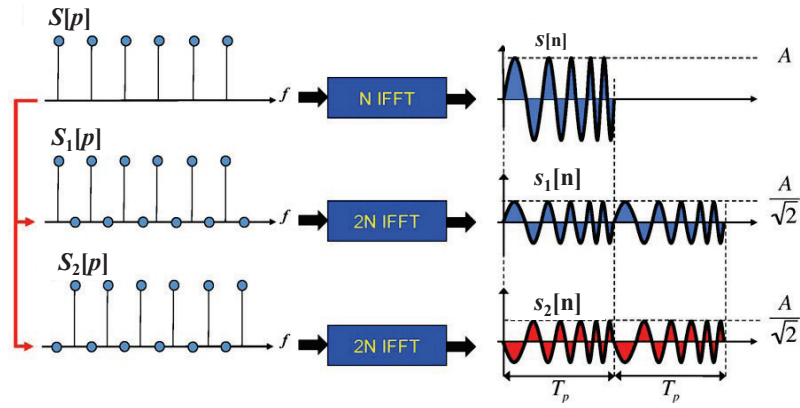
Figure 4.6.: The relationship between the signal amplitude and length in the OFDM chirp waveforms: the original input spectrum and its Fourier transform pair(top), the zero-interleaved spectrum and its Fourier transform pair for the odd (middle), and even subcarriers(bottom). The zero-interleaving increases the time domain signal length twofold with an amplitude reduction.

Consequently, the zero-interleaving in the OFDM waveform generation from the input sequence $S[p]$ does not affect the total energy. The OFDM modulated waveforms conserve the total energy, however the peak power is reduced by a factor of 2 in this case. It is worth noting that a duty cycle of the OFDM signal also increases by a factor of 2 for a given PRF, due to the pulse length extension:

$$\text{Duty cycle } [\%] = 2\frac{T_p}{PRI} \times 100. \tag{4.29}$$

4.2. OFDM SAR Signal Demodulation

This section is dedicated to the development of an OFDM demodulation algorithm applicable to a received SAR signal, which is typically much longer than the OFDM pulse length. The demodulation algorithm developed in this section consists of the segmentation of echo signal by spatial filtering (digital beamforming), the circular-shift addition, and the conventional OFDM demodulation using DFT. Before pursuing a development, the following requirements must be clearly highlighted.

4.2.1. Requirements for the OFDM Demodulation

According to the classical OFDM demodulation scheme, the orthogonality of subcarriers can be exploited only if the following requirements are strictly fulfilled:

- **The same length of modulator (IDFT) and demodulator (DFT)**

- **Maintenance of entire waveforms in IDFT/DFT windows**

The above conditions are necessary to implement the traditional and efficient DFT-based demodulator [129], and to also recover two orthogonal spectra without mutual interferences in the present MIMO SAR system. Detailed explanations are given as follows.
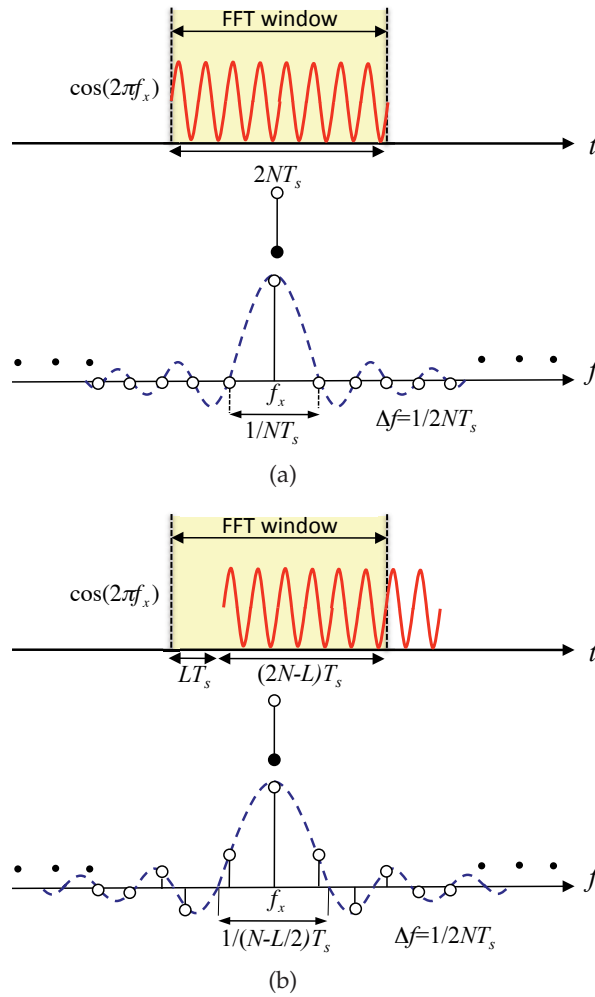
Figure 4.7.: Illustration of the waveform truncation effect on the orthogonality: (a) optimum condition and (b) truncated waveform increasing the main lobe width of the sinc function at f_x in spectrum.

As shown in Figure 4.7, a sinusoidal pulse with a single subcarrier frequency f_x, and its length $2NT_s$ is considered. If the whole pulse fits the DFT window exactly, the spectrum is represented by a sinc function sampled with the sampling rate $1/2NT_s$. Since the sampling rate corresponds to the null spacing of the sinc function, the spectrum has a single peak at the sub-
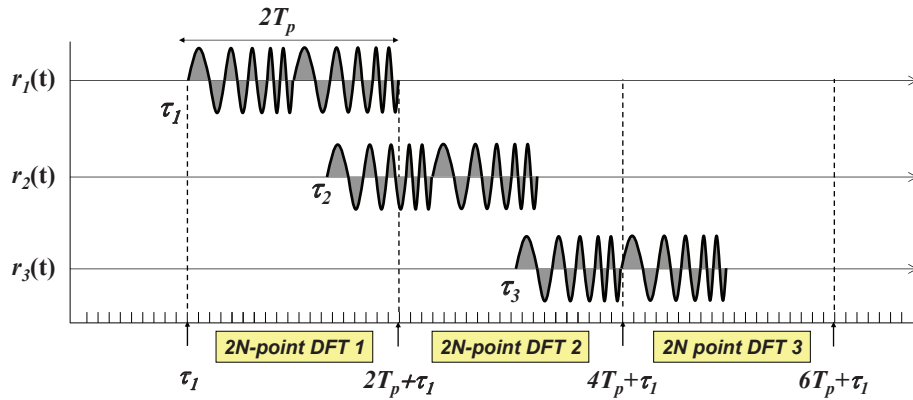
Figure 4.8.: A simple DFT division example for a long OFDM SAR echo signal.

carrier frequency f_x, and the other spectral components remain as zeros, like shown in Figure 4.7 (a).

In any other case, where the pulse does not exactly fit the time window, the pulse is truncated by the window. If the sinusoidal pulse is shifted by L samples from the original position, the time window captures only $2N - L$ samples of the pulse and the first L samples are filled by zeros, as shown in Figure 4.7 (b). The sinc function in its spectrum is broadened due to a truncated pulse with the length $(2N - L)T_s$, while the sampling rate remains constant $(1/2NT_s)$. Therefore the sampling rate is not equal to the null spacing and energy of the subcarrier frequency f_x is distributed over other frequencies, which means the interference. It occurs via a simple division of a SAR return signal longer than the window length. Figure 4.8 depicts this time division.

For instance, let us assume three separated point targets with the delay times τ_1, τ_2, and τ_3. Each echo signal is denoted by $r_k(t)$ ($k = 1, 2, 3$), and then the received signal is a superposition of these ($r(t) = r_1(t) + r_2(t) + r_3(t)$). When this signal is divided into three blocks by successive DFT windows, with the length $2T_p$, as shown in Figure 4.8, every DFT window truncates at least one signal, and thereby the orthogonality of those waveforms is broken. To avoid the truncation, the present work decomposes the echo signal into several angular sectors by means of DBF. The following section describes the angular segmentation approach, as the first step of demodulation, in detail.

4.2.2. Segmentation: Spatial Filtering

A respective choice of weighting factors allows the steering of a sharp and high-gain beam to the corresponding angular region. This angular sectoring is called *spatial filtering*, which is an important functionality of digital beamforming. This process divides a whole swath into multiple subswaths, so that the echo length of each subswath is significantly reduced. It should be emphasized that the spatial filter is time-invariant, providing a constant gain over the delay time domain, and its pattern only varies with the elevation angle.

A signal model for the spatial filtering is developed on the flat Earth model. Figure 4.9 shows the geometry used in the signal model. The ground range from the nadir ($x = 0$) to the swath center is denoted by x_c, and the whole swath width is $2x_o$. The main lobe width of the spatial
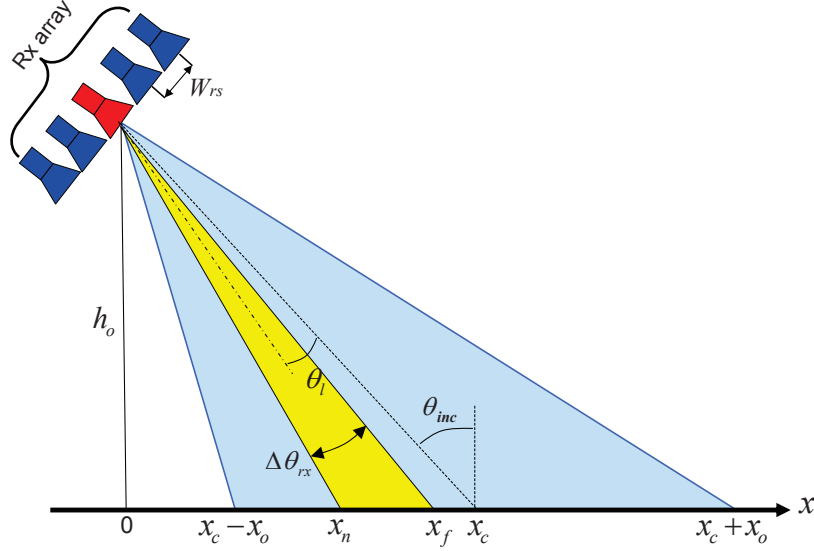
Figure 4.9.: Spatial filter pattern parameters and geometric parameters. The wide pattern indicates the transmit antenna beam illuminating the wide swath, and the narrow pattern depicts the main lobe of a spatial filter beam.

filter is denoted by $\Delta\theta_{rx}$, and the boresight angle of lth beam is indicated by the offset θ_l from the incident angle θ_{inc}. Firstly, only the main lobe signal is considered:

$$r_{l,main}(t) = \sum_{j=1}^{M_T} \int_{x_n}^{x_f} C_{tx}(\theta(x)) \cdot C_{rx}(\theta(x)) \cdot a_j(x) \cdot s_j\left(t - \frac{R_{tx,j} + R_{rx}}{c_o}\right) \mathrm{d}x \qquad (4.30)$$

where $C_{tx}(\theta(x))$ is the transmit antenna pattern in elevation on receive; $C_{rx}(\theta(x))$ is the spatial filter pattern; M_T is the number of transmit antennas; $a_j(x)$ denotes the complex scattering coefficient for the OFDM chirp waveform $s_j(t)$; x_n and x_f denote the nearest and the furthest ground range covered by the main lobe of a spatial filter. The subswath width is then given by $x_f - x_n$. It must be noted that R_{rx} is the range from the target to the phase center of the receive array. Under the assumption that the Tx antenna patterns are identical, the two-way antenna pattern $C_{2way}(\theta)$ is introduced in (4.30):

$$r_{l,main}(t) = \sum_{j=1}^{M_T} \int_{x_n}^{x_f} C_{2way}(\theta(x)) \cdot a_j(x) \cdot s_j\left(t - \frac{R_{tx,j} + R_{rx}}{c_o}\right) \mathrm{d}x. \qquad (4.31)$$

In practice, the side lobes of the beam capture echo signals, which are given by

$$r_{l,side}(t) = \sum_{j=1}^{M_T} \int_{x_c-x_o}^{x_n} C_{2way}(\theta(x)) \cdot a_j(x) \cdot s_j\left(t - \frac{R_{tx,j} + R_{rx}}{c_o}\right) \mathrm{d}x + \qquad (4.32)$$

$$\sum_{j=1}^{M_T} \int_{x_f}^{x_c+x_o} C_{2way}(\theta(x)) \cdot a_j(x) \cdot s_j\left(t - \frac{R_{tx,j} + R_{rx}}{c_o}\right) \mathrm{d}x.$$

A total received signal is expressed by the sum of the main lobe and the side lobe signals, which correspond to the signals from within the subswath and signals coming from outside the subswath respectively:

$$r_l(t) = r_{l,main}(t) + r_{l,side}(t). \tag{4.33}$$

It is required that the spatial filtering sufficiently suppresses the side lobe signal. Put simply, the spatial filtered signal is desired to be

$$r_l(t) \approx r_{l,main}(t). \tag{4.34}$$

The performance of the spatial filtering plays a critical role in the demodulation. A further consideration is made to the main lobe width, since it determines the received signal length. The main lobe width $\Delta\theta_{rx}$ is defined as

$$\Delta\theta_{rx} = \theta(x_f) - \theta(x_n), \tag{4.35}$$

and the subswath width S_{sub} is given by [30]

$$S_{sub} = x_f - x_n \tag{4.36}$$

$$= \Delta\theta_{rx} \cdot \frac{h_o}{\cos^2(\theta_{inc} - \theta_l)}.$$

The spatial filtering leads to a selection of the subswath, which corresponds to a specific range of delay times. The delay spread $\Delta\tau$ is proportional to the subswath width and the main lobe width. Using (4.35) and (4.36), the relation between the delay length and the main lobe width is formulated as follows:

$$\Delta\tau = 2 \cdot S_{sub} \cdot \frac{\sin(\theta_{inc} - \theta_l)}{c_o} \tag{4.37}$$

$$= 2 \cdot \Delta\theta_{rx} \cdot \frac{h_o \cdot \tan(\theta_{inc} - \theta_l)}{c_o \cdot \cos(\theta_{inc} - \theta_l)}.$$

In spite of the spatial filtering, the signal length within the main lobe is still longer than $2T_p$. The following section presents a processing step, which converts the spatially filtered signal to fit the length of $2T_p$.

4.2.3. Circular-Shift Addition

The approach presented in this section is to exploit the periodicity of the discrete Fourier transform, which implies that a finite segment of DFT is a single period of an infinitely extended periodic signal [97]. Figure 4.10 compares an aperiodic and a periodic signal shift. Let $s(t)$ be the aperiodic in Figure 4.10 (a). In the infinite time domain, the aperiodic signal $s(t)$ is shifted by τ, and the shifted signal is just partially included in the fixed time window. On the other hand, the shift in a periodic signal is circular, so that the shifted part reappears in the window, as in Figure 4.10 (b).
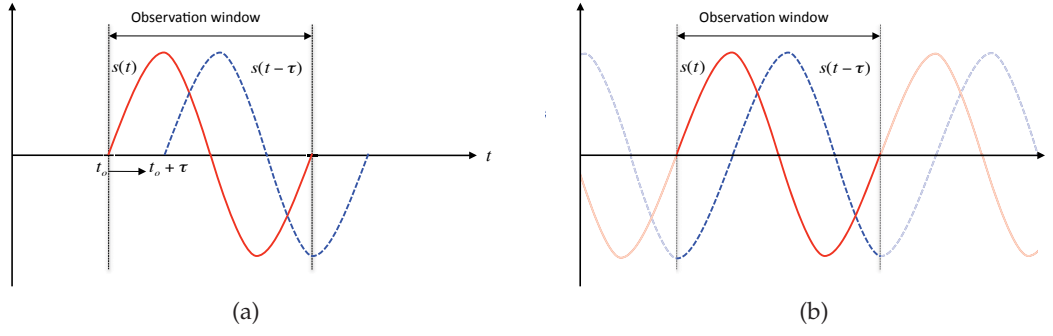
Figure 4.10.: Illustration of the shift of an aperiodic signal (a) and a periodic signal (b).

In the case of periodic signals, the time shift is represented by the phase rotation. If the time shift reaches the signal period length, the phase rotation via the shift becomes 2π, and the original and shifted signals are no longer distinguishable. Therefore, on the premise that the maximum delay spread does not exceed the signal period, any delay of the periodic signal can be represented within the single period. Based on this principle, the spatially filtered signal is circularly shifted to fit the length $2N$, and the delay information is conserved. Since the OFDM pulse is a combination of two successive chirps, and the original chirp duration is T_p, the echo delay of T_p results in 2π phase rotation. In other words, two signals separated by T_p delay overlap after the circular-shift addition. Therefore the spatially filtered signal must satisfy a strict condition that

Lemma 1. *The maximum delay spread $\Delta\tau$ of the main lobe signal must be shorter than T_p ($\Delta\tau < T_p$).*

Assuming a total of K point scatterers within a subswath ($K < N$), each target delay time is then given by $t = T_n + (n - k){\cdot}T_s$ where T_n is the round-trip delay from the sensor to a target at x_n. Using these discrete time indices n and k, (4.34) is rewritten in a discrete signal form of

$$r_l[n] = \left(\sum_{j=1}^{M_T} \sum_{k=0}^{K-1} C_{2way}[k]{\cdot}a_j[k]{\cdot}s_j[n - k] \right) \cdot \mathrm{rect}\left[\frac{n}{2N + K} \right] \tag{4.38}$$

where $n = 0, 1, 2, \cdots, 2N + K - 1$. Note that the echo signal length within the subswath is equal to $(2N + K){\cdot}T_s$ which is the sum of the OFDM pulse length ($2T_p = 2NT_s$) and the delay spread (KT_s). If the first $2N$ samples are directly taken by a DFT window, the $2N$ data samples contain only one complete waveform, and the rest are truncated by the DFT window. In this case, even though the IDFT/DFT is synchronized, its result will be spoiled. To resolve this problem, the aforementioned periodic property is exploited.

Using two successive time windows each with lengths of $2N$ and K respectively, the signal is divided into two parts as follows:

$$r_l[n] = \left(\sum_{j=1}^{M_T} \sum_{k=0}^{K-1} C_{2way}[k]{\cdot}a_j[k]{\cdot}s_j[n - k] \right) \cdot \mathrm{rect}\left[\frac{n}{2N} \right] +$$

$$\left(\sum_{j=1}^{M_T} \sum_{k=0}^{K-1} C_{2way}[k]{\cdot}a_j[k]{\cdot}s_j[n - k] \right) \cdot \mathrm{rect}\left[\frac{n - 2N}{K} \right]. \tag{4.39}$$
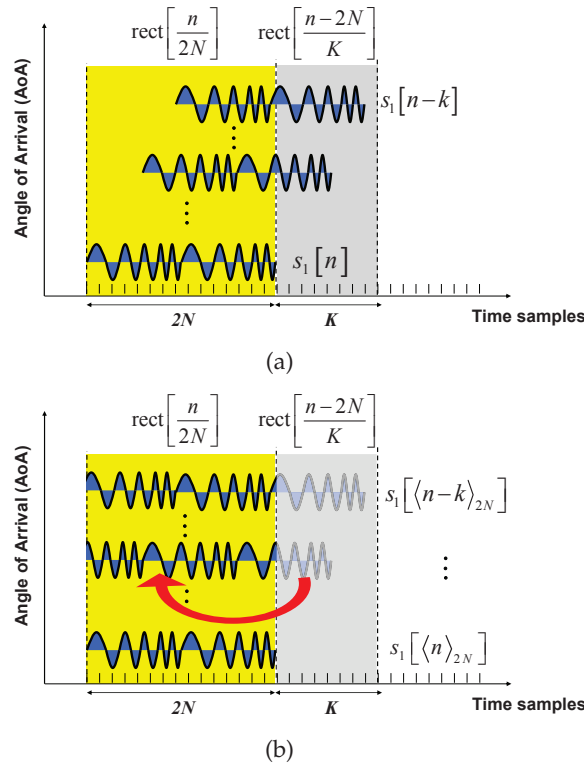
Figure 4.11.: Received signals from the subswath with the length (a) before and (b) after the circular-shift addition.

In (4.39), the second term on the right-hand side is circularly shifted and added to the first term in order to make the main lobe signal periodic at each $2N$ sample. The signals before and after the circular-shift addition are illustrated in Figure 4.11 (a) and (b) respectively. The circular-shift addition process can be described by the modulo operation:

$$r_l[n] = \sum_{j=1}^{M_T} \sum_{k=1}^{K} C_{2way}[k] \cdot a_j[k] \cdot s_j[\langle n - k \rangle_{2N}] \tag{4.40}$$

where $n = 0, 1, 2, \cdots, 2N - 1$, and $\langle \cdot \rangle_{2N}$ denotes the arithmetic modulo $2N$[4]. Therefore the circular-shift addition reduces the signal length from $2N + K$ to $2N$ (see Figure 4.11 (b)). Following this, the first $2N$ samples contain all delayed waveforms, so that no truncation of the signal occurs. In the following section, the classical OFDM demodulation based on DFT is derived.

4.2.4. Demodulation with 2N-DFT

The traditional demodulation by DFT with the length $2N$ is now applicable to the OFDM signals. The Fourier transform of (4.40) is

$$\mathcal{F}\{r_l[n]\} = \sum_{n=0}^{2N-1} \left(\sum_{j=1}^{M_T} \sum_{k=0}^{K-1} C_{2way}[k] \cdot a_j[k] \cdot s_j[\langle n - k \rangle_{2N}] \right) \cdot \exp\left(-j\frac{2\pi}{2N} np \right). \tag{4.41}$$

Since the transmitted signal $s_j[n]$ is the inverse Fourier transform of its spectrum $S_j[p]$, (4.41) becomes

$$
\mathcal{F}\{r_l[n]\} = \sum_{n=0}^{2N-1} \sum_{j=1}^{M_T} \sum_{k=0}^{K-1} C_{2way}[k] \cdot a_j[k] \cdot
$$

$$
\frac{1}{2N} \sum_{p=0}^{2N-1} S_j[p] \cdot \exp\left(j\frac{2\pi}{2N}(n-k)p \right) \cdot \exp\left(-j\frac{2\pi}{2N}np \right). \tag{4.42}
$$

Rearranging (4.42) with respect to indices, the following formula is obtained:

$$
\mathcal{F}\{r_l[n]\} = \sum_{j=1}^{M_T} \sum_{k=0}^{K-1} C_{2way}[k] \cdot a_j[k] \cdot \exp\left(-j\frac{2\pi}{2N}kp \right) \cdot
$$

$$
\sum_{n=0}^{2N-1} \left(\frac{1}{2N} \sum_{p=0}^{2N-1} S_j[p] \cdot \exp\left(j\frac{2\pi}{2N}np \right) \right) \cdot \exp\left(-j\frac{2\pi}{2N}np \right)
$$

$$
= \sum_{j=1}^{M_T} \sum_{k=0}^{K-1} C_{2way}[k] \cdot a_j[k] \cdot \exp\left(-j\frac{2\pi}{2N}kp \right) \cdot S_j[p] \tag{4.43}
$$

where $S_j[p]$ for $j = 1, 2$ is derived in (4.7) and (4.8). Finally, the demodulated signal is given by

$$
\mathcal{F}\{r_l[n]\} = \sum_{k=0}^{K-1} C_{2way}[k] \cdot a_1[k] \cdot \exp\left(-j\frac{2\pi}{2N}k\frac{p}{2} \right) \cdot \exp\left(-j\pi\frac{(p \cdot \Delta f)^2}{K_r} \right) +
$$

$$
\sum_{k=0}^{K-1} C_{2way}[k] \cdot a_2[k] \cdot \exp\left(-j\frac{2\pi}{2N}k\frac{p-1}{2} \right) \cdot \exp\left(-j\pi\frac{((p-1) \cdot \Delta f)^2}{K_r} \right)
$$

$$
= H_1 S_1[p] + H_2 S_2[p] \tag{4.44}
$$

where H_1 and H_2 denote the channel transfer functions delivered by the OFDM waveform S_1 and S_2, respectively. The demodulated signal is indeed separable with respect to each waveform by the polyphase decomposition, which divides the demodulated signal spectrum into odd and even components. Hence each spectrum length is reduced by N. This reduction never leads to any loss of information since the waveforms s_1 and s_2 are actually carried by N subcarriers, and the other N subcarrier frequencies are redundant zeros, so as to apply $2N$-point DFT in demodulation. The channel transfer functions H_1 and H_2 can be recovered by the conventional matched filtering for each waveform:

$$
H_1 = \sum_{k=0}^{K-1} C_{2way}[k] \cdot a_1[k] \cdot \exp\left(-j\frac{2\pi}{N}k\frac{p}{2} \right) \cdot \underbrace{\exp\left(-j\pi\frac{(p \cdot \Delta f)^2}{K_r} \right)}_{S_1[p]} \cdot \underbrace{\exp\left(j\pi\frac{(p \cdot \Delta f)^2}{K_r} \right)}_{S_1^*[p]}
$$

$$
= \sum_{k=0}^{K-1} C_{2way}[k] \cdot a_1[k] \cdot \exp\left(-j\frac{2\pi}{N}k\frac{p}{2} \right). \tag{4.45}
$$

In the same manner, the channel transfer function, H_2, is recovered:

$$H_2 = \sum_{k=0}^{K-1} C_{2way}[k] \cdot a_2[k] \cdot \exp\left(-j\frac{2\pi}{N}k\frac{p+1}{2}\right) \cdot$$

$$\underbrace{\exp\left(-j\pi\frac{((p-1)\cdot\Delta f)^2}{K_r}\right)}_{S_2[p]} \cdot \underbrace{\exp\left(j\pi\frac{((p-1)\cdot\Delta f)^2}{K_r}\right)}_{S_2^*[p]} \tag{4.46}$$

$$= \sum_{k=0}^{K-1} C_{2way}[k] \cdot a_2[k] \cdot \exp\left(-j\frac{2\pi}{N}k\frac{p}{2}\right) \cdot \exp\left(-j\frac{\pi}{N}k\right)$$

whereby the second exponential term accounts for the linear phase ramp depending on the target delay, which is caused by the subcarrier spacing Δf. Therefore there is a linear phase difference between two images reconstructed by each OFDM chirp waveform, which should be compensated, prior to coherent post-processing.

In summary, the developed OFDM chirp waveform demodulation scheme is diagrammed in Figure 4.12. First of all, the spatial filters divide the echo signal to satisfy Lemma 1. Secondly, the circular-shift addition is carried out, so that $2N$ samples from each spatial filter are obtained. As a conventional OFDM demodulation, $2N$-point DFT block demodulates the OFDM signals. Consequently, the polyphase decomposition block easily separates the waveforms. The decomposed signals are independently compressed by parallel matched filters. Reference functions for the matched filters can be directly obtained from the input data sequence, or can also be generated, using the signal model.
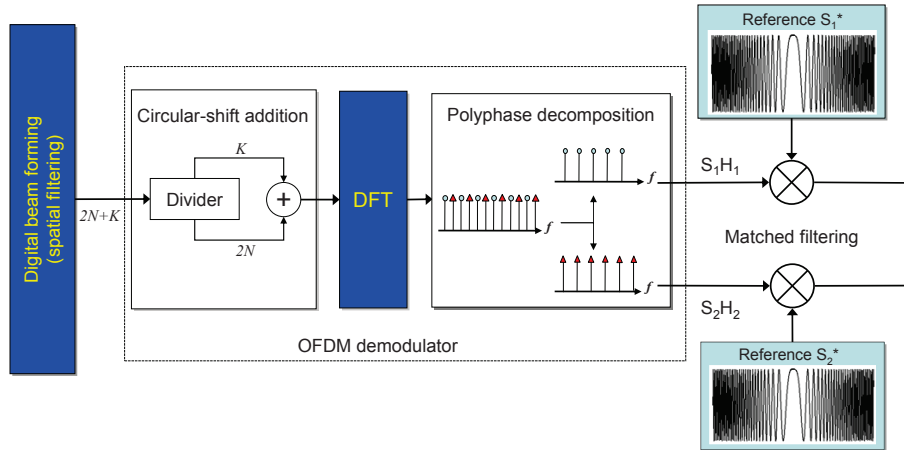
Figure 4.12.: A generic schematic of the OFDM demodulator combined with the spatial filtering and parallel matched filters for the range compression.

4.2.5. Verification

The OFDM chirp waveform scheme is verified by simulations in this section. The simulation is carried out under the following two assumptions: the optimum spatial filter and the simple

delay channel. The optimum spatial filter means a rectangular filter pattern covering the angular range of interest, i.e. a perfect side lobe suppression. The channel is assumed only to cause delay and to include the thermal noise.
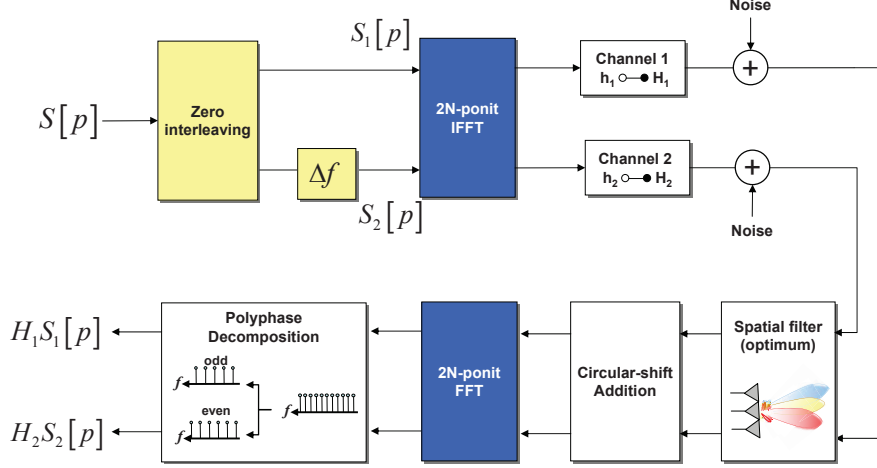
Figure 4.13.: Simulation schematic for the verification: two independent channels and demodulation blocks.

The simulation schematic is depicted in Figure 4.13. The first step of simulation is to generate two OFDM chirp waveforms. The spectrum of up-chirp signal, $S[p]$, is chosen as the input sequence. As described in (4.7) and (4.8), the zero-interleaving block inserts N zeros to each spectrum in order to make them $2N$ long and afterwards one of these spectra is shifted by Δf. The resulting two orthogonal spectra, $S_1[p]$ and $S_2[p]$, are modulated by the IDFT block[4]. Thereby two OFDM waveforms in the time domain are obtained. The modulated OFDM chirp parameters are summarized in Table 4.1.

The signal power is set to be 0dBm, and the thermal noise with its power, N_o of -94dBm ($k_{bol} \cdot f_o \cdot T = 1.38 \times 10^{-23}$[J/Kelvin] $\cdot 1 \times 10^8$[Hz] $\cdot 300$[Kelvin]), is added to the generated waveform signals, which are transferred into channels h_1 and h_2 respectively. The optimum spatial filter ensures that the maximum delay does not exceed T_p. The circular-shift addition block converts the signals to fit $2N$-point DFT, which demodulates the converted signals.

Table 4.1.: Parameters used in simulation.

Parameter	Value	Parameter	Value
$2N$	2048	f_o	100MHz
$2T_p$	17.067μsec	N_o	-94dBm
S_o	0dBm		

Figure 4.14 (a) shows the spectra of demodulated signals within 1MHz range from 3MHz to 4MHz for clarity. The circular symbols denote the spectral components of H_1S_1, and the triangular symbols indicate them for H_2S_2. It is clearly observed that these two spectral components are out of joint, which translates to an orthogonal meaning. To measure the orthogo-

---

[4]In practice, DFT/IDFT are carried out by FFT/IFFT.

nality between the demodulated output signal before the polyphase decomposition, the cross-correlation function is calculated and plotted in Figure 4.14 (b). Let $Y_1 = H_1 S_1$ and $Y_2 = H_2 S_2$, so that their correlation is obtained by calculating

$$\sigma_{xy} = \mathcal{F}^{-1}\left\{ \sum_{p=0}^{2N-1} Y_1[p] \cdot Y_2^*[p] \right\}. \tag{4.47}$$

(a)   (b)
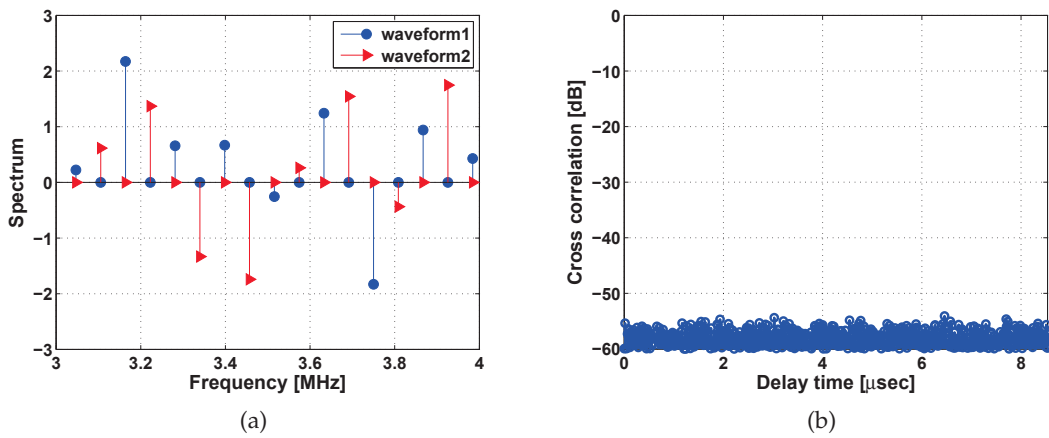
Figure 4.14.: Demodulated discrete spectra of both waveforms within 3MHz and 4MHz (a), and cross-correlation function between the output signals (b).

In the ideal case, the cross-correlation between two OFDM signals will be zero. However, in this simulation, the added thermal noise yields the cross-correlated level under -55dB.
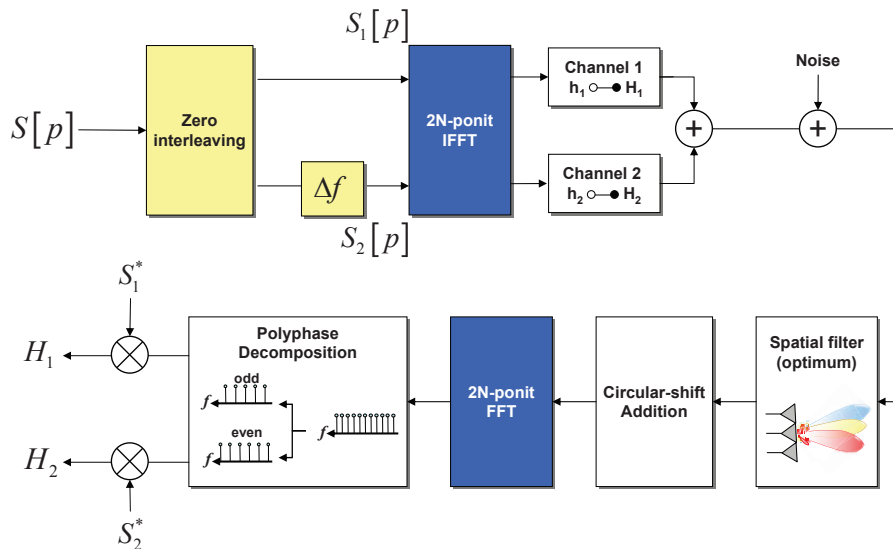
Figure 4.15.: Simulation schematic for verification: two independent channels and a single de-modulator.

Next, the two OFDM signals are combined to demonstrate that the waveforms are separable as shown in Figure 4.15. Both of them are processed by a single demodulator. In this simulation, each channel transfer function is reconstructed by the range matched filtering and compared to its original channel impulse response. Figure 4.16 shows the original channel impulse response functions h_1 and h_2, which are used in this simulation. These channels contain several impulses, indicating the delay and scattering coefficient of each target. Note that the maximum delay of each channel never exceeds T_p of 8.53μsec (see Table 4.1).
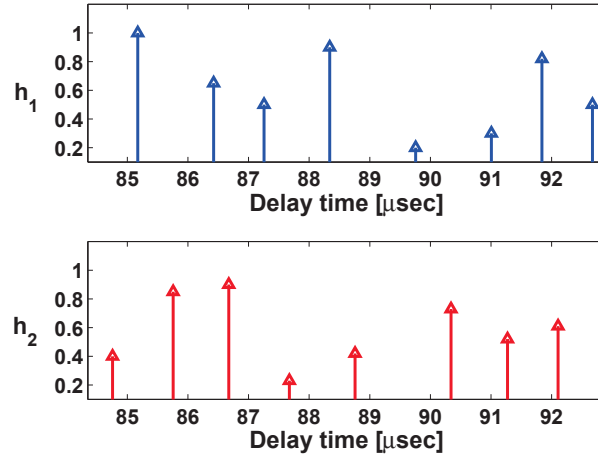
Figure 4.16.: Impulse response functions of channel h_1 and h_2
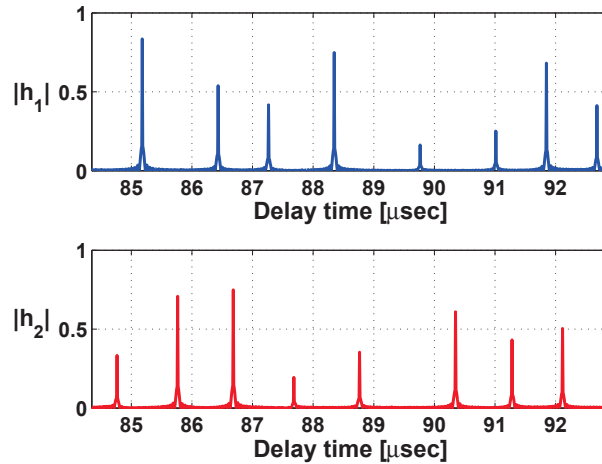
Figure 4.17.: Reconstructed channel impulse responses from each OFDM signal.

The reconstructed channel impulse responses are plotted in Figure 4.17. Apart from a slight change of the peak magnitude due to the Fourier transform of the band-limited signal, both range profiles recovered by the single demodulator and independent matched filters correspond to the original channel impulse response functions.

To summarize, the introduced demodulation scheme was verified by simulations. The OFDM waveforms preserve the orthogonality, so long as they are processed by the presented demod-

ulation scheme. This has been directly shown in their spectra and by measuring the cross-correlation. The restriction arising from the fixed DFT length in the demodulation can be mitigated by the multiple spatial filters in elevation, possibly increasing the pulse length with a consideration of the duty cycle and PRF also.

4.3. Performance Investigation for Doppler Effect

The orthogonality between the subcarriers with a small spacing is fragile in complex propagation channels. A typical example is the Doppler effect. In side-looking SAR, the Doppler effect resulting from the relative motion between the sensor and targets is exploited in order to obtain a high spatial resolution in azimuth. In contrast, the Doppler shift in fast-time domain is ignored in SAR processing since it is not recognizable within a SAR pulse length. To detect the Doppler shift, the pulse length should be at least one period of the Doppler frequency. This condition is generally not met in a pulse-based radar operation [110]. However, it is worth investigating the Doppler effect in fast-time signals when the OFDM chirp length is increased, in order to extend a subswath width. In this case, the Doppler effect becomes more significant. This section investigates the performances of the proposed waveform scheme regarding the Doppler shift and derives a compensation algorithm to improve Doppler tolerance in the OFDM waveform.

4.3.1. Inter-Carrier Interference (ICI)

In OFDM communication systems, the Doppler shift is a major cause of disturbance to the orthogonality between subcarriers. Figure 4.18 shows the Doppler shift effect on a single subcarrier. The horizontal axis denotes the subcarrier frequency normalized by Δf. The dotted line indicates an ideal orthogonal subcarrier (sinc function) at the normalized frequency of unity. This subcarrier function is sampled with the sampling rate equal to Δf, due to the periodicity of DFT, and this suppresses the other frequency components with its nulls. The Doppler shift moves the subcarrier function, so that the original subcarrier function produces other non-zero samples corresponding to interferences. In addition, the amplitude at the original subcarrier frequency is reduced.
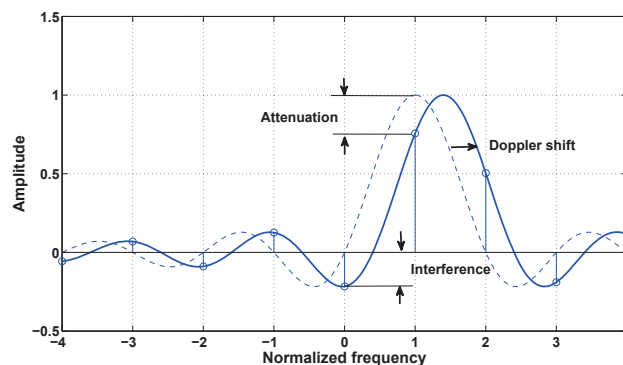
Figure 4.18.: Doppler shift effect disturbing the orthogonality with an attenuation of the subcarrier amplitude.

In many cases, this Doppler influence is mitigated by increasing the subcarrier spacing Δf. However, for a fixed symbol duration, a reduction in the subcarrier spacing leads to a reduction in the number of subcarriers, which decreases the data rate. In the present MIMO SAR with the OFDM chirp waveform, the reciprocal of the subcarrier spacing Δf corresponds to the pulse length, which determines the subswath width. Therefore the subcarrier spacing should be properly chosen.

The parameter *Inter-Carrier Interference* (ICI) is used to specify a boundary of the minimum subcarrier spacing for given channels. The ICI is a ratio between single subcarrier power and interference power contributed by all other subcarriers due to the Doppler shift. Thus the ICI indicates the degree of orthogonality loss. To sum up, the Doppler shift results in the ICI and the amplitude attenuation of the subcarrier, as shown in Figure 4.18. Since the Doppler shift is not described by a single value due to multipath signals, the Doppler spectrum model is commonly used in the ICI estimation. In this section, the ICI is formulated for the MIMO SAR system by using the analytical model in [136].

If $s[n]$ is a conventional OFDM signal, the received signal, $r[n]$ is described as follows:

$$r[n] = \frac{1}{2N} \sum_{p=0}^{2N-1} S[p] \cdot \exp\left(j\frac{2\pi}{2N}(n-k)(p+\Delta p)\right) \text{rect} \cdot \left[\frac{n-k}{2N}\right] \tag{4.48}$$

where Δp represents the Doppler shift of the pth subcarrier. Note that the signal amplitude and antenna pattern[5] are omitted in this derivation for simplicity. The signal is demodulated by the $2N$-point DFT on receive. As in the prior section, the demodulated signal is derived as

$$\mathcal{F}\{r[n]\} = \sum_{n=0}^{2N-1} \left(\frac{1}{2N} \sum_{p=0}^{2N-1} S[p] \cdot \exp\left(j\frac{2\pi}{2N}(n-k)(p+\Delta p)\right) \cdot \text{rect}\left[\frac{n-k}{2N}\right]\right) \cdot \exp\left(-j\frac{2\pi}{2N}np\right) \tag{4.49}$$

$$= S[p] \cdot \exp\left(-j\frac{2\pi}{2N}k(p+\Delta p)\right) \cdot \text{sinc}\,(p+\Delta p).$$

In the following, this signal spectrum with the Doppler shift is reformulated in terms of a specific subcarrier and the rest. Figure 4.19 depicts the principle of the following signal model. The received signal spectrum is decomposed into the discrete frequency domain p, and the subcarrier domain q. Thereby one can describe the interferences from the side lobes of subcarrier functions ($q \neq q_o$) to the reference subcarrier q_o. Of course if there is no Doppler shift, the side lobes of all subcarrier functions correspond to the nulls. Put simply, they are orthogonal.

To derive the ICI on the q_o subcarrier, (4.49) is described again as:

$$\mathcal{F}\{r[n]\} = R[p] = S[p] \cdot \text{sinc}\,(p - q_o + \Delta q_o) \cdot \exp\left(-j\frac{2\pi}{2N}k(p - q_o + \Delta q_o)\right) +$$

$$\sum_{\substack{q=0 \\ q \neq q_o}}^{2N-1} S[p] \cdot \text{sinc}\,(p - q + \Delta q) \cdot \exp\left(-j\frac{2\pi}{2N}k(p - q + \Delta q)\right) \tag{4.50}$$

[5]The antenna pattern is reflected to a Doppler spectrum model for a side-looking SAR geometry.
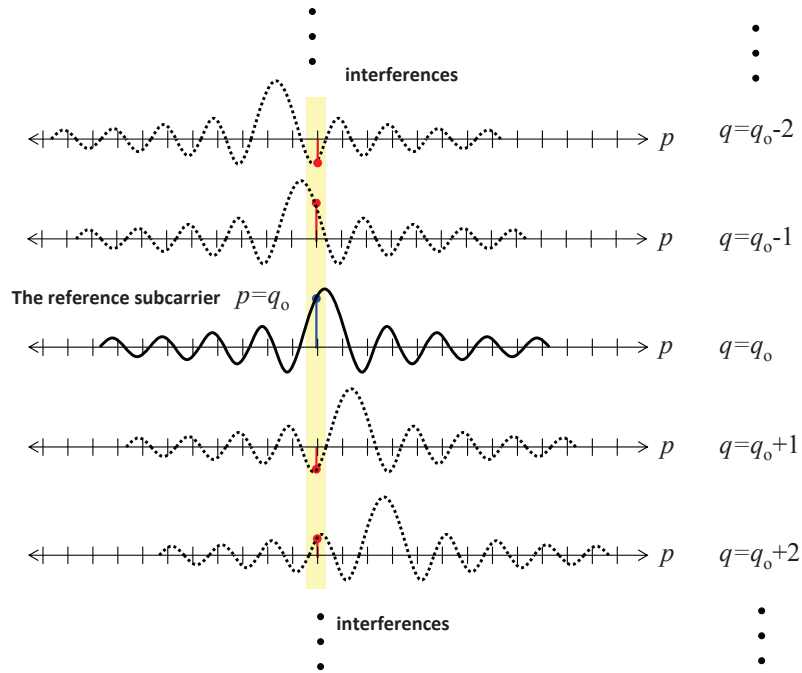
Figure 4.19.: ICI contributions of other subcarriers ($q \neq q_o$) to the reference subcarrier q_o.

where Δq_o and Δq denote the Doppler shift of the reference q_oth subcarrier and the other subcarriers, respectively. (4.50) consists of two terms: the first term describes the q_o subcarrier with the Doppler shift, and the second term presents the ICI contribution of the others to the q_o subcarrier. For convenience, (4.50) is rewritten in a continuous signal form, according to the relationship $2\pi/NT_s = 2\pi\Delta f$ and $T_p = 2NT_s$, as follows:

$$R(f_p) = S(f_p) \cdot \text{sinc}\left(2(f_p - f_{q_o} + f_d^{q_o})T_p\right) \cdot \exp\left(-j2\pi(f_p - f_{q_o} + f_d^{q_o})kT_s\right) +$$

$$\sum_{\substack{q=0 \\ q \neq q_o}}^{2N-1} S(f_p) \cdot \text{sinc}\left(2(f_p - f_q + f_d^q)T_p\right) \cdot \exp\left(-j2\pi(f_p - f_q + f_d^q)kT_s\right) \qquad (4.51)$$

where $f_q = 2\pi \cdot q \cdot \Delta f$ and $f_d^q = 2\pi \cdot \Delta q \cdot \Delta f$. In the same way, $f_p = 2\pi \cdot p \cdot \Delta f$. The interest is the power level of interference. The exponential terms in (4.51) have no effect on the ICI due to the amplitude of unity, and $|S(f_p)|$ is also assumed to be unity. Therefore these can be omitted in further power calculations. The spectral power at f_{q_o} (i.e. $p = q_o$) is a sum of the reference subcarrier power and the ICI power:

$$|R(f_{q_o})|^2 = \underbrace{\text{sinc}^2\left(2 \cdot f_d^{q_o} \cdot T_P\right)}_{\text{reference}} + \underbrace{\sum_{\substack{q=0 \\ q \neq q_o}}^{2N-1} \text{sinc}^2\left(2(f_{q_o} - f_q + f_d^q) \cdot T_P\right)}_{\text{ICI}}$$

$$= |R_{sig}(f_{q_o})|^2 + |R_{ici}(f_{q_o})|^2 \qquad (4.52)$$

where $|R_{sig}|^2$ is the reference subcarrier signal power, and $|R_{ici}|^2$ denotes the total interference

power from the other subcarriers ($q \neq q_o$) to the q_oth subcarrier. For a large number of subcarriers ($N \to \infty$), the ICI power on the subcarrier is estimated as [105]:

$$\lim_{N \to \infty} \sum_{\substack{q=0 \\ q \neq q_o}}^{2N-1} \mathrm{sinc}^2\left(2(f_{q_o} - f_q + f_d^q) \cdot T_p\right) \approx \left(1 - \mathrm{sinc}^2\left(2 \cdot f_d^q \cdot T_p\right)\right). \tag{4.53}$$

The above derivation is expanded to a practical SAR scenario. In reality, multipath signals from a wide target area in SAR yield a Doppler spectrum broadening, known as Doppler spread [138, 102]. Therefore the total ICI power should be calculated by applying a statistical distribution for the Doppler frequency. If the total ICI power is denoted by P_{ICI}, it is defined as an expected value of the Doppler distribution [136]:

$$P_{ICI} \overset{!}{=} \int_{-\infty}^{\infty} \left(1 - \mathrm{sinc}^2\left(2 \cdot f_d \cdot T_p\right)\right) \cdot p_d(f_d) \mathrm{d}f_d \tag{4.54}$$

where $p_d(f_d)$ is the Doppler *Probability Density Function* (PDF), and f_d^q is replaced by f_d since f_d^q denotes the Doppler shift for the arbitrary qth subcarrier. In SAR, the Doppler spectral power is limited by the antenna azimuth pattern. Thus a certain Doppler bandwidth can be considered in order to calculate P_{ICI}. Using the fact that the integral of a PDF is defined to be unity, (4.54) is simplified as follows:

$$P_{ICI} \approx 1 - \int_{-f_{d,max}}^{f_{d,max}} p_d(f_d) \cdot \mathrm{sinc}^2\left(2 \cdot f_d \cdot T_p\right) \mathrm{d}f_d \tag{4.55}$$

where $f_{d,max}$ is the maximum Doppler shift. In the case of a known Doppler PDF, the total ICI power can be directly estimated by (4.55). A study has shown that the Doppler PDF in a 3-dimensional scattering environment has a uniform distribution rather than the classic Jake's model [105]. Furthermore, a narrow SAR antenna pattern must be taken into account. Therefore the Doppler PDF in side-looking SAR is equivalent to the azimuth pattern of a SAR antenna.

Figure 4.20 shows the calculated ICI versus the maximum Doppler shift, normalized by the subcarrier spacing Δf. The circular symbols in Figure 4.20 indicate the ICI power for the azimuth antenna pattern distribution, and the triangular symbols show this for the uniform distribution. The lower gain of the antenna for large azimuth angles diminishes the high Doppler frequency contribution, unlike that in the uniform model. Therefore the estimated ICI value is lower than that of the uniform distribution. This plot could be used to specify a lower bound of acceptable subcarrier spacing, in regard to the number of subcarriers. For example, if the threshold of the ICI level is set to -30dB, then the maximum allowable Doppler frequency must be lower than approximately 6% of a given subcarrier spacing from Figure 4.20. Fortunately, the restriction can be relaxed by compensating the Doppler shift in the 2-D frequency domain of SAR signal. This will be specifically presented in section 4.3.3.

4.3.2. Compression Loss

In this section, the compression loss caused by the Doppler shift is explored. As shown in Figure 4.18, the Doppler shift affects the subcarrier amplitude as well as the ICI. The compression
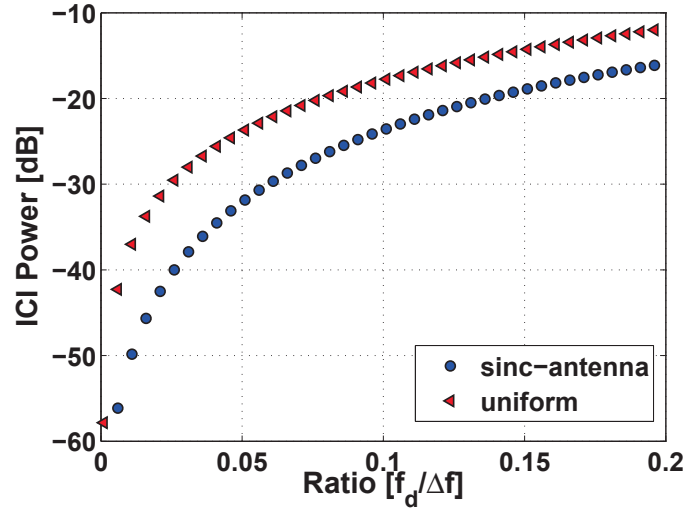
Figure 4.20.: Estimated ICI power for the uniform Doppler PDF and the antenna pattern PDF (sinc function).

loss is a measure of this attenuation, which occurs in the Doppler effect. From (4.51), only the q_oth subcarrier component is considered:

$$R_{sig}(f_{q_o}) = S(f_{q_o}) \cdot \text{sinc}\left(2 \cdot f_d^{q_o} \cdot T_p\right) \cdot \exp\left(-j2\pi \cdot f_d^{q_o} \cdot k \cdot T_s\right) \tag{4.56}$$

where the exponential term accounts for the phase response due to a delay in the q_oth subcarrier and an additional phase change caused by the Doppler frequency, called the Doppler phase rotation. The compression loss L_c is defined as the reciprocal of the power of the shifted subcarrier [44]:

$$L_c = \frac{1}{|R_{sig}(f_{p_o})|^2} = \frac{1}{\text{sinc}^2\left(2 \cdot f_d^{q_o} \cdot T_p\right)}. \tag{4.57}$$

In [44], the maximum Doppler is specified by 1dB point of the compression loss, which is remarked in Figure 4.21.

To conclude, the OFDM signals allow greater tolerance for the attenuation due to the Doppler shift, by comparison with the ICI. Therefore OFDM signal parameters in regards to the ICI will meet a desired compression loss level.

4.3.3. Doppler Tolerance Improvement

In a complex mobile communication channel, it is very difficult to remove the Doppler effect. By comparison, in the spaceborne SAR, the continuous platform movement is the predominant cause of Doppler shift, even in fast-time signals. Moreover, the spaceborne sensor movement is much more stable than the airborne sensor flight. Hence the Doppler shift due to the sensor motion can be more precisely estimated.

By exploiting the well-known SAR geometry, this section derives a modified matched filter to compensate for the Doppler effect on fast-time signals, and thereby improves the Doppler tolerance of the OFDM waveform scheme. This idea is based on the matched filtering for *Frequency*
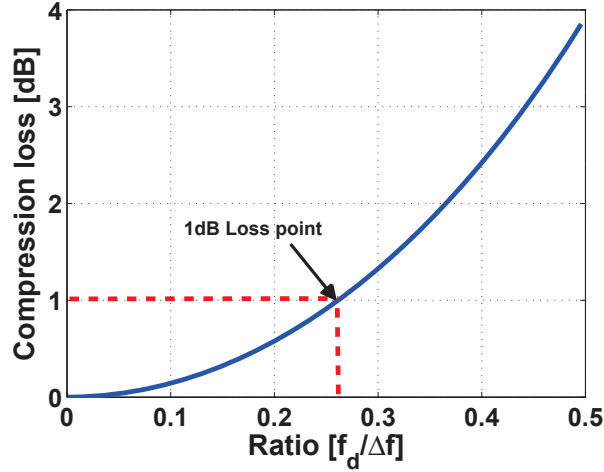
Figure 4.21.: The compression loss for the ratio of the maximum Doppler frequency and sub-carrier spacing. The 1dB point indicates the maximum Doppler shift to be approximately 26% of the subcarrier spacing.

Modulated Continuous Wave (FMCW) SAR signals [86]. The Doppler shift is introduced to the 2-D frequency domain signal model in Chapter 3, and a modified matched filter is derived from this signal model. From (3.10) and (3.14), the channel transfer function H_{ij} for a point target is given by

$$H_{ij}(f,u) = A_{ij}(f)\cdot\exp\left(-j\frac{4\pi}{\lambda}\sqrt{X_{s,ij}^2 + (y-u)^2}\right) \qquad (4.58)$$

where $X_{s,ij}$ is the minimum slant range from the sensor to a target at the boresight direction; u is the effective phase center position of $i-j$ bistatic antenna pair in azimuth; and y is the azimuth coordinate of the point target. The continuous platform movement is introduced in (4.58):

$$H_{ij}(f,u) = A_{ij}(f)\cdot\exp\left(-j\frac{4\pi}{\lambda}\sqrt{X_{s,ij}^2 + (y-(u+V_p\cdot t))^2}\right). \qquad (4.59)$$

The term added to the azimuth position implies that the platform position is consecutively changing within a pulse period. The channel transfer function is transformed into 2-D frequency domain. Substituting $\bar{u}$ for $u + V_p\cdot t$, the Fourier transform is performed in azimuth:

$$H_{ij}(f,k_u) = \int A_{ij}(f)\cdot\exp\left(-j\frac{4\pi}{\lambda}\sqrt{X_{s,ij}^2 + (y-\bar{u})^2}\right)\cdot\exp\left(-jk_u\cdot\bar{u}\right)\cdot\exp\left(jk_u\cdot V_p\cdot t\right)\,\mathrm{d}\bar{u} \quad (4.60)$$

where the third exponential term including $V_p\cdot t$ is independent of $\bar{u}$. Applying the principle of stationary phase, the integral can be solved as follows:

$$H_{ij}(f,k_u) = A_{ij}(f)\cdot\exp\left(-jX_{s,ij}\sqrt{4\left(\frac{2\pi}{\lambda}\right)^2 - k_u^2} - jk_u\cdot y\right)\cdot\exp(jk_u\cdot V_p\cdot t) \qquad (4.61)$$

where the last exponential term represents the frequency shift due to the sensor motion, which is linear and range-independent. This frequency shift term is denoted by $e(f, k_u)$ in further developments. As aforementioned, the Doppler shift within a single pulse is detectable if the pulse length is longer than one cycle of the Doppler shift. To show the relationship between the pulse length and the Doppler shift term, the fast-time is transformed into the range frequency f, based on the linear frequency modulation of chirp signals, as follows:

$$t = \frac{T_p}{f_o} \cdot f \tag{4.62}$$

where f_o is the signal bandwidth. The frequency shift term, $e(f, k_u)$ is modified with (4.62):

$$e(f, k_u) = \exp(jk_u \cdot V_p \cdot t)$$

$$= \exp\left(jk_u \cdot V_p \cdot \frac{T_p}{f_o} \cdot f\right). \tag{4.63}$$

For a specific PRF, (4.63) can be expressed for the duty cycle $T_p \cdot PRF$:

$$e(f, k_u) = \exp\left(j \frac{k_u}{PRF} \cdot V_p \cdot \frac{f}{f_o} \cdot \underbrace{(T_p \cdot PRF)}_{\text{duty cycle}}\right). \tag{4.64}$$

By substituting $\frac{2\pi f_d}{V_p}$ for k_u, the final form is derived as follows:

$$e(f, f_d) = \exp\left(j2\pi \cdot \frac{f_d}{PRF} \cdot \frac{f}{f_o} \cdot (T_p \cdot PRF)\right) \tag{4.65}$$

where $f_d \in [-PRF/2, PRF/2]$ and $f \in [0, f_o]$. It is relatively straightforward to eliminate this term from the 2-D spectrum by multiplying its complex conjugate. Hence a matched filter function to compensate for the Doppler shift is given by the complex conjugate.

$$M_e(f, f_d) = e^*(f, f_d). \tag{4.66}$$

Figure 4.22 plots $e(f, f_d)$ for several duty cycle values. In the case of the stripmap mode, its duty cycle is typically smaller than 20%. Thus the Doppler shift is negligible in signal processing in fast-time domain. On the other hand, it is obvious that the Doppler effect becomes significant for the subcarrier orthogonality, as the duty cycle increases, as shown in Figure 4.22 (a)-(e). In the case of the 100% duty cycle, which is a FMCW system, the phase varies $360°$ over the frequency as shown in Figure 4.22 (f).

The Doppler shift threatening the orthogonality of the OFDM waveforms can be removed in the 2-D frequency domain. It brings an enhancement of the ICI and the compression loss, and therefore the Doppler tolerance of the developed OFDM waveform can be improved. For example, the minimum subcarrier spacing regarding the ICI is relaxed, so that the OFDM pulse length can be extended. This is an important merit for the MIMO SAR system design since the receive array height in the MIMO SAR system is inversely proportional to the pulse length.
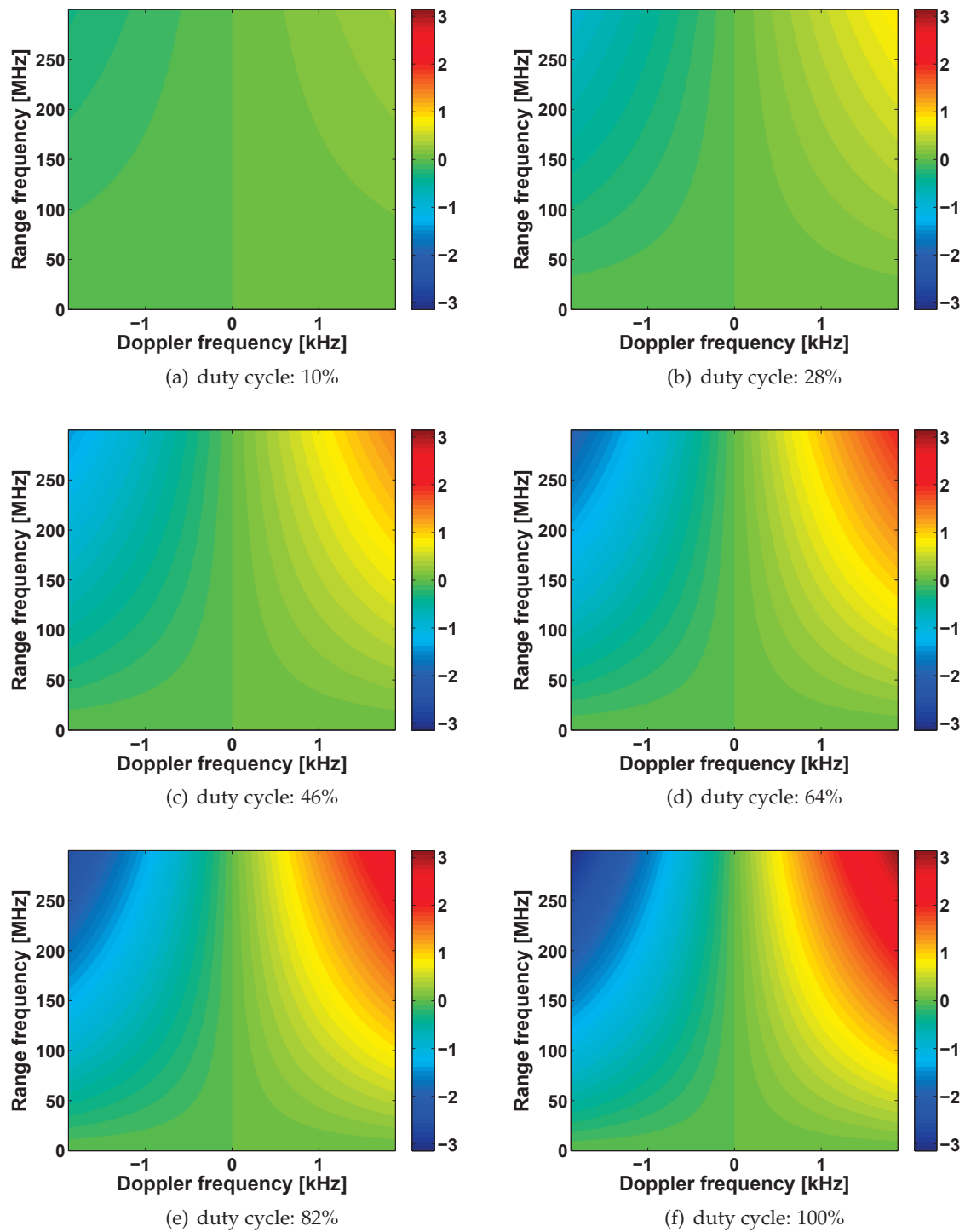
Figure 4.22.: Doppler shift reflected on the phase in radian. The influence becomes more crucial for higher frequencies and higher duty cycles.

4.4. Performance Investigation for Multiple Targets

In this section, the developed OFDM waveform scheme is evaluated for practical SAR channel characteristics. First of all, the spatial filtering performance for a wide image scene is considered since the rigid requirement of the OFDM demodulation is met by this spatial filtering. Secondly, the orthogonality of the OFDM waveforms is tested for speckle noise.

4.4.1. Signal-to-Leakage Power Ratio

Mutual interference between two OFDM waveforms due to imperfection of the spatial filter is considered in this section. As described in (4.33), the received signal includes the side lobe signal $r_{l,side}(t)$ as well as the main lobe signal $r_{l,main}(t)$. Since the received signal is processed by the circular-shift addition in order to have the length $2T_p$, some part of the side lobe signals are also circularly shifted and their energy permeates the main lobe signal. This effect has a significant impact on the orthogonality between both of the OFDM chirp waveforms since the side lobe signals are mostly *truncated* after the circular-shift addition process.

Figure 4.23 illustrates the leakage effect. The truncation distributes the spectral power of the even subcarrier components in $S_2[p]$, over the odd spectral components. These odd components interfere $S_1[p]$ in the main lobe, consisting only of the odd spectral components and vice versa $(S_1 \rightarrow S_2)$. This interference power is defined as the leakage power from one to the other waveform.
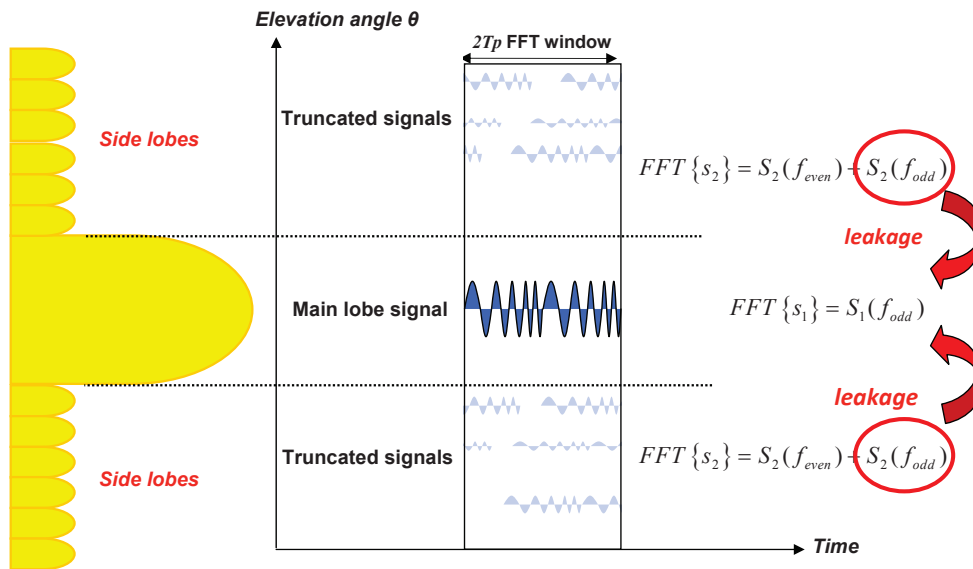
Figure 4.23.: Leakage due to imperfect spatial filtering. Truncated waveforms in the side lobes cause the leakage after the circular-shift addition process.

This leakage impact is quantified by measuring the *Signal to Leakage Power Ratio* (SLPR) which is the ratio of a total spectral power of one waveform pulse in the main lobe to a total leakage power from the other OFDM waveform pulses in the side lobes. In the present OFDM wave-

form scheme, the leakage occurrence can be measured after the demodulation (DFT), so this parameter is defined in the frequency domain.

From (4.44), the total power of the demodulated single pulse is given as follows:

$$P_s = \int_{-f_o/2}^{f_o/2} \left| C_{2way}(\theta_o) \cdot a_1(\theta_o) \cdot \exp(-j\omega\tau(\theta_o)) \cdot S_1(f_{odd}) \right|^2 \mathrm{d}f, \tag{4.67}$$

and similarly, the total leakage signal power is defined as:

$$P_l = \int_{-f_o/2}^{f_o/2} \left| \int_{\Delta\theta_{side}} C_{2way}(\theta) \cdot a_2(\theta) \cdot \exp(-j\omega\tau(\theta)) \cdot S_2(f_{odd}) \mathrm{d}\theta \right|^2 \mathrm{d}f \tag{4.68}$$

where $\Delta\theta_{side}$ denotes the angular range of side lobes. For clarity, the discrete signal notation in (4.44) is rewritten in the continuous signal form. θ_o denotes the boresight angle where the main lobe signal is acquired. S_1 is modulated by the odd subcarrier f_{odd}, and S_2 is modulated by the even subcarrier f_{even}. Thus the leakage from S_2 to S_1 means the odd components of S_2 that overlap S_1. From (4.67) and (4.68), SLPR is defined as

$$\mathrm{SLPR} = \frac{P_s}{P_l} \tag{4.69}$$

$$= \frac{\int_{-f_o/2}^{f_o/2} \left| C_{2way}(\theta_o) \cdot a_1(\theta_o) \cdot \exp(-j\omega\tau(\theta_o)) \cdot S_1(f_{odd}) \right|^2 \mathrm{d}f}{\int_{-f_o/2}^{f_o/2} \left| \int_{\Delta\theta_{side}} C_{2way}(\theta) \cdot a_2(\theta) \cdot \exp(-j\omega\tau(\theta)) \cdot S_2(f_{odd}) \mathrm{d}\theta \right|^2 \mathrm{d}f}$$

for the signal spectrum $S_1(f_{odd})$, or

$$\mathrm{SLPR} = \frac{\int_{-f_o/2}^{f_o/2} \left| C_{2way}(\theta_o) \cdot a_2(\theta_o) \cdot \exp(-j\omega\tau(\theta_o)) \cdot S_2(f_{even}) \right|^2 \mathrm{d}f}{\int_{-f_o/2}^{f_o/2} \left| \int_{\Delta\theta_{side}} C_{2way}(\theta) \cdot a_1(\theta) \cdot \exp(-j\omega\tau(\theta)) \cdot S_1(f_{even}) \mathrm{d}\theta \right|^2 \mathrm{d}f} \tag{4.70}$$

for the signal spectrum $S_2(f_{even})$. In real SAR scenarios, a_1 and a_2 are random variables, therefore this work adopts the Monte-Carlo method in order to estimate this parameter. Under the assumption of a homogeneous clutter scene, $a_2(\theta)$ and $a_1(\theta)$ can be given by Raleigh random variables [50]. A total of 2^9(=512) point targets is assumed in the side lobe region.

This section estimates the SLPR for two different side lobe levels. Two spatial filter patterns for the side lobe level of -50dB and -60dB are generated, using Dolph-Chebyshev windows. The angle θ is converted to the time delay according to (3.46), and thereby the spatial filter pattern is drawn in terms of the delay time. Figure 4.24 (a) and (b) show the pattern versus the delay time normalized by T_p. Figure 4.24 (c) and (d) present the estimated SLPR distribution by means of the Monte-Carlo simulations.

The mean values of each histogram are 35.66dB and 45.36dB, and the standard variations are 0.34dB and 0.365dB respectively. As a consequence, these simulations verify that the proposed demodulation scheme provides reasonable performance, even in multiple target scenarios. However, the performance is strongly dependent on the spatial filter pattern. Therefore, to improve SLPR, a lower side lobe level may be required at the cost of antenna size (height).
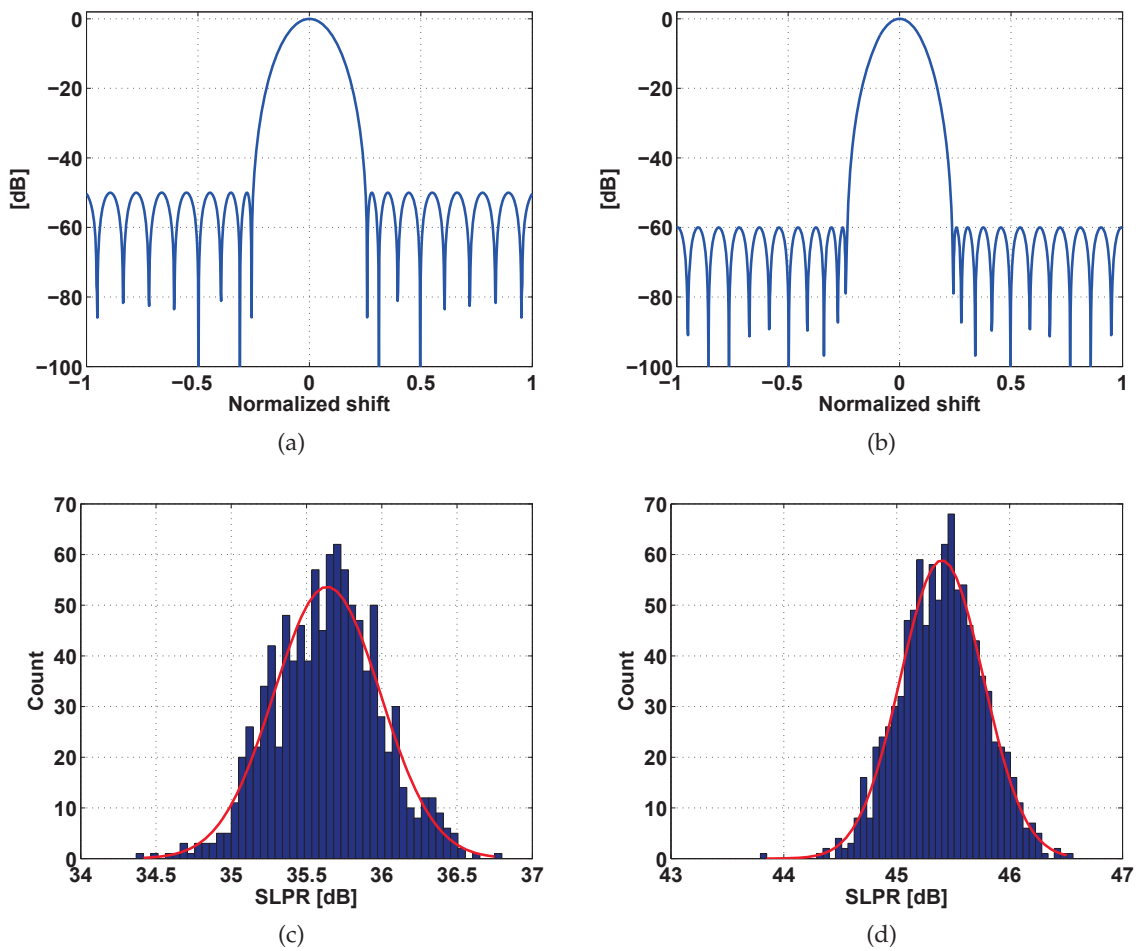
Figure 4.24.: Spatial filter patterns and estimated SLPR histograms from the Monte-Carlo simulations. (a) and (b) show two different spatial filter patterns with the side lobe level of -50dB and -60dB, respectively. (c) and (d) present the estimated SLPR after the demodulation including the circular-shift addition (Number of iterations: 2000).

4.4.2. Speckle Effect

A typical phenomenon of SAR signals is the speckle produced by interferences in scattered pulses of randomly distributed scatterers, in a unit resolution cell that is much larger than the signal wavelength [34, 74]. An important aspect of the speckle noise is its signal-dependent multiplicative behavior. It means that the speckle noise level increases proportionally to the signal power. The following shows 1-D simulations which are carried out in order to test the orthogonality of OFDM waveforms under the speckle noise condition. In real systems, the noise is added to the received OFDM signal, and afterwards the orthogonality is barely observable in the frequency domain, since the interleaved zeros in the odd or the even spectrum are filled by the spectral noise. Therefore the orthogonality of the demodulated signal is tested in the time domain before the polyphase decomposition.

The idea behind the time domain observation is as follows: according to the time domain repetition property of the OFDM waveform (see section 4.1.2), the focused channel response, i.e. the range *Impulse Response Function* (IRF), will have a repetition with the separation of T_p

in the fast-time domain only if the orthogonality is preserved. Therefore, in these simulations, the repetition in the received signal before and after the range focusing is the major point of observation. Additionally, the impulse responses are compared to the reference response of the conventional chirp simulated in the same channel condition.

Figure 4.25 shows the simulation schematic of the speckle noise effect. For this simulation, a chirp signal at the carrier frequency of 5.2GHz, with 100MHz bandwidth, and 100μsec long, is adopted, and is modulated only by odd subcarriers. The resulting OFDM pulse length is double that of the original chirp ($2T_p = 200\mu$sec). The channel, which is denoted by h in Figure 4.25, is composed of 1000 resolution cells in range and each unit resolution cell of $1.5 \times 3m^2$ includes 200 randomly distributed point targets, each with different scattering coefficient.
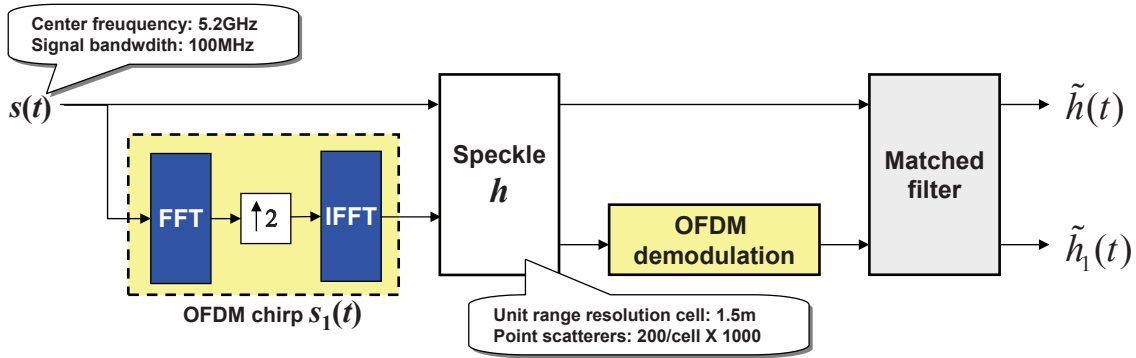
Figure 4.25.: Simulation schematic for the speckle effect.

Under the assumption of homogenous clutters, the amplitude and phase of speckle noise are modeled by a Rayleigh and uniform distribution [34, 74, 50]. The amplitude distribution is then given by

$$p(a) = \frac{2|a|}{\sigma} \exp\left(-\frac{|a|^2}{\sigma^2}\right) \tag{4.71}$$

where $|a|$ is the amplitude of complex scattering coefficient as defined in (3.3), and σ^2 denotes the variance. In these simulations, the variance and the mean value are 0.427 and 1.25 respectively. The phase distribution is, as a rule, given by the uniform distribution:

$$p(\varphi) = \frac{2\pi}{2 \times 10^5} \tag{4.72}$$

where φ denotes the arbitrary phase change of scattered signal. It is worth noting that frequency-dependent scattering coefficient of a single point target is not directly applied, since it is very slow-varying compared to the phase variation of signal spectrum. Nevertheless, the frequency dependency becomes observable in the spectrum of both signals, due to the superposed target responses. The probability density functions of the amplitude and the phase are plotted in Figure 4.26. As the simulation schematic in Figure 4.25 shows, both the chirp and OFDM signals are transmitted into the same speckle noisy channel, and the same Gaussian noise is added to both signals as well. Figure 4.27 shows received baseband signals of the chirp and OFDM signal in time domain.

(a) Rayleigh
(b) Uniform
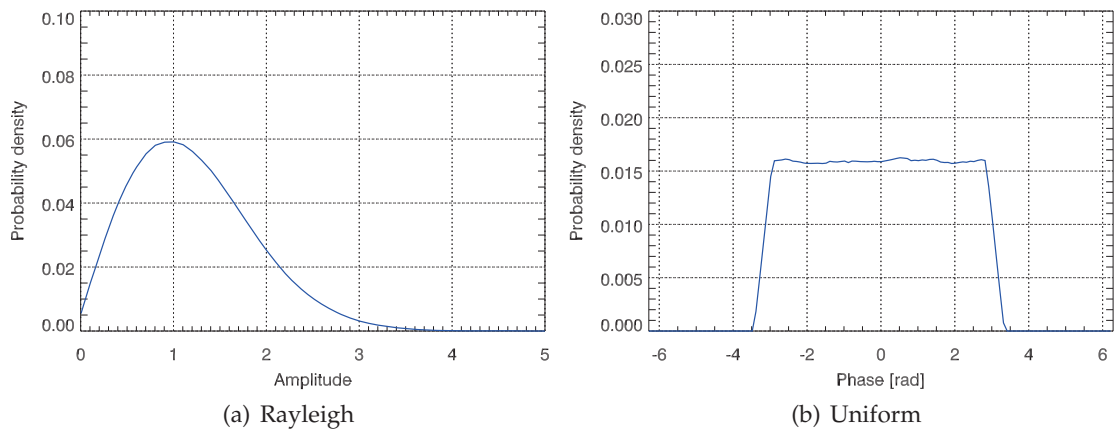
Figure 4.26.: Simulated speckle noise PDF of the amplitude (a) and the phase (b).

The time domain signals show the characteristic of random noise signal in amplitude, which is caused by the superposition of numerous amplitudes and phases of echo signals. As the azimuth antenna pattern is reflected in the amplitude pattern of the Doppler spectrum [30, 113], this amplitude fluctuation directly affects the signal spectrum. As a result, the frequency-dependent scattering is equivalently included in this investigation. An interesting observation point is the periodic pattern of the OFDM signal, since the periodicity means the orthogonality of the OFDM waveform. However, it is difficult to figure periodic pattern out due to the noise-like signal as shown in Figure 4.27 (b). To test the orthogonality of the OFDM signal, both reference chirp and OFDM signal are compressed by the same matched filter function, respectively. It must be noted that the OFDM signal in Figure 4.27 (b) is already processed by the circular-shift addition. The compressed range signals are presented in Figure 4.28.

(a) reference chirp
(b) OFDM
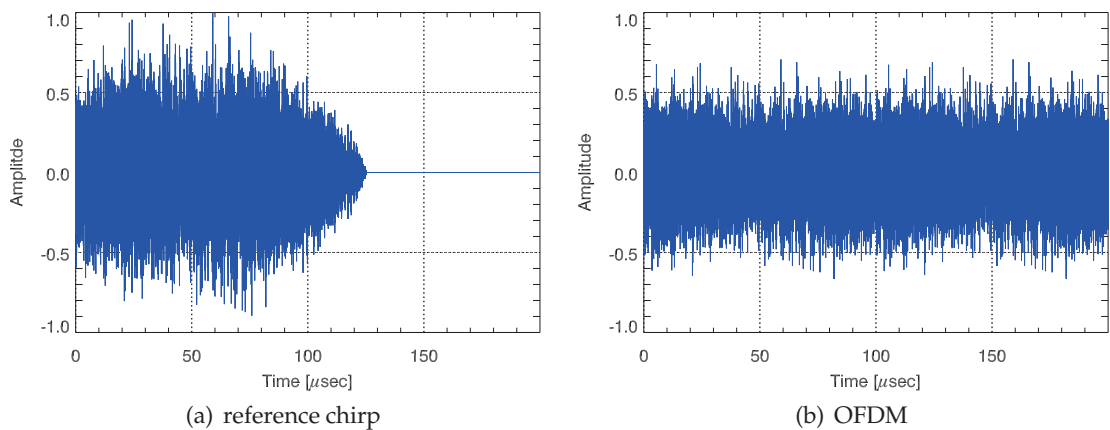
Figure 4.27.: Received baseband signal of the reference chirp (a) and the OFDM signal (b). The OFDM signal amplitude is lower than that of the reference chirp, in accordance with the Parseval's theorem.

The repetition is clearly observed in the range impulse response function before the polyphase decomposition. As shown in Figure 4.28 (b), the IRF of the OFDM signal shows the typical repetitive characteristic and the separation between peaks corresponding to half of the OFDM pulse length, $100\mu sec$. For clarity, the IRF of the even components of the received OFDM signal

85

(a) reference chirp (b) OFDM
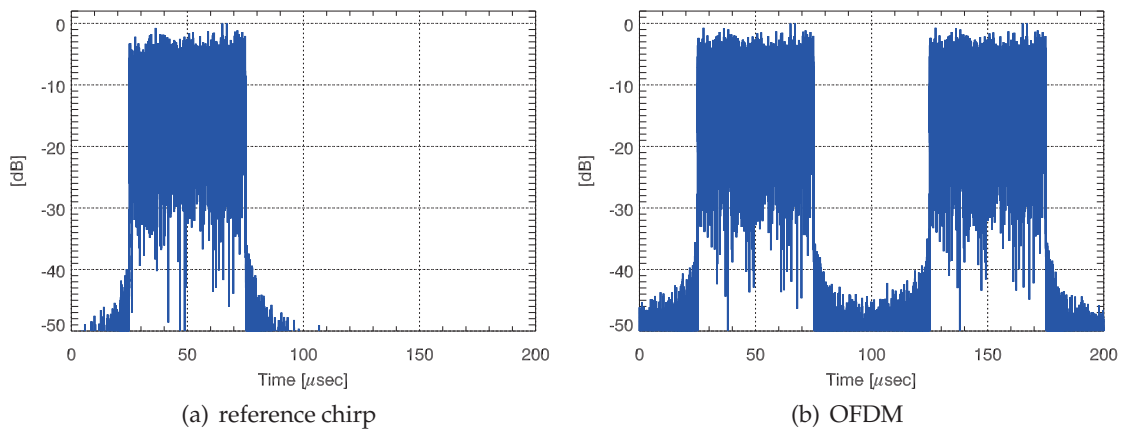
Figure 4.28.: Full range view of the impulse response functions under the same speckle noise condition, prior to the polyphase decomposition.

is also plotted in Figure 4.29. This IRF shows approximately the coupling level of -60dB, which indicates the orthogonality of the OFDM signal for the simulated speckle channel. Moreover, to check the imaging performance, the IRFs of the OFDM signal and the reference chirp are compared in Figure 4.30. It is clear that both IRFs are quasi-identical.
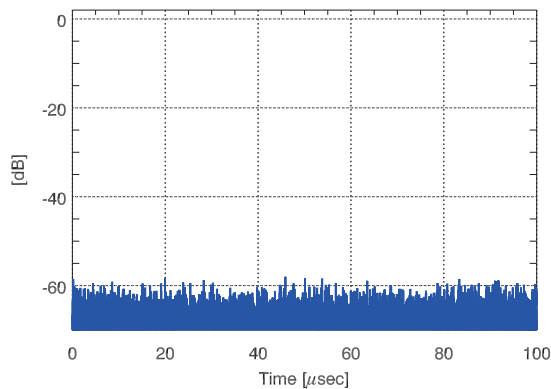
Figure 4.29.: Cross-correlation of the even spectral components of the OFDM signal. This is equivalent to the coupling level from the odd spectral components to the even components in the speckle channel.

As a consequence, the OFDM chirp waveform maintains the orthogonality in the speckle channel, and its imaging performance is equivalent to the conventional chirp. According to the property of repetition and expansion in Fourier transform (see Appendix C), the time domain repetition leads to zero-interleaving in its spectrum. It implicates that two OFDM waveforms modulated by odd and even subcarriers will preserve the orthogonality between them.

Also remarkable is the frequency dependence of the scattering coefficient, which is not directly involved in the simulation. However, the frequency dependency has barely any influence on the orthogonality of the novel waveform. This is because the spectral variation is repeated over the pulse duration as well. Consequently, the OFDM waveform scheme preserves the orthogonality and provides comparable performance with the conventional chirp waveform, even in regard to distributed targets.

| (a) reference chirp | (b) OFDM |
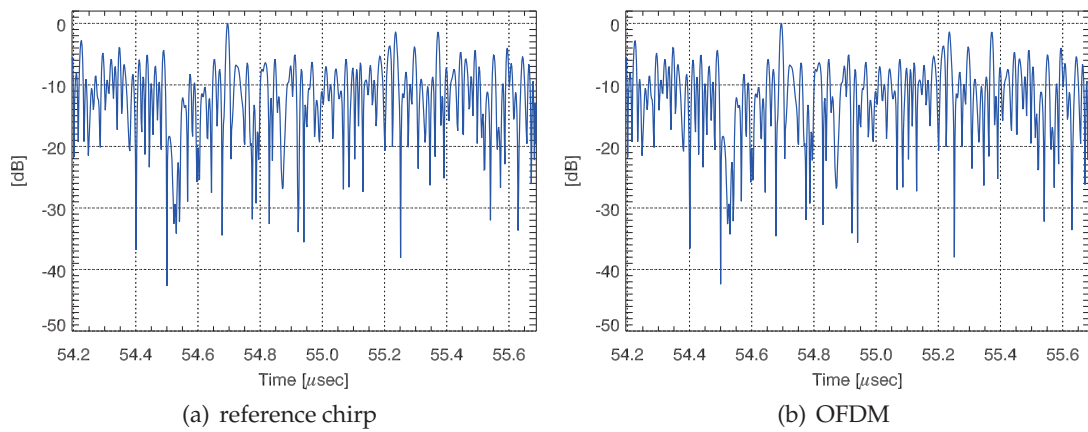
Figure 4.30.: Close-up of impulse response functions of (a) the reference chirp and (b) the OFDM signal.

4.5. Coherence Evaluation

A high spectral-temporal coherence is one of the most important design goals in the present MIMO SAR acquisition for both InSAR and PolSAR applications. This section evaluates the coherence of the novel waveforms using real SAR image data. The evaluation is carried out by measuring the interferometric coherence between equivalent OFDM SAR images[6] produced from real SAR image data and comparing them to the original data.
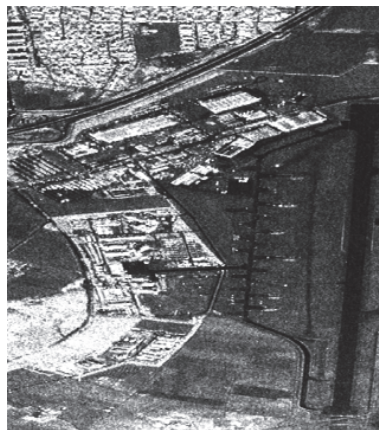
Figure 4.31.: Single polarization (VV) E-SAR image of the DLR site in Oberpfaffenhofen, Germany. The horizontal axis is the flight direction (azimuth), and the vertical axis is the range direction.

This work exploits image data acquired by the E-SAR, which is an airborne SAR system of the German Aerospace Center (DLR) with four operation frequency bands (X-, C-, L- and P-band) [3]. In this section, the L-band (1.3GHz) image data is used for the experiment. The data acquisition parameters are listed in Table 4.2. The used data sets are fully processed, which means focused SAR images composed of 1365×2000 pixels in the range and the azimuth dimension.

---

[6]This term represents a SAR image based on the OFDM chirp waveform.

Table 4.2.: Parameters of E-SAR data.

Parameter	Value	Parameter	Value
f_c	1.3GHz	Bandwidth	93MHz
polarization	quad	T_p	5μsec
PRF	400Hz	sampling rate	100MHz
range samples	1365	azimuth samples	2000

Figure 4.31 shows the E-SAR image produced from VV polarization signals. To generate equivalent OFDM SAR image data, this E-SAR image data is used as a complex channel impulse response function of target scene, $h(t)$, in this test.
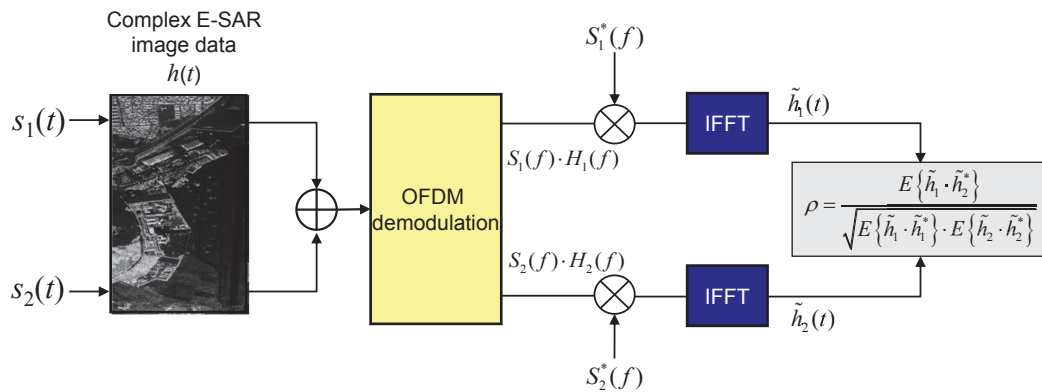
Figure 4.32.: Equivalent OFDM SAR image data generation from the original E-SAR image data for coherence evaluation.

According to the OFDM modulation process described in section 4.1.2, two OFDM waveforms, $s_1(t)$ and $s_2(t)$, are produced. Equivalent SAR echo signals are obtained by the convolution sum between each waveform and the channel impulse response function $h(t)$, respectively. Assuming a single receive channel, these echo signals are superposed and captured by a single receive antenna. The OFDM demodulator followed by parallel matched filters for the waveforms decomposes both waveforms in frequency domain. After this, both demodulated signals are compressed by the matched filtering and transformed into time domain. Therethrough, two OFDM SAR images, $\tilde{h}_1$ and $\tilde{h}_2$, are reconstructed. Figure 4.33 shows these two OFDM SAR images.

4.5.1. Interferometric Coherence

In this section, the feasibility of the OFDM waveforms for the SAR interferometry is tested by evaluating the interferometric coherence between the odd and even spectrum images. The interferometric coherence ρ is defined as [12]:

$$\rho = \frac{E\left\{\mathbf{h}_1 \cdot \mathbf{h}_2^*\right\}}{\sqrt{E\left\{\mathbf{h}_1 \cdot \mathbf{h}_1^*\right\} \cdot E\left\{\mathbf{h}_2 \cdot \mathbf{h}_2^*\right\}}} \tag{4.73}$$

where $\mathbf{h}_{1,2}$ are the OFDM image data sets. In this experiment, these are the two OFDM SAR image data sets produced in the previous section. The coherence is calculated for every 30×30

(a) $\tilde{h}_1$ (b) $\tilde{h}_2$
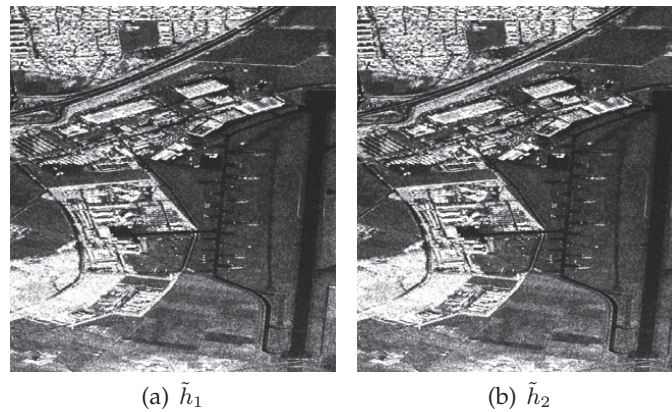
Figure 4.33.: Two OFDM SAR images generated from the E-SAR image data (VV polarization).

image pixel matrix selected by a 2-D window shifting pixel by pixel on the overall image. The resulting coherence map is plotted in Figure 4.34 (a). This result is compared to a case where the original spectrum is split into two non-overlapping bands.

An important point here is the fact that the split spectra are orthogonal as well as the OFDM SAR image spectra. However, as shown in Figure 4.34, the coherence maps are completely different. The coherence of the split spectrum is high exclusively for permanent scatters, such as artificial structures, whereas the the OFDM spectrum shows an overall high coherence. A coherence study for multiple polarizations and frequency bands in [143] lends support to these experimental results.

(a)   (b)
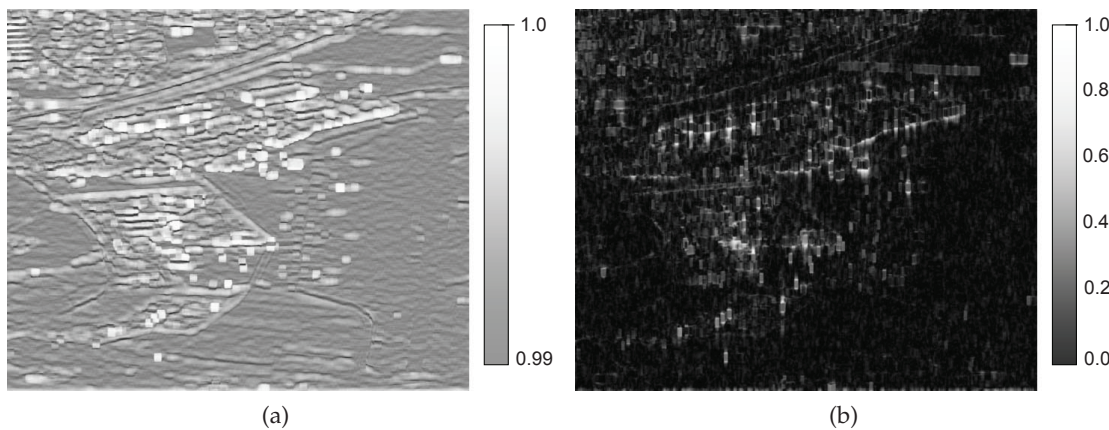
Figure 4.34.: Interferometric coherence map of the OFDM SAR images (a) and two non-overlapping spectra of the original image (b). Note that the color map scale of (a) is adjusted in order to clearly exhibit the result.

To evaluate the obtained coherence value, SNR of the E-SAR image is estimated. In a real SAR channel, the coherence is affected by diverse physical parameters, so that it is given by a scalar product of several coherence components. In this section, the following three components are considered. Using the same notation in [12], one can describe the coherence as follows:

$$\rho = \rho_{SNR} \cdot \rho_H \cdot \rho_a \tag{4.74}$$

where ρ_{SNR} stands for the influence of receiver noise; ρ_H represents the decorrelation due to

two different systems; and finally ρ_a accounts for the temporal scene coherence [12]. Since the two images in this test are generated from one SAR image acquired by the same system at single pass, ρ_H and ρ_a have no influence on the coherence ($\rho_H = \rho_a = 1$). Thus the coherence can be simply rewritten as

$$\rho = \frac{1}{\sqrt{\left(1 + \frac{1}{SNR_o}\right)\left(1 + \frac{1}{SNR_e}\right)}} \tag{4.75}$$

where SNR_o and SNR_e denote the signal to noise ratio of the odd and even spectrum images, respectively, and are assumed to be identical. Under this assumption, SNR of the OFDM image can be estimated as follows:

$$SNR = \frac{1}{\left(\frac{1}{\rho} - 1\right)}. \tag{4.76}$$

The calculated SNR value from the average coherence, 0.9986, is 28.53dB, and this result is reasonable if compared to the SNR of the original E-SAR data within 23.5∼29.7dB [104].
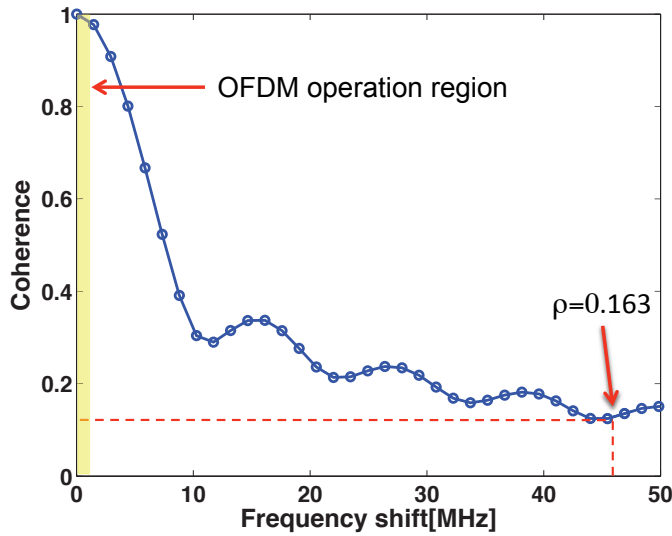
Figure 4.35.: Average interferometric coherence for various spectrum shifts with a step shift of 1.47MHz. The OFDM signals operate in a very high level of coherence, and the split spectra should pay the coherence for the orthogonality.

The split spectra are used for further investigation in order to derive the relationship between the coherence and the spectral separation. First, both spectra are converted into the baseband, so that they are completely overlapping. One of them is shifted by the frequency step of 1.47MHz, and the average coherence is calculated for every shift. Through this iterative calculation, an average coherence pattern for the spectral separation is obtained. Figure 4.35 presents the resulting plot about the relationship. In this experiment, when the spectrum separation is 46.5MHz, the two spectra are equivalent to the split spectra. In this case, the computed coherence reaches approximately 0.163.
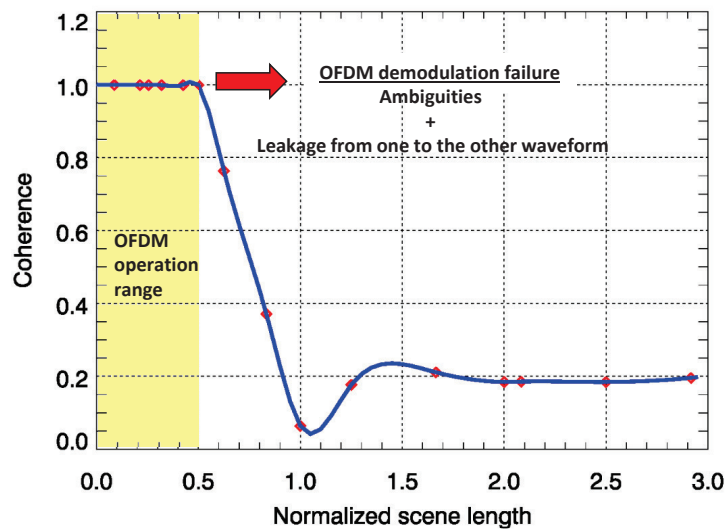
Figure 4.36.: Interferometric coherence for various target scene delay spread. The scene delay length is normalized by the OFDM pulse length. The diamond symbols denote the simulation values and the solid line is a curve-fitting using spline interpolation.

Although SAR imagery is modeled as stationary random process due to speckle [74, 91, 82, 73], the two images with a small subcarrier frequency offset are highly correlated. The reason is as follows: the image scene is a convolution sum with an OFDM pulse, which is at least two times longer than the image scene length (delay spread), and consequently its common spectral components between subcarrier bands are recovered. Therefore, images reconstructed from such long OFDM chirp pulse exhibit a high coherence. This is characterized by simulations using 2-D Gaussian[7] speckle noise data with various image scene length. All simulation procedures are equivalent to the previous experiment, depicted in Figure 4.32. The E-SAR image data are only replaced by the generated Gaussian speckle data in this simulation.

As shown in Figure 4.36, the simulation result shows the quasi-constant coherence values within the OFDM operation range, whereas the coherence rapidly drops and converges on approximately 0.2 with the increase of the scene length. When a scene length is shorter than a half OFDM pulse, the OFDM signals are successfully demodulated, and the resulting image data spectra contain overlapping frequency components. However, as the scene length increases, the interpolation effect is reduced and the OFDM demodulation also fails in the reconstruction of the image scene. Therefore, the coherence deteriorates strongly due to range ambiguities caused by OFDM demodulation as well as leakage from one to the other OFDM pulse.

To conclude, the sufficient coherence for the coherent post processing can only be obtained for a shorter scene length than the OFDM pulse length, further the operation range of OFDM waveforms is bounded by the Lemma 1 in section 7.2. This conclusion corresponds to the basic idea behind traditional OFDM transmission that the information symbols are sent within a narrow coherence bandwidth, inversely proportional to the delay spread of channel, in order to avoid the frequency selective fading [102]. Therefore, these simulations demonstrate that the present OFDM signals offer orthogonality and high coherence at the same time.

---

[7]Strictly speaking, this Gaussian hypothesis is valid for describing scattering mechanism of homogeneous scene [82].

4.5.2. Coherence between Quad-Polarization Data

This section focuses on the verification of the coherence between quad-polarization OFDM SAR images. In a similar way, the full scattering matrix is constructed from the original E-SAR data using the quad-polarization (HH, HV, VH, VV) and compared with the original data. The data conversion is completed in accordance with the fully polarimetric data acquisition scenario, with the OFDM waveforms drawn as in Figure 4.37.
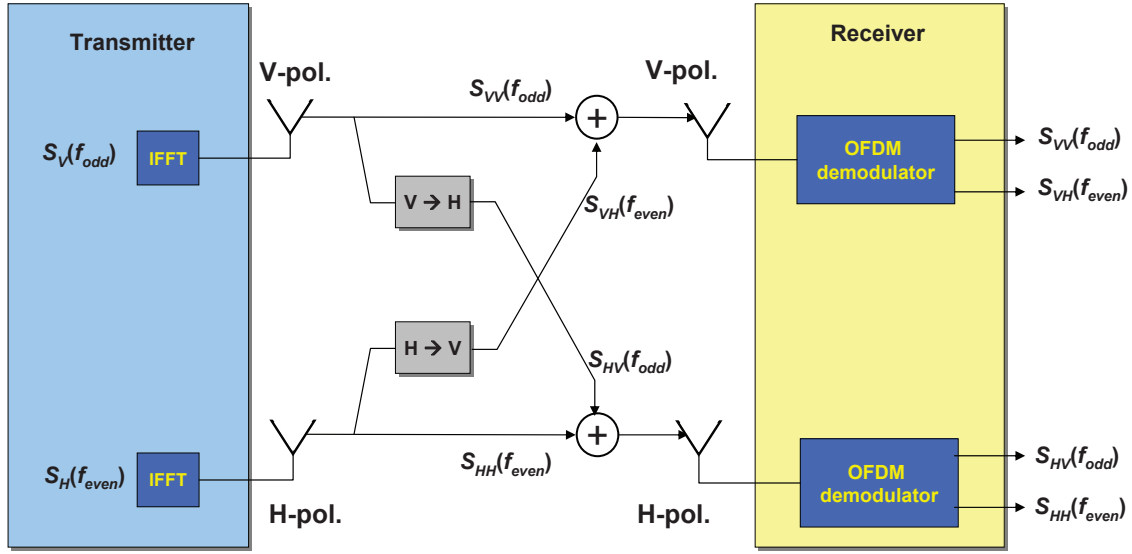
Figure 4.37.: Fully polarimetric data acquisition scenario with the two OFDM waveforms.

On the transmission, two waveforms are modulated by odd and even subcarriers, and radiated through the vertically and horizontally polarized antennas respectively. According to the polarimetric behavior of targets, each polarization either remains or is transformed from the original. On receive, the scattering components, S_{VV} and S_{VH}, are acquired by the vertical polarization channel, and S_{HV} and S_{HH} are captured by the horizontal polarization channel. Based on the orthogonality of the OFDM signals, all the scattering components are separated by the polyphase decomposition in frequency domain in each receive channel. The spectrum and polarization assignments in this acquisition mode are summarized in Table 4.3.

Table 4.3.: Equivalent OFDM quad-polarization data set.

Polarization	Tx spectrum		Rx spectrum	
	odd	even	odd	even
V	S_V	0	S_{VV}	S_{VH}
H	0	S_H	S_{HV}	S_{HH}

According to the above scenario, all quad-polarization E-SAR images are decomposed into the odd and the even spectra. From the polyphase-decomposed images[8], four images corresponding to the above acquisition scenario are used for the coherence test. Figure 4.39 shows the computed coherence maps between HH-HV, HV-VH, and VV-HH from the equivalent OFDM

---

[8]Two images from each polarization are generated, so that total eight images are reconstructed.

SAR data and the original quad-polarization E-SAR data. Since the HV and VH polarization images yield identical coherence maps, these three combinations are presented in Figure 4.39. In Figure 4.39 (a) and (b), the very high coherence is obtained in the overall scene, except for the runway due to the low SNR over the flat and homogenous runway material scattering back the energy weakly. Figure 4.39 (c) and (d) present the relatively high coherence for the region where permanent scatterers are dominant. An additional remark should be made for Figure 4.39 (e) and (f). In the case of airborne SAR data, the SNR of an image is strongly dependent of the incident angle because of a low altitude. Thus Figure 4.39 (e) and (f) present the higher coherence in near range in comparison with far range, since the SNR in the near range is much higher. In Figure 4.40, histograms of each coherence map clarify the similarity between the original E-SAR data and the OFDM data in regards to the coherence.
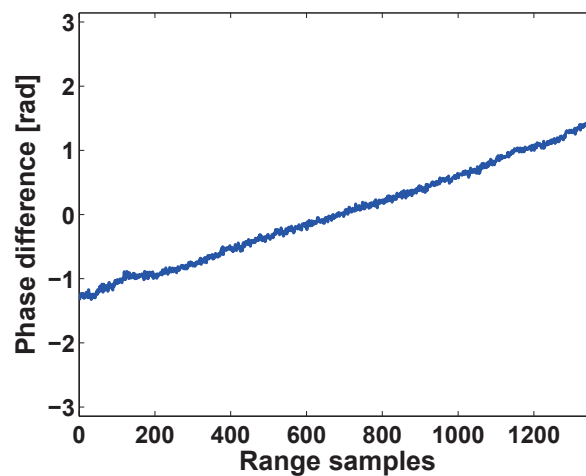
Figure 4.38.: Linear phase ramp of the coherence between the HV-VH components due to the subcarrier spacing.

To conclude, the coherence maps between the equivalent OFDM and the original quad-polarization data are quasi-identical. Therefore the OFDM signals provide sufficient coherence equivalent to the conventional polarimetric SAR signals. However, it must be noted that there is a linear phase ramp in the coherence map, which results from the subcarrier spacing, as previously mentioned. As an example, the mean phase of the coherence between HV and VH images is plotted in Figure 4.38. This phase term can be easily removed in time domain.

(a) HV-VH, OFDM

(b) HV-VH, chirp

(c) HH-HV, OFDM

(d) HH-HV, chirp

(e) HH-VV, OFDM

(f) HH-VV, chirp
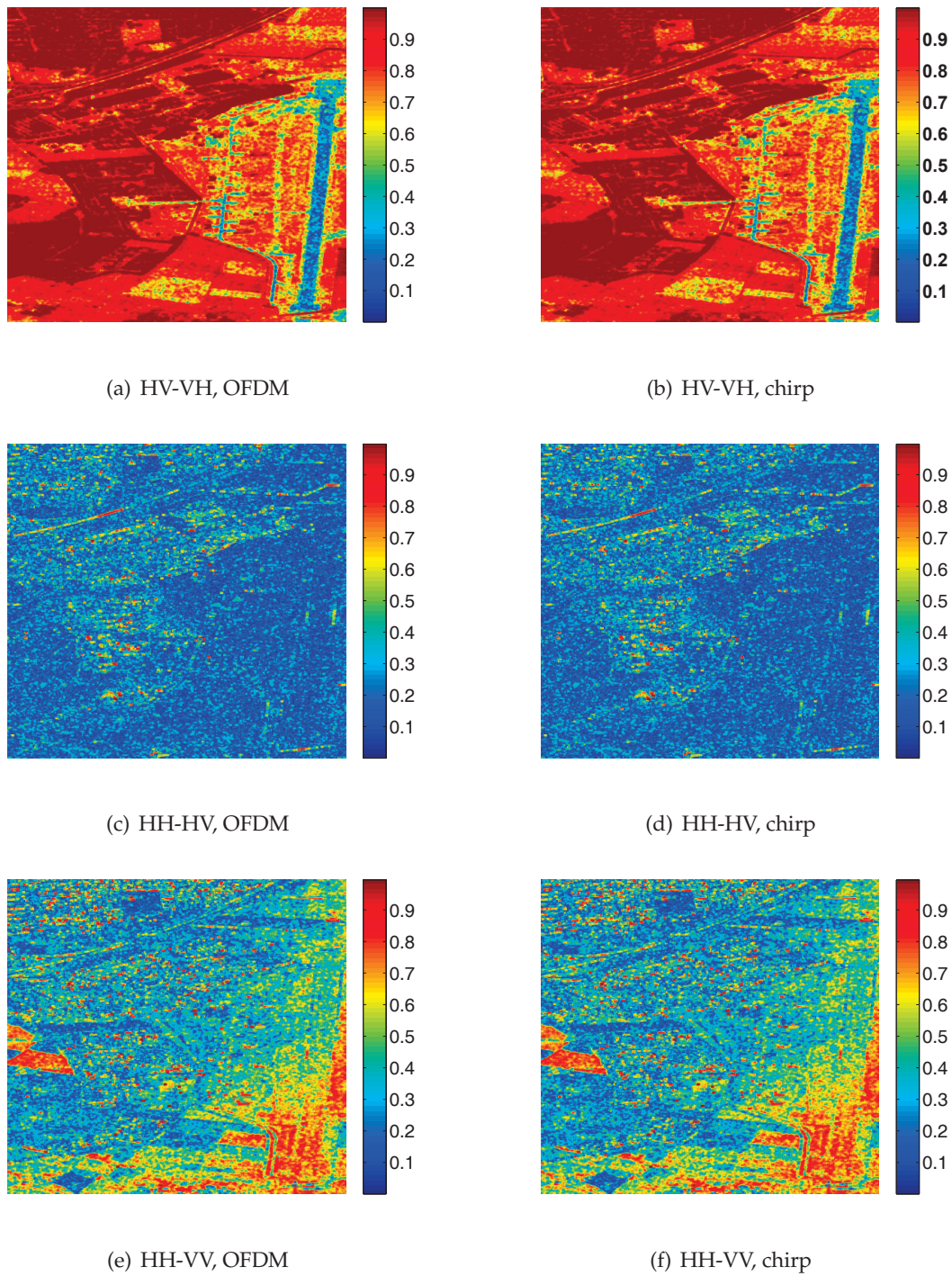
Figure 4.39.: Comparison of the coherence maps between the equivalent OFDM quad-polarization images (a),(c),(e) and the original E-SAR quad-polarization images (b),(d),(f).

(a) HV-VH, OFDM

(b) HV-VH, original

(c) HH-HV, OFDM

(d) HH-HV, original

(e) HH-VV, OFDM

(f) HH-VV, original
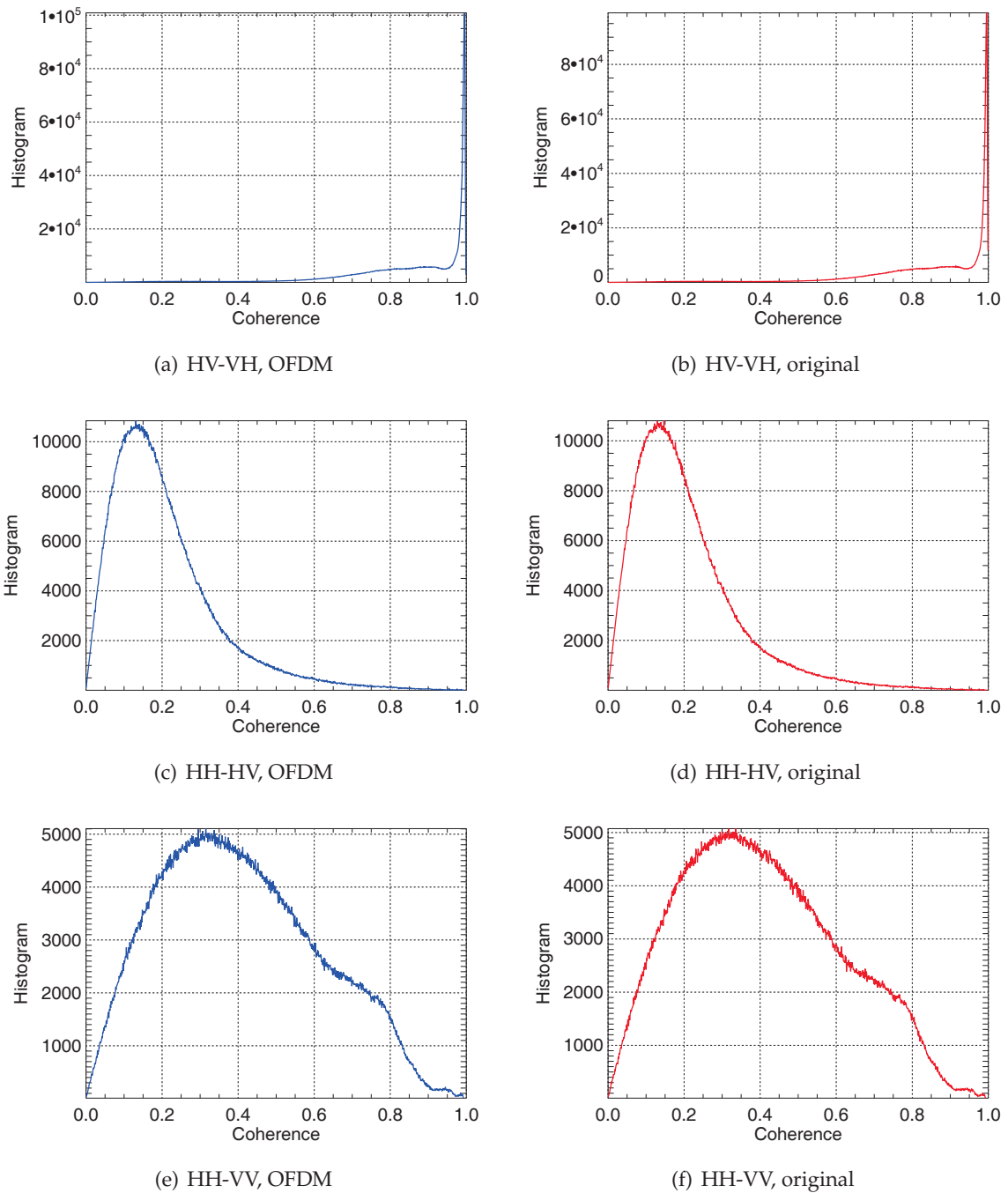
Figure 4.40.: Comparison of histograms between the equivalent OFDM quad-polarization images (a),(c),(e) and the original E-SAR quad-pol. images (b),(d),(f).

5. System Design Parameters

This chapter presents system design parameters for the MIMO SAR system implementation. Special attention is paid to the antenna design, which is directly linked to the DBF and the OFDM waveform performance. The first part of this chapter is dedicated to establishing the antenna design criteria, in regard to the digital beamforming and the OFDM waveform scheme. In the second part, according to the established design criteria, an example MIMO SAR system is designed and its performance is briefly evaluated, in terms of the system sensitivity and the range ambiguity. In this chapter, all of those design parameters and their determinations are derived under the assumption of a single platform system.

5.1. Receive Antenna Design Criteria

The receive antenna design is the most critical step in the MIMO SAR system design. In fact, the array patterns in elevation and azimuth have a direct connection to both the OFDM demodulation and the azimuth ambiguity suppression performance. This section formulates the receive array design rules for a considered planar array antenna.

5.1.1. Receive Antenna Length

The maximum spatial sampling distance in along-track is a half that of a SAR antenna length, according to the Nyquist sampling theory [118]. This rule is also applied to SAR systems with multiple apertures [137]. It is therefore straightforward to derive a total array length L_{rx} for a given PRF, using the relationship

$$L_{rx} = \frac{2V_p}{PRF}.$$

(5.1)

If the number of subarrays is M_R, the DBF in azimuth increases PRF by a factor of M_R. So an initial value of M_R can be derived by dividing the maximum Doppler bandwidth by the PRF. From (2.1) in Chapter 2, the subarray length L_{rs} is derived as follows:

$$L_{rs} = \frac{L_{rx}}{M_R} = \frac{2V_p}{M_R \cdot PRF}.$$

(5.2)

It is worth noting that the half of the subarray length is equal to the spatial sampling distance of SAR image data processed by the DBF in the present MIMO SAR. Thus the subarray length is inversely proportional to the effective PRF[1]. However one should take into account the antenna gain reduction due to the small antenna size. On the basis of the *Azimuth Ambiguity-to-Signal Ratio* (AASR), this section attempts to specify a reasonable boundary for the subarray length.

---

[1]The "effective" PRF is a reconstructed PRF from the multichannel data by the azimuth DBF.

Azimuth Ambiguity-to-Signal Ratio

The AASR is the power ratio of the ambiguous signal to the designed signal, within the SAR correlator (i.e. matched filter) azimuth processing bandwidth [30]:

$$
\text{AASR} = \frac{\displaystyle\sum_{\substack{\beta=-\infty \\ \beta \neq 0}}^{\infty} \int_{-B_p/2}^{B_p/2} A_{2way}^2 \left(f_d + \beta \cdot PRF \right) df_d}{\displaystyle\int_{-B_p/2}^{B_p/2} A_{2way}^2 \left(f_d \right)} \tag{5.3}
$$

where B_p is the Doppler processing bandwidth, β denotes the order of aliasing, and A_{2way} is the amplitude pattern of the Doppler spectrum, which is obtained from the 2-way antenna pattern[2] in azimuth. In this design, the AASR is calculated with respect to a subarray length which normalized by a transmit antenna length, as presented in Figure 5.1.
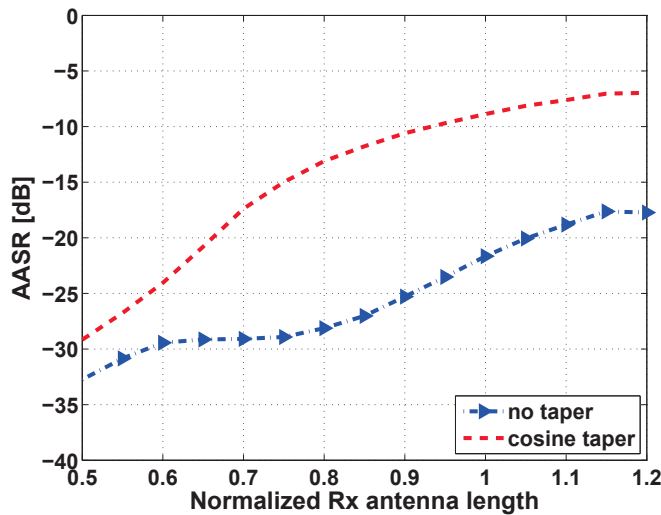
Figure 5.1.: AASR for the normalized receive subarray length. The dash-dot line with triangular symbols is the AASR for a sinc antenna pattern, and the dashed line shows the cosine tapered pattern.

The AASR value varies over the normalized antenna length in the smooth step fashion, due to side lobes of the antenna pattern. If the AASR of -25dB is required, then the subarray length should be approximately 90% of the transmit antenna length, in regard to the sinc antenna pattern (no tapering). Figure 5.1 portrays an interesting result, in that the amplitude tapering on each subarray deteriorates the AASR of the uniform linear array. This is because the phase center spacing between the subarrays is unchanged, while the antenna main lobe broadens. Therefore the spatial sampling distance is insufficient for the widened pattern. In a practical design, this fact should also be taken into account.

---

[2]The amplitude pattern is a scaled version of the 2-way azimuth antenna pattern [111].

5.1.2. Receive Antenna Height

In the MIMO SAR system, the receive array height is an important parameter which influences the spatial filtering performance. As stated in section 4.2, the main lobe width of spatial filter pattern should be specified within the maximum delay spread, which is no longer than half of an OFDM pulse length, in order to fulfill the strict requirements of the OFDM demodulation[3]. In this section, the receive array height is formulated as a function of the OFDM pulse length for a given SAR geometry. The well-known approximation of the main lobe beam width between the first nulls is given by [115]

$$\Delta\theta_{rx} = \frac{\lambda}{W_{rx}} \tag{5.4}$$

where W_{rx} is the receive array height and λ is the wavelength. Using (5.4), the receive array height will be determined.
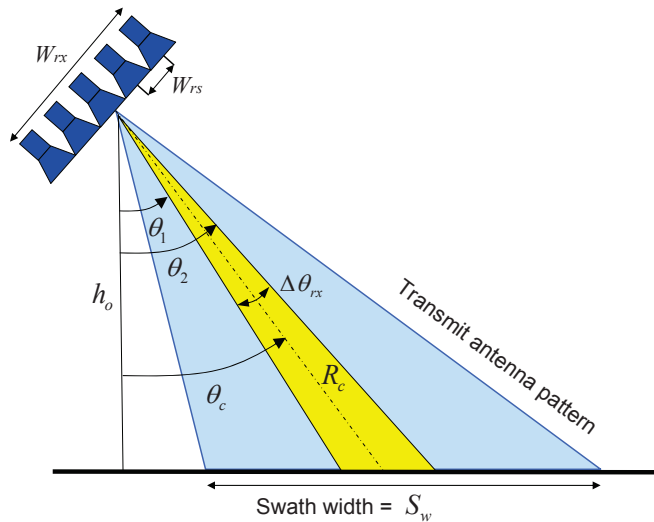
Figure 5.2.: Geometric parameters for receive array height determination. θ_c is the look angle, and R_c is the slant range from the sensor to the middle of swath. $\Delta\theta_{rx}$ denotes the main lobe width of the array pattern. θ_1 and θ_2 are the first null angles of the main lobe.

In Figure 5.2, the time delay at the first null angle θ_1, from the look angle towards the nadir direction, is given by

$$\tau(\theta_1) = \frac{2h_o}{c_o \cdot \cos\theta_1}. \tag{5.5}$$

In the same manner, the other null angle θ_2, from the look angle toward the off-nadir direction, is derived. The delay difference between signals from these two angles must be shorter than

---

[3]The beam width is defined in angle, but not in time. In a spaceborne SAR geometry, the one-to-one correspondence between the elevation angle and the delay time is valid under the assumption of no topographic height (refer to (3.46) in Chapter 3).

the half of the OFDM pulse length. Hence the allowed maximum delay of the signal from θ_2 is described as follows:

$$\tau(\theta_1) + T_p = \frac{2h_o}{c_o \cdot \cos \theta_2} \tag{5.6}$$

where T_p is half of the OFDM waveform length ($2T_p$). To determine the beam width, one needs to convert the delay in (5.5) and (5.6) into the corresponding elevation angles:

$$\theta_1 = \cos^{-1} \left(\frac{c_o \cdot \tau(\theta_1)}{2h_o} \right), \tag{5.7}$$

$$\theta_2 = \cos^{-1} \left(\frac{c_o \cdot (\tau(\theta_1) + T_p)}{2h_o} \right). \tag{5.8}$$

The beam width is given by the difference between those two angles:

$$\Delta\theta_{rx} = \theta_2 - \theta_1 \tag{5.9}$$

$$= \cos^{-1} \left(\frac{c_o \cdot (\tau(\theta_1) + T_p)}{2h_o} \right) - \cos^{-1} \left(\frac{c_o \cdot \tau(\theta_1)}{2h_o} \right).$$

Since the sensor altitude is known, $\Delta\theta_{rx}$ is a function of θ_1 for the given T_p. Replacing θ_1 with an arbitrary elevation angle θ, the minimum receive array height is specified for the elevation angle and the OFDM pulse length, from (5.4):

$$W_{rx}(\theta, T_p) \geq \frac{\lambda}{\Delta\theta_{rx}(\theta, T_p)} \tag{5.10}$$

$$\geq \frac{\lambda}{\cos^{-1} \left(\frac{c_o \cdot (\tau(\theta) + T_p)}{2h_o} \right) - \cos^{-1} \left(\frac{c_o \cdot \tau(\theta)}{2h_o} \right)}.$$

Note that the above derivation is based on the flat surface model. Taking the Earth's curvature into account but no topography, the arc-cosine terms of the denominator in (5.10) are replaced by (3.46):

$$W_{rx}(\theta, T_p) \geq \frac{\lambda}{\cos^{-1} \left(\frac{4(h_o+R_E)^2 - 4R_E^2 + (c_o(\tau(\theta)+T_p))^2}{4(h_o+R_E)c_o(\tau(\theta)+T_p)} \right) - \cos^{-1} \left(\frac{4(h_o+R_E)^2 - 4R_E^2 + (c_o\tau(\theta))^2}{4(h_o+R_E)c_o\tau(\theta)} \right)}. \tag{5.11}$$

The side lobes of the receive array beam must also be considered in order to achieve the required SLPR value (see Chapter 4). For example, a Dolph-Chebyshev amplitude taper is adopted and through this, the main lobe width becomes broader. The beam-broadening, due to the Dolph-Chebyshev taper, can be quantified by introducing a broadening factor b_{HP} of the HPBW [116]:

$$b_{HP} = \sqrt{\frac{1}{\pi} \ln(20^{-\frac{SL}{20}})} \tag{5.12}$$

where SL denotes the desired side lobe level in decibel and $\ln$ means the natural logarithm. This broadening factor can be slightly different for the null-to-null beam width. It is nevertheless an acceptable approximation, since the main lobe pattern decreases rapidly from the 3dB points towards the null points. Multiplying this broadening factor by (5.10), the minimum array height, with respect to the desired beam width and the side lobe level, is obtained as follows:

$$W_{rx}(\theta, T_p) \geq b_{HP} \frac{\lambda}{\Delta\theta_{rx}(\theta, T_p)}. \tag{5.13}$$

Figure 5.3 shows the minimum array height calculated by (5.11) and (5.13), in the case of -50dB and -60dB side lobe levels. The upper plots portray the array heights, derived using (5.13), in 3-dimensional coordinates, and the lower plots are their contour plots. The broadening factor is 1.51 for -50dB, and 1.56 for -60dB. The minimum array height is proportional to the elevation angle, due to an extension of antenna footprint on the Earth's surface. In contrast, the array height is inversely proportional to the OFDM pulse length since a long pulse relaxes the required array beam width. To fulfill the OFDM demodulation requirements within the whole angular range of interest, the array height should be determined in regard to the largest incident angle for a selected OFDM pulse length.

5.1.3. Height of Array Elements in Elevation

Another issue associated with the antenna height is the determination of the number of multiple beams covering the whole swath width. As a rule, assuming the 3dB beam width of a single beam covers one subswath, the required number of subswaths (or angular sectors) N_{sub} can be calculated as follows:

$$N_{sub} = \text{ceil}\left[\frac{\theta_{3dB,Tx}}{\theta_{3dB,Rx}}\right] \tag{5.14}$$

where $\text{ceil}[\cdot]$ is the operator which is used to round up the argument towards the positive infinity. $\theta_{3dB,Tx}$ and $\theta_{3dB,Rx}$ denote the 3dB beam width of both transmit and receive antennas in elevation respectively. The derived number of subswaths, N_{sub}, is equivalent to the minimum number of array elements in elevation, since an array with M_E elements can generate M_E multiple beams simultaneously [56]. Thus the number of array elements must be equal to or more than N_{sub} ($N_{sub} \leq M_E$), and then the single element height W_{rs} should meet the following condition:

$$W_{rs} \leq \frac{W_{rx}}{N_{sub}}. \tag{5.15}$$

The height of the array element is determined by considering the grating lobes at each array beam direction. The decision formula in [137] is used to specify the element height in this design:

$$W_{rs} = \frac{\lambda}{\sin\left(\frac{\theta_{3dB,Tx}}{2}\right) + \sin\left(\eta\frac{\theta_{3dB,Tx}}{2}\right)} \tag{5.16}$$

where η is the positive integer describing the grating lobe order, which is set to be a higher value than 3 for separating grating lobes of the array further away from the main lobe. The high η is also of use for the side lobe reduction using an amplitude tapering, because it increases the number of elements in the array for a fixed total array size [115].

(a) -50dB

(b) -60dB

(c) -50dB

(d) -60dB
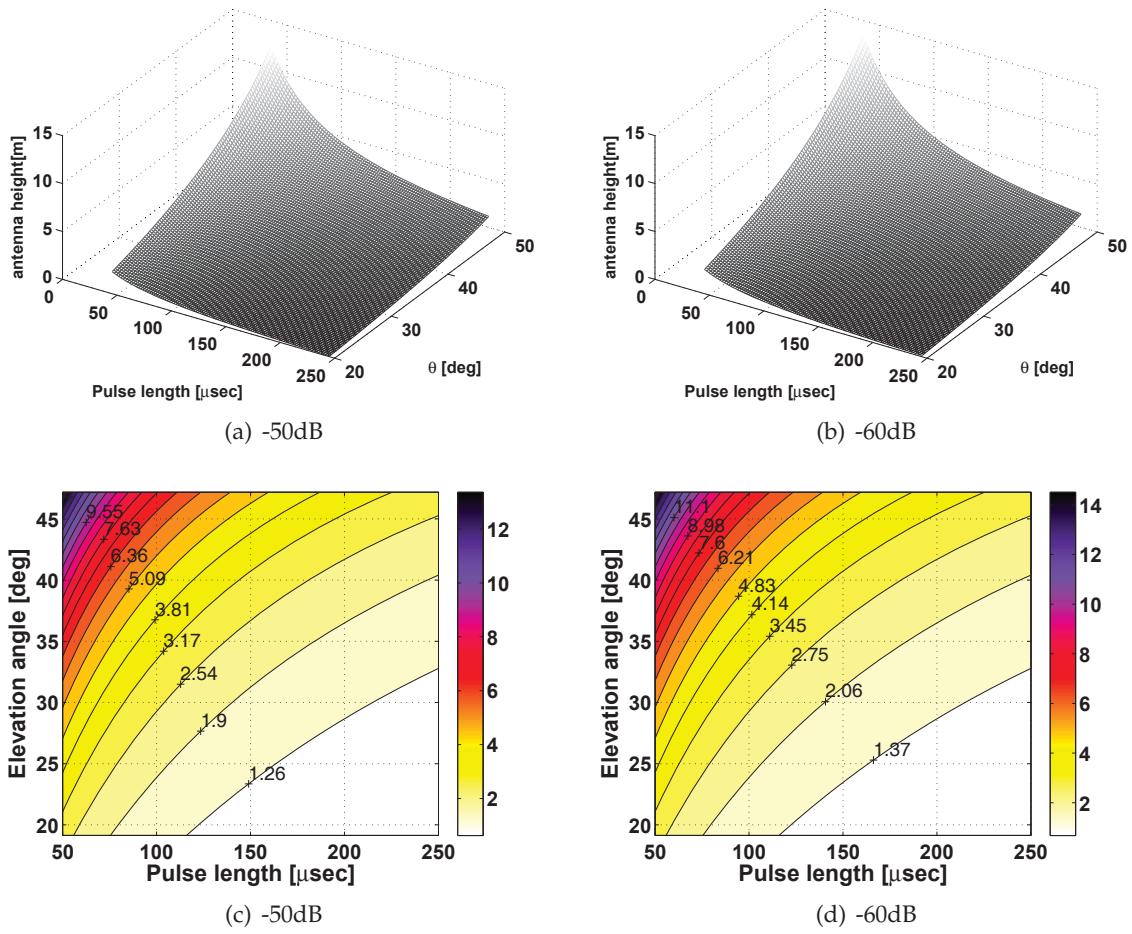
Figure 5.3.: Receive array height versus elevation angle and OFDM pulse length for the side lobe level of -50dB (a), (c), and for -60dB (b), (d).

5.2. Transmit Antenna Design Criteria

The transmit antenna is specified from the SAR geometric parameters, such as the look angle, swath width, and spatial resolution. In the following formulations, a single aperture antenna, not an array, is considered for the transmission.

5.2.1. Transmit Antenna Height

If the sensor altitude h_o and the look angle θ_c are known, then the transmit antenna height W_{tx} is derived from the relation [30]

$$S_w = 0.886 \frac{\lambda \cdot R_c}{W_{tx} \cdot \cos(\theta_c)} \tag{5.17}$$

$$= 0.886 \frac{\lambda \cdot h_o}{W_{tx} \cdot \cos^2(\theta_c)}$$

where S_w is the swath width, and R_c is the slant range from the sensor to the center of a target area. The transmit antenna height is easily obtained by

$$W_{tx} = 0.886 \frac{\lambda \cdot R_c}{S_w \cdot \cos(\theta_c)} \tag{5.18}$$

$$= 0.886 \frac{\lambda \cdot h_o}{S_w \cdot \cos^2(\theta_c)}.$$

5.2.2. Transmit Antenna Length

A straightforward approach to determine the SAR antenna length is to take the antenna length, which is double that of the finest geometric azimuth resolution [30]. If this theoretical antenna length of a monostatic SAR system is denoted by L_{mono} for a given azimuth resolution, the antenna length is described as

$$L_{mono} = 2\delta A \tag{5.19}$$

where δA is the azimuth resolution. For example, if a desired azimuth resolution is 2m, then the monostatic SAR antenna length becomes 4m in principle. This SAR antenna theory is used to formulate the Tx antenna length in the MIMO SAR system. Let us assume two SAR systems, a monostatic and a bistatic system. If the azimuth resolution is defined by the HPBW of 2-way antenna pattern in azimuth, both systems should have the same HPBW in order to achieve the same azimuth resolution:

$$\frac{(0.886 \cdot \lambda)^2}{L_{tx} \cdot L_{rs}} \stackrel{!}{=} \left(\frac{0.886 \cdot \lambda}{L_{mono}} \right)^2 \tag{5.20}$$

where L_{tx} and L_{rs} denote the transmit and receive subarray length respectively. The numerators in (5.20) can be eliminated. Therefore one obtains

$$L_{tx} \cdot L_{rs} \stackrel{!}{=} L_{mono}^2. \tag{5.21}$$

Substituting (5.19) for L_{mono}, the transmit antenna length L_{tx} can be determined as:

$$L_{tx} = \frac{(2\delta A)^2}{L_{rs}} \tag{5.22}$$

where the azimuth resolution δA will be given in the system specification. It is worth noting that the receive antenna length L_{rs} derived in (5.2), can be changed by the AASR and then the transmit antenna length must be recalculated with respect to a new receive antenna length.

5.3. OFDM Parameters: Δf and N

Dealing with OFDM parameters is valuable, since the OFDM pulse length is a key parameter to determine the receive array height, as presented in section 5.1.2. Relationships between the subcarrier spacing, number of subcarriers, and pulse length are given by simple formulas in this section.

A sampling frequency is usually set at a slightly higher frequency than the Nyquist sampling rate, in order to include guard bands in practical systems. The ratio between the sampling frequency and signal bandwidth α is defined as

$$\alpha = \frac{f_s}{f_o} \tag{5.23}$$

where f_s is the sampling frequency and f_o is the signal bandwidth. The subcarrier spacing Δf is calculated from

$$\Delta f = \alpha \frac{f_o}{2N} = \frac{f_s}{2N} \tag{5.24}$$

where $2N$ is the total number of subcarriers of the OFDM waveform. An important remark in (5.24) is that the subcarrier spacing is calculated with respect to the sampling frequency f_s, but *not the signal bandwidth* f_o. Substituting the reciprocal of the sampling interval T_s for f_s, the subcarrier spacing for the pulse length is rewritten as:

$$\Delta f = \frac{1}{2NT_s} = \frac{1}{2T_p}. \tag{5.25}$$

The simple relationship shown above implies that a longer OFDM pulse results in a smaller subcarrier spacing, which could be highly sensitive to a Doppler shift. However, the long pulse length is desirable in order to reduce the receive array height. Therefore the OFDM pulse length and the Doppler tolerance have the trade-off relationship. Fortunately, as shown in section 4.3.3, the trade-off can be relaxed by compensating the Doppler effect in 2-D wavenumber domain.

5.4. System Design Example

Using the design parameters and the formulations, an example MIMO SAR system is designed in this section. In this design, the orbital and the radiometric parameters are referred to as TerraSAR-X. Table 5.1 lists the design goals and specifications.

Table 5.1.: System specifications

Parameter	Value	Parameter	Value
altitude	560km	Pulse length	150μsec
range resolution, δR	max. $1m$	azimuth resolution, δA	max. $1.5m$
swath width	~ 100km	SLPR	≤ -35dB
NESZ	≤ -19dB	AASR	≤ -25dB

The MIMO SAR system designed in this section is an X-band system centered at 9.65GHz as TerraSAR-X. The desired swath width is up to 100km on ground and is selected within the angular range, from $20°$ to $50°$ in elevation, as a rule. This design aims for the geometric resolution 1m, optimally both in range and azimuth. The OFDM pulse length of 150μsec, with a 250MHz bandwidth, is chosen and the SLPR of -35dB is desired. To achieve the required SLPR value, the side lobe level of -50dB is needed, according to the study in section 4.4.1. The NESZ and the AASR values of this example system should meet the specification of -19dB and -25dB respectively. In this design, no beam-steering capacity of transmit antennas is assumed.

5.4.1. PRF Selection

For the given orbit, one can select a proper PRF range using the timing diagram [35] (see the derivation in Appendix E). The timing diagram shows the nadir echo arrival time instance and the pulse transmission time instance, as a function of PRF and look angles. Using this diagram, one can determine the adequate PRF range and incident angles, in which the sensor can acquire backscattered signals without any interruption. Figure 5.4 shows the timing diagram with respect to the orbit parameter in Table 5.1.
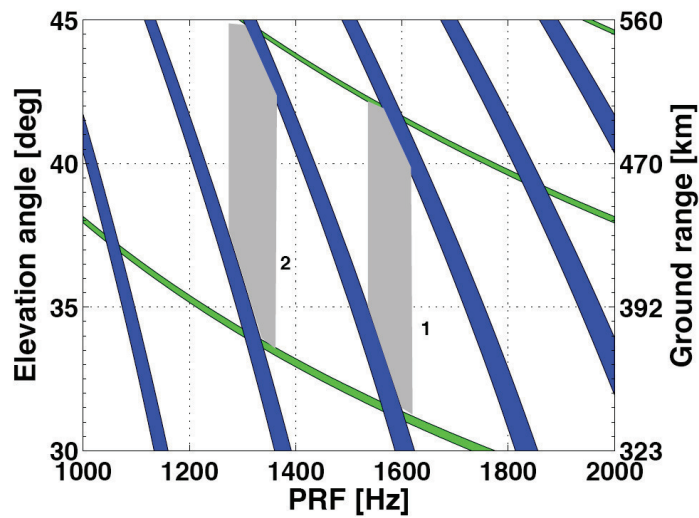
Figure 5.4.: Timing diagram with respect to an altitude of 560km and the OFDM pulse duration of 150μsec.

To satisfy the requirement of the 100km swath width, two candidate PRF ranges, [1565, 1610] and [1295, 1355], are considered. For these two PRF ranges, the corresponding angular ranges are [32°, 42.5°] and [33.7°, 45°] respectively, as highlighted in Figure 5.4. Table 5.2 summarizes the selected PRFs and angular ranges.

Table 5.2.: Candidate PRF ranges and the corresponding angular ranges

Swath No.	PRF	Angular range	Swath width
1	$1565 - 1610$Hz	$32° - 42.5°$	$\sim 100km$
2	$1295 - 1355$Hz	$33.7° - 45°$	$\sim 100km$

If transmit antennas enable the steering of the beam in elevation or the variation of the beam width, the available PRF range will be increased. However, the transmit antennas are fixed in this design. Thus the first PRF range is chosen in regard to the antenna length and height.

5.4.2. Antenna Dimension Specification

For the given specification and the PRF, the transmit and receive antenna parameters are determined in this section.

Antenna Height Determination

The height of transmit and receive antennas can be derived from the OFDM pulse length and SAR geometric parameters in Table 5.1. Figure 5.5 exhibits the antenna height design procedures and the formulas used in each step.
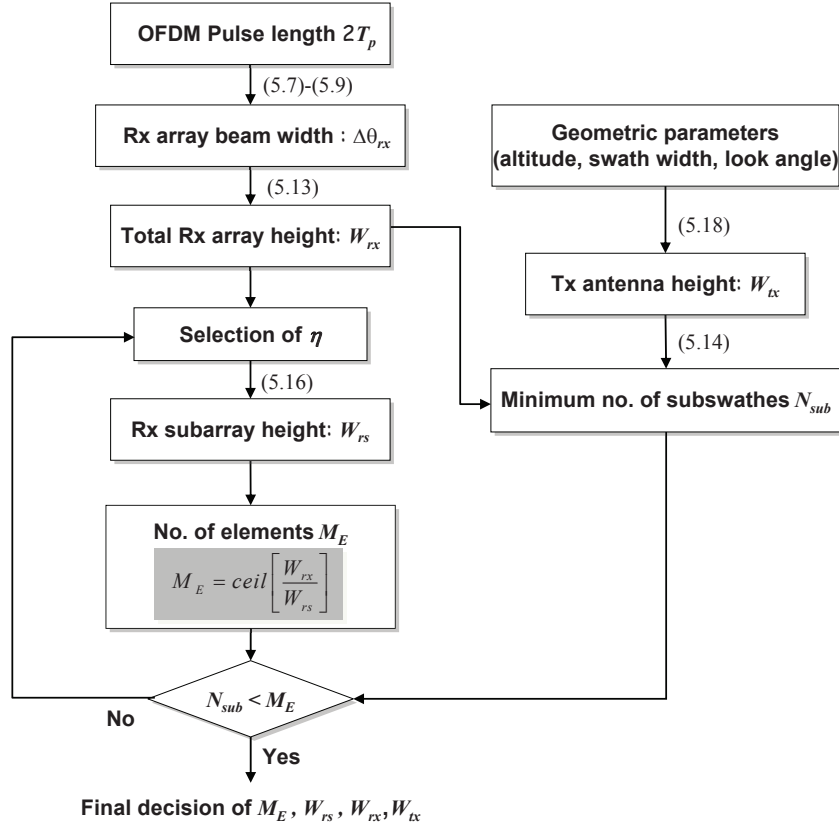
Figure 5.5.: Antenna height decision flow chart.

Firstly, the transmit antenna height is determined from (5.18), with respect to the given sensor altitude, look angle at the scene center, and the swath width. Figure 5.6 plots the required transmit antenna height to illuminate the swath width of 100km over look angles. From the timing diagram, the center look angle $37.5°$ is determined, and the corresponding antenna height 0.248m is found in Figure 5.6.

The receive array height is determined by the specified OFDM pulse length. Using (5.9), the required beam width is calculated and the array height can then be decided. During these steps, the SLPR must be taken into account. The example system adopts a Dolph-Chebyshev window in order to reach the side lobe level of -50dB and satisfy the desired SLPR value. Thus the antenna height is derived from (5.13). From Figure 5.3 (a) and (c), one can also decide the array height with respect to the selected angular range. In this design, the height of 3.5m is sufficient to cover the selected angular range $[32°, 42.5°]$. The calculated transmit and receive antenna heights are used to calculate the minimum number of subswaths N_{sub} in (5.14). This value provides the low bound of the number of array elements in elevation, determined by the relationship between η, M_E, and W_{rs}, as shown in Figure 5.7 at a glance.
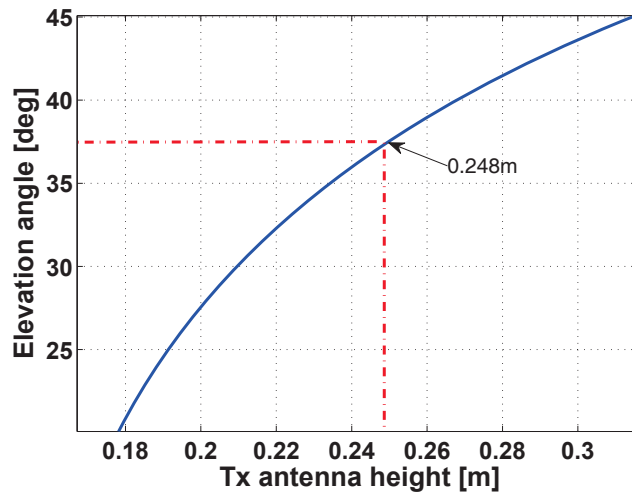
Figure 5.6.: Estimated transmit antenna height versus elevation angles.
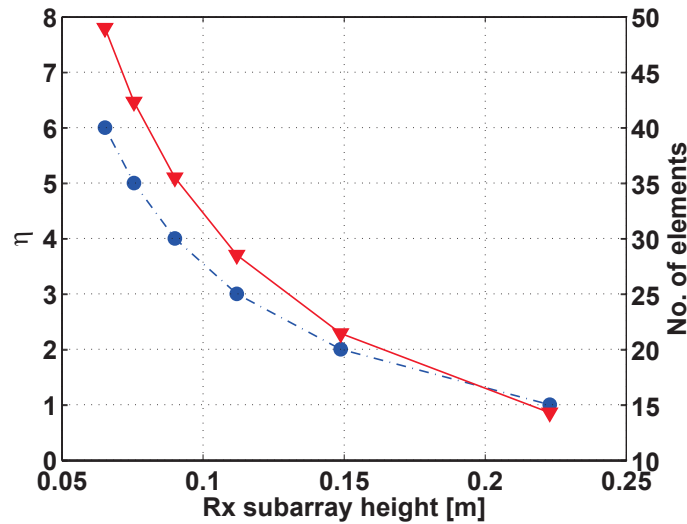
Figure 5.7.: Subarray height W_{rs} versus the order of grating lobes η and the required number of subarray elements M_E are presented by dash-dot line with circular symbols and solid line with triangular symbols respectively.

The dash-dot line with the circular symbols indicates the subarray height versus the order of grating lobes, and the solid line with the triangular symbols shows the number of array elements for each subarray height. In this design, η in (5.16) is set to be 5 and 42 elements are then required. The corresponding W_{rs} is 0.0762m, which is 2.458λ. Before finalizing the parameter values, the number of subswaths N_{sub} is used to see if the determined M_E is sufficient for it.

Antenna Length Determination

The antenna length decision is closely related to spatial sampling specifications. Figure 5.8 presents the decision procedures. To begin, the receive array length L_{rx} is derived from the minimum PRF of 1.565kHz and the platform velocity V_p by (5.1). To recover the Doppler pro-

cessing bandwidth required for the 1.5m azimuth resolution, at least 5 subarrays in azimuth are necessary. In this case, the subarray length L_{rs} is 1.93m from (5.2) and the transmit antenna length L_{tx} of 2.07m is decided by (5.22). This initial design is evaluated in regard of the AASR. In Figure 5.1, the AASR value for this design is approximately -23dB, which does not satisfy the design goal. This is because the ratio between L_{rs} and L_{tx} is 0.93. Hence the number of subarrays M_R is increased by 6 and the above procedures are repeated. The receive subarray length is reduced to 1.61m and the transmit antenna length is adjusted to 2.48m. The ratio between the new designs becomes 0.648 yielding the AASR of -29dB. Table 5.3 compares the final receive subarray length with its initial design value.
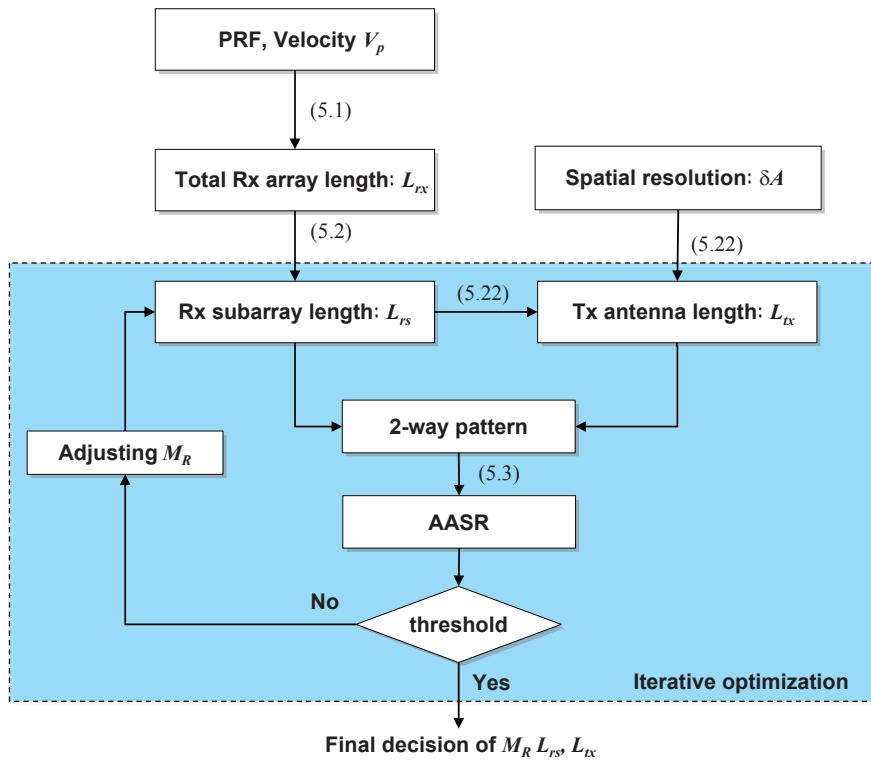
Figure 5.8.: Antenna length decision flow chart.

Table 5.3.: Comparison between the initial and final designs

	Initial design			Final design		
L_{rx}	L_{rs}	M_R	AASR	L_{rs}	M_R	AASR
9.66m	1.93m	5	-23dB	1.61m	6	-29dB

5.4.3. Summary of Design

This section summarizes the designed example MIMO SAR system. Beside the antenna parameters, other system and geometric parameters, which are not introduced in this chapter, are chosen according to traditional rules, such as the radar equation, or the parameters of prior systems. The transmit antenna constellation is assumed to be changeable, depending on the

operation mode. The baseline between transmit antennas is directly associated with satellite structures and mechanical design issues. Accordingly, the baseline issue is excluded in this design.

Table 5.4 lists the designed system and geometric parameters. The pulse duration of 150μsec leads to the duty cycle of 24.1% for the highest PRF of 1610Hz. This value can be reduced by employing a shorter OFDM pulse at the cost of increasing the receive array height W_{rx}. The spatial sampling distance varies from 4.70m to 4.83m, depending on the PRF. In this system operation, a serious non-uniform sampling will not occur due to the narrow PRF range. In the case that a wide range of PRF is considered, the degree of non-uniform sampling will be significant and reach the maximum at the highest PRF.

In this designed system, it is assumed that all receive channels have the identical noise figure 3.75dB, and cable loss 3dB. The required peak and average power of this system are much higher than the TerraSAR-X system (its peak power of 2kW) in order to achieve the desired NESZ over the 100km swath width. As a rule, the sampling frequency of 275MHz includes a 10% guard band, and then the pulse length 150μsec leads to 41250 subcarriers with the 6.67kHz subcarrier spacing. To improve the computation speed of DFT/IDFT, one can select a number of subcarriers equal to a power of 2^4.

This example system was designed for the multimodal operation, based on the developed techniques. If the designed MIMO SAR system is dedicated to the HRWS SAR imaging operation mode, the multiple transmit antennas can be used to reduce the total antenna size as well. The total area of the 6 receive subarrays and two transmit antennas in this design is $35.04m^2$. By arranging the second transmit antenna in along-track at a proper distance, only 3 receive subarrays are required for the same HRWS SAR imaging performance of the original design, instead of the 6 subarrays, according the co-array concept [53]. In this case, the total antenna area is reduced to $18.14m^2$, which is 51.76% smaller than the original design.

---

[4]It must be emphasized that within a given signal bandwidth, changing N leads to the variation of T_p.

Table 5.4.: System parameters of the example design.

Parameters		Values	Remarks / Symbols
Geometry	swath width	~100km	S_w
	No. of subswaths	14	No. of spatial filters
	orbit height	560km	h_o
	velocity	7560 m/sec	V_p
	PRF	1565-1610Hz	
	incident angle	32°- 42.5°	
	spatial resolution	$\sim 1m, \sim 1.5m$	$\delta R, \delta A$
Tx antenna	length	2.48m	L_{tx}
	height	0.248m	W_{tx}
	gain	39.05dBi	G_T
	No. of antennas	2	identical characteristics
	Tx baseline	$\sim 40m$	
Rx array	total length	9.66m	L_{rx}
	total height	3.5m	W_{rx}
	gain	56.46dBi	G_R
	subarray length	1.61m	L_{rs}
	subarray height	0.0762m	W_{rs}
	azimuth panel	6	M_R
	elements in elevation	42	M_E
H/W system	peak power	6kW	67.8dBm
	average power	max. 1.407kW	61.48dBm
	bandwidth	250MHz	f_o
	pulse duration	$150\mu sec$	$2T_p$
	duty cycle	24.1%	for max. PRF
	system NF	3.75dB	noise figure
	loss	3dB	L_{ant}
	sampling frequency	275MHz	f_s
	subcarrier spacing	6.67kHz	Δf
	No. of subcarriers	4.125×10^4	FFT/IFFT length

5.5. Performance Estimation

This section is dedicated to the evaluation of the performance of the designed MIMO SAR system, in terms of the system sensitivity and the range ambiguity.

5.5.1. Noise Equivalent Sigma Zero

The *Noise Equivalent Sigma Zero* (NESZ) is a parameter indicating the system radiometric sensitivity, which is defined as the back scattering coefficient, corresponding to SNR equal to unity[5] [118]. The bistatic configuration of the MIMO SAR leads to different antenna gains in the transmission and reception, meaning that the NESZ is formulated for these gains as follows:

$$\text{NESZ} = \frac{256(\pi \cdot R_s)^3 \cdot k_{bol} \cdot T_{sys} \cdot L_{ant} \cdot V_p \cdot f_o \cdot \sin\theta}{P_t \cdot 2T_p \cdot PRF \cdot G_T(\theta) \cdot G_R(\theta) \cdot \lambda^3 \cdot c_o} \tag{5.26}$$

where T_{sys} is the equivalent system noise temperature; k_{bol} is the Boltzmann's constant of $1.3807 \times 10^{-23} J \cdot K^{-1}$; P_t is the peak transmit power; L_{ant} is loss of antenna feed networks; R_s is the slant range; f_o is the signal bandwidth; T_p is the half of the OFDM pulse length; and finally G_T and G_R are the gain patterns of the transmit antenna and the receive array respectively. Figure 5.9 shows the estimated NESZ values for the designed 2×6 MIMO SAR system.
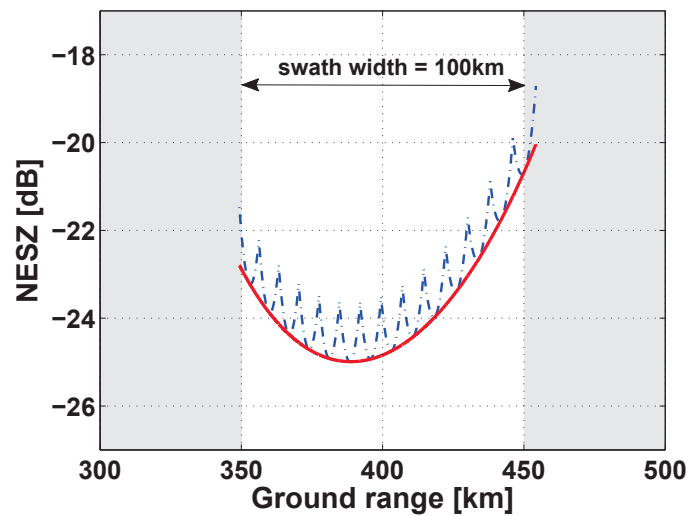
Figure 5.9.: NESZ of the example system. The dash-dot line denotes the NESZ of each subswath and the solid line highlights the coherent combination of the subswath data.

The calculated NESZ of each subswath is indicated by the dash-dot line. There is approximately 5dB difference between the best and the worst values within the whole swath. In the designed system, 14 beams, i.e. subswaths, cover the whole swath. The multiple subswaths cause a ripple of the NESZ over the whole swath, however this effect can be compensated by coherently combining each subswath data after the co-registration and phase synchronization

---

[5]The back scattering coefficient is often denoted by σ_o (sigma zero).

in the stitching process, which is commonly used in the *SPECtral ANalysis* (SPECAN) algorithm [29]. The solid line shows the NESZ after the coherent combination process.

It should be emphasized that the NESZ was separately calculated for each transmit antenna. In other words, one transmit antenna does not contribute to the NESZ calculation of the other transmit antenna. For the multimodal operation, this system reconstructs multiple images independently for the interferometry or the polarimetry. The multiple transmit antennas can be used for the NESZ improvement as well, so long as the multiple images are coherently summed after the co-registration.

5.5.2. Range Ambiguity-to-Signal Ratio

Range ambiguities are caused by overlapping echoes from preceding and succeeding pulses to desired signals [30]. The antenna side lobes have a decisive influence on the range ambiguity level. The *Range Ambiguity-to-Signal Ratio* (RASR) is used to indicate the range ambiguity effect in SAR images. For the MIMO SAR system, this parameter is defined as follows:

$$\text{RASR} = \frac{R_s^3 \cdot \sin(\theta_{inc})}{|C_{2way}(\theta)|^2} \cdot \left(\sum_{\substack{m \neq 0 \\ m=-N_n}}^{N_f} \frac{|C_{2way}(\theta_m)|^2}{R_s^3(m) \cdot \sin(\theta_{inc,m})} + \frac{|C_{2way}(\theta + \Delta\theta)|^2}{R_s^3 \cdot \sin(\theta_{inc} + \Delta\theta_{inc})} \right) \qquad (5.27)$$

$$= \underbrace{\frac{R_s^3 \cdot \sin(\theta_{inc})}{|C_{2way}(\theta)|^2} \cdot \sum_{\substack{m \neq 0 \\ m=-N_n}}^{N_f} \frac{|C_{2way}(\theta_m)|^2}{R_s^3(m) \cdot \sin(\theta_{inc,m})}}_{\text{RASR}_{con}} + \underbrace{\frac{R_s^3 \cdot \sin(\theta_{inc})}{|C_{2way}(\theta)|^2} \cdot \frac{|C_{2way}(\theta + \Delta\theta)|^2}{R_s^3 \cdot \sin(\theta_{inc} + \Delta\theta_{inc})}}_{\text{RASR}_{ofdm}}$$

where θ_{inc} denotes the incident angle and θ denotes the elevation angle. N_n and N_f give the number of pulses considered in the calculation in both the near and far range respectively. (5.27) is composed of two parts. The first stands for the conventional RASR value, denoted by RASR_{con}, and the second represents the additional value, RASR_{ofdm}, caused by the circular-shift addition process in the OFDM demodulation, which are $2T_p$ apart from the original position in time domain (see section 4.2). $\Delta\theta$ and $\Delta\theta_{inc}$ are the elevation look angle and incident angle separations corresponding to $2T_p$ respectively.

Figure 5.10 (a) shows the conventional RASR term in (5.27). The range ambiguities are suppressed in the antenna pattern by 60dB. The narrow elevation beam of the receive array reduces the echo spread of each subswath and the reduced PRF, via the multiple receive subarrays in azimuth, results in an increase of the angular separation between the desired signal and the range ambiguity signals. In addition, the side lobe reduced by the Dolph-Chebyshev tapering also improves the range ambiguity suppression in this design.

However, the range ambiguity caused by the circular-shift addition in Figure 5.10(b) has a major contribution to the final RASR shown in Figure 5.10 (c). It is noted that the RASR_{ofdm} indicates the interference level from adjacent subswaths, since the circularly shifted signal originates from the succeeding subswath region. This result implies that the spatial filtering performance is critical in this system.

(a) RASR$_{con}$

(b) RASR$_{ofdm}$

(c) RASR
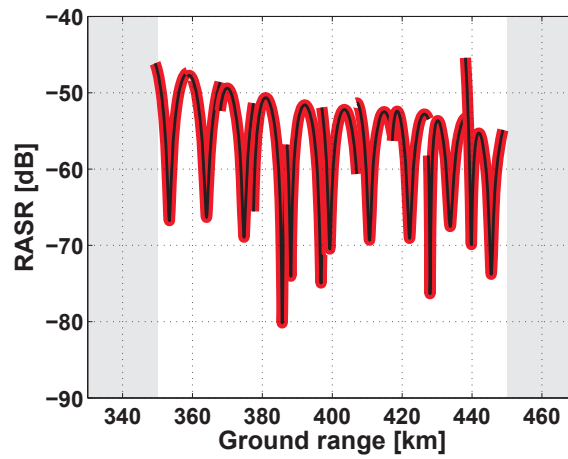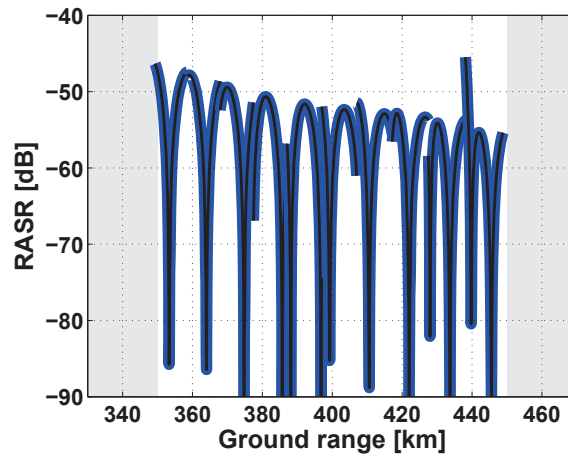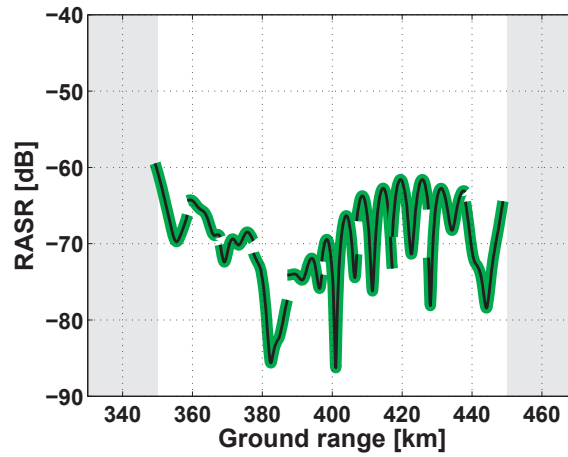
Figure 5.10.: Computed RASR over the whole swath: (a) the conventional RASR, (b) the addition section of RASR due to the circular-shift addition in the OFDM demodulation, and (c) the final RASR.

6. Ground-Based Multichannel SAR Demonstrator

This chapter presents a ground-based SAR system composed of multiple receive channels, which contributes to experiments of the MIMO SAR techniques, the digital beamforming and the OFDM chirp waveform scheme, introduced in the earlier chapters. From the design consideration to the system characterization, this chapter deals with overall system development issues. In the next section, an overview of the GB SAR system configuration and operation is given, and subsequently each subsystem block is separately presented in detail.

6.1. System Configuration and Specification

This demonstrator is an X-band pulsed radar system where the platform moves along rails. The whole system is composed of the antenna subsystem, the transceiver subsystem, the positioning system, and the operation software. Figure 6.1 depicts the system block diagram.

The antenna subsystem includes a separated single transmit antenna and five receive subarrays, which are connected to the receiver through a *Single-Pole 5-Through* (SP5T) RF switch module with the control digital circuitry. The antennas are mounted upon a reconfigurable antenna holder, so that various antenna constellations are feasible. The switch control unit distributes 5V *Transistor-Transistor Logic* (TTL) signals to select an operating receive subarray. The transceiver subsystem is composed of a transmitter directly fed by an *Arbitrary Waveform Generator* (AWG) and the data acquisition block. Owing to the integrated analog circuitry (amplifiers and filters) in the AWG, the transmitter has a relatively simple architecture. The AWG creates a chirp signal directly at the *Intermediate Frequency* (IF) band with its center frequency at 200MHz. The transmitter amplifies and converts the IF signal to the RF signal. The data acquisition block includes a Low-IF receiver and a wide band oscilloscope for digitizing analog input signals. The analog part of the receiver, implemented using surface-mounted devices, converts the acquired RF signal to the IF band. The wide band oscilloscope digitizes the IF signals in each I-Q channel. A set of parallel mixers, implemented by software, converts the IF digital signals to the baseband. During the final conversion, image frequencies are rejected. The digital baseband signal which is ready for SAR processing is stored in the main computer. The positioning system consists of a stepper motor and its controller, which enables the precise movement control of the platform. Figure 6.2 shows the antenna and RF subsystems mounted on the platform with the stepper motor under test.

All instruments used in the demonstrator are synchronized with a 10MHz reference clock and are connected to the main computer. The operation software, programmed using Matlab, adjusts parameter setting of each system, and commands those instruments and the RF switch. The system specifications are summarized in Table 6.1.

The demonstrator operates at the center frequency of 9.65GHz with the signal bandwidth of 300MHz and the IF band specified within 50MHz and 350MHz. To digitize the IF signal, in principle a sampling rate higher than 700MHz is required. However, the implemented system
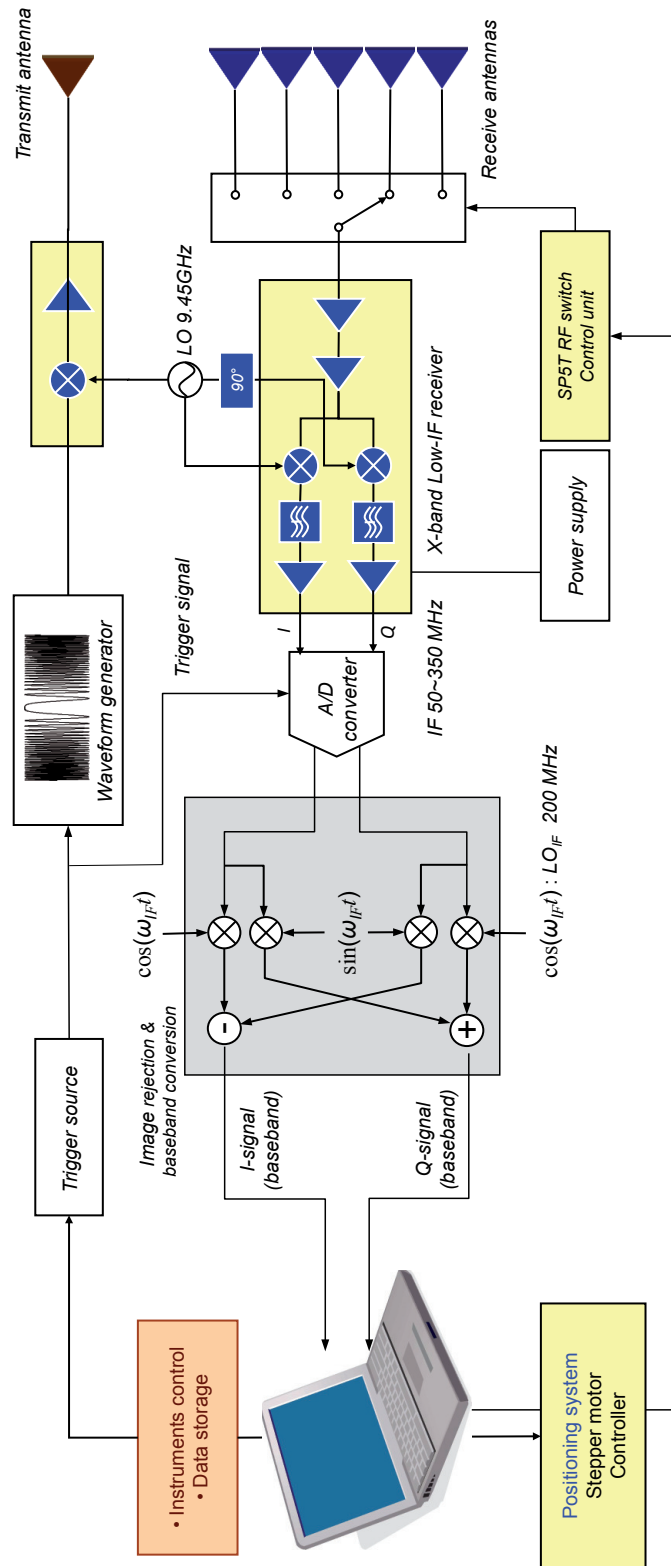
Figure 6.1.: Block diagram of the GB multichannel SAR demonstrator.
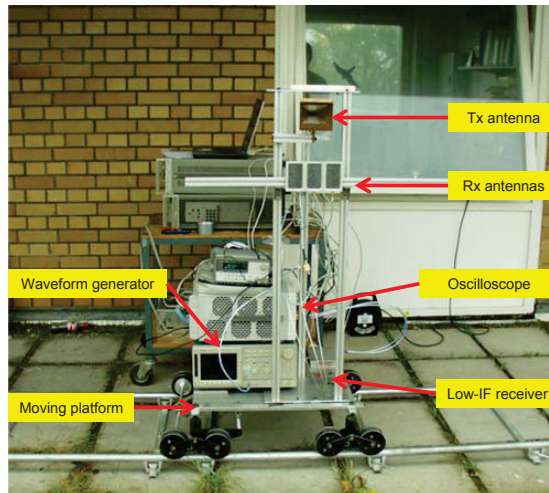
Figure 6.2.: GB multichannel SAR demonstrator assembled with a stepper motor and gears for moving the platform and external instruments for a test.

Table 6.1.: Specifications of the GB multichannel SAR system.

Parameter	Symbol	Value	Parameter	Symbol	Value
center frequency	f_c	9.65GHz	bandwidth	f_o	300MHz
pulse length	T_p	1 μsec	Rx window		2 μsec
noise figure	NF	4.65dB	SFDR		49.5dB
No. of Tx	M_T	1	No. of Rx	M_R	5
Tx power	P_T	max 19dBm	sampling rate	f_s	1.067GHz

is disturbed by a strong interference at 420MHz[1]. To filter it out, the sampling frequency is increased up to 1.067GHz. With the higher sampling rate, the overlapping of the interference with the baseband signal after the digitization is avoided. The receiver *Noise Figure* (NF) of 4.65dB is achieved in this system due to the 3dB insertion loss in the SP5T RF switch and the coaxial cables, connecting the receive antennas and the RF switch. The *Spurious Free Dynamic Range* (SFDR)[2] of 49.5dB is achieved without any gain control blocks, such as *Automatic Gain Control* (AGC) devices. At the early design stage, several types of receiver topologies were evaluated in terms of the SFDR for a given design condition, and among these, the Low-IF topology provided the best SFDR [47]. Therefore the demonstrator is equipped with the Low-IF receiver. The chirp signal length and the data acquisition time are set to 1μsec and 2μsec respectively, considering the short-range geometry of GB measurements.

6.2. SAR Data Acquisition

A notable feature of this system is the use of a single receiver for all receive subarrays. The transmitter sends the generated chirp pulse, and the SP5T RF switch subsequently activates the receive subarrays at each transmission event one after another. Hence a measurement cycle is

---

[1]If the signal is sampled with 700MHz, this interference is folded back into the baseband (aliasing) and cannot be filtered out.

[2]SFDR is defined as a difference between the minimum detectable signal power level and the third-order interception point (IP3) of a receiver [103].

117

completed after five transmission and reception events in one position. Afterwards, the sensor moves to the next position and repeats the data acquisition. This acquisition mode is only valid for temporally invariant channels with stationary targets. Figure 6.3 shows the time diagram of command sequences in the case of three receive antennas for the acquisition of data.
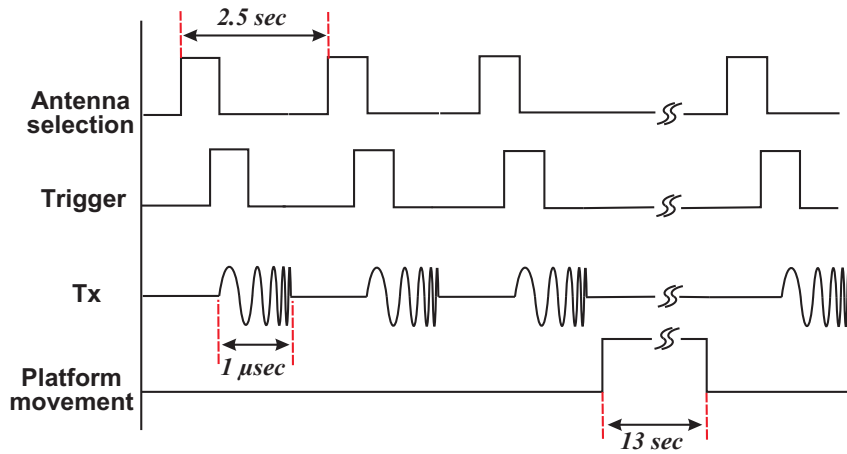
Figure 6.3.: Command sequences and operation timing of the GB SAR demonstrator in the case of three receive antennas.

First of all, a receive subarray is selected by the RF switch controller, and then a trigger source signal activates the synchronized waveform generator and the oscilloscope, which enables the data acquisition. The transmitter sends a chirp pulse, and the activated receive subarray acquires reflected signals during the time window of 2μsec. This data acquisition is repeated for the other receive subarrays every 2.5sec, including a guard interval, to ensure the data storage and the data transfer from the oscilloscope to the main computer. After a complete measurement cycle, the platform slowly moves to the next position, in order to avoid any vibration of the antenna holder.

6.3. Antenna Subsystem

During the acquisition period, undesired signals, such as the nadir echo and the signal coupled from the transmit antenna, are captured by the subarray, as illustrated in Figure 6.4. In short range radar measurements, these signals cause considerable interference in the measured data, since these signals overlap the desired signal and cannot be easily separated. Regarding the interference, the antenna subsystem is designed with an aim to minimize its side lobes and focus on the target area.

6.3.1. Transmit Antenna: Corrugated Pyramidal Horn Antenna

This demonstrator employs a pyramidal horn antenna for transmission, due to its high gain and the ease of excitation over broadband signal through a waveguide. The feed waveguide is flared to produce a narrow beam in both E- and H-planes. The pyramidal horn antenna has the uniform field distribution in E-plane, so that it causes the typical side lobe level of -13dB. On the other hand, in an optimal design with a cosine-tapered field distribution, this antenna has no side lobes in H-plane [116]. This is a positive aspect of the pyramidal horn for the GB
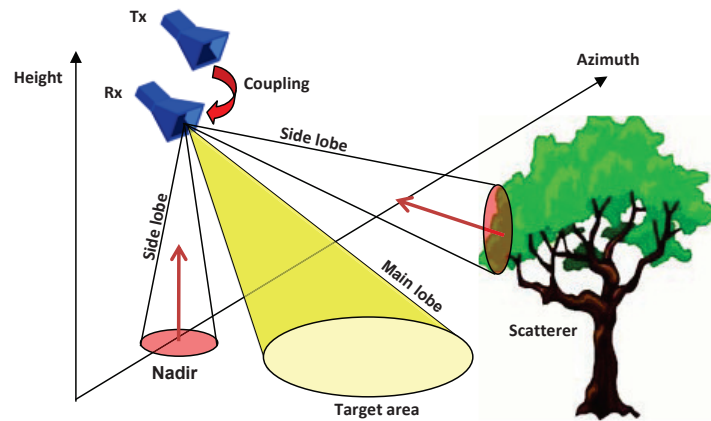
Figure 6.4.: Consideration of interferences in the ground-based SAR measurement.
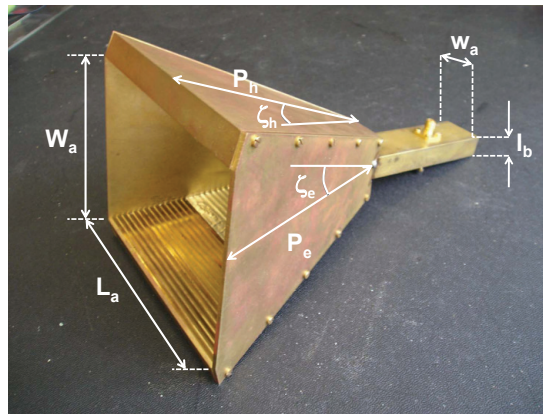
Figure 6.5.: Implemented corrugated horn antenna with its geometric parameters.

Table 6.2.: Geometric parameters of the corrugated horn antenna.

Parameter	Value	Parameter	Value
w_a	0.26 cm	l_b	0.13 cm
L_a	12 cm	W_a	9 cm
ξ_h	20°	ξ_e	16°
P_h	12.3 cm	P_e	12.3 cm

measurement. To reduce the side lobes in E-plane, the inner surface of the horn is corrugated. Therefore the surface currents of the corrugated wall are destructively interfered with each other, leading to the significant reduction of the electric field strength near the surface [11].

The built corrugated horn antenna is shown in Figure 6.5. The corrugations are implemented on surfaces perpendicular to the electric field vectors. The geometric parameters of the antenna are determined, in regard to the specified radiation patterns which were required to illuminate the area of interest. Table 6.2 summarizes the geometric parameters of the implemented corrugated horn antenna [95]. The aperture size $W_s \times L_a$ is calculated from the relationship between the feed waveguide size $a \times b$ and the flare angles, ξ_e and ξ_h.

Radiation Characteristics

The measured radiation patterns are plotted in Figure 6.6 and listed in Table 6.3. The E-plane pattern shows that the implemented corrugation suppresses the side lobes by up to 18.9dB. As mentioned before, the H-plane pattern presents no side lobes since the tangential component of the electric field on the inner metal surface perpendicular to the H-plane is zero, according to the electrostatic boundary conditions [11].

Table 6.3.: Radiation characteristics of Tx horn antenna [95]

Parameter	E-plane	H-plane
HPBW	21.5°	19.5°
peak side lobe	-18.9dB	none
Gain	18.2 - 18.8dBi	

The measured gain of the antenna varies from 18.2 to 18.8dBi over the signal bandwidth, which means 0.6dB fluctuation. This gain variation results from the electrical aperture size change, which is inversely proportional to the wavelength. The measured 3dB beamwidth at the center frequency, 9.65GHz, is 21.5° and 19.5° in E-plane and H-plane respectively.

(a) E-plane   (b) H-plane
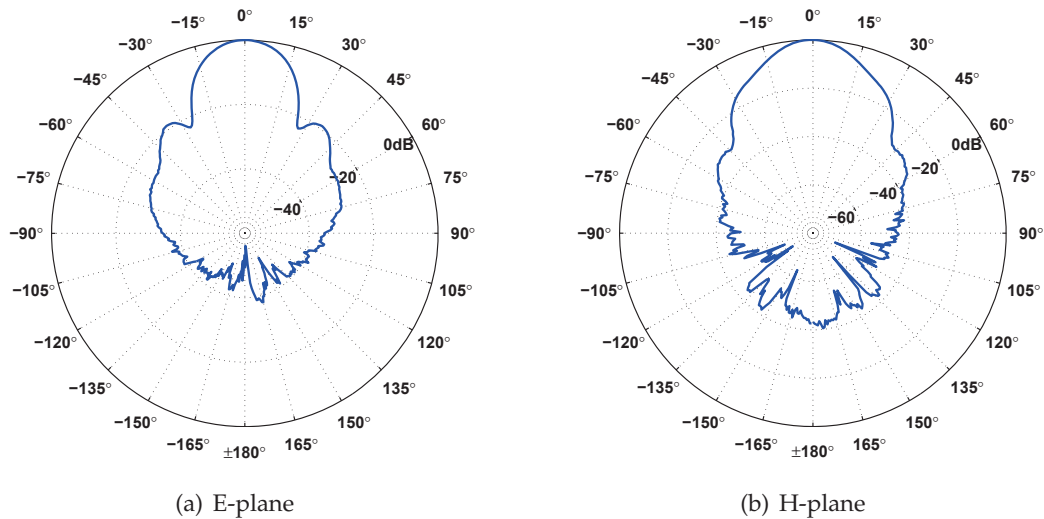
Figure 6.6.: Measured radiation patterns of the implemented corrugated horn antenna at the center frequency of 9.65GHz.

Return Loss

The operation bandwidth of an antenna is commonly defined by the frequency range where the return loss[3] is better than -10dB. To improve the antenna efficiency, the design goal in terms of the return loss is set to be better than -15dB over the system bandwidth (9.5-9.8GHz) and is achieved by adjusting tuning screws of the feed waveguide. The measured result meets the desired specification, as shown in Figure 6.7. Within system bandwidth, the return loss level is below -18dB with its minimum of -28.3dB at 9.6GHz.

---

[3]The return loss is also defined by S_{11} of the S parameters. To avoid any confusion with other symbols in this dissertation, only the term "return loss" will be only used.
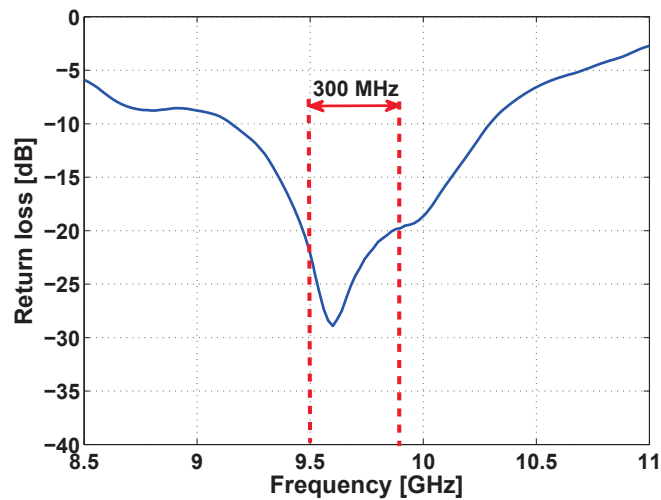
Figure 6.7.: Measured return loss of the corrugated horn antenna.

6.3.2. Receive Antenna: Microstrip Patch Array

As aforementioned in Chapter 5, design of receive antennas is closely related to the AASR performance, since the length of the receive antennas corresponds to an effective spatial sampling distance in the case of a linear uniform array (see section 5.1.1). Using the implemented transmit horn antenna, a virtual two-way antenna pattern is calculated, and thereby the AASR is estimated.

Array Geometry

For the reception, microstrip patch arrays, based on the aperture-coupling technique, are implemented. In this antenna structure, patch elements and a feed network are geometrically isolated, yet electrically coupled through rectangular slot arrays on the ground plane. The array geometry is illustrated in Figure 6.8. The array consists of 4×2 rectangular patch elements below the upper substrate Rogers RT5880 with the dielectric constant ϵ_r of 2.2 and the thickness of 0.508mm. The same substrate is also used for the microstrip feed network. To achieve 300MHz bandwidth, a Rohacell foam with the thickness of 2.2mm is inserted between the patch array and the ground plane. The patch length is preliminarily selected to be 140% of the theoretical patch length for the purpose of increasing the radiation efficiency. The single element of the array is optimized by electromagnetic field simulations using CST Microwave Studio. The optimized geometries of a single element are listed in Table 6.4.

Four patch elements are arranged in the E-plane with a separation of 21.756mm from the patch center to center, and the two elements are arrayed in the H-plane in the same manner. The parallel feed network distributes signals to each radiation element. To reduce the side lobes and meet the design specification, the feed network is tapered by the cosine amplitude window in E-plane. The current intensity ratio, normalized by the maximum incoming to the radiation elements, is [0.71, 1, 1, 0.71]. The resulting antenna array is 100.91mm in length, 61.436mm in width and vertically polarized. Figure 6.9 shows the realized Rx array.

Patch substrate
Rogers RT5880
Thickness 0.508 mm
$\varepsilon_r = 2.2$

4X2 patch array

Rohacell
Thickness 2.2 mm
$\varepsilon_r = 1.05$

Coupling slot

Ground plane

Feeding network substrate
Rogers RT5880
Thickness 0.508 mm
$\varepsilon_r = 2.2$

Feeding network
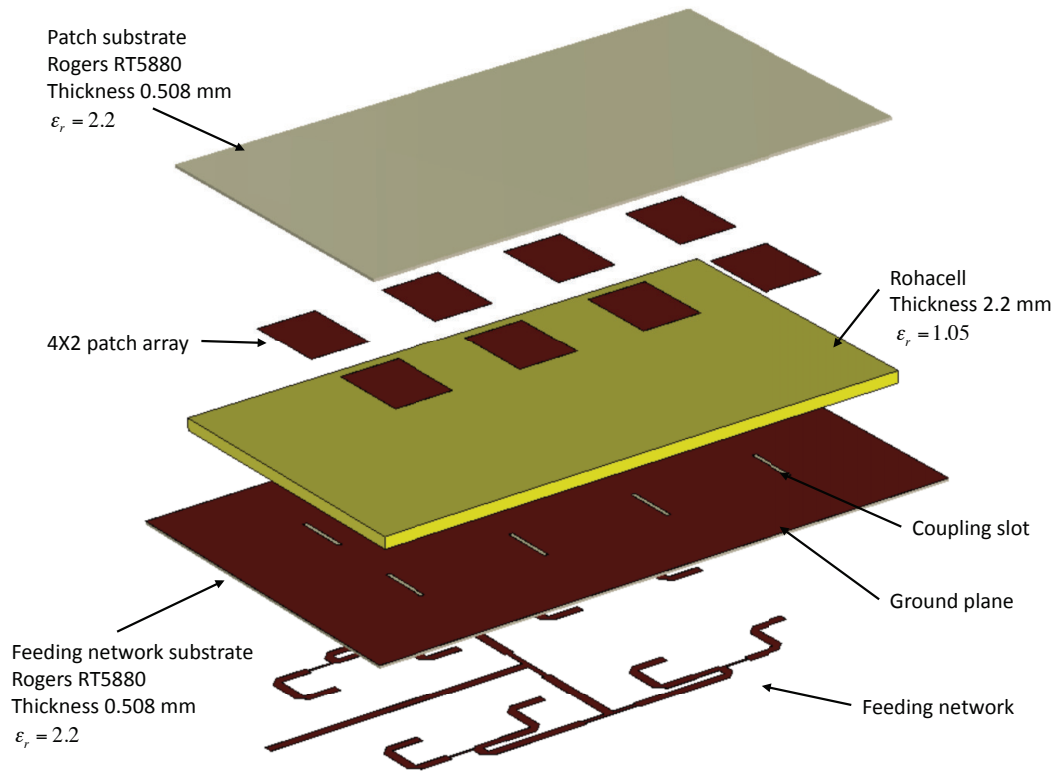
Figure 6.8.: Geometry of the aperture-coupled microstrip patch array for the reception.

Table 6.4.: Geometric parameters of a single element.

Parameter		Value
patch dimension	length	14.14mm
	width	10.1mm
slot dimension	length	9.168mm
	width	0.7mm
50Ω line width		1.585mm

The microstrip patch array is combined with an aluminium frame and a reflector to reduce its back radiation. The aluminium frame shields the array and sustains the multilayered structure of the array. The implemented antennas are equipped with the flexible antenna holder. The corrugated horn antenna and the microstrip subarrays compose the antenna constellation for the MIMO SAR experiment. Figure 6.10 shows the photos of these antennas, mounted on the antenna holder.
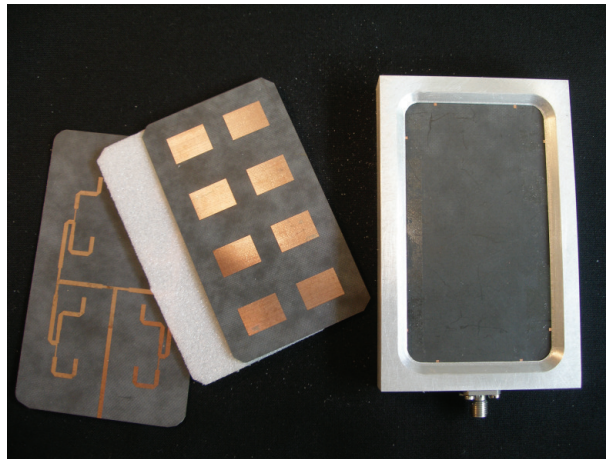
Figure 6.9.: Photo of each layer of the implemented microstrip patch array (left) and the complete subarray combined with an aluminium shield (right).

(a) front view

(b) side view

Figure 6.10.: Transmit antenna and receive array combined with the antenna holder for the side-looking SAR measurement.

Radiation Characteristics

The radiation pattern of each subarray is characterized in both E- and H-planes. The measured patterns of all arrays are plotted in Figure 6.3.2. The measurements present quasi-identical radiation characteristics for all antennas. In E-plane, the cosine amplitude taper suppresses the side lobes by 19dB in the worst case. The aluminum shield minimizes the back radiation effect from the coupling slot. It is observable that the beamwidth in H-plane is wider than that of the transmit antenna, while the E-plane beamwidth is analogous to the transmit antenna case.

Table 6.5.: Radiation characteristics of the microstrip patch arrays.

Parameter	E-plane	H-plane
HPBW	19°	36.5°
peak side lobe	-19.4dB	-20.3dB
Gain	14 - 14.3dBi	
cross-pol. level	-23.7dB	-27.7dB

The GB SAR antennas contain the vertical polarization characteristic. The polarization purity of an antenna is characterized by measuring its cross-polarization level. The implemented microstrip antennas provide the cross-polarization level of -23.7dB and -27.7dB in the E- and the H-plane respectively. Average radiation characteristics of the arrays are summarized in Table 6.5.

(a) E-plane, Nr.1

(b) H-plane, Nr.1

(c) E-plane, Nr.2

(d) H-plane, Nr.2

(e) E-plane, Nr.3

(f) H-plane, Nr.3

(g) E-plane, Nr.4

(h) H-plane, Nr.4

(i) E-plane, Nr.5

(j) H-plane, Nr.5
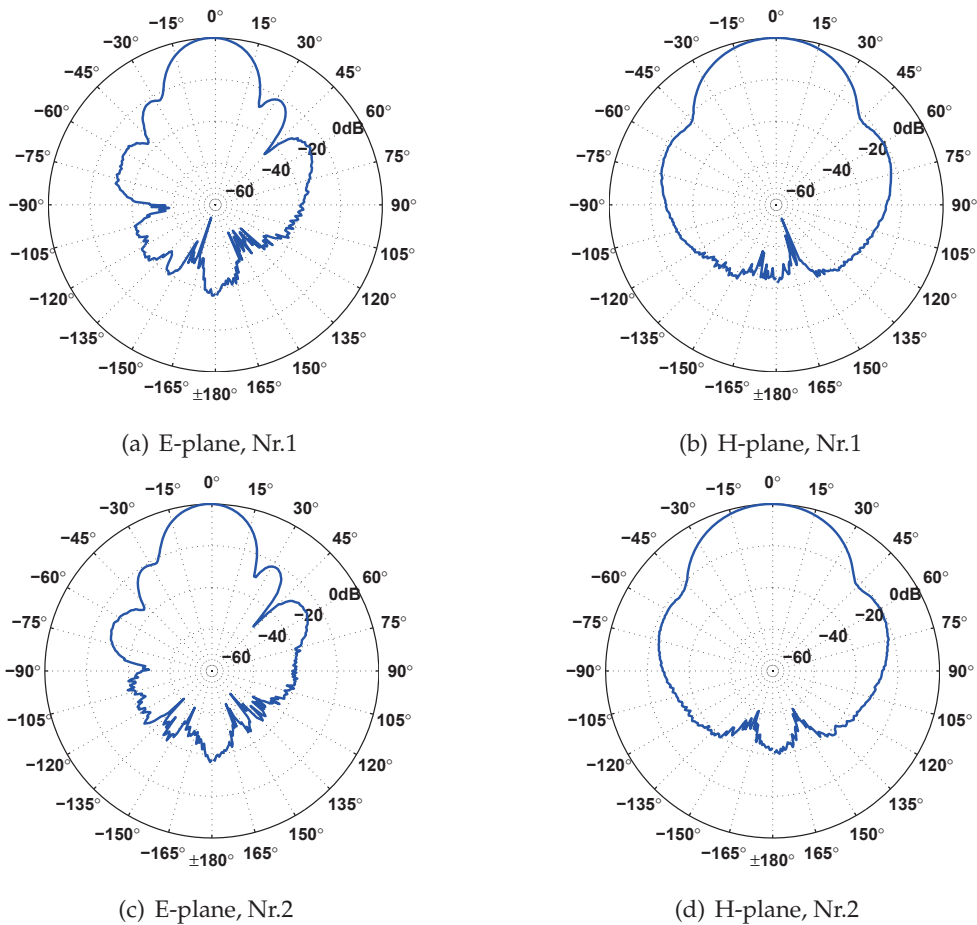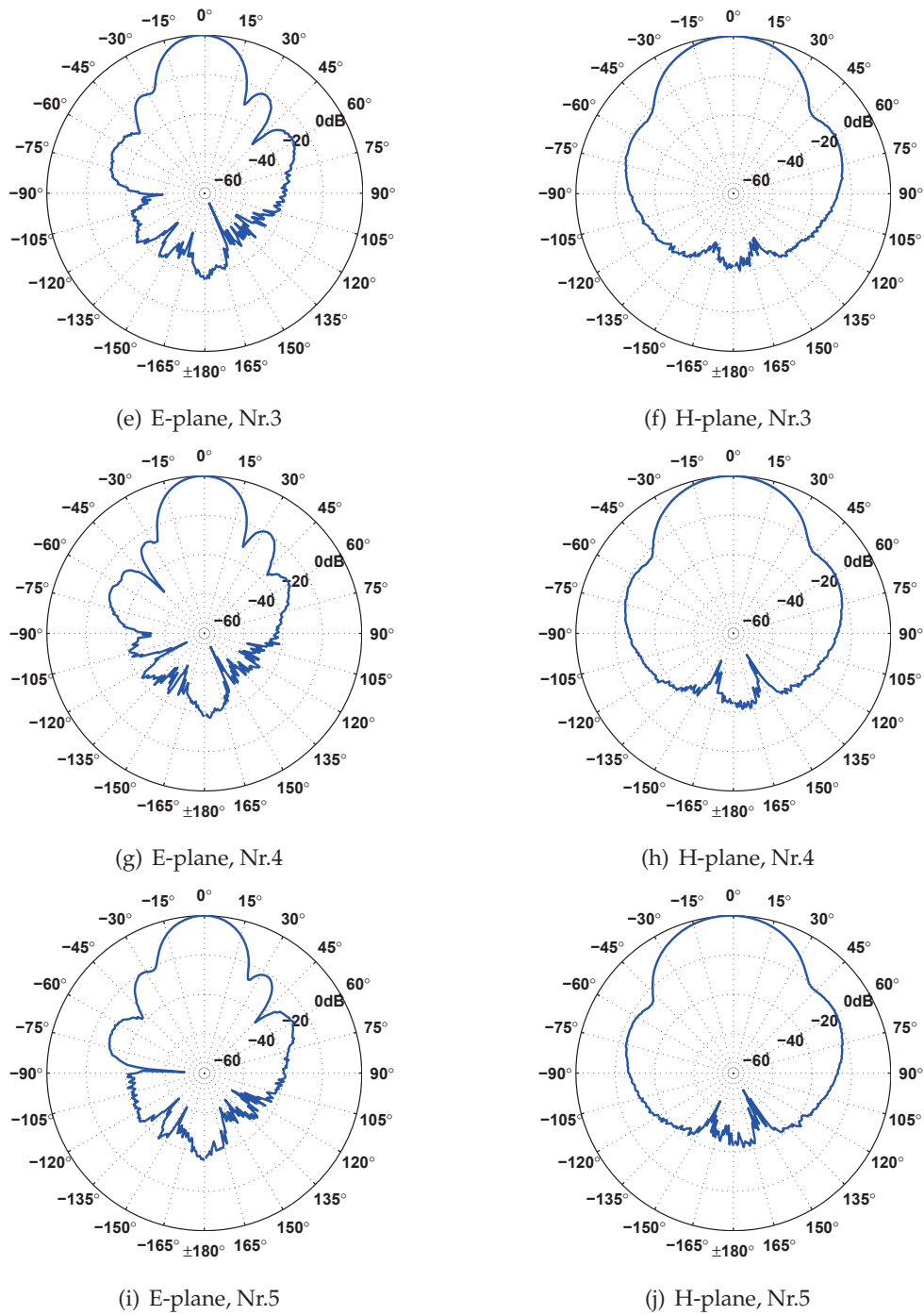
Figure 6.11.: Measured radiation patterns of all implemented microstrip array antennas at 9.65GHz.

Return Loss

In the microstrip patch antennas, increasing the distance between the patch and ground plane, as well as using a lower permittivity of substrate, improves the antenna bandwidth [48]. The inserted Rohacell foam therefore contributes to the bandwidth improvement in this antenna. The return loss of each implemented microstrip patch array is measured in the integration with

the aluminium frame. Figure 6.12 shows the measured return loss of the microstrip patch array. The return loss is optimized at around 9.5GHz but not at the center frequency of 9.65GHz. A possible reason for this shift is the changing in reactance from the aluminum shield at the array input port. Nevertheless, the return loss meets the required value over the signal bandwidth of interest.
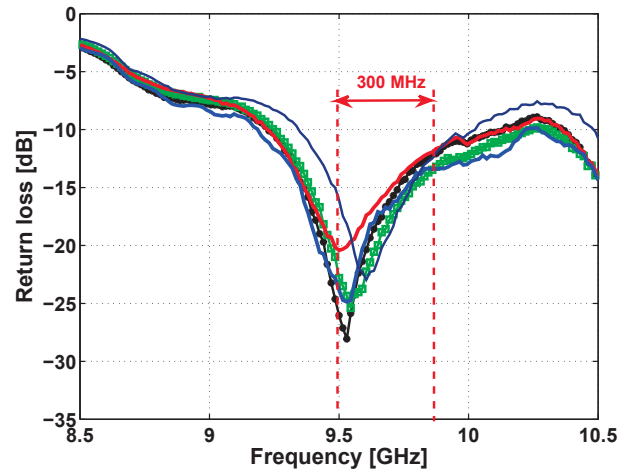
Figure 6.12.: Measured return loss of all arrays.

6.4. Transceiver Subsystem

The transceiver subsystem in the demonstrator is responsible for the chirp signal generation, the signal conversion, the amplification and finally, the digitization. This subsystem is divided into the RF and the digital parts, depending on signal frequencies. The RF part is implemented using mostly commercial components and the digital part is composed of several digital instruments. This section considers the transceiver subsystem in more detail. In particular, the Low-IF receiver is highlighted.

6.4.1. Transmitter

The block diagram of the transmitter is illustrated in Figure 6.13. The transmitter is simply implemented using an Arbitrary Waveform Generator instrument, AWG710 from Tektronix, based on the DDS technique. The chirp signal is generated at the IF band which its center frequency is 200MHz, and then converted to the carrier frequency of 9.65GHz. Before the antenna, the high power amplifier pulls the signal power up to the maximum 19dBm.

An image rejection filter is usually needed in order to suppress the image frequencies resulting from the real signal multiplication. However, in this transceiver, the image rejection is carried out by digital processing on receive. Thus, no image rejection filter is used in this transmitter. Detailed principles will be encountered in the next section and in Appendix F. A chirp waveform with specific parameters is pre-programmed and stored in AWG710 as a source file. The waveform has the maximum $0.25n$sec in time (4GHz sampling rate) and 8bits vertical (amplitude) resolution. The AWG710 recalls the stored waveform function and generates it when a
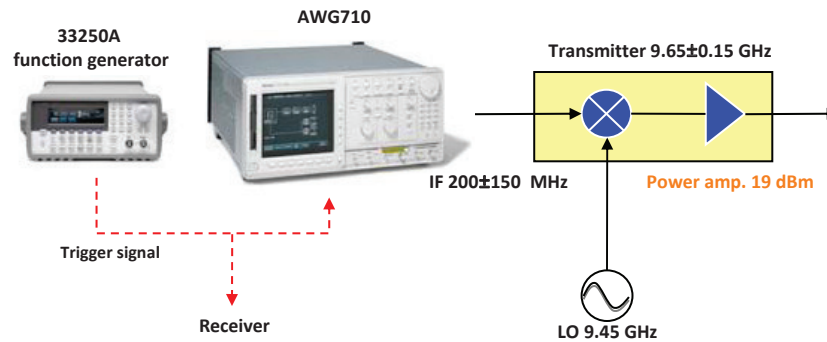
Figure 6.13.: Transmitter configuration.

trigger command impinges on. The transmit signal amplitude can vary from 200mV to 2V with 50Ω input impedance. The most important point here is the coherence between the transmitter and the receiver. For this purpose, the AWG710 is also synchronized with other instruments using the 10MHz reference clock and an external trigger source is used to activate all instruments simultaneously.

6.4.2. Receiver

The main feature of the receiver is the employment of the Low-IF topology, which is a combination of the heterodyne and the homodyne receiver topology. The transmitter always generates a double-sideband signal, since there is no I-Q modulator included. Therefore the image band[4] is unavoidable and must be suppressed on receive. A typical approach is to filter the image band out at the RF stage. However, the signal bandwidth of the demonstrator, 300MHz, is only 3.1% of the carrier frequency (9.65GHz). Thus a narrow band image rejection filter is required. Such a narrow band filter suffers from a high Q-factor (Quality factor) and a large insertion loss [124]. In the Low-IF receiver, the image band rejection is carried out at either the IF band or the baseband [28]. Therefore specification of the image rejection filter is alleviated or not even needed at all. For this reason, the Low-IF topology simultaneously improves the selectivity and sensitivity of the receiver.

Low-IF Receiver Principles and Configuration

The Low-IF receiver is based on the heterodyne type of conversion, which means a double-stage down-conversion. Depending on filter types, there are two possible approaches in the implementation of the Low-IF receiver. One is to directly use polyphase IF band pass filters[5], and the other is to implement a set of parallel I-Q demodulators at the final baseband conversion. In the former approach, after the first I-Q demodulation, only the desired IF band signal is

---

[4]The term, "image band", means one of the sidebands resulting from the signal conversion by the mixer. Depending on the local signal frequency, the upper or the lower sideband is regarded as the image band. In some literatures, the image band is also called the mirror band.

[5]The polyphase filter is also called complex signal filter because it filters only the positive frequency band or the negative frequency band of a real signal, while the real signal filter operates symmetrically in both bands.

selected by the polyphase filters suppressing the image and then the final baseband conversion is carried out by the second I-Q demodulator in digital domain. In the latter approach, real band pass filters can be employed instead of the polyphase filters, but the set of parallel I-Q demodulators realizes complex signal filtering in order to remove the image. In the demonstrator, the latter method is chosen since the receiver can be realized using commercial devices at the desired IF band (50-350MHz).

(a) RF spectrum

(b) IF spectrum

(c) Baseband spectrum
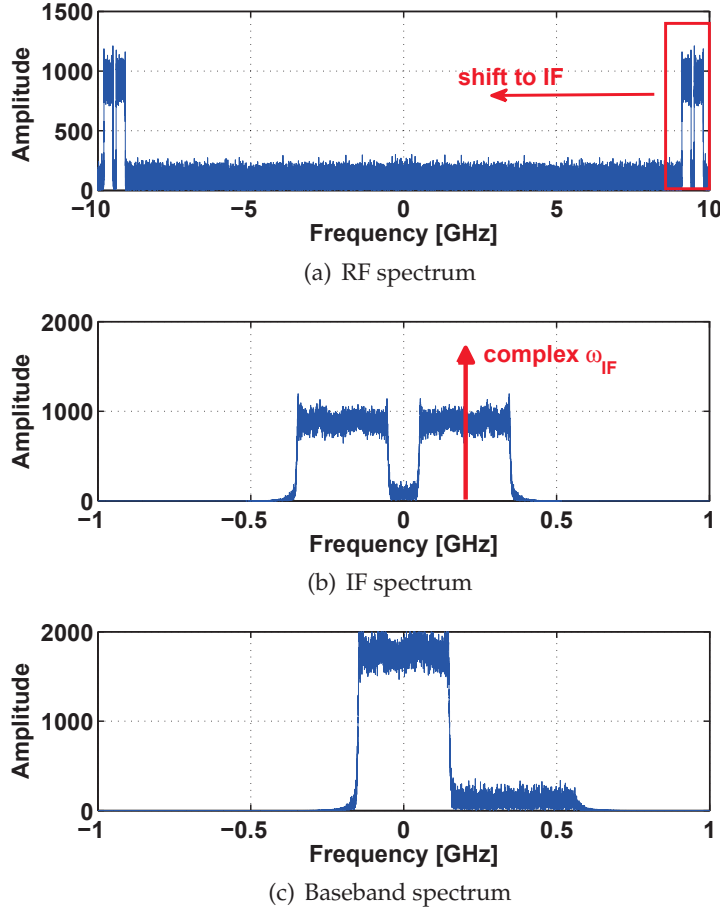
Figure 6.14.: Principle of baseband conversion through two-stage demodulations using complex local signals in the Low-IF topology.

The Low-IF receiver structure is derived from the complex signal theory discussed in [85]. Figure 6.14 (a) shows a real RF signal spectrum consisting of both the positive and negative frequency bands. The first I-Q mixer shifts the positive frequency bands close to the baseband, which is the very *Low-IF* band obtained through the complex LO signal mixing. At this stage, the IF band signal is filtered by two real LPFs in the block diagram, and then multiplied by the second complex LO signal as Figure 6.14 (b) shows. Following this, the resulting baseband is also presented by a simple shift of the IF bands, as shown in Figure 6.14 (c). Eventually, the image band is canceled out during the complex signal multiplication.

The procedure in Figure 6.14 is described by a simple multiplication of a real RF signal input $s(t)$, and the cascade complex local signal, $x_{Lo}(t)$ and $x_{IF}(t)$:

$$s_b(t) = s(t) \cdot x_{Lo}(t) \cdot x_{IF}(t) \tag{6.1}$$
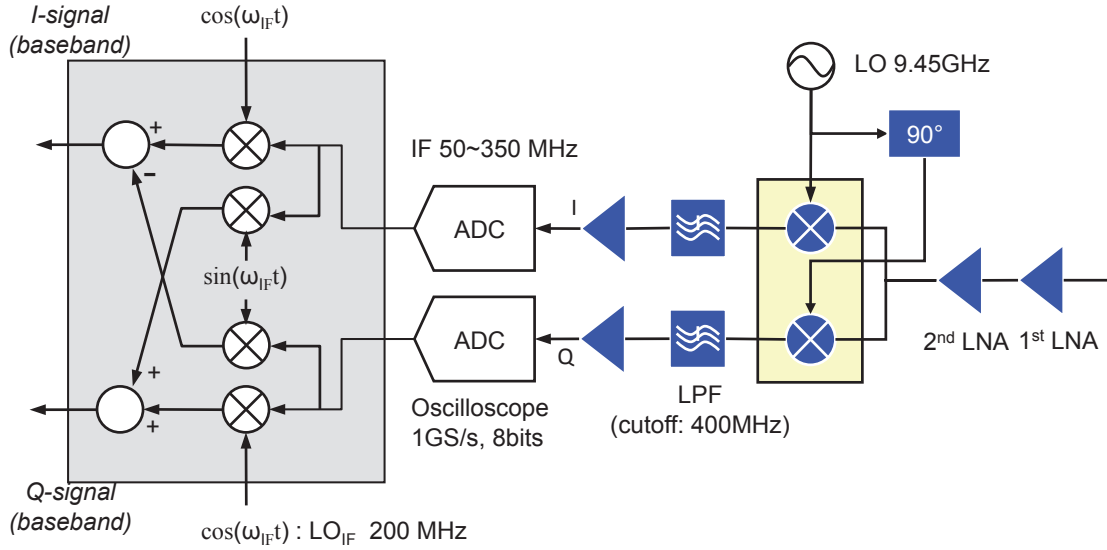
Figure 6.15.: Block diagram of the implemented Low-IF receiver. Actual implementation of digital I-Q demodulation following the ADC is realized in software.

where $x_{Lo}(t)$ and $x_{IF}(t)$ are given by

$$x_{Lo}(t) = \exp(j2\pi \cdot f_{Lo} \cdot t), \tag{6.2}$$
$$x_{IF}(t) = \exp(j2\pi \cdot f_{IF} \cdot t) \tag{6.3}$$

where f_{Lo} and f_{IF} denote the first and the second LO oscillator frequency respectively. The complex signal multiplication is implemented through multiple real signal mixing [28, 85]. Using Euler's identity, the complex local signal is expanded as follows:

$$
\begin{aligned}
x_{Lo}(t) \cdot x_{IF}(t) &= \exp(j2\pi \cdot f_{Lo} \cdot t) \cdot \exp(j2\pi \cdot f_{IF} \cdot t) \\
&= (\cos(2\pi \cdot f_{Lo} \cdot t) + j\sin(2\pi \cdot f_{Lo} \cdot t)) \cdot (\cos(2\pi \cdot f_{IF} \cdot t) + j\sin(2\pi \cdot f_{IF} \cdot t)) \\
&= (\cos(2\pi \cdot f_{Lo} \cdot t) \cdot \cos(2\pi \cdot f_{IF} \cdot t) - \sin(2\pi \cdot f_{Lo} \cdot t) \cdot \sin(2\pi \cdot f_{IF} \cdot t)) + \\
&\quad j\,(\cos(2\pi \cdot f_{Lo} \cdot t) \cdot \sin(2\pi \cdot f_{IF} \cdot t) + \sin(2\pi \cdot f_{Lo} \cdot t) \cdot \cos(2\pi \cdot f_{IF} \cdot t)).
\end{aligned}
\tag{6.4}
$$

The Low-IF receiver structure is designed according to (6.4). Its configuration is shown in Figure 6.15. The RF signal is amplified by LNA and converted to the IF band, centered at 200MHz. The real LPF selects the IF band signal at each channel, and the drive amplifier improves the signal strength. The IF signal is digitized after the IF amplifiers and the final down-conversion is implemented digitally. Detailed formulations of the image rejection in this architecture are described in Appendix F.

Implementation

The Low-IF receiver is implemented on the basis of the multilayer technology, as shown in Figure 6.16. The substrate Rogers4004 with the dielectric constant ϵ_r of 3.38 is used for the RF layer and is isolated from other DC signal networks.
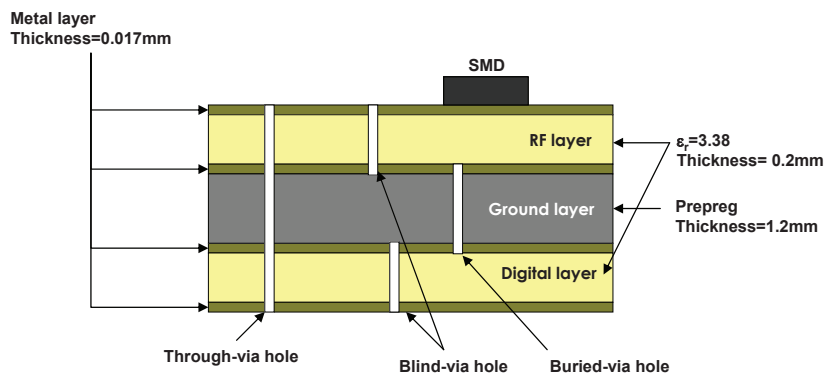
Figure 6.16.: The multilayer structure used in the receiver implementation.

Digital signal layers are located under the ground layer in order to minimize the interference between the RF and digital signals. All RF components and DC bias circuits are mounted on the upper layer and the analogue signal is transferred through *Grounded Coplanar Wave Guide* (GCPW) on the same layer. The ground layers are electrically connected by three different types of via holes: through-via holes, blind-via and buried-via. The implemented Low-IF receiver before ADC is exhibited in Figure 6.17.
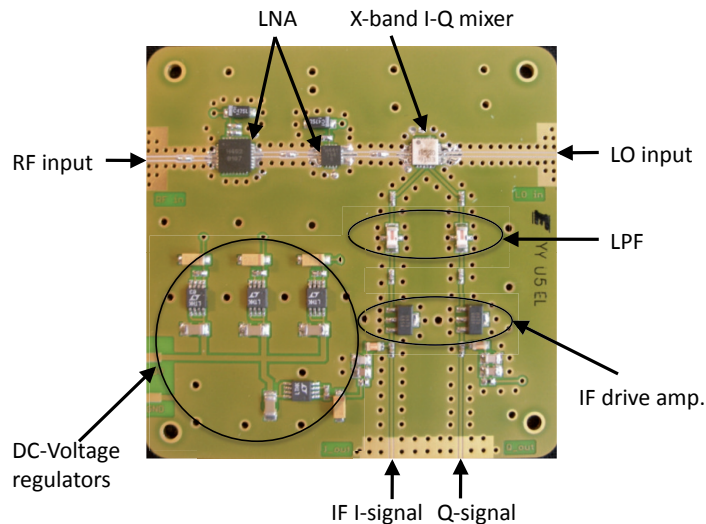
Figure 6.17.: RF and IF sections of the implemented Low-IF receiver. All components are mounted on the RF layer. The GCPW RF transmission line is surrounded by densely implemented blind-via holes, in order to block the leakage of analog signals.

The Low-IF receiver is shielded by an aluminium frame, along with the SP5T RF switch and its control circuit as shown in Figure 6.18. The digital SP5T switch controller is isolated from the Low-IF receiver by the aluminium housing as well. The switch controller receives three bits TTL signal from the main computer through the parallel port, and thus selects an operating channel.
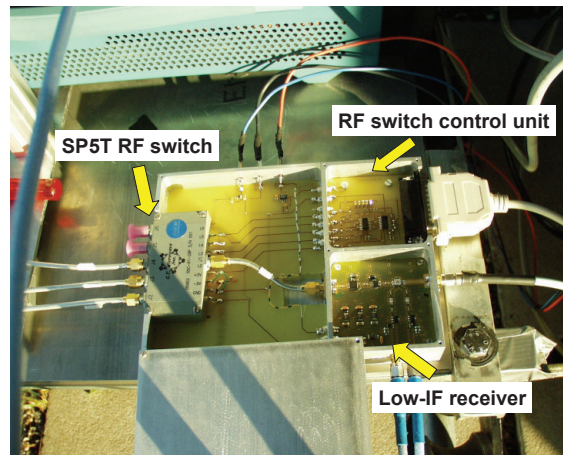
Figure 6.18.: Deployed Low-IF receiver and SP5T RF switch with its control unit.

Evaluation

The image rejection performance of the implemented Low-IF architecture strongly depends on the I-Q channel balance [85, 83, 28, 133]. The gain and phase imbalances between I-Q channels are defined as

$$\Delta A = \frac{|Q(t)|}{|I(t)|}, \tag{6.5}$$

$$\Delta \phi = \angle I(t) - \angle Q(t) - \frac{\pi}{2} \tag{6.6}$$

where $I(t)$ and $Q(t)$ denote the IF band signals of I- and Q-channels respectively. The I-Q channel imbalances are measured over the system bandwidth and plotted in Figure 6.19.

(a) Gain imbalance
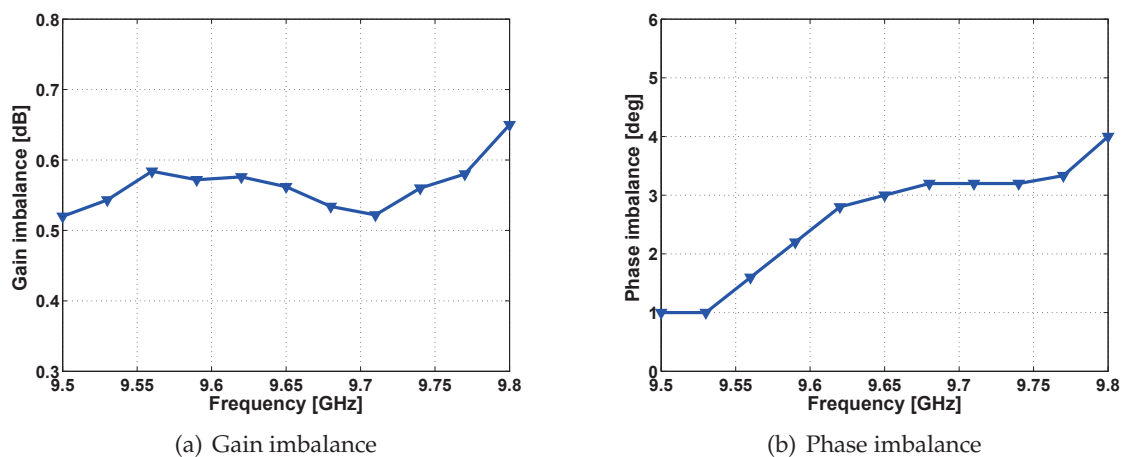
(b) Phase imbalance

Figure 6.19.: Measured gain and phase imbalance of the implemented Low-IF receiver.

The gain imbalance reaches the maximum of 0.65dB, and the phase imbalance increases up to 4 degrees at the highest frequency (9.8GHz). Unfortunately, it is relatively tough to measure

the residual image power. Consequently this work estimates the image rejection performance using the analytic signal model presented in [133]. The model used in this work is derived in Appendix F. The implemented receiver may yield approximately 30dB image suppression.

To evaluate the implemented receiver performance, a single pulse experiment is carried out. The transmitter and the receiver are directly connected by a coaxial cable. A chirp signal with the given specification is used to measure the receiver performance. The obtained baseband spectrum of the single chirp pulse is shown in Figure 6.20. In the negative frequency, the residue of the desired signal and the image band signal is suppressed by approximately -27dB. This level is equivalent to the power level of image band signal within the baseband (see Appendix F). The negative band signal can be suppressed using a digital LPF. However, the image band signal in the baseband is not easily removed. To see its influence on SAR imaging, a cross-correlation function between the received chirp signal and the ideal chirp signal is compared to the optimum response, which is the auto-correlation function of the ideal chirp signal.
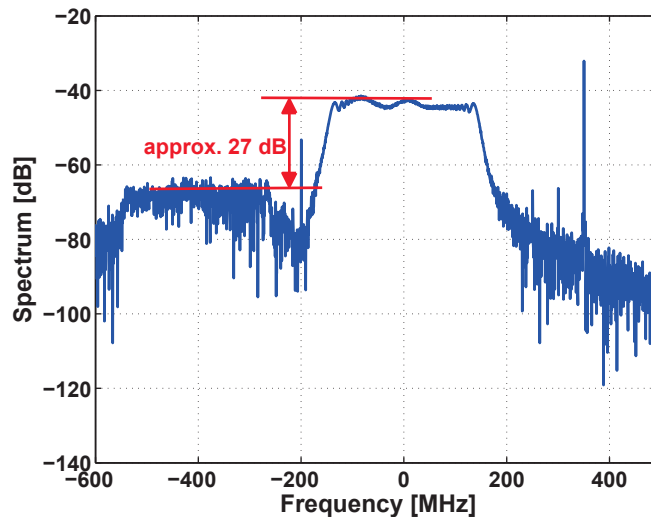
Figure 6.20.: Baseband spectrum of the single pulse experiment.

Figure 6.21 shows the ideal response and the experimental result in time domain. The 3dB width of the main lobes are 0.48m in both cases. Compared to the ideal response, the experimental result presents only the slight reduction of its peak value by 0.53dB and the asymmetric side lobes. In conclusion, the implemented receiver presents acceptable performance for the ground-based SAR experiment.

6.5. Platform and Operation Software

The developed subsystems and instruments are carried by a metallic platform which travels discretely along the rails set on the roof of a building. Considering the switching interval and data storage time, the platform stays at the fixed position during one measurement cycle[6]. This operation is easily achieved by employing a stepper motor. It must be noted that, since the PRF is not specified in this system, the travel length of the platform is only decided by the

---

[6]One measurement cycle is defined for the multiple data acquisition events equal to the number of the receive antennas. See section 6.2.
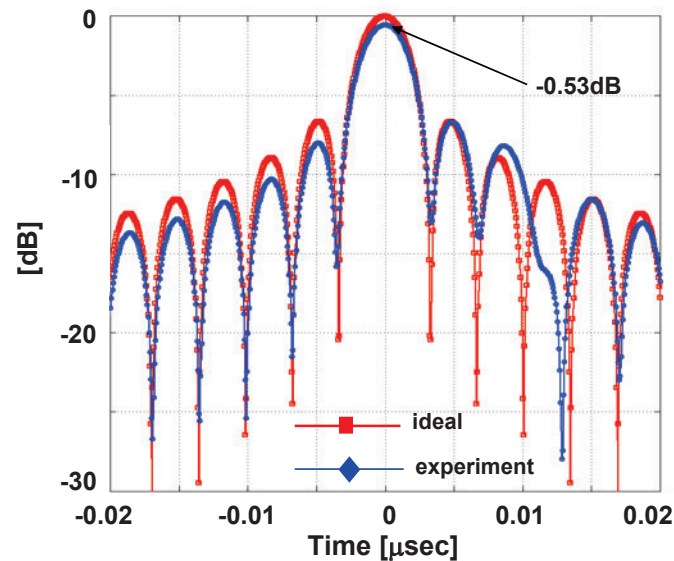
Figure 6.21.: Comparison of the ideal correlation response and the measurement.

spatial sampling distance. Hence it requires precise movement control. The stepper motor employed for the platform contains a 56:1 internal gear and rotates 360 degrees in 22400 steps. One rotation step leads to a movement of 0.1215mm in the case of the wheel diameter of 8.7cm used in the demonstrator.
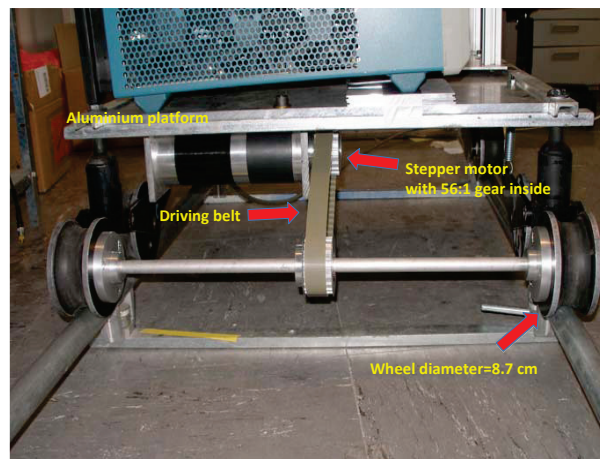
Figure 6.22.: Photo of the assembled stepper motor and gears for the moving platform

All instruments and subsystems are sophisticatedly controlled by the main operation software programmed using Matlab. The operation software consists of four major functions: the SAR parameter set-up, instrument control, raw data storage and transfer control, and platform operation. Figure 6.23 shows the instrument control, plus the SAR parameter set-up window of the software, as an example. The antenna configuration and SAR geometric parameters are specified through the *Graphic User Interface* (GUI) window and the other required parameters are at first computed. According to the parameters, the main software conducts all system operation. Refer to Figure 6.3 regarding the command sequence.
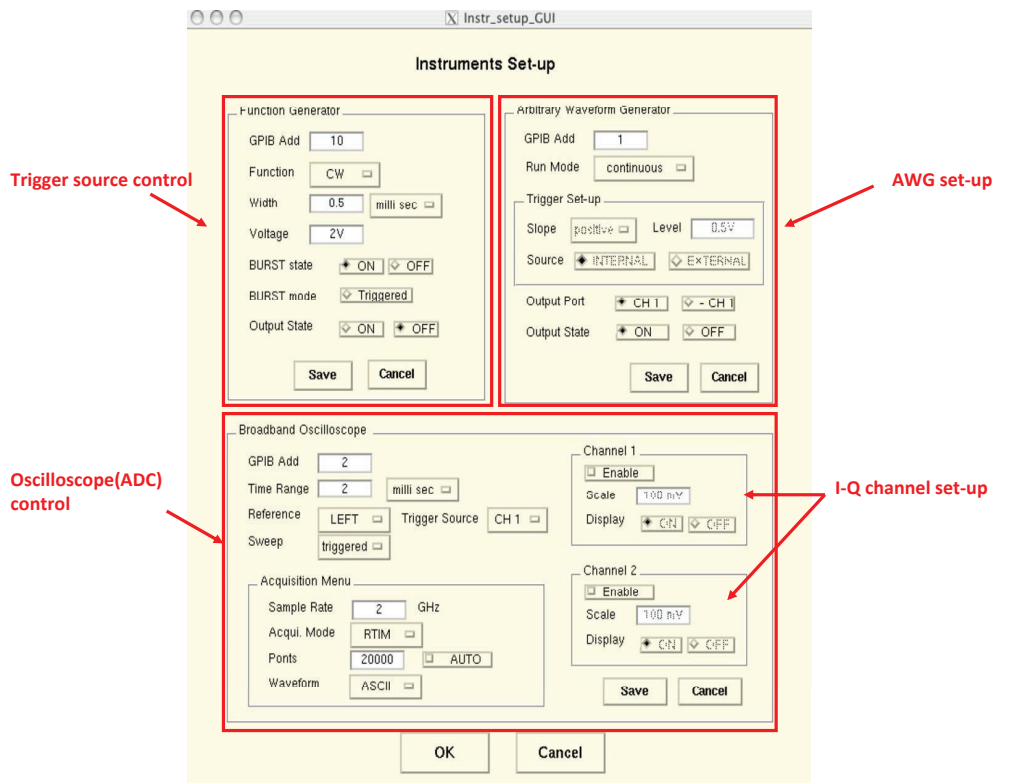
(a)
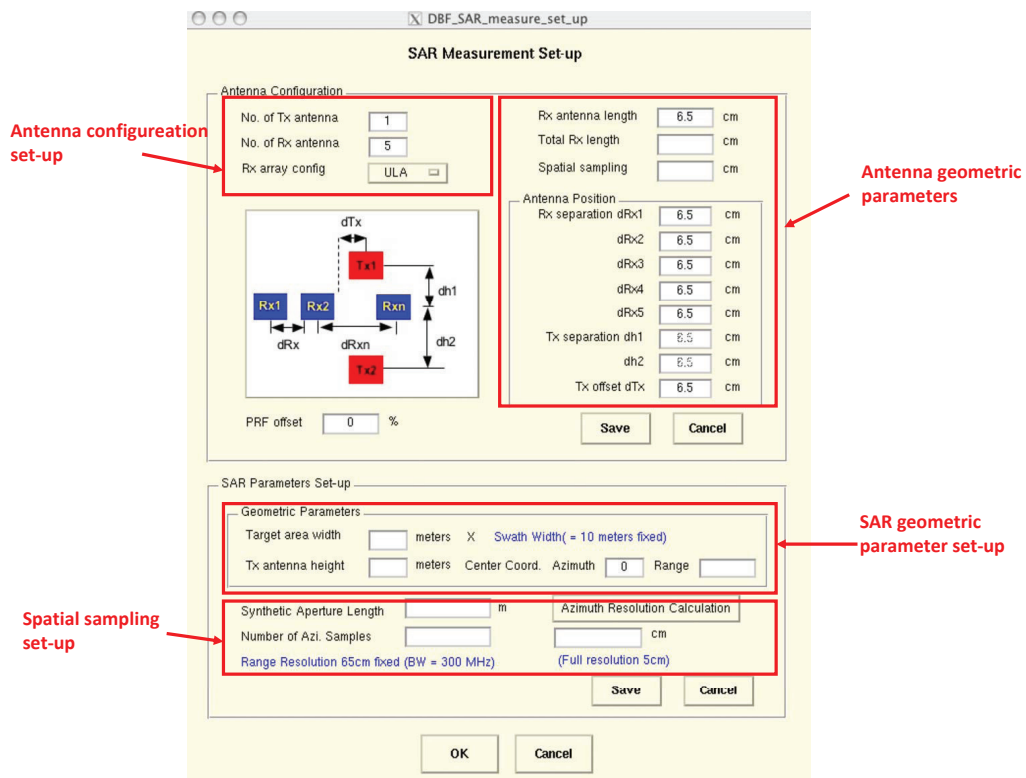
(b)

Figure 6.23.: GUI set-up windows for the instrument control (a) and the SAR geometric parameters (b).

7. Ground-Based Experiments for MIMO SAR Techniques

This chapter presents ground-based experiments of the MIMO techniques derived in prior chapters. In particular, the first laboratory demonstration of the DBF algorithm for the azimuth ambiguity suppression is carried out by this experiment. The GB SAR experiment is extended to the OFDM waveform scheme, so that the whole MIMO techniques are experimentally verified. The GB SAR demonstrator introduced in Chapter 6 is used for measuring multichannel SAR signals and from this data, hardware-related issues, such as a channel imbalance between the receive channels, are addressed. This experiment is aimed at the following main objectives:

- Demonstration of the DBF capability of the azimuth ambiguity suppression for the HRWS SAR imaging

- DBF performance evaluation for spatially uniform and non-uniform sampling

- Verification of the overall processing combined with the OFDM scheme and the DBF

This chapter starts with the development of an experimental MIMO SAR processor. Besides the SAR imaging module, this processor contains the digital beamformer, OFDM demodulator, channel balancing module, and post-processor for a residual phase error correction. Using this processor, the acquired GB SAR data are processed and evaluated. Section 7.2 presents the demonstration of the DBF for the uniform sampling. The experimental geometries and calibration results are shown in this section, and then the SAR imaging with the DBF is presented. The DBF performance for the non-uniform sampling is described in section 7.3 separately. Using the comparison between the processed images by the reconstruction algorithm and the spatial data interleaving, this work highlights the distinction of the reconstruction algorithm in the ambiguity suppression. Finally, section 7.4 describes the experiment for the OFDM waveform scheme. Due to the single transmission channel of the demonstrator, desired OFDM signals could not be acquired at the same time. In this experiment, the DBF SAR measurement data is converted to the equivalent OFDM data. Section 7.4 illustrates the detailed experiment procedures and results.

7.1. Experimental MIMO SAR Processor

For the GB SAR experiment, an experimental MIMO SAR processor is implemented. As pointed out in section 2.3, an important advantage of the MIMO SAR processing is that the DBF and the OFDM demodulation can be easily integrated to the conventional SAR processing algorithms. The MIMO SAR processor is modularized exploiting this aspect. This section gives an overview of the experimental SAR processor and briefly introduces the principle of the channel balancing technique, implemented for this experiment.

7.1.1. Overview

Figure 7.1 depicts the block diagram of implemented processor. The experimental processor is based on the $\omega - k$ SAR processing algorithm, which is known as the wavenumber domain

processor [113]. The OFDM demodulator, digital beamformer, channel balancing block and residual phase error correction block are properly integrated into the conventional SAR processor based on $\omega - k$ algorithm. These additional blocks are indicated by the circled number from ① to ⑤, and their functions are briefly described as follows.

① **OFDM demodulation block**

As introduced in Chapter 4, this module performs the circular-shift addition, the FFT in fast-time and the polyphase decomposition. The output signals at this module are the separated odd and even spectra of each receive channel data. This module is switched off for an experiment using the conventional chirp waveform.

② **Correction of frequency offset**

This module is used for the correction of the linear phase ramp in time-domain, resulting from the subcarrier offset. This module is switched off for an experiment using the conventional chirp waveform.

③ **Channel balancing block**

This part synchronizes the multiple receive channels in phase and amplitude prior to performing the DBF. The detailed method is derived in the following section 7.1.2.

④ **Digital beamformer**

In this experiment, the reconstruction algorithm in [69] is the default module. For further experiments, it can be replaced by any other beamformers.

⑤ *Post-signal processor*

This module estimates residual phase errors in reconstructed SAR images, using the *Phase Gradient Autofocus* (PGA) algorithm.

Every receive channel data is independently processed for each waveform, up to the DBF block which coherently combines all channel data. In the following section, the channel balancing issue is further investigated and some comments to the post-processing are given due to its importance in this experiment.

7.1.2. Channel Balancing

For processing the multichannel data acquired from experiments, the receive channels of the GB demonstrator must have identical characteristics. Otherwise, azimuth ambiguities resulting from a spatial sub-sampling are not completely eliminated by the DBF process [58, 63]. This section describes a channel balancing approach for both phase and amplitude. Since the GB SAR demonstrator has no function for internal calibration, the technique introduced in this section therefore estimates the imbalances from the measured image data signals. The phase imbalance issue is dealt with in the following section.

Phase Balancing

For the array calibration, the most well-known approach is to measure the array antenna manifold in an anechoic chamber with a single point target at a known position, and then to estimate the phase error by comparing the ideal antenna manifold. If any additional phase distortion occurs in operation with the SAR antenna array, then this error must be compensated in flight. In the case that point-like targets or dominant scatterers exist in SAR images, the array can be
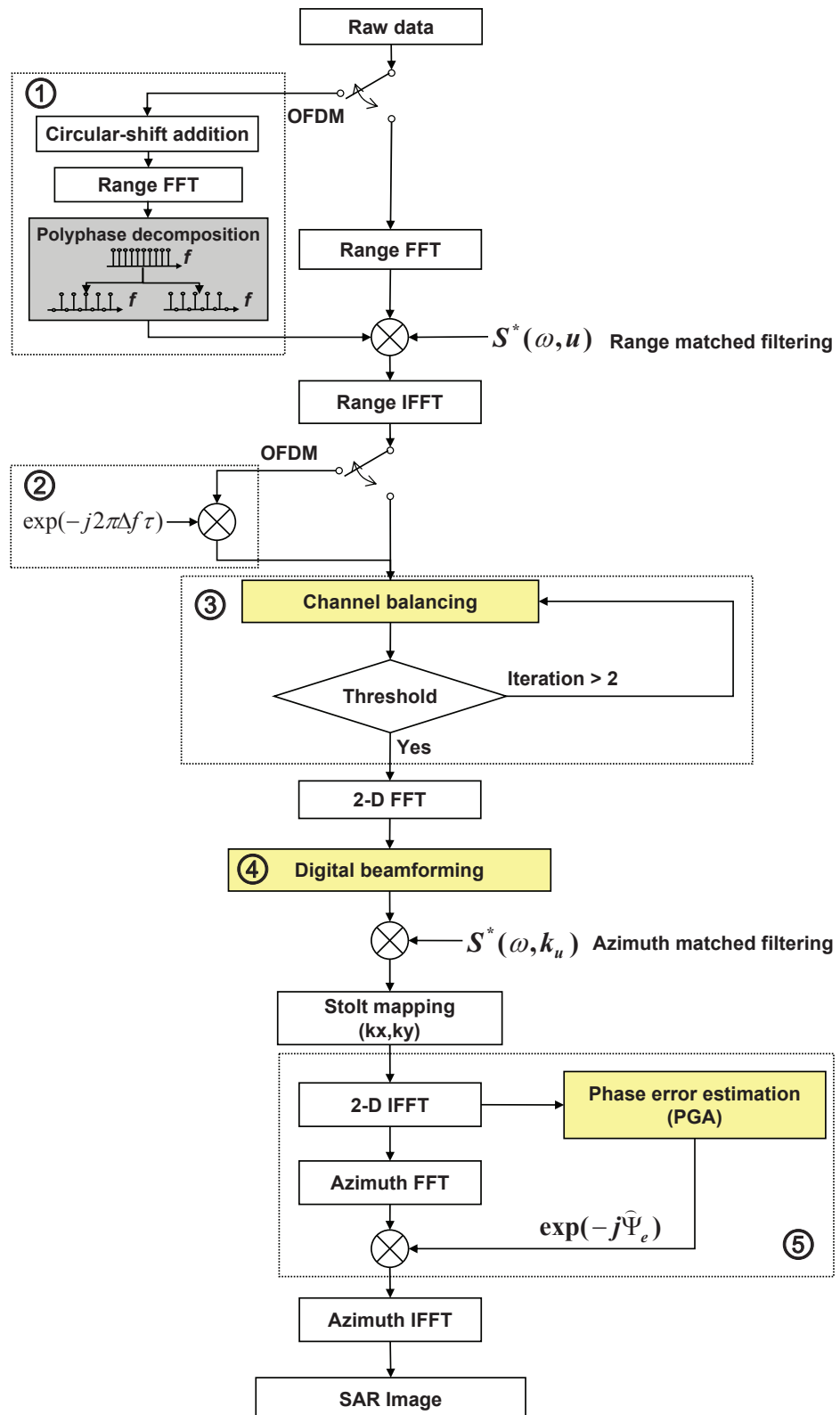
Figure 7.1.: Experimental MIMO SAR processor signal flow chart.

calibrated by using the angle of arrival estimated from the eigenstructure of the array signals [46]. In an other case, a study in [10] has shown that the phase of all array elements can be synchronized on the basis of the spatially incoherent signal property. For the GB SAR experiment, this work adopts the phase balancing algorithm based on the method in [10] for the correction of constant phase imbalances between the receive channels.

According to the Van Cittert-Zernike theorem [16], the spatial coherence between two channels is given by the Fourier transform of the intensity distribution over the target scene. When the ith channel contains a constant phase offset denoted by $\varphi_{e,i}$, the receive signal is described by

$$s_i(t, u) = s_{d,i}(t, u) \cdot \exp(j\varphi_{e,i}) \tag{7.1}$$

where $s_{d,i}$ is the complex signal of the distortionless ith channel, and the exponential term stands for the phase offset. The spatial covariance between adjacent two channels is calculated as

$$\sigma_{i,i+1}(u) = E\{s_i(t, u) \cdot s_{i+1}^*(t, u)\} \tag{7.2}$$

where $\sigma_{i,i+1}$ denotes the covariance between the i- and $(i+1)$th channels, and is calculated at every azimuth position u. The amplitude of spatial covariance is used to estimate the amplitude imbalance, dealt with in the next section. Here, the only interest is its phase. The phase term is given by

$$arg\{\sigma_{i,i+1}(u)\} = \varphi_i(u) + (\varphi_{e,i} - \varphi_{e,i+1}) \tag{7.3}$$

where $arg\{\}$ is the complex argument, and $\varphi_i(u)$ denotes the phase of covariance between the ideal i and $i+1$ channels. The phase function φ_i plays a major role in this algorithm. If φ_i varies rapidly in a nonlinear fashion which occurs in a non-uniform array, this approach will fail to detect the phase imbalance [10]. However, the φ_i is linear in a uniform array over the azimuth position, and is identical for all adjacent channel pairs:

$$\Delta\varphi(u) = \varphi_1(u) = \varphi_2(u) = \varphi_3(u) \cdots = \varphi_{M_R-1}(u). \tag{7.4}$$

Therefore the only difference is caused by the two channel phase offsets $(\varphi_{e,i} - \varphi_{e,i+1})$ in (7.3). This employed method attempts to synchronize the phase offset of each channel (not to remove these offsets), using the accumulated sum of the covariance phase. From (7.3) and (7.4), the accumulated sum of phase Ψ_i is derived as follows:

$$\Psi_\nu(u) = \sum_{i=1}^{\nu-1} (\varphi_i(u) + \varphi_{e,i} - \varphi_{e,i+1}) \tag{7.5}$$

$$= \sum_{i=1}^{\nu-1} \varphi_i(u) + (\varphi_{e,1} - \varphi_{e,\nu})$$

where i and ν denote the receive channel and the accumulated receive channel index respectively ($i = 1, 2, 3, \cdots, M_R - 1$ and $\nu = 2, 3, \cdots, M_R$). According to (7.4), the summation can be replaced by $(\nu - 1)\Delta\varphi$. Thus, the phase is composed of a constant plus a linear term. If the covariance is real and positive, then $\sum_{i=1}^{\nu-1} \varphi_i$ becomes null, which means the ideal balancing. If not, the linear phase term will exhibit a beam pointing error, which is proportional to $\Delta\varphi$ [10]. To minimize this phase effect, the expectation of the cumulated phase term is used in this work. Thanks to the symmetry of the antenna pattern and the zero squint angle, its expected value is close to null in this experiment:

$$E\{\Psi_\nu(u)\} \approx \varphi_{e,1} - \varphi_{e,\nu}. \tag{7.6}$$
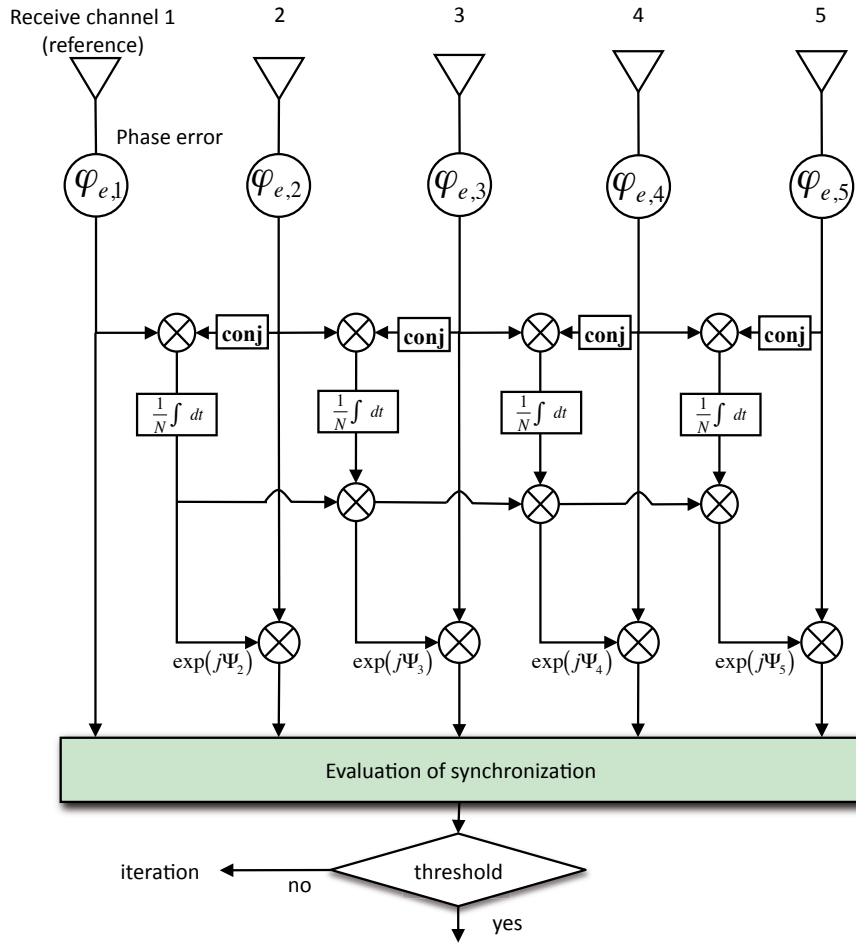
Figure 7.2.: Schematic of the phase balancing algorithm based on the spatial correlation method.

When the accumulated phase is added to each channel, the signal in (7.1) becomes

$$s_i(t, u) \approx s_{d,i}(t, u) \cdot \exp\left(j \cdot \varphi_{e,1}\right). \tag{7.7}$$

It must be noted that, in a real distributed target scenario, the linear phase term leads only to an image shift. For optimizing the phase balancing, the iteration can be extended. Figure 7.2 illustrates the schematic of the synchronization algorithm.

Amplitude Balancing

The basic idea behind the amplitude balancing is to compare azimuth antenna patterns estimated from the auto-correlation of each channel data over the azimuth positions. In the similar way to the phase balancing, the first channel is set to be a reference channel, and all other channels are synchronized to the reference channel. The amplitude balancing coefficient g_ν for the νth channel is given by

$$g_v(\nu) = \sqrt{\frac{E\{s_1(t, u) \cdot s_1^*(t, u)\}}{E\{s_\nu(t, u) \cdot s_\nu^*(t, u)\}}}. \tag{7.8}$$

The expectation of the individual channel is taken with respect to the fast-time t. The auto-correlation functions in (7.8) provide the signal intensity, so that the square root of the auto-correlation value should be used for the amplitude balancing. In the experimental MIMO SAR processor, this channel balancing is carried out with the range-focused signal (see Figure 7.1). In the practical implementation, the amplitude balancing can be combined with the phase balancing. Following this, a complex channel balancing factor is derived:

$$s_\nu(t, u) = s_\nu(t, u) \cdot \underbrace{g_\nu(u) \cdot \exp(j \cdot E\{\Psi_\nu(u)\})}_{\text{channel balancing factor}}. \tag{7.9}$$

7.1.3. Post-Processing: Higher Order Phase Error Correction

This section briefly introduces the need of post-processing for the correction of higher order phase error. This residual phase error is possibly caused by a non-linear platform motion and system hardware. In the experiment, a total platform track is realized by a serial connection of 7 pieces of sub-track each with a length of 2.1m. Although the GB SAR demonstrator motion is precisely controlled by the stepper motor controller IXE-α during the data acquisition (see Chapter 6), a non-linear motion can take place at the junctions between the sub-tracks and may result in a higher order phase error. The experimental processor takes such possible systematic distortion into consideration. In this experiment, the PGA algorithm is adopted and implemented into the experimental MIMO SAR processor. The PGA makes a robust estimation of the derivative of the higher order phase errors, using only defocused point-like targets in a complex SAR image [125]. The detailed principles are described in Appendix D.

7.2. Demonstration of Digital Beamforming in SAR

This section deals with the GB SAR measurement of multiple targets for the uniform sampling. In this section, the channel balancing and post-processing results are also presented stage by stage, in order to highlight the influence of the systematic distortions. Following this, the final imaging results demonstrate the azimuth ambiguity suppression capability of the DBF in a sub-sampling condition.

7.2.1. Geometry of the Ground-Based SAR Experiment

The ground-based SAR demonstrator collects raw data from targets deployed on ground in a side-looking SAR geometry. The GB demonstrator is set up on the roof of a building and looks down at a target scene from a height of 13.6m. Unlike a real SAR geometry, strong nadir reflections occur at the edge of the building. For the purpose of the minimization of this influence and the line-of-sight between the sensor and targets, the demonstrator is placed close to the edge of the building as shown in Figure 7.3.

The geometry of GB SAR experiment is depicted in Figure 7.4, and Table 7.1 summarizes the geometric parameters of this experiment. The antenna look angle is set to $40°$ for all antennas. A total of 5 Rx subarrays are used, so that its total length is 0.34m. For a uniform sampling in along-track, the spatial sampling distance should be a half of the total Rx array length, which is 0.17m in this system. This sampling distance leads to 71 samples acquired by each receive

(a)
(b)

Figure 7.3.: Photos of the demonstrator for the ground-based SAR experiment: (a) the set-up of the demonstrator on the test site and (b) the side view to indicate the sensor position close to the edge of the building and the look angle.
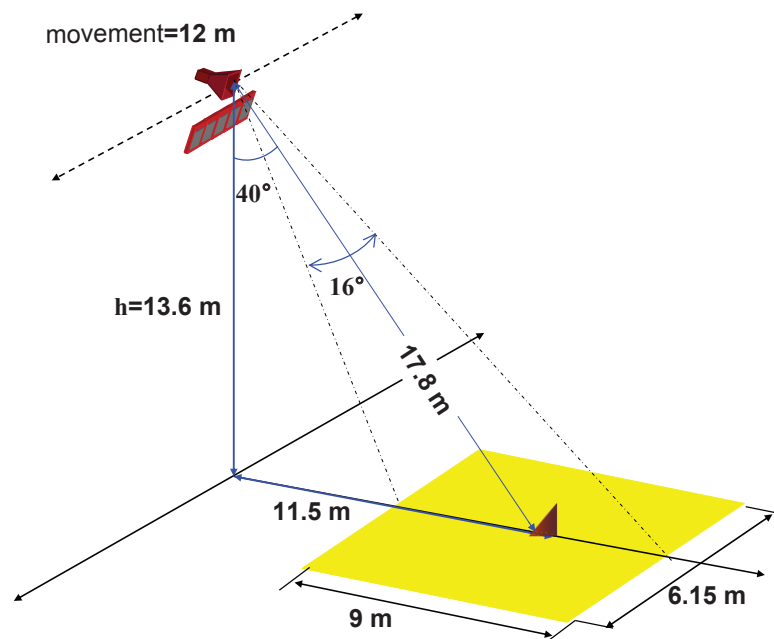
Figure 7.4.: Geometry of the GB side-looking SAR experiment

subarray in along track, and the GB demonstrator travels 12.07m along the track. As introduced in Chapter 6, the data acquisition in fast-time is $2\mu sec$, which is sufficient to gather signals from the target scene. The transmit and receiver antennas are separated vertically by 0.25m in order to minimize coupling between them. The azimuth resolution calculated from the 6dB width of the round-trip azimuth antenna pattern is 0.039m, however, a real resolution will be worst than this theoretical resolution, due to an amplitude taper effect via the 2-way azimuth antenna pattern. The swath width is determined in regard to the HPBW of the transmit antenna pattern in elevation. In the experiment, several different types and sizes of corner reflectors are used and deployed in the target area. A photo of targets and their coordinates are shown in

Figure 7.5. Assuming that the target height above ground is negligible, target positions are expressed in Cartesian coordinates. The broad 3dB beamwidth of a trihedral corner reflector (approximately $40°$) is a sufficient condition to regard the corner reflector as a point target, even in the case of wide beam SAR measurements [96].

Table 7.1.: Parameters of the GB SAR experiment

Parameter		Value	Parameter		Value
Rx subarray length		0.068m	Nr. of Rx subarrays		5
Rx array length		0.34m	spatial sampling		0.17m
acquisition time		2μsec	azimuth samples		70
Tx-Rx separation		0.25m	Tx-Rx coupling		$\leq$-80dB
synthetic aperture		5.85 m	slant range		15.2$\sim$20.9m
HPBW of Tx	azimuth	19.5°	HPBW of Rx	azimuth	36.5°
	elevation	21.5°		elevation	19°
2way HPBW	azimuth	17.6°	2way 6dB width	azimuth	23°
	elevation	16°		elevation	20.3°

(a)   (b)
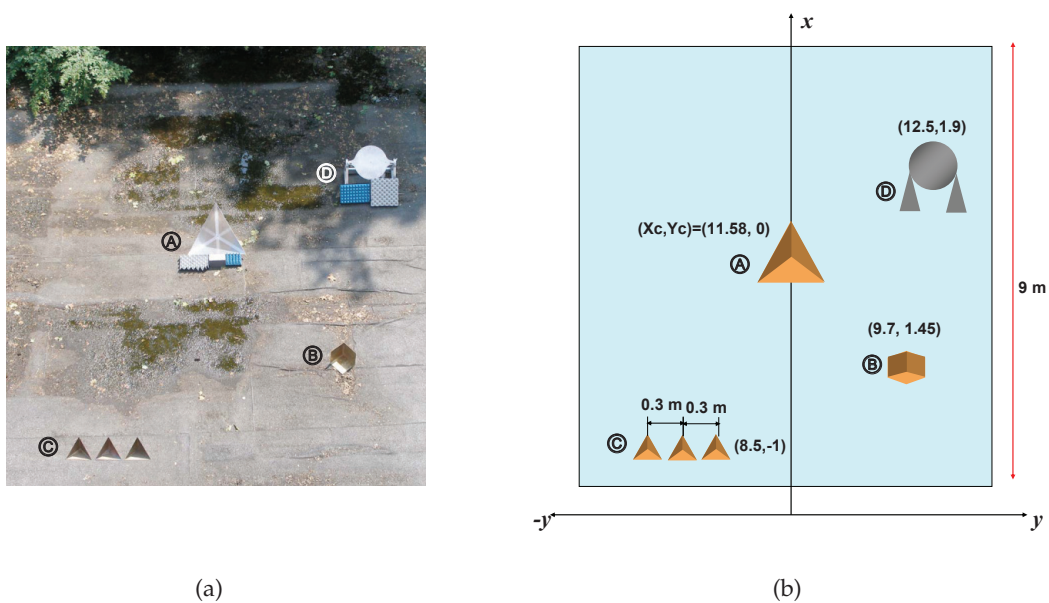
Figure 7.5.: Photo of the target scene (a) and coordinates of the targets (b).

The target Ⓐ is a big trihedral corner reflector with the length of 60cm from the trihedral vertex to the dihedral vertex, and is situated at the center of the target scene. Absorbing materials in front of the reflectors prevent the multi-bounded reflection, which could result in multiple responses of the reflectors in SAR image [131]. A square trihedral and a flat plate marked by Ⓑ and Ⓓ are used as well. The target Ⓒ, three small trihedral corner reflectors, are located at near range, regarding their small RCS. These are approximately 30cm apart from each other in y-axis at the same range, and used to show the fine azimuth resolution. The maximum RCS is obtained when the incident angle is matched to the broadside of a corner reflector. However in this experiment, the maximum RCS is not considered a critical parameter, since the radiometric

calibration is not performed, and yet only the calibration between receive channels is taken into account.

7.2.2. SAR Image Reconstruction with DBF

This section presents detailed SAR imaging procedures and results. Before coming to the final image, this section exhibits imaging results at intermediate processing stages in order to show the influence of the channel imbalance and the higher order phase error on DBF and SAR imaging. Subsequently, the first experimental SAR image with the DBF is presented.

Channel Balancing

From the measured GB SAR data, the covariance matrix is obtained for the channel balancing. First, the phase imbalance is considered. Figure 7.6 shows the phase functions of covariance between adjacent receive channels before the balancing. For clarity, each phase is fitted by the *Least Square* (LS) method.

(a) $\angle\sigma_{12}$

(b) $\angle\sigma_{23}$

(c) $\angle\sigma_{34}$

(d) $\angle\sigma_{45}$
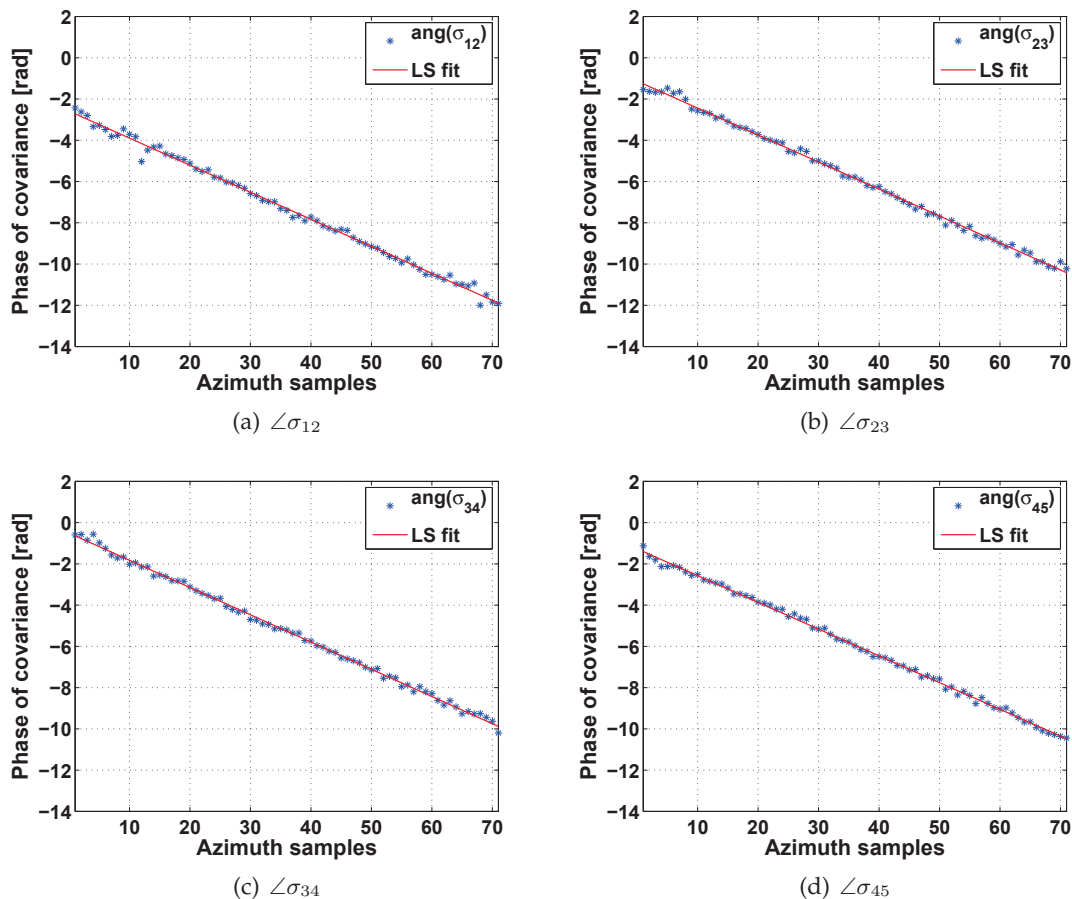
Figure 7.6.: Phase histories of the calculated spatial covariances between the adjacent receive channels in along-track.

143
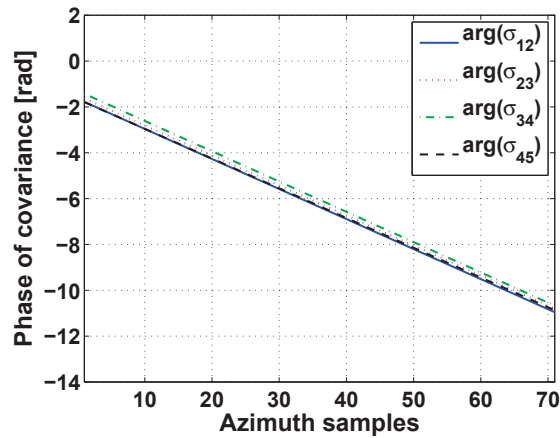
Figure 7.7.: Phase functions of the covariance after the phase balancing.

As aforementioned, the phases and the slopes of all covariances are supposed to be identical in an ideal uniform array, since they are only dependent on the array geometry. However, due to different phase offsets of each channel, these phase functions are vertically shifted by the offset difference $(\varphi_{e,i} - \varphi_{e,i+1})$ in (7.3). The phase balancing technique derived in the previous section synchronizes those offsets, and then all the phase functions appear identical. Figure 7.7 reveals the balanced covariance phases.

In the same manner, the amplitude imbalance is estimated from the covariance. In Figure 7.8 (a), all azimuth intensity patterns before the the amplitude balancing are plotted. During the experiment, it was detected that channel 2 was incorrectly connected to the RF switch, so this channel delivers only 15% of signal power to the receiver, compared to the reference channel.

(a) before balancing
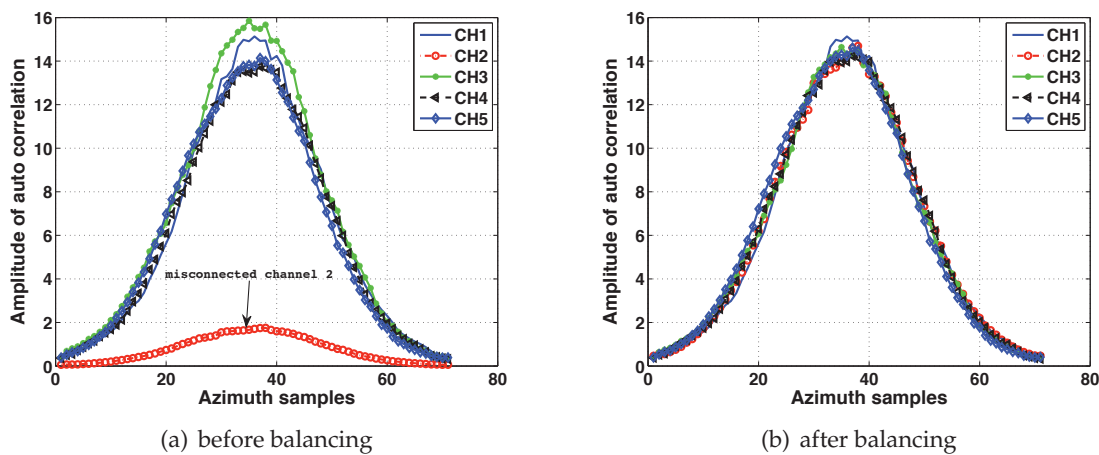
(b) after balancing

Figure 7.8.: Amplitude imbalance correction.

The amplitude balancing compensates for this loss in the misconnected channel 2, and equalizes all the channel amplitudes. The resulting azimuth patterns after the balancing are shown in Figure 7.8 (b). These balanced data are applicable to the DBF and the further process.

SAR Imaging

The channel-balanced data is processed by the digital beamforming block implementing the reconstruction algorithm, introduced in section 3.3.2. The output signal at the beamformer is equivalent to a monostatic signal with an improved Doppler bandwidth by a factor of the number of receive subarrays. The experimental processor based on the $\omega - k$ algorithm focuses the data and produces a SAR image. Figure 7.9 shows the preliminary SAR image distorted by the channel imbalance and the image improved by the channel balancing.

(a)

(b)
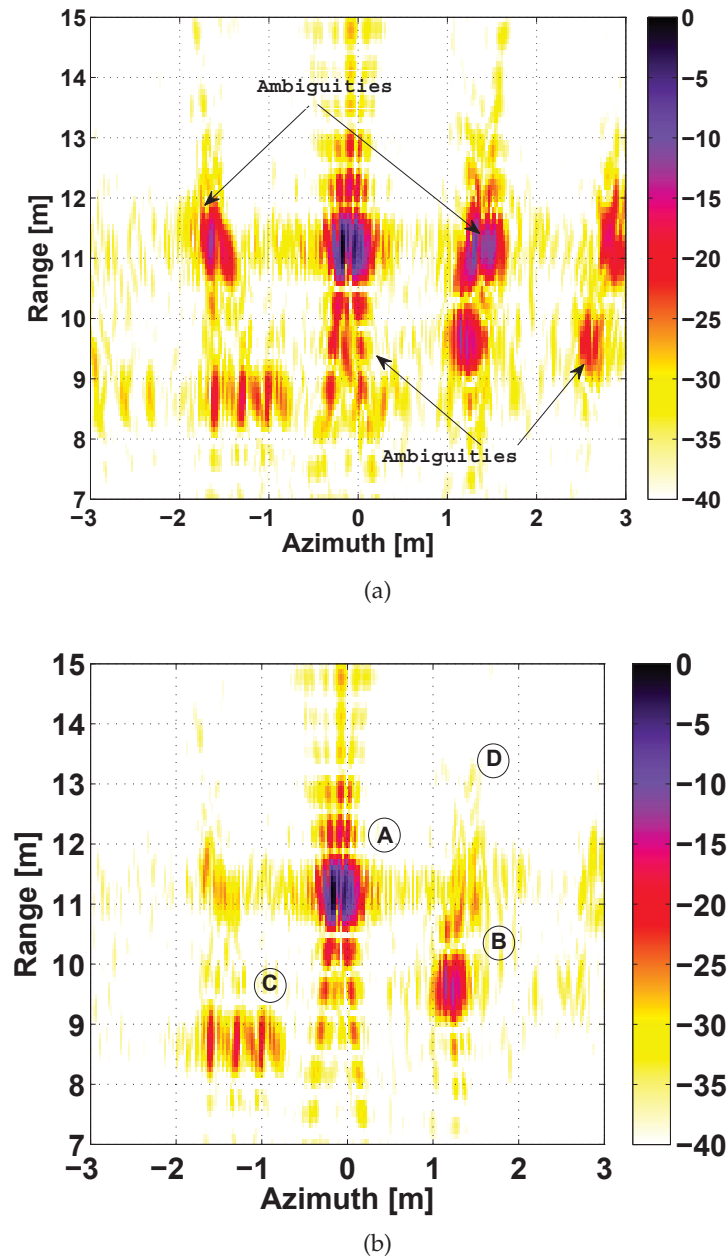
Figure 7.9.: GB SAR images before the channel balancing (a) and after the channel balancing (b)

The target responses in Figure 7.9 (a) exhibit strong azimuth ambiguities caused by the channel imbalance, and the maximum level reaches approximately -10dB even after the DBF. Note that the target Ⓓ (circular metal plate) is not shown in the image. This is because the target Ⓓ reflects the pulse impinging on its flat surface forward and as a result, the reflected signals from this target are not synthesized by the SAR processing.

Figure 7.9 (b) presents the image of the same scene after the channel balancing. Despite the strong sub-sampling (only 25% of the optimum sampling rate), the azimuth ambiguities are suppressed up to 28dB by the DBF. For clarity, the azimuth profiles of the focused images are compared. Figure 7.10 plots the azimuth profiles of the target Ⓐ (big corner reflector) at the center of the scene. The ambiguity level in these plots clearly reflects the channel imbalance influence. It is worth emphasizing that the channel imbalance is not corrected by post-processing like an autofocus algorithm, and must therefore be compensated prior to the digital beam-forming.

In this experiment, the processed Doppler bandwidth is 122.57[rad/m] which leads to the theoretical resolution of 0.0512m in azimuth. However, the target responses are still dispersive, which implies that the image data is disturbed by a residual phase error independent from the DBF and channel the balancing. In the next section, this residual phase error is estimated and corrected.

(a)   (b)
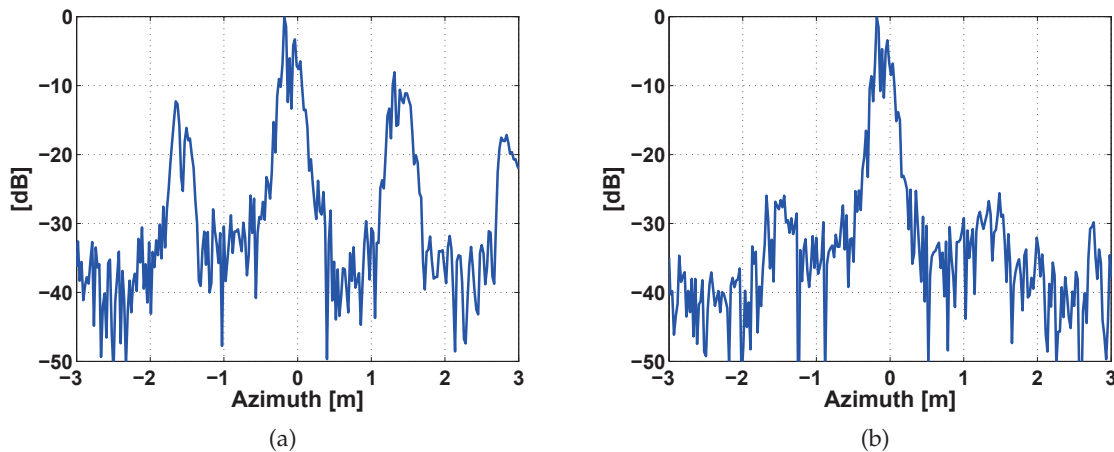
Figure 7.10.: Comparison of the azimuth profiles of the target Ⓐ after the DBF without the channel balancing (a) and with the balancing (b). In this experiment, the phase imbalance is a dominant cause which produces such high ambiguities.

Image Improvement by Post-Processing

The GB multichannel SAR imaging is completed with the addition phase error correction using the PGA algorithm (see Appendix D). The PGA algorithm exploits the redundancy of the phase error information contained in the imagery, which is independent of the range and the azimuth position of targets [125, 21]. A typical example is the motion error in spotlight image mode. Since the spotlight mode produces a SAR image over an entire target scene with data acquired within a common synthetic aperture, phase errors caused by the non-linear motion of sensor are identical for all target responses. By contrast, in stripmap imagery, this type of phase error is dependent on each target coordinate. Consequently, the direct application of the PGA algorithm

to a stripmap image yields a wrong estimation of phase error. To apply the PGA algorithm to this experiment, the focused SAR image data is divided into three segments, which contain one or more corner reflectors, as shown in Figure 7.11. Phase error estimated from the each segment will reveal a particular segment of the phase error in the stripmap SAR image. Thus, combining these phase error segments in along-track, one can estimate the whole phase error function contained in the image.
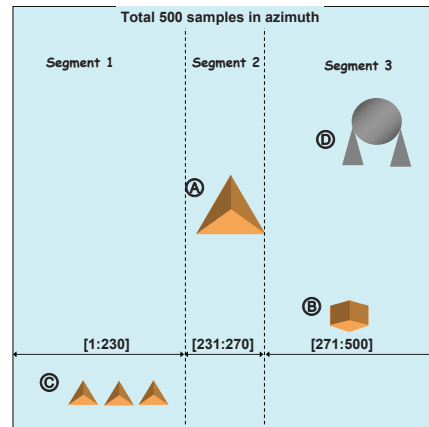
Figure 7.11.: Segmentation of the target scene in order to apply the PGA algorithm to this stripmap SAR data.

Figure 7.12 shows the estimated phase error of each segment. The estimated phase errors are theoretically the residues of phase functions of Doppler spectra, after removing linear phase ramps of the focused target responses. Note that the small corner reflectors are positioned close to each other, so they are included in the same segment.

The phase error of each channel varies in the Doppler domain in a similar fashion. A possible cause is a non-linear motion of the sensor, due to the cascade sub-track connection. The PGA compensates for those errors separately and optimizes the estimation and the correction by means of iteration.

Figure 7.13 presents the phase function of target Ⓐ before and after the non-linear phase removal. The main lobe phase in Figure 7.13 (a) is significantly disturbed by the non-linear, i.e. higher order phase error. The PGA removes this phase error, and in consequence, only the linear phase remains after the correction. It should be pointed out that the channel balancing and the PGA are independent of the DBF process and only affect to the systematic distortions.

Figure 7.14 exhibits the fully processed SAR image and compares it with a single channel SAR image in the same spatial sampling condition. In Figure 7.14 (a), the achieved spatial resolution is 0.53m in range and 0.046m in azimuth. The DBF reduces the spatial sampling distance from 0.17m to an effective sampling distance of 0.034m, and suppresses the azimuth ambiguity by up to approximately 30dB in this experiment. On the other hand, the single channel SAR image is disturbed by the strong ambiguities resulting from the sub-sampling, and the azimuth resolution is degraded to 0.22m. This result demonstrates that the DBF reconstructs a wide Doppler spectrum from the sub-sampled multichannel data, whereas the single channel system suffers from the severe spectral aliasing in the same sampling condition. Table 7.2 summarizes the achieved parameters.

(a) channel 1

(b) channel 2

(c) channel 3

(d) channel 4
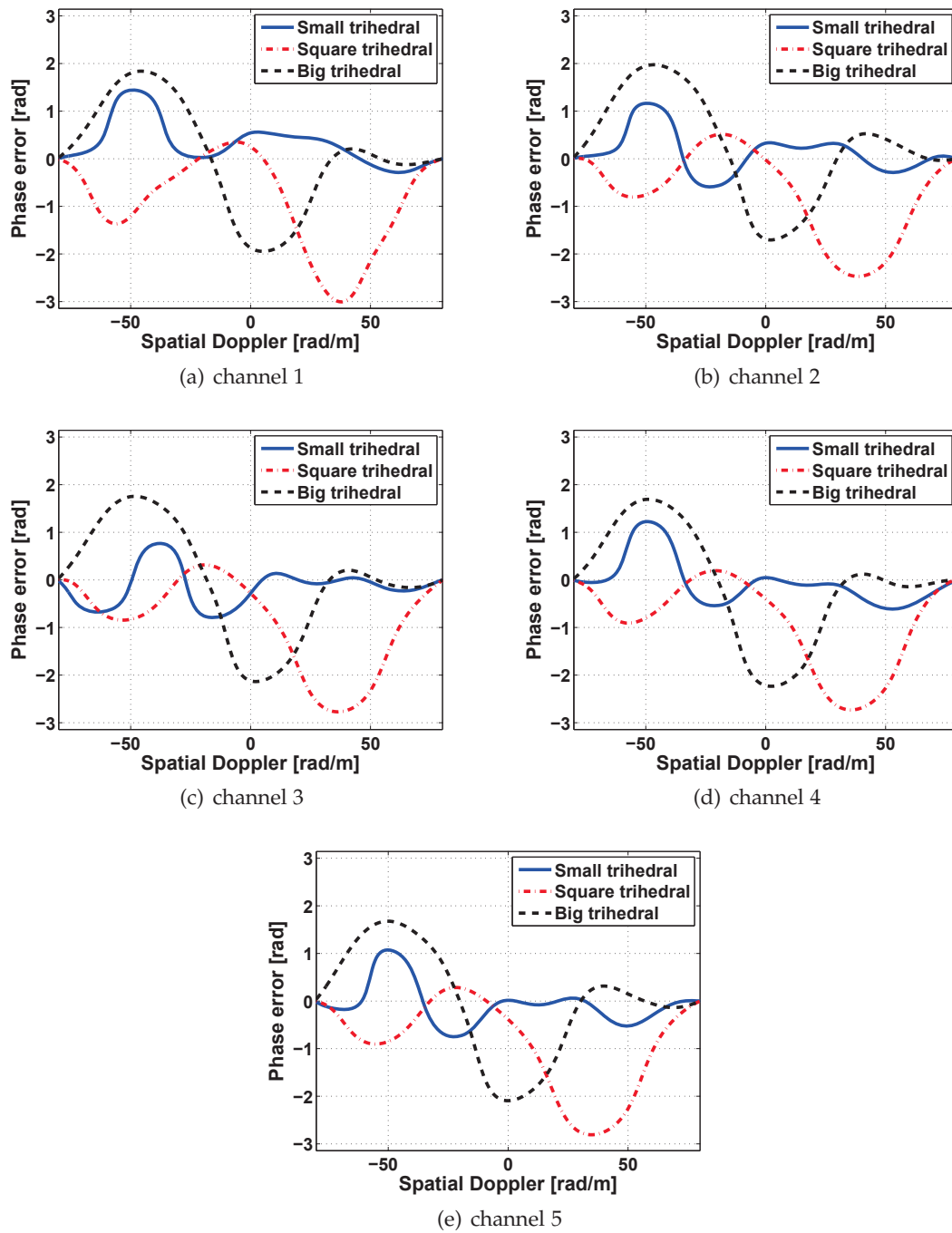
(e) channel 5

Figure 7.12.: Estimated residual phase error of each receive channel.

Table 7.2.: Achieved radiometric performance parameters.

Parameter	Value	Parameter	Value
range resolution	0.53m	azimuth resolution	0.046m
AASR	approx. -30dB	effective sampling distance	0.034m
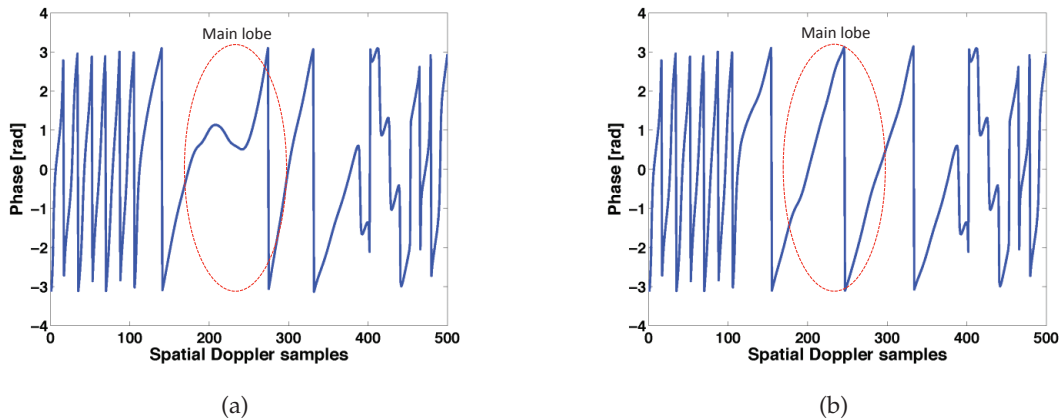
Figure 7.13.: Phase of the target Ⓐ (big trihedral corner reflector) (a) before and (b) after the PGA processing, which only removes the non-linear phase functions in Doppler frequency domain.

In principle, the DBF SAR image is equivalent to an image of a single channel SAR system, in that its spatial sampling distance is equal to the effective sampling distance 0.034m of the DBF system. In Figure 7.15, the azimuth profiles of both the DBF SAR image and the reference single channel (receive channel Nr.1) SAR image are compared. To put simply, both responses are identical but are mutually shifted by approximately 0.07m. This shift takes place since the phase center of the reference channel is 0.068m away from the receive array phase center.

Accordingly, this experiment successfully demonstrates the azimuth ambiguity suppression capability and the Doppler spectrum reconstruction of the DBF in the sub-sampling condition. So far, the DBF algorithm is experimentally verified for the uniformly sampled data. In the next section, the performance for non-uniform sampling cases is presented.
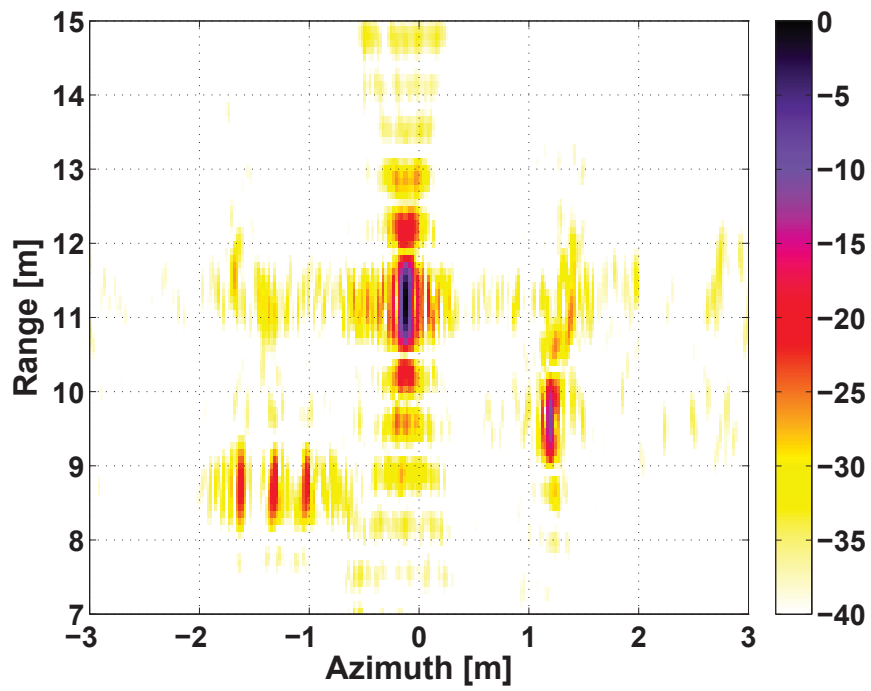
(a)
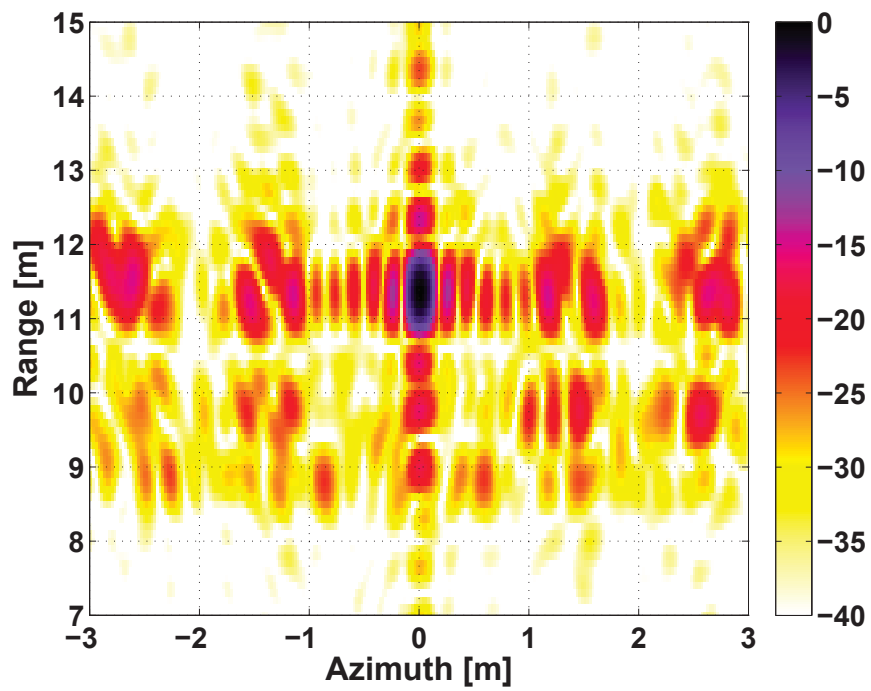
(b)

Figure 7.14.: Fully processed GB SAR image from (a) the whole receive channels with the DBF, and (b) a single channel SAR in the same spatial sampling condition (0.17m).

(a) target Ⓐ, reference

(b) target Ⓐ, DBF

(c) target Ⓑ, reference

(d) target Ⓑ, DBF

(e) target Ⓒ, reference

(f) target Ⓒ, DBF
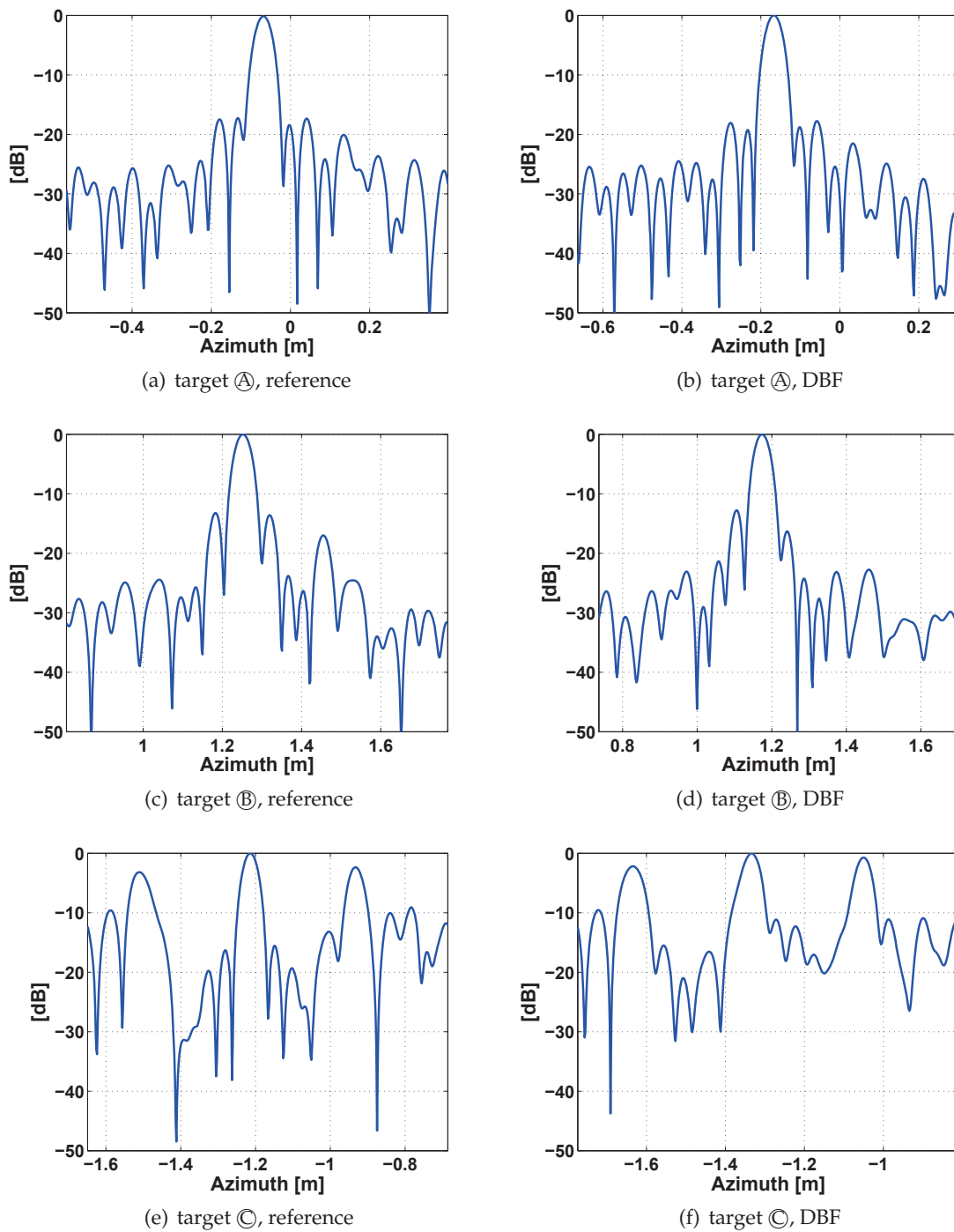
Figure 7.15.: Azimuth profiles of the target responses produced by the reference single channel SAR with the sampling distance of 0.034m (a),(c),(e) and by the DBF SAR with the sampling distance of 0.17m (b),(d),(f).

7.3. Digital Beamforming with Non-uniformly Sampled Data

One of the critical issues in the digital beamforming is the capability to effectively suppress the ambiguity for non-uniformly sampled data, which occurs when the travel distance within the pulse repetition interval does not match a half of the receive antenna length [139, 69]. In the practical SAR operation, it is desirable to have a specific range of PRF selection. Thus the non-uniform sampling scenario should be taken into account. This section is dedicated to an experiment of DBF in terms of various non-uniform sampling rates.

7.3.1. Geometry and Data Acquisition

For clarity, this experiment employs a single corner reflector. Figure 7.16 illustrates the geometry of the non-uniform sampling experiment.
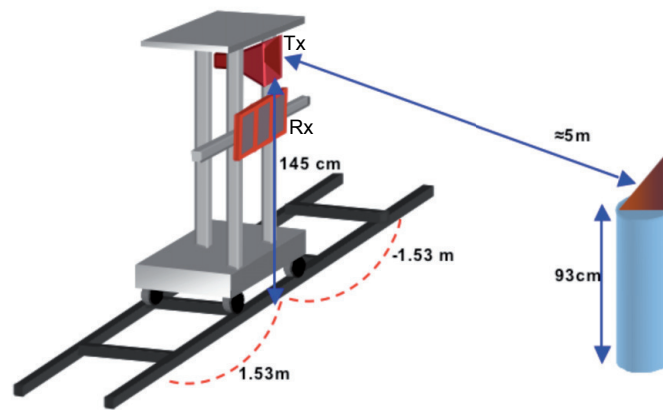
Figure 7.16.: Geometry of the GB SAR experiment for the non-uniform sampling with a single corner reflector. Three receive channels are used and the corner reflector is approximately 5m apart from the sensor. The total travel distance of the sensor is 3.06m.

Table 7.3.: Parameters of the non-uniform sampling experiment.

Parameter	Value	Parameter	Value
Rx subarray length	0.068m	No. of Rx subarrays	3
total length of Rx array	0.204m	spatial sampling	0.0102m
acquisition time	2μsec	azimuth samples	300

The experiment is carried out in a simple 2-D geometry using three receive antennas. To obtain SAR image data with diverse non-uniform sampling from this experiment, the GB demonstrator acquires data with a very high spatial sampling rate. Figure 7.17 depicts the highly dense data acquisition concept. The total array length is 0.204m, and the corresponding uniform sampling distance is 0.102m, denoted by $\Delta d_\circ$ in Figure 7.17. In this experiment, the GB SAR system captures data at every 0.0102m, which is tenfold higher than the uniform sampling distance of this given array geometry. Through such a dense sampling, various non-uniform sampling
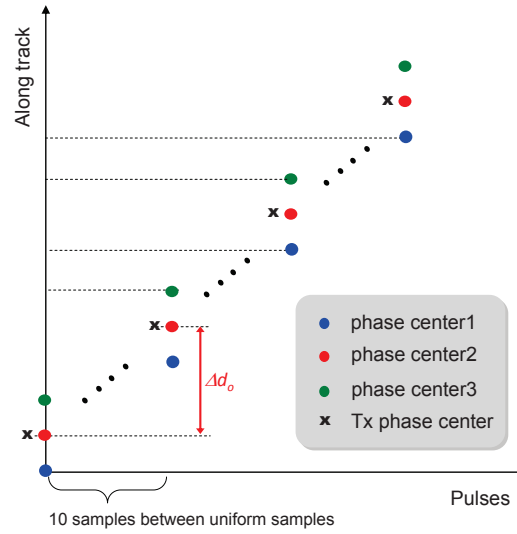
Figure 7.17.: Dense spatial sampling for the non-uniform data acquisition.

rates can be effectively recovered. Table 7.3 summarizes the geometric parameters of this measurement.

7.3.2. Ambiguity Suppression Performance

In this experiment, SAR images are generated in the same manner as the previous experiment. To highlight the adaptive ambiguity suppression capability of the reconstruction algorithm, the resulting images are compared with images produced by interleaving the multichannel data[1]. First, the non-uniform rate is defined in this chapter as follows:

$$\text{non-uniform rate} = 100 \times \left[1 - \frac{\Delta d}{\Delta d_\circ} \right] \tag{7.10}$$

where Δd is the real sampling distance, and Δd_o is the uniform sampling distance. The non-uniform rate basically indicates a decrement or increment of the sampling distance from the uniform sampling distance $\Delta d_\circ$ before the DBF process. For example, a positive value indicates a decrement which is over-sampling, and a negative value implies an increment of the sampling distance, i.e. sub-sampling.

Figure 7.18 shows the SAR images produced by the reconstruction algorithm plus the data interleaving for several over-sampling rates, and Figure 7.19 presents the azimuth profiles of each target response in Figure 7.18. In both beamformers, the uniform sampling yields the same results. When the non-uniform rate becomes negative, the sampling distance becomes larger than the Nyquist sampling distance of $0.102m$. Therefore the strong ambiguities occur in both images regardless of beamformer, as shown in Figure 7.18 (a) and (b).

---

[1]The spatial data interleaving is equivalent to the beamforming using multiple orthogonal beams, generated by the conventional steering vector.
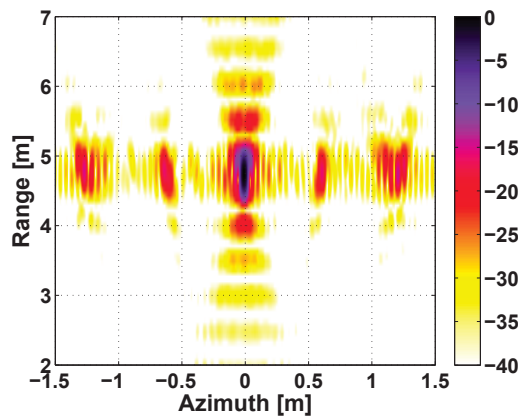
(a) -20%, interleaving
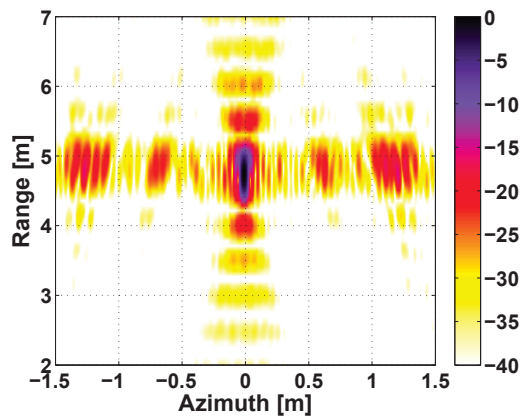
(b) -20%, reconstruction
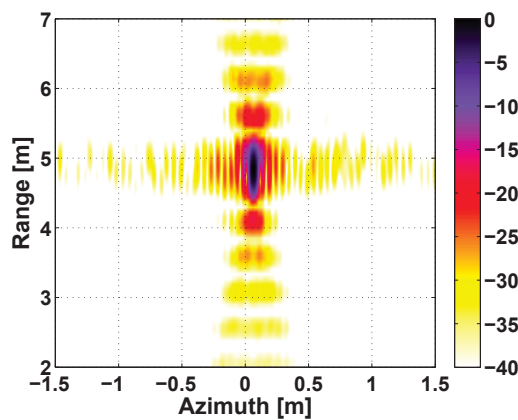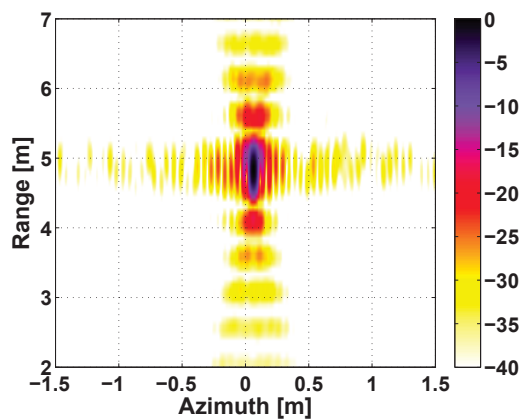
(c) 0%, interleaving
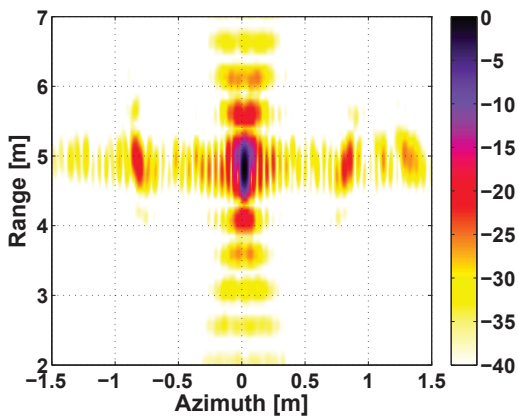
(d) 0%, reconstruction
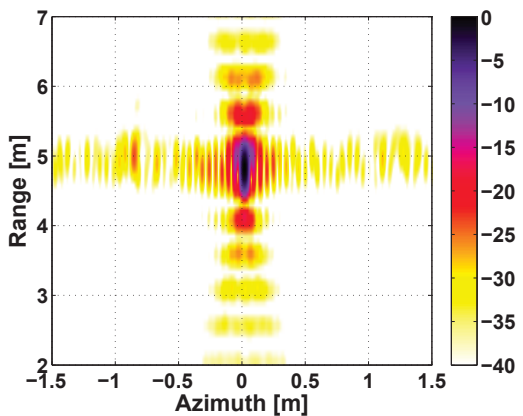
(e) 10%, interleaving

(f) 10%, reconstruction

If the sampling distance decreases, i.e. over-sampling, there are obvious differences between the reconstruction algorithm and the interleaving. For instance, the non-uniform rate of 10% (sampling distance of 0.0918m) raises the ambiguity level up to -22dB, in the case of the interleaving. If the non-uniform rate increases further, the ambiguities in the images also increase, but shift outwards from the target response, since the azimuth ambiguity separation is proportional to the sampling rate (PRF) [30]. If the non-uniform rate increases over 50%, then the ambiguities will disappear in the image.

(g) 30%, interleaving

(h) 30%, reconstruction

(i) 50%, interleaving

(j) 50%, reconstruction
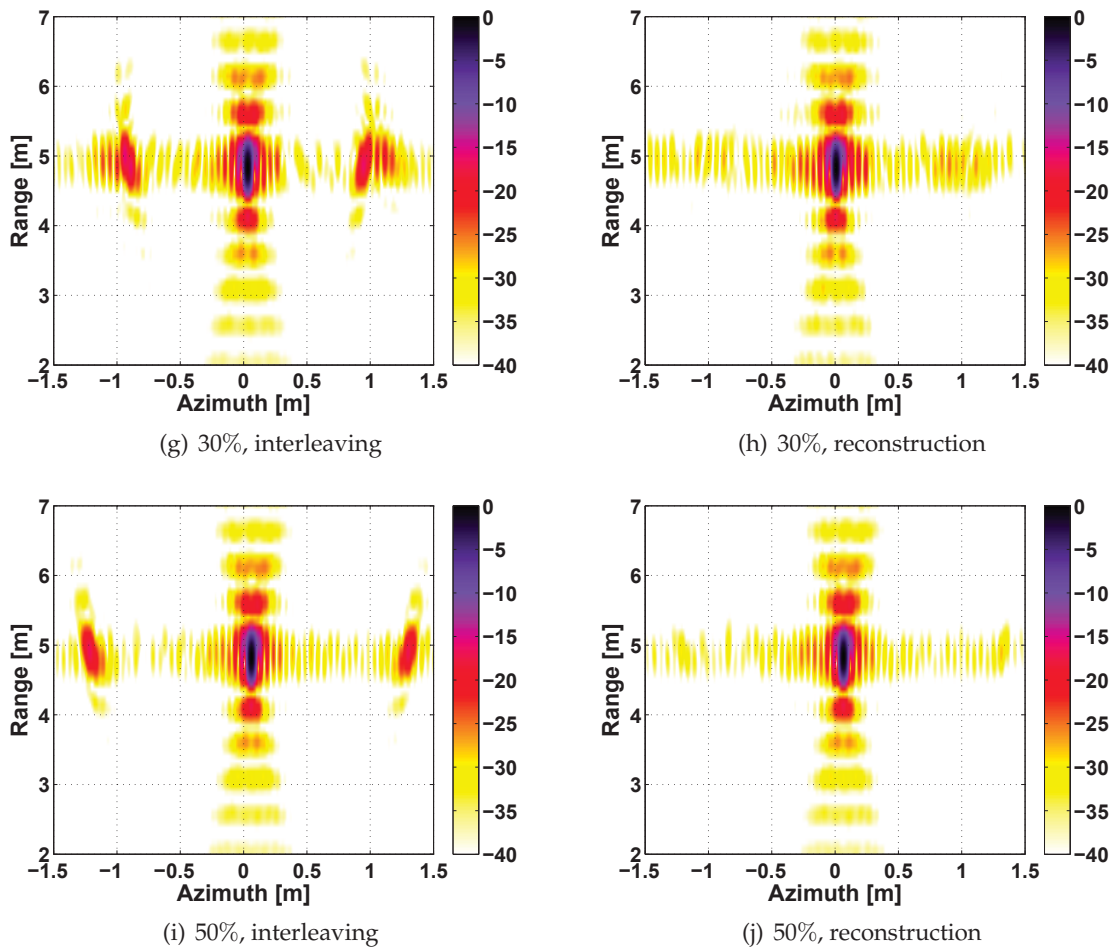
Figure 7.18.: The reconstructed point target images: (a),(c),(e),(g),(i) from the data interleaving and (b),(d),(f),(h),(j) from the reconstruction algorithm.

Contrary to this, the reconstruction algorithm shows the steady suppression performance over the various non-uniform rates. As explained in Chapter 3, the reconstruction algorithm (as well as the MVDR algorithm) compensates the additional phase rotation, due to the non-uniform sampling and afterwards combines multichannel signals. Therefore it presents a stable performance.

This work attempts to quantify the performance by measuring the *Peak Side lobe Ratio* (PSLR) and the *Integrated Side Lobe Ratio* (ISLR) of both images. The PSLR expresses the difference between the peak value and the maximum side lobe of target response. In the data interleaving, the maximum side lobe is equivalent to the azimuth ambiguity. In Figure 7.20 the measured PSLR is plotted.

The PSLR presents the azimuth ambiguity suppression performance of both beamformers at a glance. An interesting point in this plot is that the reconstruction algorithm fails in the ambiguity suppression and even in the SAR focusing at the non-uniform rate of 70%. An explanation for this phenomenon is that the spatial samples coincide in space at approximately $L_{rs}/2$, and in consequence of these spatial samples overlapping, the channel matrix used for the reconstruction filter matrix becomes singular, i.e. not invertible. In contrast, the same sampling condition leads to the performance enhancement for the interleaving, since the spatial sampling distance
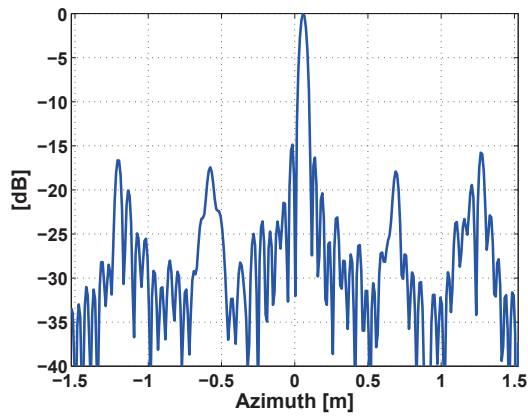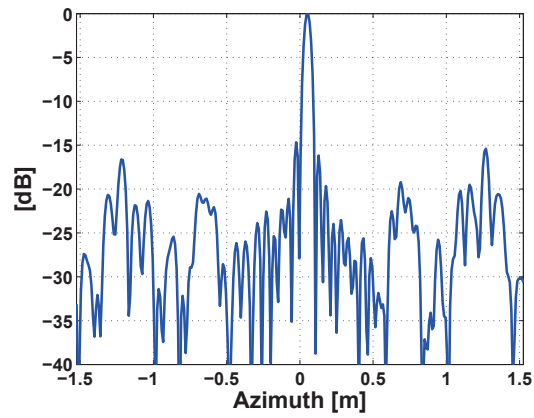
155

(a) -20%, interleaving

(b) -20%, reconstruction
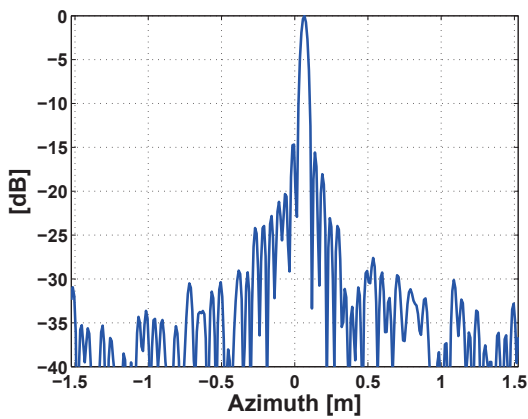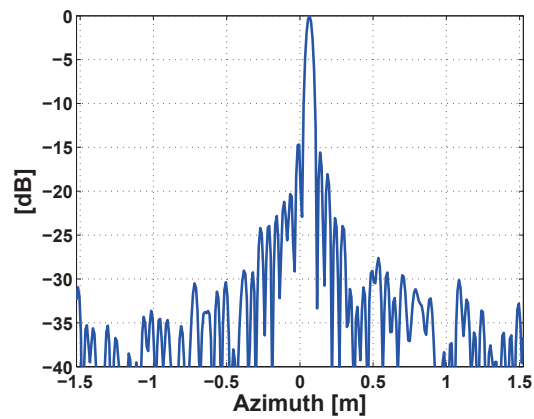
(c) 0%, interleaving
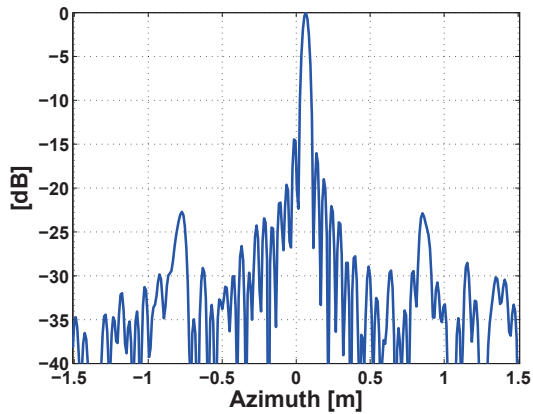
(d) 0%, reconstruction

(e) 10%, interleaving
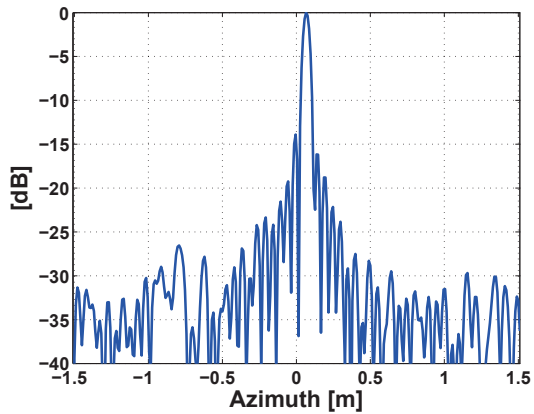
(f) 10%, reconstruction

(0.0306m) becomes shorter than the Nyquist sampling distance of 0.034m for every single channel.

The ISLR is the ratio of all energy in the side lobes of the system impulse response to energy in the main lobe[2] [20]. The increase of ISLR reflects the influence of a wide band phase error

---

[2]This parameter is commonly defined in one-dimension. In this work, this is defined in azimuth.

(g) 30%, interleaving

(h) 30%, reconstruction

(i) 50%, interleaving

(j) 50%, reconstruction
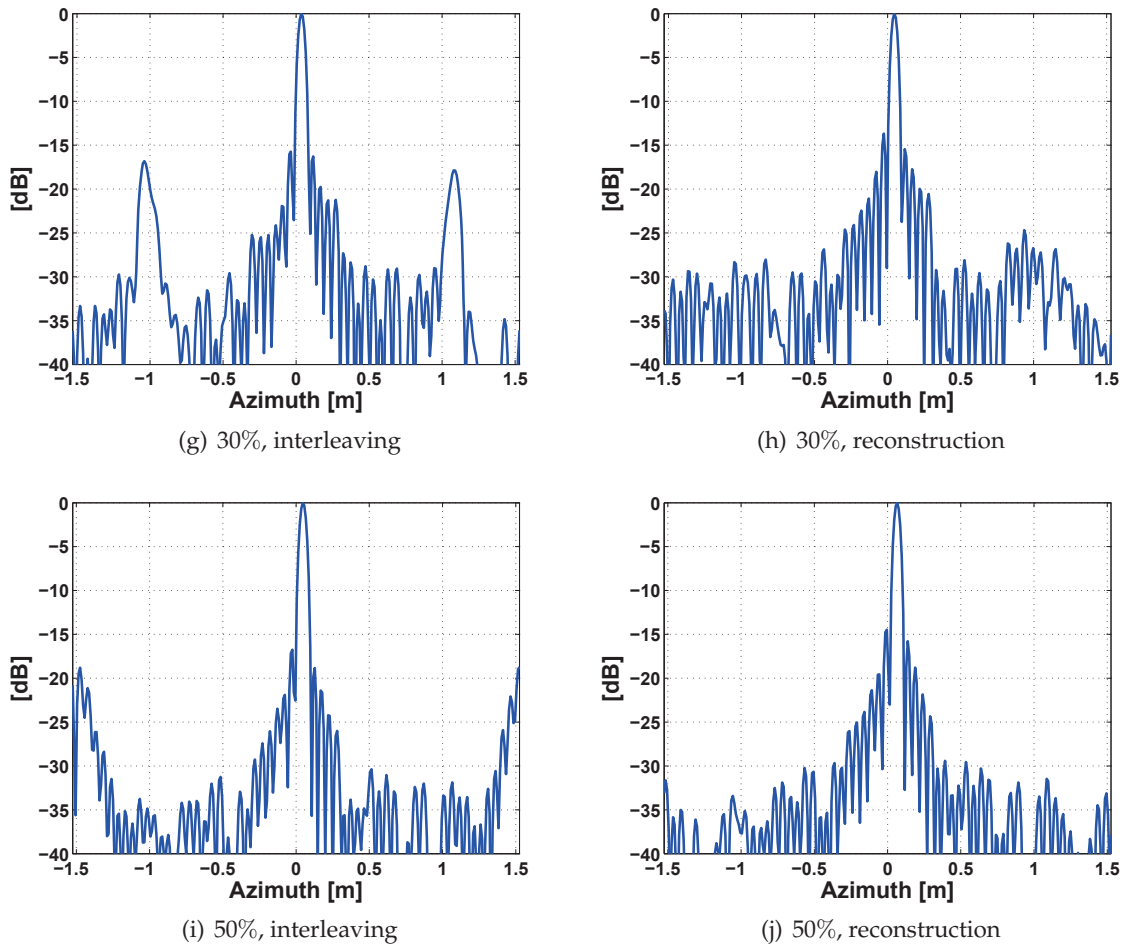
Figure 7.19.: Azimuth profiles of the reconstructed point target image: (a),(c),(e),(g),(i) from the data interleaving and (b),(d),(f),(h),(j) from the reconstruction algorithm.
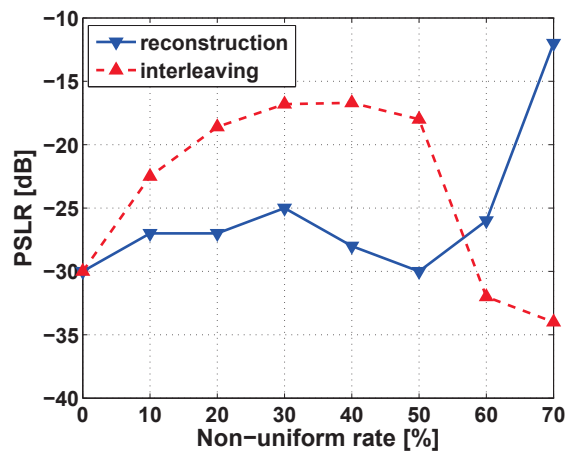
Figure 7.20.: Measured PSLR versus non-uniform rate.

on SAR images [30]. In this experiment, this parameter may indicate the influence of a residual phase error, which is possibly caused by the non-uniform sampling and the imperfect compen-

157

(a) interleaving   (b) reconstruction
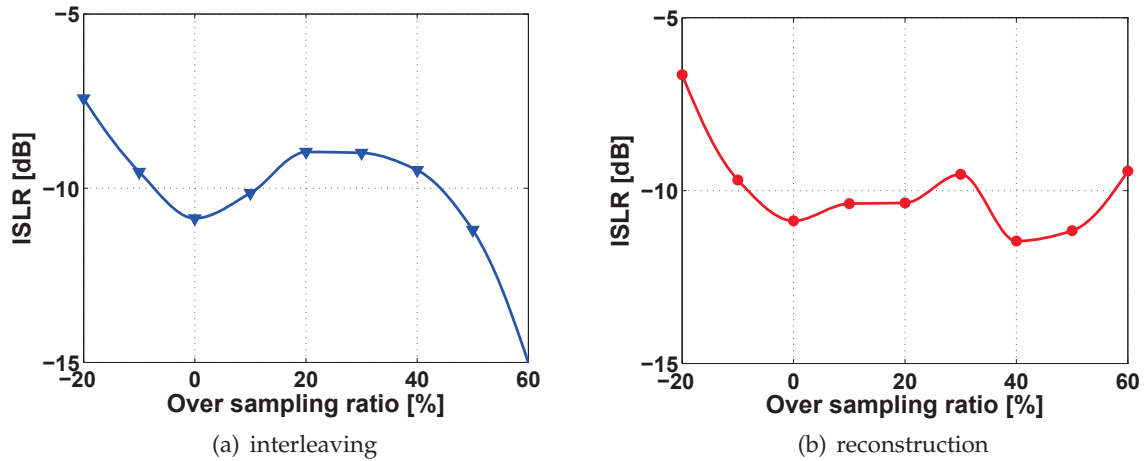
Figure 7.21.: Measured one-dimensional ISLR versus non-uniform rate.

sation by DBF. Figure 7.21 shows the measured ISLR versus the non-uniform rate within -20% and 60%.

Figure 7.21 (a) presents the ISLR of the data interleaving. Increasing degrees of the non-uniform sampling will degrade the ISLR in both cases. However, beyond the non-uniform rate of 40%, the ISLR of the interleaving is improved again, since the ambiguities move outwards and the increased spatial sampling rate contributes to the reduction of the noise level in the image. That of the reconstruction algorithm is shown in Figure 7.21 (b). Thanks to the steady performance of the reconstruction algorithm, a large fluctuation of ISLR does not occur for sampling rate changes. However, it is the worth noting that the variation of noise floor is reflected in the ISLR. For example, the increase of noise floor in Figure 7.19 (h) resulted in the degradation of the corresponding ISLR value. The measured ISLR sustains the study result of that the non-uniformity increases noise floor in the reconstruction filtering as well [69]. Therefore the ISLR can be used to indicate the variation of the noise level after the DBF, in the case of the reconstruction algorithm.

In summary, these experiments demonstrated the adaptivity of the DBF in the azimuth ambiguity suppression. In particular, it was proven that the reconstruction algorithm provides the reliable suppression performance even in the non-uniform cases.

7.4. Experiments of MIMO OFDM SAR

In this section, the novel OFDM waveform scheme is validated on the basis of virtual MIMO SAR configurations. The term "*virtual*" implies that the MIMO configuration is equivalently realized by exploiting multiple Rx data sets from the GB SAR demonstrator. Such a virtual configuration is effective in the following conditions:

- Time-invariant channel for a data acquisition period
- Delay spread much shorter than a transmitted pulse length

For this experiment, MIMO OFDM SAR signals are produced by converting two subsequent *Single-Input Multiple-Output* (SIMO)[3] data sets to MIMO data sets. This signal conversion is valid only for the time-invariant channel within the successive data acquisition cycles. Otherwise, serious temporal decorrelation can occur during the measurement cycles, meaning that those data sets cannot be equivalent to real MIMO data sets. In addition, a short delay spread is desired for making a converted signal more equivalent to the original OFDM signal design. The equivalent MIMO OFDM SAR data is processed by the developed OFDM demodulation scheme, and final images are reconstructed with the DBF in the same way in the previous experiments.

7.4.1. Virtual MIMO Antenna Constellation

Figure 7.22 (a) depicts the original SIMO configuration and its spatial sample positions within two successive data acquisitions. For clarity, two subsequent phase center groups (three samples for each) are marked by the symbols "x" and "o" respectively in the figure. In reality, the first three phase centers are acquired at the nth data acquisition, and afterwards, the remaining group of three is obtained at the $(n+1)$th data acquisition. For these spatial sample distribution, one can draw an equivalent MIMO antenna constellation, which produces the same spatial samples according to the DPCA principle (see Appendix A.). The corresponding MIMO antenna constellation is shown in Figure 7.22 (b). In this configuration, two transmit antennas are symmetrically positioned around the receive array center, and their separation is equal to the receive array length. Resultantly, the two subsequent phase center groups become equivalent to the phase centers of the 2×3 MIMO antenna which produces six spatial samples at the same time. The spatial sampling distance of this MIMO antenna system therefore becomes double that of the original SIMO antenna system. In the following section, the detailed data conversion process is described.
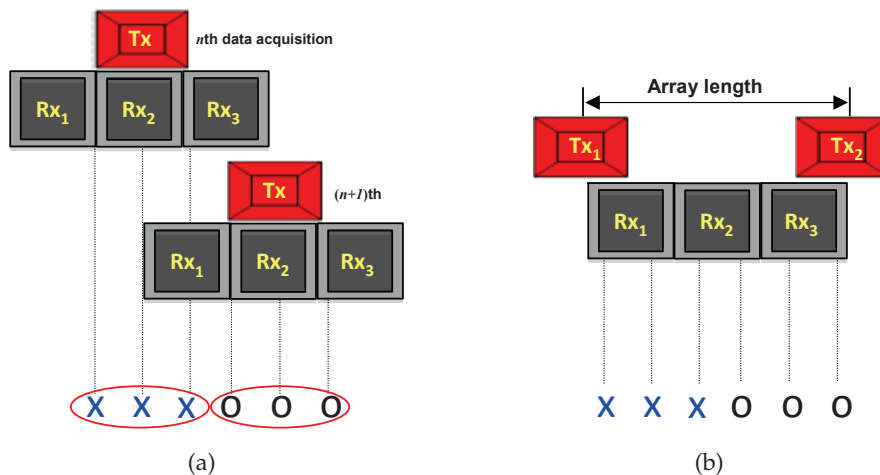
Figure 7.22.: Original 1×3 SIMO configuration for the nth and the $(n + 1)$th data acquisition, plus the phase center positions (a), and the virtual 2×3 MIMO configuration using two subsequent data samples and the phase center positions (b).

---

[3]According to the definition of input and output in MIMO channel model in Chapter 3, the SIMO configuration corresponds to a single Tx and multiple Rx antennas configuration.

7.4.2. Data Conversion

The data conversion is based on the time domain properties of the OFDM signal, which are the repetition and the phase shift, as stated in section 4.1.3. Figure 7.23 depicts the conversion procedures in fast-time. First, the received signal is duplicated and concatenated to the original signal in time domain. As stated in Table 6.1, the window length in fast-time is 2μsec, yet the whole duration is not required, since the delay spread is only approximately 0.1387μsec in the GB SAR measurement. Therefore the first 1.183μsec of the signal with a guard interval is selected and duplicated for the concatenation. The guard interval is added to avoid any phase discontinuity at the junction between the preceding and the succeeding chirps. The original signal of the ith receiver at nth acquisition, $r_i(t, u)$, is converted to an OFDM signal $s_{1,i}(t, u)$, modulated by odd subcarriers. In the same manner, the signal $r_i(t, u + \Delta d)$ at the $(n + 1)$th acquisition is converted to $s_{2,i}(t, u)$. An additional step for the even subcarrier signal is the multiplication of an exponential term representing a phase shift, due to a subcarrier offset between the odd and even spectra.
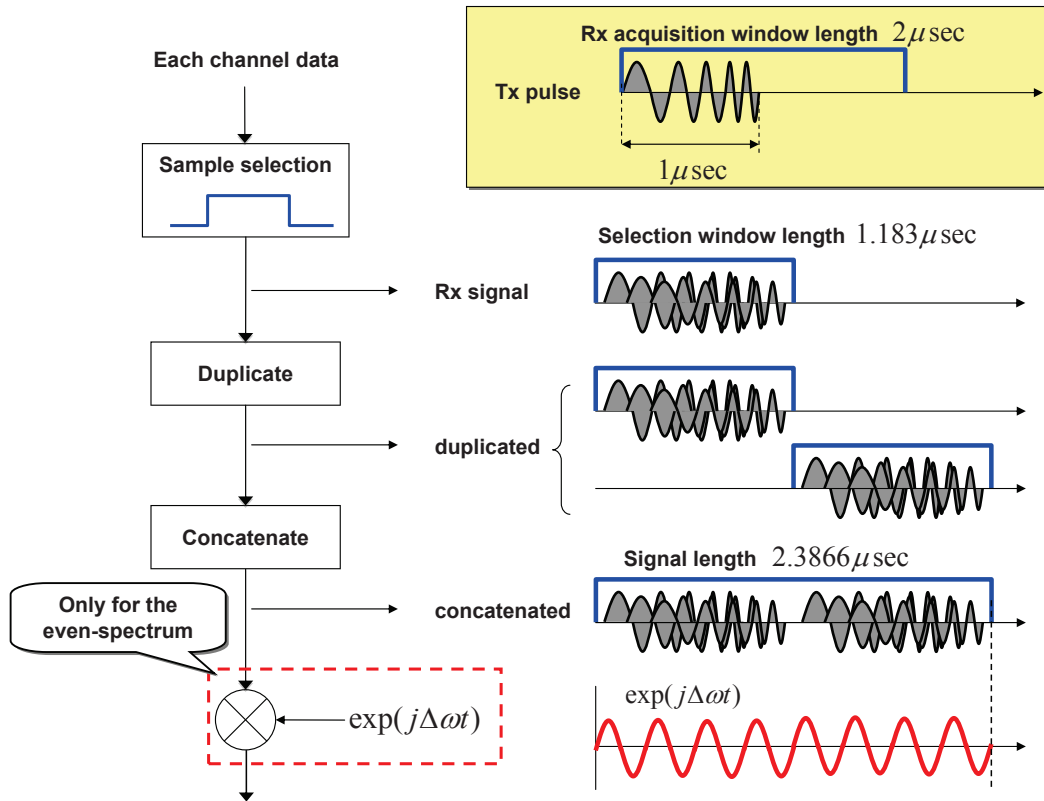
Figure 7.23.: Schematic of the data conversion process from the received signal to the equivalent OFDM signal in fast-time domain.

The converted signals are described as follows:

$$s_{1,i}(t, u) = r_i(t, u) \cdot \text{rect}\left[\frac{t}{T_p}\right] + r_i(t - T_p, u) \cdot \text{rect}\left[\frac{t - T_p}{T_p}\right] \tag{7.11}$$

$$s_{2,i}(t, u) = \left(r_i(t, u + \Delta d) \cdot \text{rect}\left[\frac{t}{T_p}\right] + r_i(t - T_p, u + \Delta d) \cdot \text{rect}\left[\frac{t - T_p}{T_p}\right]\right) \cdot e^{j2\pi\Delta ft} \tag{7.12}$$
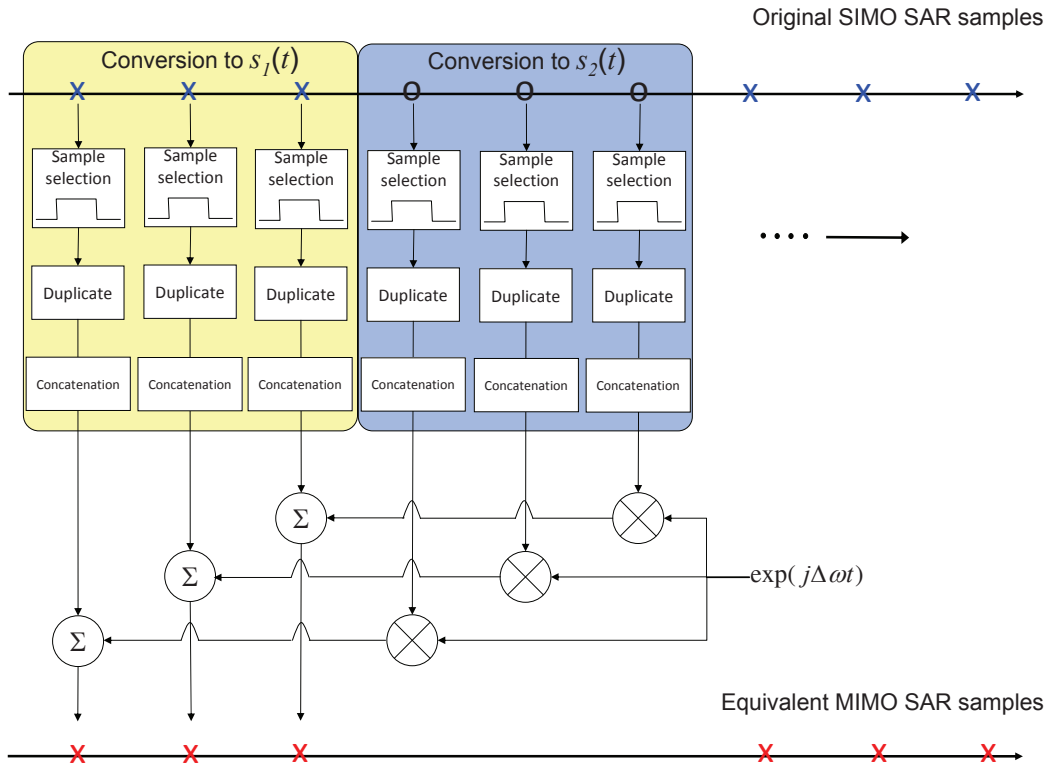
Figure 7.24.: Along-track process of the data conversion. The three channel data are converted to the odd subcarrier signals, and the same channel data at the next position are converted to the even-subcarrier signals. They are merged in along-track.

where u is the sensor position in along-track, and Δd is the spatial sampling distance before the DBF. The rectangular window length equals to the half of OFDM pulse length T_p, which is 1.183μsec in this experiment. The equivalent received OFDM signal $r_{i,o}(t)$ at the ith receive antenna is now given by

$$r_{i,o}(t, u) = s_{1,i}(t, u) + s_{2,i}(t, u) + n_i(t, u) \tag{7.13}$$

where $n_i(t)$ is the noise added after the conversion[4]. Figure 7.24 illustrates the conversion process of each channel data in along-track. The converted signal of each channel is combined with the same channel data at the next position. Therefore the spatial sampling distance is increased, and the number of spatial samples in the equivalent MIMO SAR is reduced by a factor of 2. All these data will be recovered by the OFDM demodulation.

Figure 7.25 shows the converted MIMO OFDM signals. The phase of $s_{2,i}$ varies over time due to the subcarrier offset Δf of 422.4kHz, while $s_{1,i}$ shows the repetition of the same chirp. It may be emphasized that the guard interval does *not* affect the orthogonal property of the OFDM signal, as long as the repetition behavior is ensured in fast-time.

---

[4]The conversion process duplicates and concatenates the original noise signal as well. It leads to the perfect orthogonal condition of the converted signal. In order to allow a more realistic scenario, this noise signal is added to the equivalent OFDM signal after the conversion.
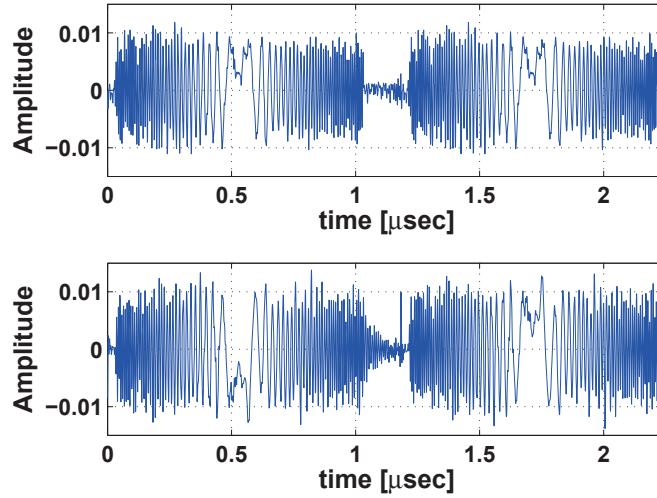
Figure 7.25.: Equivalent OFDM modulated chirp signal: real part of $s_{1,i}$ (top) and real part of $s_{2,i}$ (bottom).

7.4.3. Processing of MIMO OFDM SAR signal

As shown in Figure 7.1, the processing algorithm of the MIMO OFDM SAR signal is quasi-identical to the previous experiment, except for the OFDM demodulation parts (see ① and ② in Figure 7.1). A notable thing about the OFDM demodulation in this processor is the fact that the processor dispenses with the spatial filtering and the circular-shift addition process. This is because the delay spread of the target scene does not exceed the guard interval 0.183μsec. Therefore the received signal length is equal to the pulse length (2.3866μsec), and the spatial filtering and the circular-shift addition are not required.

The converted raw data in the previous section is transformed into the frequency domain. Subsequently, the polyphase decomposition block separates the received OFDM waveform signal into the odd and even spectra. Each spectrum signal is independently compressed by the matched filtering in range. In practice, the demodulated waveforms are different in phase. The frequency offset Δf results in an additional phase rotation, which is proportional to delay time. This phase rotation term remains after the OFDM demodulation, and thus must be compensated prior to DBF processing. The range compression filter focuses energy at the target position, so that the phase rotation appears as a linear function $2\pi\Delta f\tau$ in every azimuth bin[5]. The rest of processing is the same as in the former experiment. To optimize the performance, the array calibration and the higher order phase error correction by the PGA algorithm are carried out as well.

7.4.4. MISO OFDM SAR Experiment

This section presents an experiment of the equivalent OFDM SAR signal for a single target, using a single receive channel. In this case, the converted data are equivalent to 2×1 *Multiple-Input Single-Output* (MISO) data.

---

[5]This effect has been actually shown in Figure 4.38 with E-SAR data experiment.

Geometric and Data Acquisition Parameters

Before showing this experimental results, geometric and data acquisition parameters of this MISO SAR system are briefly described. The target geometry of this experiment accords to the single target experiment in section 7.3. Regarding the single receive subarray length 6.8cm, data at the every sampling distance Δd of 3.06cm is taken and converted. The MISO antenna constellation is similar to Figure 7.22. Two transmit antennas are symmetrically arranged around the single receive channel and separated by 6.12cm, since the phase centers of the original Tx and Rx antennas coincide in azimuth. The spatial is sampling distance of the MISO system is equal to 6.12cm ($2\Delta u$=6.12cm). Table 7.4 summarizes these geometric and acquisition parameters.

Table 7.4.: MISO geometric and acquisition parameters.

Parameter	Value	Parameter	Value
OFDM pulse length	2.366μsec	original sampling distance Δd	0.0306m
virtual Tx baseline	0.0612m	Δd after the conversion	0.0612 m

Imaging Results

Figure 7.26 shows the phase history of both OFDM signals before and after the DBF. The top and middle plots are showing the phase history of each OFDM waveform, where azimuth ambiguities are obviously visible due to the spatial sub-sampling. Both waveform responses, separated by the OFDM demodulation, are coherently combined by the DBF block in order to recover a wide Doppler spectrum. The bottom plot in Figure 7.26 is the phase history of the reconstructed signal after the DBF. It is obvious that the phases of higher frequencies are recovered from the aliasing.
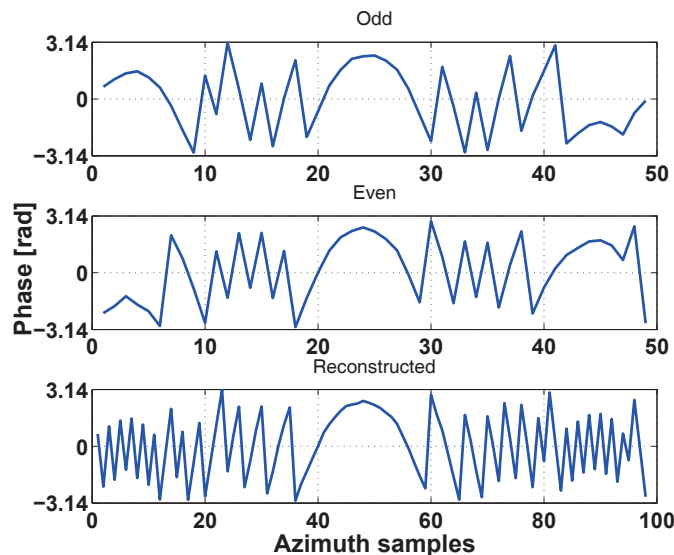
Figure 7.26.: Phase history of the odd subcarrier signal (top), the even subcarrier signal (middle), and the reconstructed signal (bottom).

The fully processed target image is presented in Figure 7.27. From the range and the azimuth profiles in Figure 7.27 (a) and (b), it can be shown that the OFDM waveforms were successfully separated and processed. The achieved spatial resolution in both directions is equivalent to the prior experiment (see Table 7.2). Figure 7.27 (c) and (d) exhibit the 2-D image in linear scale and in decibels respectively. Despite the sub-sampling, the azimuth ambiguities are properly suppressed by the DBF. Hence this result shows that two OFDM waveform signals separated from a single receiver can be used for the DBF like a SIMO system.

(a)

(b)

(c)

(d)
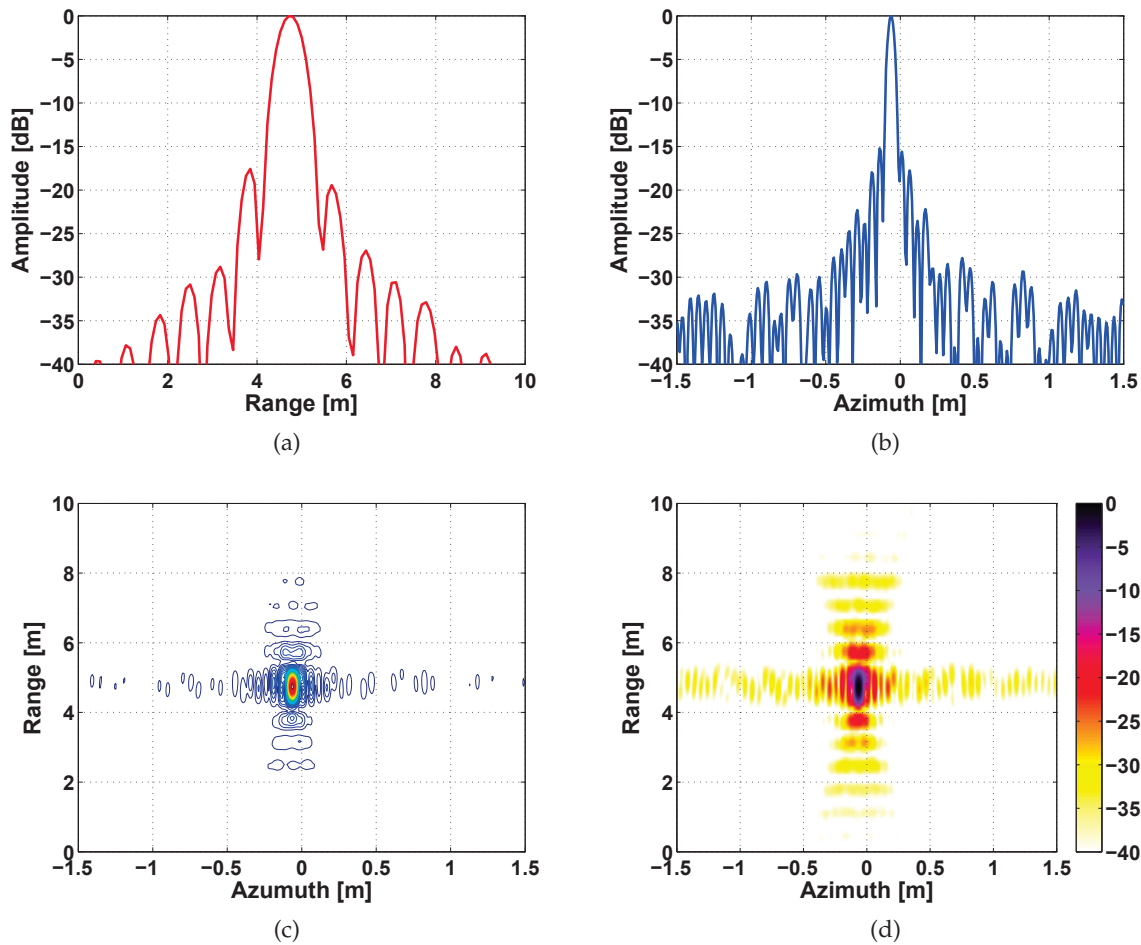
Figure 7.27.: Fully processed MISO SAR image: (a) the range profile, (b) the azimuth profile, (c) 2-D image in linear scale and (d) 2-D image in decibels.

The residual phase rotation via the frequency offset and the delay is also considered. The phase rotation of the target in this experiment yields only 0.014 radian (422.4kHz $\times$ 33.36nsec), which is $0.807°$. Therefore the phase rotation effect is negligible in this experiment. The phase histories before and after the residual phase correction are plotted in Figure 7.28. It is worth noting once again that, in practical spaceborne systems, the phase rotation effect must be removed in time domain before performing the digital beamforming. Since the phase rotation results from the subcarrier offset and varies with the delay time in the linear fashion, its removal can be easily accomplished with range compressed data.
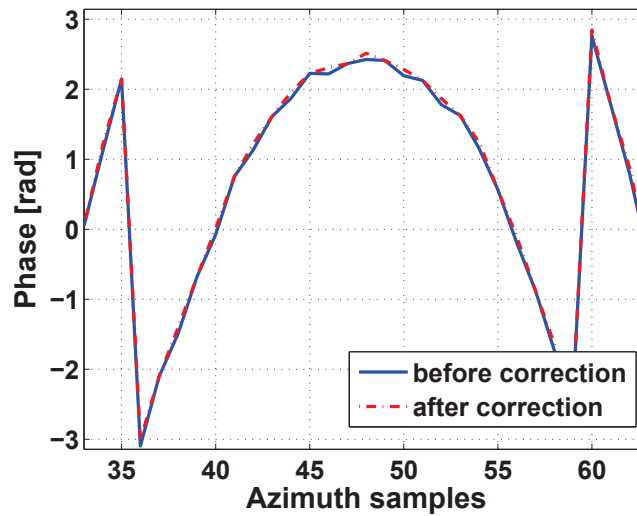
Figure 7.28.: Comparison of the phase histories before and after correction.

7.4.5. MIMO OFDM SAR Experiment: Multiple Targets Imaging

The equivalent MIMO OFDM SAR experiment is extended to a 2×5 MIMO SAR configuration on a multiple targets scenario.

Geometric and Data Acquisition Parameters

Geometric parameters of this experiment in Table 7.5 are analogous to the DBF demonstration in section 7.2. In this experiment, 5 receive subarrays are used, so that the spatial sampling distance and the virtual transmit antenna baseline are extended. Like the former experiment, the used OFDM pulse is 2.366μsec, which is sufficiently long for the delay spread of this target deployment.

Table 7.5.: MIMO geometric parameters.

Parameter	Value	Parameter	Value
OFDM pulse length	2.366μsec	original sampling distance Δd	0.17m
virtual Tx baseline	0.34m	Δd after the conversion	0.34m

The transmit antenna baseline is determined by the original spatial sampling distance, and then the effective sampling distance of the equivalent MIMO system becomes 0.34m, which is double of the optimum sampling distance of the original 1×5 SIMO SAR system. Compared to the 70 azimuth samples in the previous DBF SAR experiment (Table 7.1), the 35 azimuth samples are acquired for each waveform in this MIMO configuration. The OFDM demodulation separates the waveforms and thereby the total 70 samples are recovered.

Imaging Results

The OFDM demodulation is carried out for each receive antenna independently, so that two waveform signals from a single receive channel are recovered at every spatial sample position. These signals actually originate from different spatial positions due to the Tx baseline, so that the separated MIMO signals increase azimuth spatial samples. The DBF exploits these spatial sample data for the azimuth ambiguity suppression.

The measured data is processed with respect to several Doppler processing bandwidths, 100%, 50% and 25% of the full Doppler bandwidth. The resulting images are presented in Figure 7.29. The results do not differ from the DBF demonstration in the prior experiments. The obtained azimuth resolution is 0.046m, 0.092m and 0.184m for each processing bandwidth and the azimuth ambiguity is suppressed up to -30dB. Therefore those overall performances correspond to the DBF SAR experimental results.

Based on the experimental results, the conclusion to be drawn here is that the OFDM waveforms can be successfully separated by the developed demodulation scheme in the multiple targets scenario and exploited in the present MIMO SAR. Furthermore, this experiment verified that the OFDM processing algorithm can also be easily combined with the conventional SAR processing and the DBF.
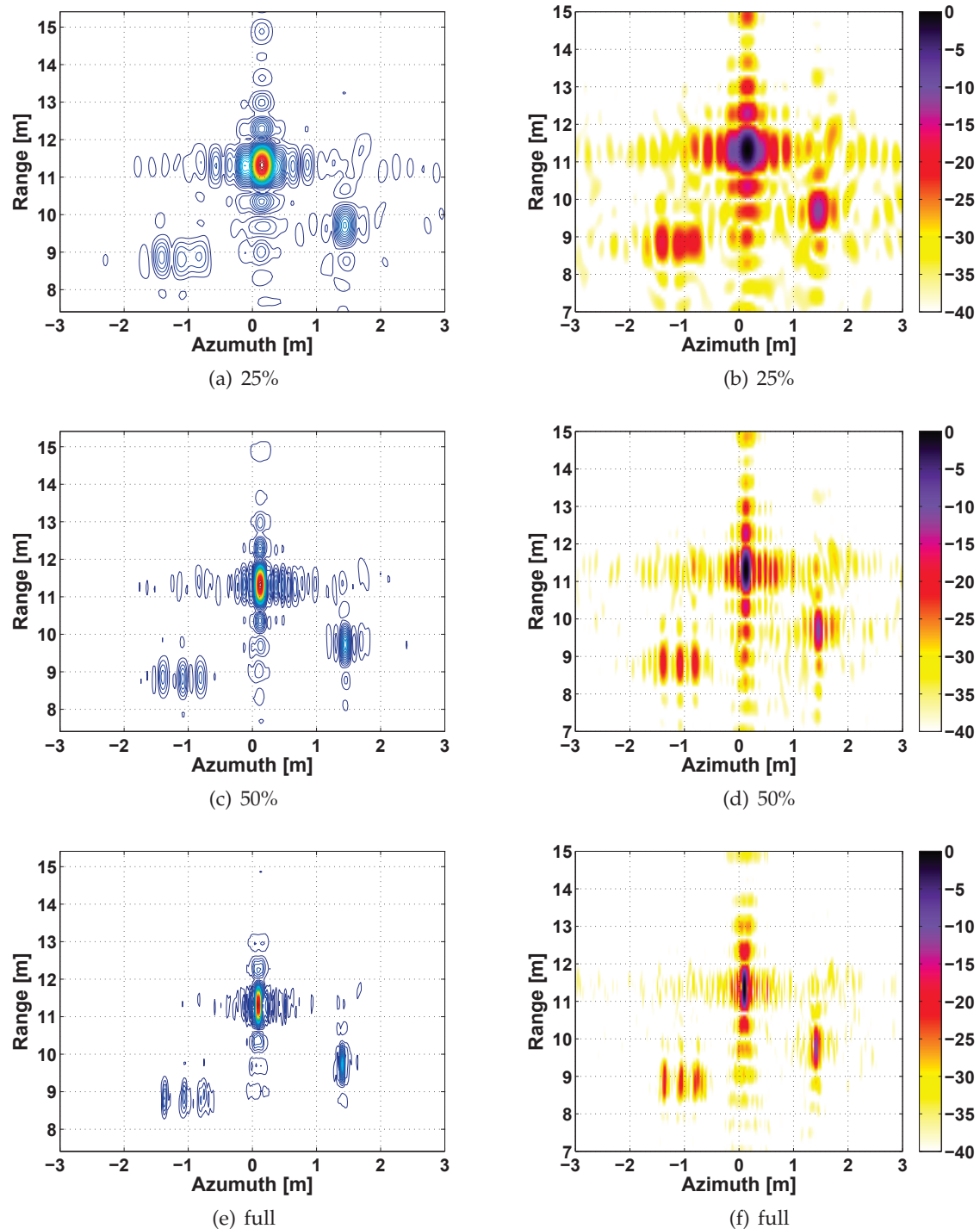
Figure 7.29.: Multiple targets images of the equivalent MIMO OFDM SAR experiments with various Doppler processing bandwidths. The first column presents images in the linear scale, and the second column presents the images in decibels. Each row shows the images built with 25%, 50%, and 100% of the full Doppler processing bandwidth, respectively.

8. Conclusions

The use of multiple antennas in SAR imaging has been spotlighted as a promising method to overcome the current system limitations, however this has also been the most challenging topic at the same time. The state-of-the-art SAR also utilizes multiple receive channels for stereo imaging, in order to retrieve geometric, dynamic and physical information of targets. Yet the ongoing approaches have difficulty expanding current systems to simultaneous multimodal operation systems, due to deficient degrees of freedom in modern system concepts.

In this context, the underlying work has developed a novel multichannel SAR system concept based on multiple antennas both on transmit and receive, called MIMO SAR, and has intensively investigated relevant processing techniques, the digital beamforming and the OFDM waveform scheme. The main achievements of this work are listed as follows:

- Development of a novel MIMO SAR concept and multimodal operation strategies

- Establishment of a new orthogonal waveform scheme based on the OFDM principle and processing algorithms for SAR applications

- Feasibility studies of the novel OFDM waveform scheme with respect to practical SAR channel characteristics and coherence evaluation using real airborne SAR (E-SAR) data

- Hardware development for ground-based multichannel SAR experiments

- Demonstration of the MIMO SAR techniques, in particular digital beamforming in azimuth for the HRWS SAR imaging.

The MIMO SAR aims at the multimodal operation, overcoming the inherent limitations of the state-of-the-art SAR system. The basic idea behind the multimodal operation is to increase spatial samples, which are regarded as degrees of freedom, and to exploit them for various operation modes without any loss of SAR imaging performance. To put it more concretely, this work has extended a digital receive array system by adding extra transmit antennas in order to increase the number of effective antenna phase centers. By reconfiguring the transmit antenna constellation, the MIMO SAR system composes baselines between the phase centers in along- or across-track, and can effectively satisfy the needs of the HRWS imaging and other multichannel data acquisition modes at the same time.

The premise of the versatility of the MIMO SAR system is the simultaneous transmission of multiple orthogonal waveforms through the spatially separated antennas and appropriate processing on receive. However the parallel transmission of multiple waveforms has been a bottleneck, since the complex SAR channel effects, such as the speckle and the RCS fluctuation, lead to the degradation of orthogonality between waveforms, and even a small impurity of orthogonality significantly deteriorates the SAR image quality in distributed target scenarios. This work has resolved the problem by exploiting the OFDM principle for the purpose of multiple orthogonal waveform generation. The novel waveform scheme is based on the polyphase decomposition of orthogonal subcarriers and provides a simple and robust orthogonality between waveforms. In the present work, it has been demonstrated that dual OFDM waveforms from a single chirp signal can be developed. The generated OFDM chirp waveforms have the same characteristics of the original chirp signal. This aspect will be of a special interest for

the implementation of the MIMO SAR system with the modern hardware and digital synthesis technologies. Another very important feature of the novel waveform scheme is high adaptability. It implies that the novel waveform scheme can be easily combined with other waveform schemes, such as the orthogonal phase coding or the multidimensional encoding technique [70]. This is because the waveform scheme is based on the orthogonality of every single subcarrier, which is independent of the type of modulated input signal and dimensions. For example, if the space-frequency modulation is combined with this OFDM waveform scheme, then it will create multiple orthogonal waveforms from each subband via the polyphase composition. In general, any phase coding technique can be applied to input sequences, in order to improve the OFDM demodulation performance or for any other purpose.

In the frame of this work, a relevant processing algorithm for the modulation and the demodulation of the waveform has also been developed, and its feasibility has been intensively investigated in regards to the real SAR channel properties, such as the Doppler effect and the speckle noise, using simulation models. This study result has shown that the developed waveform scheme ensures the orthogonal property in the complex SAR channel, if the OFDM pulse length is shorter than the coherence time[1] of the channel. Furthermore, this work has evaluated the coherence between the waveforms, which is the most critical parameter for the radar polarimetry and interferometry, using real airborne SAR (E-SAR) data. The experimental results lead to the conclusion that the interferometric coherence between two OFDM waveform images is sufficiently high both for distributed and permanent scatterers. In terms of polarimetry, this work has produced equivalent quad-polarization image data from the OFDM waveforms according to the fully polarimetric data acquisition scenario, and thereby investigated the polarimetric performance. By comparison with conventional quad-polarization images, this work has shown that the novel OFDM waveform scheme provides the polarimetric coherence comparable to that of the conventional polarimetric SAR image data. One thing that should be noted is a linear phase ramp in the coherence image, due to the subcarrier offset between the waveforms. This phase term however can be easily estimated and compensated from known OFDM parameters. In conclusion, these experimental results produce decisive evidence to sustain the multimodal operation principles of the present MIMO SAR system.

The underlying work has contributed not only to the development of a new system concept and techniques but also to experimental verifications. For this purpose, a hardware demonstrator has been designed and built up for GB SAR measurements. The GB SAR demonstrator is implemented using commercial RF and digital devices and instruments. This demonstrator has contributed to the first experiment of digital beamforming in SAR and has successfully demonstrated the azimuth ambiguity suppression capability of digital beamforming in a wide range of non-uniform sampling rates.

Throughout the experiment, it has also been found that an imbalance between receive channels leads to significant performance degradation, due to redundant spectral aliasing not eliminated by the digital beamforming or an autofocus technique. In this work, the influence of the channel imbalance has been analyzed and corrected by a time domain channel balancing algorithm based on the spatial covariance between the uniform linear array elements. The channel balancing issue would be of great value when it comes to a practical spaceborne SAR system. However, it is no severe impediment towards the system realization, since the DBF system offers the software-based channel balancing opportunities, which can be more flexible and sophisticated.

---

[1]The coherence time is inversely proportional to the Doppler spread. For a coherence time longer than the OFDM pulse length, the Doppler spread is narrower than the subcarrier spacing.

The experimental data have also been dedicated to the verification of the novel OFDM waveform scheme by means of converting the data to equivalent MIMO OFDM SAR data sets. This experiment is important for the following reasons. Firstly, the experiment provides supportive evidence for the OFDM waveform scheme to be separable on receive. Secondly, the experiment demonstrates that the novel OFDM scheme can be easily combined with the digital beamforming. Therefore, based on the novel waveform scheme and the digital beamforming, the proposed system can achieve the system goal of the multimodal HRWS SAR imaging.

To conclude, there have been numerous approaches and attempts to enhance the SAR imaging performance. A MIMO system is regarded as the most advanced and robust way to exploit multidimensional resources for detecting and imaging targets, and for desired information retrieval. The present study regarding the MIMO SAR concept and techniques lays the foundation for exploiting the spatial, temporal and spectral resources for multiple purposes. It is emphasized that the digital beamforming and the OFDM waveform scheme are the predominant tools to manage such resources and to successfully take advantage of the MIMO system. An important future issue that should be further investigated is the performance validation for the random scattering behavior of nature scenarios [61, 62]. Experimental studies using a ground-based or airborne system is expected to provide a full understanding of the presented OFDM signal responses for a general imaging scenario with distributed targets. Besides, from a technical viewpoint, the present work also inspires further ideas to accelerate technical progress in the MIMO SAR. Here several points are suggested to be pursued and investigated in the future.

The presented OFDM waveform scheme can be combined with advanced *Space-Time Coding* (STC) techniques, such as the Alamouti coding [59, 60]. In practice, the subcarriers in OFDM signals can be encoded by a STC scheme in the frequency domain, a so-called *Space-Frequency Coding* (SFC). Such coding techniques offer the diversity order equal to the number of transmit antennas. For instance, the Alamouti scheme with dual transmission channels provides the maximum 3dB diversity gain, if the total transmission power of both channels is equal to that of a single transmission channel system (half power transmission of individual channels) [7, 100]. By using the full power in each transmission channel, the maximum 6dB gain and 3dB SNR improvement can be achieved. These gain and SNR improvement are very beneficial to the MIMO SAR when covering a wide target area. However, the large delay spreads in a real SAR channel result in a strong frequency selective fading even for the subcarrier spacing, so that the received SFC OFDM signal loses the orthogonality crucial to the decoding [75]. Modern communication systems attempt to resolve this problem using stochastic sub-optimum receiver design approaches, such as the maximum likelihood decoder, zero-forcing detector and decision feedback detector [80]. In the MIMO SAR, the frequency selective channel effect can be mitigated by the spatial filtering that reduces the delay spread of each subswath and then the sub-optimum solution can be used like the communication systems. Further investigations on this issue should be contained in future works in order to fully gain the benefits of the STC.

Another potential is to employ *Frequency Modulated Continuous Wave* (FMCW) signaling in the MIMO SAR. The FMCW technology provides advantages in the compact and simple hardware system, low power consumption and SNR enhancement. In fact, the feasibility of FMCW SAR has been demonstrated using an airborne system [86] and a simple ground-based polarimetric SAR system [135]. This small system design ability is especially valuable for the MIMO SAR composed of multiple transmitters and receivers. Moreover, the 100% duty cycle of an FMCW signal improves the SNR in a SAR image and allows to mitigate the peak transmission power [112]. These aspects also have a special significance in wide area SAR imaging, which is the operational goal of MIMO SAR imaging. From a signal processing point of view, FMCW signal

processing based on the chirp de-ramping technique is highly efficient when combined with the OFDM demodulation algorithm. Exploiting the extended length of FMCW signals, the MIMO SAR can increase the maximum allowable delay spread of a single subswath and relax the strict requirement on the spatial filtering as well. It may allow the more effective implementation of a multistatic MIMO SAR system, based on a fleet of small satellites equipped with light and low-profile antennas instead of a large array. Accordingly, the combination of the FMCW technology and the present MIMO techniques will provide high flexibility from a system design point of view.

Lastly, in future SAR missions, it is of a great interest to employ a large reflector antenna for SAR data acquisition. Tandem-L mission, which is a German proposal for an innovative interferometric L-band radar mission, is a representative example [92]. When combined with a digital feed array, the reflector antenna system allows various advanced modes with the aid of digital beamforming techniques [141, 72]. Therefore the MIMO SAR concept and techniques developed in this work should be extended and further investigated for the reflector antenna system in terms of data acquisition strategies.

A fully adaptive and high performance SAR system, so-called *Smart SAR*, is the ultimate goal of this work as well as various research activities in SAR communities. The MIMO approach presented in this work exhibits a novel way to reach the goal, combining advanced SAR techniques with emerging digital communication techniques. Although different routes and approaches are taken and attempted, the collaborative efforts will substantially boost SAR imaging capabilities and bring a technical synergy effect.

Bibliography

[1] JPL Imaging Radar: SIR-C/X SAR. `http://southport.jpl.nasa.gov/SIRCdesc.html`, Jul. 1994. [Online].

[2] ESA's Earth Observing Mission-ERS Overview. `http://earth.esa.int/ers`, Feb. 2008. [Online].

[3] German Aerospace Center (DLR), E-SAR-The Airborne SAR System of DLR. `http://www.dlr.de/hr/en/desktopdefault.aspx/tabid-2326/3776_read-5679/`, Mar. 2011. [Online].

[4] Modular Arithmetic. Wolfram Mathworld, `http://mathworld.wolfram.com/ModularArithmetic.html`, Jul. 2011. [Online].

[5] RADARSAT-1. `http://www.asc-cas.ca/eng/satellites/radarsat1/`, Feb. 2011. [Online].

[6] F. Ahmad, G. J. Frazer, S. A. Kassam, and M. G. Amin. Design and Implementation of Near-Field, Wideband Synthetic Aperture Beamformers. *IEEE Transactions on Aerospace and Electronic Systems*, 40(1):206–220, Jan. 2004.

[7] S. M. Alamouti. A Simple Transmit Diversity Technique for Wireless Communications. *IEEE Jounal of Selected Area Communications*, 16(8):1451–1458, Oct. 1998.

[8] Analog Devices, Inc. *A Technical Tutorial on Digital Signal Synthesis*, 1999.

[9] P. Antonik, M. Wicks, H. Griffiths, and C. Baker. Multi-Mission Multi-Mode Waveform Diversity. In *Proceedings of IEEE Radar Conference*, pages 580–582, Verona, NY, USA, Apr. 2006.

[10] E. Attia and B. Steinberg. Self-Cohering Large Antenna Arrays using the Spatial Correlation Properites of Radar Clutter. *IEEE Transactions on Antenna and Propagation*, 37(1):30–38, Jan. 1989.

[11] C. A. Balanis. *Antenna Theory: Analysis and Design*. John Wiley & Sons, Inc, 1997.

[12] R. Bamler and P. Hartl. Synthetic Aperture Radar Interferometry. *Inverse Problems*, 14:R1–R54, 1998.

[13] I. Bekkrman and J. Tabrikian. Target Detection and Localization using MIMO Radars and Sonars. *IEEE Transactions on Signal Processing*, 54(10):3873–3883, Oct. 2006.

[14] D. W. Bliss and K. W. Forsythe. Multiple-Input Multiple-Output (MIMO) Radar and Imaging: Degrees of Freedom and Resolution. In *Proceedings of the 37th Asilomar Conference on Signals, Systems and Computers*, volume 1, pages 54–59, Pacific Grove, CA, USA, Nov. 2003.

[15] F. Bordoni, M. Younis, E. Varona, N. Gebert, and G. Krieger. Performance Investigation on SCan-On-REceive and Adaptive Digital Beamforming for High-Resolution Wide-Swath Synthetic Aperture Radar. In *Proceedings of International ITG Workshop on Smart Antennas*, pages 114–119, Berlin, Germany, Feb. 2009.

[16] M. Born and E. Wolf. *Principles of Optics*. Pergamon, 5th edition, 1975.

[17] W. M. Börner and Y. Yamaguchi. A State-of-the-Art Review in Radar Polarimetry and Its Applications in Remote Sensing. *IEEE Aerospace and Electronic Systems Magazine*, 5(6):3–6, Jun. 1990.

[18] J. Brown. Multi-Channel Sampling of Low-Pass Signals. *IEEE Transactions on Circuits and Systems*, 28(2):101–106, 1981.

[19] J. Capon. High-Resolutin Frequency-Wavenumber Spectrum Analysis. *Proceedings of The IEEE*, 57(8):1408–1419, Aug. 1969.

[20] W. Carrara, R. Goodman, and R. Majewski. *Spotlight Synthetic Aperture Radar Signal Processing Algorithms*. Artech House, Inc, 1995.

[21] H. K. Chan and T. S. Yeo. Noniterative Quality Phase-Gradient Autofocus (QPGA) Algorithm for Spotlight SAR Imagery. *IEEE Transactions on Geoscience and Remote Sensing*, 36(5):1531–1539, Sep. 1998.

[22] R. W. Chang. *Orthogonal Frequency Division Multiplexing*. U.S. Patent 3,488,445, Jan. 1970.

[23] C. T. Charles. *A Calibrated Phase and Amplitude Control System for Phased-Array Transmitters*. PhD thesis, University of Washington, 2006.

[24] S. R. Cloude and K. P. Papathanassiou. Polarimetric SAR Interferometry. *IEEE Transactions on Geoscience and Remote Sensing*, 36(5):1551–1565, Sep. 1998.

[25] R. Crochiere and L. Rabiner. Optimum FIR Digital Filter Implementations for Decimation, Interpolation, and Narrow-band Filtering. *IEEE Transactions on Acoustics, Speech and Signal Processing*, 23(5):444–456, 1975.

[26] R. Crochiere and L. Rabiner. *Multirate Digital Processing*. Englewoold Cliffs NJ: Prentice-Hall Inc., 1983.

[27] R. Crochiere and L. Rabiner. *Advanced Topics in Signal Processing*, chapter multirate processing of digital signal. Englewoold Cliffs NJ: Prentice-Hall Inc., 1988.

[28] J. Crols and M. Steyaert. Low-IF Topologies for High-Performance Analog Front Ends of Fully Integrated Receivers. *IEEE Transactions on Circuits and Systems-II: Analog and Digital Signal Processing*, 45(3):269–282, Mar. 1998.

[29] I. G. Cumming and F. H. Wong. *Digital Processing of Synthetic Aperture Radar Data*. Arthec House, Inc., 2005.

[30] J. C. Curlander and R. N. McDonough. *Synthetic Aperture Radar Systems and Signal Processing*. John Wiley & Sons, Inc, 1991.

[31] A. Currie and M. A. Brown. Wide-swath SAR. *IEE Proceeding*, 139(2):122–135, Apr. 1992.

[32] H. Deng. Discrete Frequency-Coding Waveform Design for Netted Radar Systems. *IEEE Signal Processing Letters*, 11(2):179–182, Feb. 2004.

[33] C. Dolph. A Current Distribution for Broadside Arrays Which Optimizes the Relationship between Beam Width and Side-Lobe Level. *Processings of The IRE*, 34(6):335–348, 1946.

[34] C. Elachi. *Introduction to the Physics and Techniques of Remote Sensing*. John Wiley & Sons, Inc, 1987.

[35] C. Elachi. *Spaceborne Radar Remote Sensing: Applications and Techniques*. IEEE Press, 1987.

[36] J. Ender. MIMO SAR. In *Proceedings of International Radar Symposium*, pages 667–674, Cologn, Germany, Sep. 2007.

[37] J. Ender. Along-Track Array Processing for MIMO-SAR/MTI. In *Proceedings of European Conference on Synthetic Aperture Radar*, volume 4, pages 67–70, Friedrichshafen, Germany, Jun. 2008.

[38] J. Ender, C. Gierull, and D. Cerutti-Maori. Improved Space-Based Moving Target Indication via Alternate Transmission and Receiver Switching. *IEEE Transactions on Geoscience and Remote Sensing*, 46(12):3960–1974, Dec. 2008.

[39] M. Engels. *Wireless OFDM Systems-how to make them work?* Kluwer Academic Publishers, 2002.

[40] E. Farnet and G. Stevens. *Pulse Compression Radar in Radar Handbook*, chapter 10. New York:McGraw-Hill, second edition, 1990.

[41] J. Farooq, M. Temple, and M. Saville. Exploiting Frequency Diversity Array Processing to Improve SAR Image Resolution. In *Proceedings of IEEE Radar Conference*, pages 1–5, Rome, Italy, May 2008.

[42] C. Fischer, C. Schäfer, and C. Heer. Digital Beamforming Antenna for Synthetic Aperture Radar. In *Proceedings of the 2nd European Conference on Antennas and Propagation*, pages 1–5, Edinburgh, UK, Nov. 2007.

[43] E. Fishler, A. Hamovich, R. blum, D. Chizhik, L. Cimini, and R. Valenzuela. MIMO RADAR : An idea whose time has come. In *Proceedings of IEEE Radar Conference*, pages 71–78, Philadelphia, PN, USA, Apr. 2004.

[44] G. Franken, H. Nikookar, and P. van Genderen. Doppler Tolerance of OFDM-Coded Radar Signals. In *Proceedings of 3rd European Radar Conference*, pages 108–111, Manchester, UK, Sep. 2006.

[45] A. Freeman, G. Krieger, P. Rosen, M. Younis, W. Johnson, S. Huber, R. Jordan, and A. Moreira. SweepSAR: Beam-Forming on Receive using A Reflector-Phased Array feed Combination for Spaceborne SAR. In *Proceedings of IEEE Radar Conference*, pages 1–9, Pasadena, CA, USA, May 2009.

[46] B. Friedlander and A. Weiss. Eigenstructure Methods for Direction Finding with Sensor Gain and Phase Uncertainties. In *Proceeding of International Conference on Acoustic, Speech and Signal Processing*, volume 5, pages 2681–2684, New York, NY, USA, Apr. 1988.

[47] T. Gall. Realization of a Transceiver System for a DBF SAR Demonstrator. Master's thesis, Universität Karlsruhe, Jul. 2005.

[48] R. Garg, P. Bhartia, I. Bahl, and A. Ittipiboon. *Microstrip Antenna Design Handbook*. Artech House, Inc, 2001.

[49] N. Gebert, G. Krieger, and A. Moreira. Digital Beamforming on Receive: Techniqus and Optimization Strategies for High-Resolution Wide-Swath SAR Imaging. *IEEE Transactions on Aerospace and Electronic Systems*, 45(2):564–592, Apr. 2009.

[50] C. H. Gierull. Digital Channel Balancing of Along-Track Interferometric SAR Data. Technical report, Defence RD Canada, Mar. 2003.

[51] R. Girad, P. Lee, and K. James. The RADARSAT-2 and 3 Topographic Mission: An Overview. In *Proceedings of International Geoscience and Remote Sensing Symposium*, volume 3, pages 1477–1479, Toronto, Canada, Jun. 2002.

[52] R. C. Hansen. *Phased Array Antennas*. John Wiley & Sons, Inc, 1998.

[53] R. Hoctor and S. Kassam. The Unifying Role of the Coarray in Aperture Synthesis for Coherent and Incoherent Imaging. *Proceedings of The IEEE*, 78(4):735–752, Apr. 1990.

[54] E. Ifeachor and B. Jervis. *Digital Signal Processing: A practical approach*. Addison-Wesley Publichers Ltd., 1993.

[55] R. Joost and R. Salomon. Advantages of FPGA-based Multiprocessor Systems in Industrial Applications. In *Proceedings of 31st Annual Conference of the IEEE Industrial Electronics Society*, page 6pp, Raleigh, NC, USA, Nov. 2005.

[56] J. Joseph C. Liberti and T. S. Rappaport. *Smart Antennas for Wireless Communications*. Prentice Hall PTR, 1999.

[57] K. Jumani and K. Sarabandi. An Investigation of PN Sequences for Multistatic SAR/InSAR Applications. In *Proceedings of International Geoscience and Remote Sensing Symposium*, pages 1102–1105, Barcelona, Spain, Jul. 2007.

[58] J. Kim, A. Ossowska, and W. Wiesbeck. Experimetal Investigation of Digital Beamforming SAR Performance using a Ground-Based Demonstrator. In *Proceedings of International Geoscience and Remote Sensing Symposium*, pages 111–114, Barcelona, Spain, Jul. 2007.

[59] J. Kim, A. Ossowska, and W. Wiesbeck. Investigation of MIMO SAR for Interferometry. In *Proceedings of European Radar Conference*, pages 51–54, Munich, Germany, Oct. 2007.

[60] J. Kim and W. Wiesbeck. Investigation of a New Multifunctional High Performance SAR System Concept Exploiting MIMO Technology. In *Proceedings of International Geoscience and Remote Sensing Symposium*, volume 2, pages II–221 –II–224, Boston, MA, USA, Jul. 2008.

[61] J. Kim, M. Younis, A. Moreira, and W. Wiesbeck. A Novel OFDM Waveform for Fully Polarimetric SAR Data Acquisition. In *Proceedings of European Conference on Synthetic Aperture Radar*, pages 410–413, Aachen, Germany, Jun. 2010.

[62] J. Kim, M. Younis, A. Moreira, and W. Wiesbeck. A Novel OFDM Chirp Waveform Scheme for Use of Multiple Transmitters in SAR. *submitted for IEEE Geoscience and Remote Sensing Letters*, 2011.

[63] J. Kim, M. Younis, and W. Wiesbeck. Experimetal Performance Investigation of Digital Beamforming on Synthetic Aperture Radar. In *Proceedings of International Geoscience and Remote Sensing Symposium*, volume 4, pages 176–179, Boston, USA, Jul. 2008.

[64] Y. Kim and J. van Zyl. Overview of Polarimetric Interferometry. In *Proceedings of IEEE Aerospace Conference*, volume 3, pages 231–236, Big Sky, MT, USA, Mar. 2000.

[65] J. Klare, D. Cerutti-Maori, A. Brenner, and J. Ender. Image Quality Analysis of the Vibrating Sparse MIMO Antenna Array of the Airborne 3D Imaging. In *Proceedings of International Geoscience and Remote Sensing Symposium*, pages 5315–5318, Barcelona, Spain, Jul. 2007.

[66] J. Klare, M. Weiss, O. Peters, A. Brenner, and J. Ender. ARTINO: A New High Resolution 3D Imaging Radar System on an Autonomous Airborne Platform. In *Proceedings of International Geoscience and Remote Sensing Symposium*, pages 3842–3845, Denver, CO, USA, Jul. 2006.

[67] R. Klemm. *Space-Time Adaptive Processing: Principles and Applications*. The Institution of Electrical Engineers, London, UK, 1998.

[68] H. J. Kramer. *Observation of the Earth and Its Environment: Survey of Missions and Sensors*. Springer-Verlag, 1996.

[69] G. Krieger, N. Gebert, and A. Moreira. Unambiguous SAR Signal Reconstruction from Nonuniform Displaced Phase Center Sampling. *IEEE Geoscience and Remote Sensing Letters*, 1(4):260–264, Oct. 2004.

[70] G. Krieger, N. Gebert, and A. Moreira. Multidimensional Waveform Encoding: A New Digital Beamforming Technique for Synthetic Aperture Radar Remote Sensing. *IEEE Transactions on Geoscience and Remote Sensing*, 46(1):31–46, Jan. 2008.

[71] G. Krieger, A. Moreira, H. Fiedler, I. Hajnsek, M. Werner, M. Younis, and M. Zink. TanDEM-X: A Satellite Formation for High-Resolution SAR Interferometry. *IEEE Transactions on Geoscience and Remote Sensing*, 45(11):3317–3341, Nov. 2007.

[72] G. Krieger, M. Younis, N. Gebert, S. Huber, F. Bordoni, A. Patyuchenko, and A. Moreira. Advanced Digital Beamforming Concepts for Future SAR Systems. In *Proceedings of International Geoscience and Remote Sensing Symposium*, pages 245–248, Honolulu, Hawaii, USA, Jul. 2010.

[73] J. Lee and E. Pottier. *Polarimetric Radar Imaging:from basis to applications*. CRC Press, 2009.

[74] J. S. Lee, K. Hoppel, and S. A. Mango. Unsupervised Estimation of Speckle Noise in Radar Image. *Internal Journal of Imaging Systems and Technology*, 4:298–305, 1992.

[75] K. F. Lee and D. B. Williams. A Space-Frequency Transmitter Diversity Technique for OFDM Systems. In *IEEE Global Telecommunications Conference (GLOBECOM)*, volume 3, pages 1473–1477, San Francisco, CA, USA, Nov/Dec. 2000.

[76] N. H. Lehmann, E. Fishler, A. M. Haimovich, R. blum, D. Chizhik, L. Cimini, and R. Valenzuela. Evaluation of Transmit Diversity in MIMO Radar Direction Finding. *IEEE Transactions on Signal Processing*, 55(5):2215–2225, May. 2007.

[77] N. Levanon. Multifrequency Complementary Phase-Coded Radar Signal. *IEE Proceedings Radar, Sonar and Navigation*, 147(6):276–284, Dec. 2000.

[78] J. Li, X. Zheng, and P. Stoica. MIMO SAR Imaging: Signal Synthesis and Receiver Design. In *Proceedings of 2nd IEEE International Workshop on Computational Advances in Multi-Sensor Adaptive Processing (CAMPSAP)*, pages 89–92, Virgin Islands, USA, Dec. 2007.

[79] Z. Li, Z. Bao, H. Wang, and G. Liao. Performance Improvement for Constellation SAR using Signal Processing Techniques. *IEEE Transactions on Aerospace and Electronic Systems*, 42(2):436–452, 2006.

[80] D. Lin, P. Chiang, and H. Li. Performance Analysis of Two-Branch Transmit Diversity Block-Coded OFDM Systems in Time-Varying Multipath Rayleigh-Fading Channels. *IEEE Transactions on Vehicular Technology*, 54(1):136–149, Jan. 2005.

[81] P. Lombardo. A Multichannel Spaceborne Radar for the COSMO-Skymed Satellite Constellation. In *Proceedings of IEEE Aerospace Conference*, volume 1, pages 111–119, Big Sky, MT, USA, Mar. 2004.

[82] C. Lopez-Martinez and E. Pottier. On the Extension of Multidimensional Speckle Noise Model from Single-Look to Multilook SAR Imagery. *IEEE Transactions on Geoscience and Remote Sensing*, 45(2):305–320, Feb. 2007.

[83] J. Mahattanakul. The Effect of I/Q Imbalance and Complex Filter Component Mismatch in Low-IF Receivers. *IEEE Transactions on Circuits and Systems*, 53(2):247–254, Feb. 2006.

[84] A. Maria, M. Limbach, R. Horn, and A. Reigber. Reflectarray Membrane Study for Deployable SAR Antenna. In *Proceedings of European Conference on Antennas and Propagation (EuCAP)*, pages 3720–3723, Berlin, Germany, Jun. 2009.

[85] K. Martin. Complex Signal Processing is Not Complex. *IEEE Transactions on Circuits and Systems*, 51(9):1823–1836, Sep. 2004.

[86] A. Meta, P. Hoogeboom, and L. Ligthart. Signal Processing for FMCW SAR. *IEEE Transactions on Geoscience and Remote Sensing*, 45(11):3519–3532, Nov. 2007.

[87] J. Mittermayer. *Hochauflösende Verarbeitung von Radardaten mit Synthetischer Apertur*. PhD thesis, Universität Siegen, 2000.

[88] J. Mittermayer, A. Moreira, and O. Loffeld. Spotlight SAR Data Processing using the Frequency Scaling Algorithm. *IEEE Transactions on Geoscience and Remote Sensing*, 37(5):2198 – 2214, Sep. 1999.

[89] R. A. Monzingo. *Introduction to Adaptive Array*. John Wiley & Sons, Inc, 1980.

[90] R. K. Moore, J. P. Claassen, and Y. H. Lin. Scanning Spaceborne Synthetic Aperture Radar with Integrated Radiometer. *IEEE Transactions on Aerospace and Electronic Systems*, ASE-17:410–421, 1981.

[91] A. Moreira. *Radar mit Synthetischer Apertur: Grundlagen und Signalverabeitung*. Hablitationsschrift, Universität Karlsruhe (TH), Oct. 2000.

[92] A. Moreira, I. Hajnsek, G. Krieger, K. Papathanassiou, M. Eineder, F. D. Zan, M. Younis, and M. Werner. Tandem-L: Monitoring the Earth's Dynamics with InSAR and Pol-InSAR. In *Proceedings of the International Workshop on Applications of Polarimetry and Polarimetric Interferometry (Pol-InSAR)*, Frascati, Italy, Jan. 2009.

[93] E. Mozeson and N. Levanon. Multicarrier Radar Signals with Low Peak-to-Mean Envelope Power Ratio. *IEE Proceedings Radar, Sonar and Navigation*, 150(2):71–77, April. 2003.

[94] C. E. Muehe and M. Labitt. Displaced-Phase-Center Antenna Technique. *Lincoln Laboratory Journal, MIT*, 12(2):281–296, 2000.

[95] D. S. Navarro. Design and Evaluation of Antenna System for DBF SAR Demonstrator. Master's thesis, Universität Karlsruhe, Jul. 2005.

[96] J. Norris, P. Vachon, D. Schlingmeier, R. English, and L. Gallop. Expendable Trihedral Corner Reflectors for Target Enhancement and Position Control in RADARSAT-1 Fine Beam Mode SAR Imagery. Technical report, Defence RD Canada, Sep. 2004.

[97] A. Oppenheim, A. Willsky, and S. Nawab. *Signals and Systems*. Prentice-Hall International, Inc., second edition, 1997.

[98] S. Parashar. RADARSAT Program. In *Proceedings of International Geoscience and Remote Sensing Symposium*, volume 3, pages 1709–1713, Pasadena, California, USA, August 1994.

[99] A. Paulraj and T. Kailath. Increasing Capacity in Wireless Broadcast Systems using Distributed Transmission/Directional Reception. US Patent 5 345 599, 1994.

[100] A. Paulraj, R. Nabar, and D. Gore. *Introduction to Space-Time Wireless Communications*. Cambridge University Press, 2003.

[101] A. Peled and A. Ruiz. Frequency Domain Data Transmission using Reduced Computational Complexity Algorithms. In *Proceedings of IEEE International Conference on Acoustics, Speech and Signal Processing*, volume 5, pages 964–967, Toulouse, France, Aprl. 1980.

[102] T. Rappaport. *Wireless Communications: Principles and Practice*. Prentice-Hall International, Inc., second edition, 2002.

[103] B. Razavi. *RF Microelectronics*. Prentice-Hall Inc., 1998.

[104] H. Ricken, H. Schute, R. Horn, R. Scheiber, and M. Wendler. ProSmart II: E-SAR Level 3 Product Specifications for TerraSAR Simulation. Technical note, Institut für Hochfrequenztechnik und Radarsysteme (HR), Deutsches Zentrum für Luft- und Raumfahrt (DLR), 1999.

[105] P. Robertson and S. Kaiser. Analysis of Doppler Spread Perturbations in OFDM(A) Systems. *European Transactions on Telecommunications*, 11(6):585–592, Nov/Dec. 2000.

[106] F. C. Robey, S. Coutts, D. Weikle, J. C. McHarg, and K. Cuomo. MIMO Radar Theory and Experimental Results. In *Proceedings of the 38th Asilomar Conference on Signals, Systems and Computers*, volume 1, pages 300–304, Pacific Grove, CA, USA, Nov. 2004.

[107] R. Sabry and G. Geling. A New Approach for Radar/SAR Target Detection and Imagery Based on MIMO System Concept and Adaptive Space-Time Coding. Technical report, Defence R&D Canada, May 2007.

[108] M. Sato, M. Watanabe, and K. Iribe. Polarimetric SAR Observation by ALOS. In *Proceedings of the Asia-Pacific Microwave Conference 2007*, pages 1–4, Bangkok, Thailand, Dec. 2007.

[109] K. Schuler. *Intelligente Antennensysteme für Kraftfahrzeug-Nahbereichs-Radar-Sensorik*. PhD thesis, Institut für Hochfrequenztechnik und Elektronik (IHE), Universität Karlsruhe, Nov. 2007.

[110] M. I. Skolnik. *Introduction to Radar Systems*. McGRAW-HILL Companies, third edition, 2001.

[111] M. Soumekh. Bistatic Synthetic Aperture Radar Inversion with Application in Dynamic Object Imaging. *IEEE Transactions on Signal Processing*, 39(9):2004–2055, Sep. 1991.

[112] M. Soumekh. FM-CW SAR and Phased Array Spatial-Velocity Imaging. In *Proceedings of IEEE International Conference on Image Processing (ICIP)*, volume 1, pages 471–475, Austin, TX, USA, Nov. 1994.

[113] M. Soumekh. *Synthetic Aperture Radar Signal Processing with Matlab Algorithms*. John Wiley & Sons, Inc, 1999.

[114] M. Stangl, R. Werninghaus, B. Schweizer, C. Fischer, M. Brandfass, and J. Mittermayer. TerraSAR-X Technologies and First Results. *IEE Proceedings Radar, Sonar and Navigation*, 153(2):86–95, Apr. 2006.

[115] B. D. Steinberg. *Principles of Aperture and Array System Design*. John Wiley & Sons, Inc, 1976.

[116] W. L. Stutzman and G. A. Thiele. *Antenna Theory and Design*. John Wiley & Sons, Inc, 1998.

[117] M. Suess, B. Grafmueller, and R. Zahn. A Novel High Resolution Wide Swath SAR System. In *Proceedings of International Geoscience and Remote Sensing Symposium*, pages 1013–1015, Sydney, Australia, Jul. 2001.

[118] R. J. Sullivan. *Microwave Radar Imaging and Advanced Concepts*. Arthec House, Inc., 2000.

[119] M. Süß and W. Wiesbeck. *Side-Looking Synthetic Aperture Radar System*. European Patent 1 241 487 A1, Sep. 2002.

[120] Tektronix. *AWG710 and AWG710B Arbitrary Waveform Generator User Manual*, 2004.

[121] S. Thompson, A. Ahmed, J. Proakis, J. Zeidler, and M. Geile. Constant Envelope OFDM. *IEEE Transactions on Communications*, 56(8):1300–1312, Aug. 2008.

[122] K. Tomiyasu. Tutoral Review of Synthetic Aperture Radar (SAR) with Applications to Imaging of the Ocean Surface. *Proceedings of The IEEE*, 66(5):563–583, May 1978.

[123] B. D. V. Veen and K. M. Buckley. Beamforming: A Versatile Approach to Spatial Filtering. *IEEE Acoustics, Speech, Signal Processing (ASSP) Magazine*, 5:4–24, Aprl. 1988.

[124] P. Vizmuller. *RF Design Guide: Systems, Circuits, and Equations*. Artech House, Inc, 1995.

[125] D. Wahl, P. Elchel, D. Ghiglia, and C. J. Jr. Phase Gradient Autofocus - A Robust Tool for High Resolution SAR Phase Correction. *IEEE Transactions on Aerospace and Electronic Systems*, 30(3):827–835, Jul. 1994.

[126] J. Walker. Range-Doppler Imaging of Rotating Objects. *IEEE Transactions on Aerospace and Electronic Systems*, 16(1):23–52, Jan. 1980.

[127] L. Wang and C. Tellambura. An Overview of Peak-to-Average Power Ratio Reduction for OFDM Systems. In *Proceedings of IEEE International Symposium on Signal Processing and Information Technology*, pages 840–845, Vancouver, Canada, Aug. 2006.

[128] W. Wang. Applications of MIMO Technique for Aerospace Remote Sensing. In *Proceedings of IEEE Aerospace Conference*, pages 1–10, Big Sky, MT, USA, Mar. 2007.

[129] S. Weinstein and P. Ebert. Data Transmission by Frequency-Division Multiplexing using the Discrete Fourier Transform. *IEEE Transactions on Communications*, 19(5):628–634, Oct. 1971.

[130] W. Wiesbeck. SDRS: Software Defined Radar Sensors. In *Proceedings of International Geoscience and Remote Sensing Symposium*, volume 7, pages 3259–3261, Sydney, Australia, Jul. 2001.

[131] W. Wiesbeck. *Lecture script: Radar System Engineering*. Institut für Hochfrequenztechnik und Elektronik (IHE), Universität Karlsruhe, 2009.

[132] C. Wiley. Synthetic Aperture Radars - A Paradigm for Technology Evolution. *IEEE Transactions on Aerospace and Electronic Systems*, AES-21:440–443, May 1985.

[133] M. Windisch and G. Fettweis. Blind I/Q Imbalance Parameter Estimation and Compensation in Low-IF Receivers. In *Proceedings of 1st International Symposium on Control, Communications and Signal Processing (ISCCSP)*, pages 75–79, Hammamet, Tunisia, Mar. 2004.

[134] P. Wu, H. Chang, M. Tsai, T. Huang, and H. Wang. New Miniature 15-20GHz Continuous Phase/Amplitude Control MMICs using 0.18μm CMOS Technology. *IEEE Transactions on Microwave Theory and Techniques*, 54(1):10–19, Jan. 2006.

[135] Y. Yamaguchi, T. Nishikawa, M. Sengoku, and W. Boerner. Two-Diemensional and full Polarimetric Imaging by a Synthetic Aperture FM-CW Radar. *IEEE Transactions on Geoscience and Remote Sensing*, 33(2):421–427, Mar. 1995.

[136] L. Ye(Geoffrey) and J. L.J. Cimini. Bounds on the Interchannel Interference of OFDM in Time-Varying Impariments. *IEEE Transactions on Communications*, 49(3):401–404, Mar. 2001.

[137] M. Younis. *Digital Beamforming for High Resolution Wide Swath Real and Synthetic Aperture Radar*. PhD thesis, Institut für Hochfrequenztechnik und Elektronik (IHE), Universität Karlsruhe, Jul. 2004.

[138] M. Younis, M. Baldauf, and W. Wiesbeck. *Lecture script: Advanced Radio Communication I*. Institut für Hochfrequenztechnik und Elektronik (IHE), Universität Karlsruhe, 2006.

[139] M. Younis, C. Fischer, and W. Wiesbeck. Digital Beamforming in SAR Systems. *IEEE Transactions on Geoscience and Remote Sensing*, 41(71):1735–1739, Jul. 2003.

[140] M. Younis, S. Huber, A. Patyuchenko, F. Bordoni, and G. Krieger. Performance Comparison of Reflector- and Planar-Antenna based Digital Beamforming SAR. *Internal Journal of Antenna and Propagation*, pages 1–13, 2009.

[141] M. Younis, A. Patyuchenko, S. Huber, G. Krieger, and A. Moreira. A Concept for a High Performance Reflector-Based X-Band SAR. In *Proceedings of European Conference on Synthetic Aperture Radar*, pages 740–743, Aachen, Germany, Jun. 2010.

[142] K. Yu and D. Murrow. Adaptive Digital Beamforming Radar for Monopulse Angle Estimation in Jamming. *IEEE Transactions on Aerospace and Electronic Systems*, 37(2):508–523, Apr. 2001.

[143] R. Zandona-Schneider, L. Marotti, and K. P. Papathanassiou. Coherent Scatters at Different Polarizations and Frequencies. In *Proceedings of European Conference on Synthetic Aperture Radar*, Dresden, Germany, May 2006.

[144] H. A. Zebker and J. J. V. Zyl. Imaging Radar Polarimetry. *Proceedings of The IEEE*, 79(11):1583–1606, Nov. 1991.

[145] J. Zhang and A. Papandreou-Suppappola. MIMO Radar with Frequency Diversity. In *Proceedings of International Waveform Diversity and Design Conference*, pages 208–212, Kissimmee, FL, USA, Feb. 2009.

Appendices

A. DPCA Principle: Geometric Aspect

In this Appendix, the geometric aspect of the DPCA is highlighted. The DPCA technique was originally developed for the purpose of the performance improvement of the *Ground Moving Target Indicator* (GMTI) [31, 67, 94, 110]. From an antenna constellation, as shown in Figure A.1, two separated effective phase centers are produced. The DPCA technique exploits these two antenna phase centers in order to suppress stationary clutter responses and to detect moving target responses.
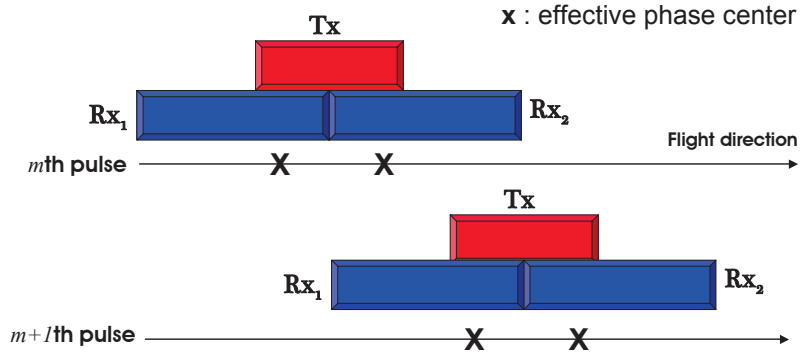
Figure A.1.: Distribution of the effective phase centers generated from the quasi-bistatic configuration with a single Tx antenna and two Rx antennas along the flight direction in the successive pulse transmission.

The first two effective phase centers are generated at the mth data acquisition, and subsequently the other two phase centers are obtained at the next $(m + 1)$th acquisition, due to the sensor movement. The number of the effective phase centers are equal to the number of bistatic pairs (Tx-Rx$_1$ and Tx-Rx$_2$), and located at the middle of the baseline between the Tx and Rx antennas [31]. The effective phase center of the $i-j$th bistatic pair is illustrated in Figure A.2.

In this figure, it is assumed that the transmit and receive antennas are separated in only the flight direction, plus the distances from both antennas to the target is incomparably longer than the baseline (dash line). Thus the interior angle φ is small enough ($\varphi \ll 1$). The round-trip distance of the bistatic pair is equivalent to the diagonal length from the target position to the opposite in the parallelogram. In other words, the round-trip distance is two times the value of the diagonal vector length, $|\vec{P}_{e,ij}|$, in Figure A.2:

$$|\vec{P}_{e,ij}| = \frac{|\vec{Tx}_j + \vec{Rx}_i|}{2}. \tag{A.1}$$

According to the property of that the the diagonals of a parallelogram bisect each other, the other diagonal (baseline) from the transmitter to the receiver is equally divided. Therefore the
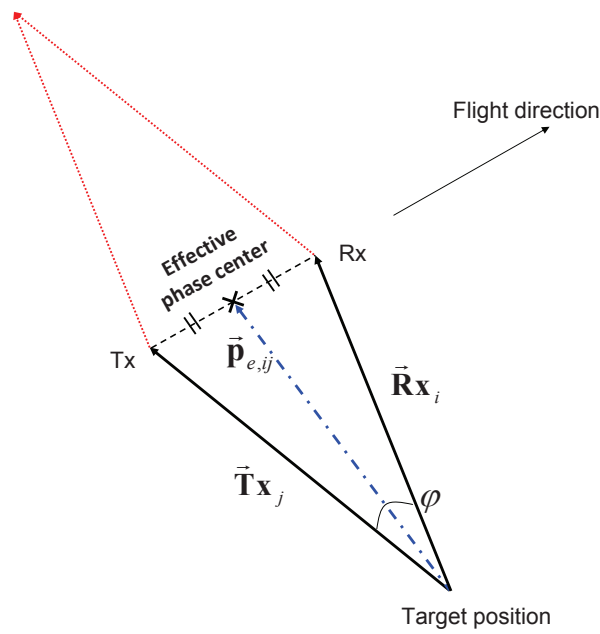
Figure A.2.: Effective phase center position vector of the *i-j*th bistatic pair using a parallelogram.

vector $\vec{\mathbf{P}}_{e,ij}$ points to the center of the parallelogram and this point is the effective phase center of the bistatic configuration.

In summary, the DPCA principle makes it possible to map the separated Tx-Rx constellation into an equivalent monostatic configuration and simplifies the establishment of the spatial sampling criterion in multiple aperture SAR systems [69, 139, 137]. Although higher order phases remain, they can be estimated by an analytic signal model and compensated in the case of a single platform system [137].

B. Derivation of MVDR Beamformer

The section describes a mathematical derivation of the MVDR method, which allows a high-resolution spectral estimation, by means of adaptively altering a weight [19]. The wavenumber, also known as the spatial frequency, is the magnitude of a wave vector which indicates its propagation direction. When the wavenumber is measured in the boresight direction of a sensor, then it varies with the incident angle ψ_o. Figure B.1 depicts the wavenumber change, depending on the incident angle.
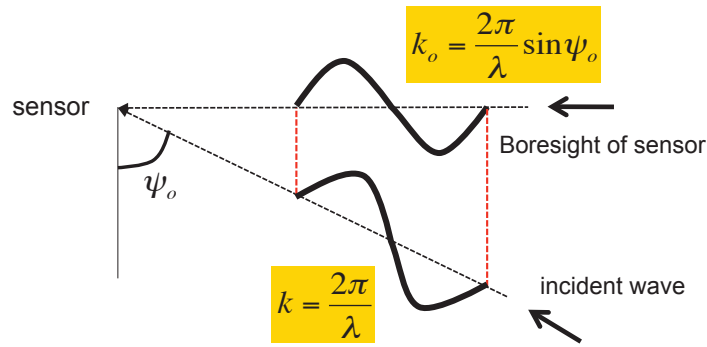
Figure B.1.: Illustration of the wavenumber depending on the incident angle.

Therefore the estimation of the wavenumber is in accordance with finding the direction of the wave impinging on the sensor. Recalling the constrained optimization problem described in (3.58) in section 3.3.3, it is rewritten as the general form:

$$\min_{\mathbf{w}} \mathbf{w}^H \mathbf{R}_{rr} \mathbf{w} \quad \text{subject to} \quad \mathbf{w} \cdot \mathbf{a}(k_o) = 1 \tag{B.1}$$

where k_o is the wavenumber of desired signal; $\mathbf{R}_{rr}$ is the covariance matrix; $\mathbf{w}$ is the optimum weight vector; and $\mathbf{a}$ is the steering vector. An optimum beamforming weight can be found by minimizing the following Lagrangian:

$$\mathcal{L} = \mathbf{w}^H \mathbf{R}_{rr} \mathbf{w} + \xi \cdot (\mathbf{w} \cdot \mathbf{a} - 1) \tag{B.2}$$

where $\mathcal{L}$ is the *Lagrangian* that is a function of the angular frequency ω and wavenumber, and ξ is the Lagrange multiplier. To find the minimum value of (B.2), the gradient is taken with respect to the angular frequency ω, and the minimum value can be found at the point of that the gradient is equal to zero:

$$\frac{\partial}{\partial \omega} \mathcal{L} \overset{!}{=} 0. \tag{B.3}$$

Using the symmetry of the covariance matrix $\mathbf{R}_{rr}$, the gradient of the first term in (B.2) can be simplified as the following:

$$\frac{\partial}{\partial \mathbf{w}} \mathbf{w}^H \mathbf{R}_{rr} \mathbf{w} = 2 \mathbf{R}_{rr} \mathbf{w}, \tag{B.4}$$
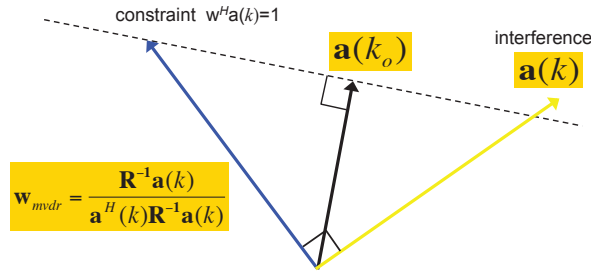
Figure B.2.: Relationship between the constraint, optimum solution and interference in the MVDR beamformer.

and the gradient of the second term in (B.2) is given by

$$\frac{\partial}{\partial \mathbf{w}} \xi \cdot (\mathbf{w} \cdot \mathbf{a} - 1) = \xi \cdot \mathbf{a}. \tag{B.5}$$

Rewriting (B.3) with (B.4) and (B.5) yields

$$2\mathbf{R}_{rr}\mathbf{w} + \xi \cdot \mathbf{a} = 0. \tag{B.6}$$

An optimum weight is now determined by solving (B.6):

$$\mathbf{w} = -\frac{1}{2} \cdot \xi \cdot \mathbf{R}_{rr}^{-1} \mathbf{a} \tag{B.7}$$

where ξ remains to be determined. The weight in (B.7) is substituted into the constraint given in the optimization problem. Thus, it leads to

$$\mathbf{w} \cdot \mathbf{a} = -\frac{1}{2} \cdot \xi \cdot \left(\mathbf{R}_{rr}^{-1} \mathbf{a} \right)^H \mathbf{a} = 1 \tag{B.8}$$

Since the multiplier is a constant, by rearranging (B.8) with respect to the Lagrangian multiplier ξ, one can obtain

$$\xi = -\frac{2}{\mathbf{a}^H \mathbf{R}_{rr}^{-1} \mathbf{a}}. \tag{B.9}$$

Finally, the optimum solution of the optimization problem is determined by

$$\mathbf{w}_{mvdr} = \frac{\mathbf{R}_{rr}^{-1} \mathbf{a}}{\mathbf{a}^H \mathbf{R}_{rr}^{-1} \mathbf{a}}. \tag{B.10}$$

The physical meaning of this optimum beamformer is illustrated in Figure B.2. When a steering vector for a desired wavenumber k_o is given as $\mathbf{a}(k_o)$, the constraint of the MVDR method allows the weight vector to only change along the dotted line which is perpendicular to the desired steering vector in Figure B.2[1]. Thereby the optimum weight preserves the inner product between the desired steering vector and the optimum weight to be unity, while the weight is orthogonal to the undesired (or interference) steering vector $\mathbf{a}(k)$.

---

[1]It is in accordance with the orthogonal projection of the weight vector on the desired steering vector.

C. Discrete Signal Theories

Information data carried by an analog signal will experience miscellaneous physical phenomena in the propagation channel and will arrive at the receivers. The acquired signal may hence be strongly distorted and the desired information cannot be directly retrieved from the acquired signal. Digital processing techniques have been contributing to improving the detection and estimation performance of such a *dirty* signal in radar and communication. In MIMO systems, the digital processing will play an even more critical role. This section gives a review of several important digital signal theories that form the keynote in MIMO SAR techniques.

C.1. Polyphase Decomposition

The idea behind the polyphase decomposition is to divide a discrete sequence, here called a mother sequence, into several subsequences, in order to implement efficient parallel signal processing known as the *multirate processing*. This technique is increasingly used in modern digital systems [25, 26, 27, 54]. The polyphase decomposition is a primary operation of the multirate processing and reduces the data rate (or sampling rate) of a single data stream without the loss of desired information.
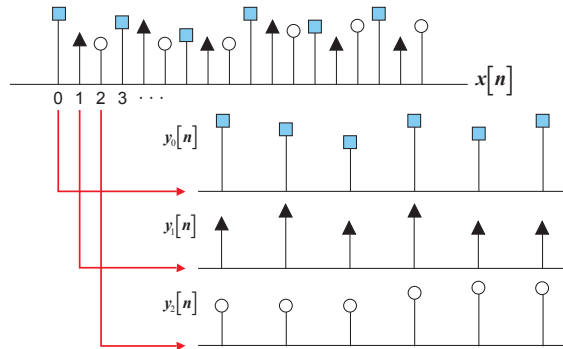
Figure C.1.: Polyphase decomposition concept of the sequence $x[n]$ into three subsequences ($M_T = 3$).

The polyphase decomposition is illustrated in Figure C.1. Assuming a digital sequence $x[n]$ with the length of N, the polyphase decomposition takes every M_Tth component of the mother sequence to compose subsequences. Thus, the length of a single sequence becomes $\frac{N}{M_T}$.

The subsequences are consequently sub-sampled by a factor of M_T. The jth subsequence y_j resulting from the polyphase decomposition is formulated as:

$$y_j[n] = x[M_T \cdot n + j] \qquad \text{where } j=0, 1, 2, \cdots, M_T\text{-}1. \tag{C.1}$$

In a practical implementation, the polyphase decomposition consists of several decimators and shifters, as shown in Figure C.2. The input $x[n]$ is fed into the delay line one step at a time.

The collection process of every M_Tth sample in the polyphase decomposition is basically the decimation symbolized by the down-arrow [54]. The Z^j indicates the advance of j samples in the block diagram. The decomposed sequences are followed by parallel multiple filters[1] H_j. The processed version of the mother sequence is reconstructed by parallel interpolators and single step shifters in the same manner [54].
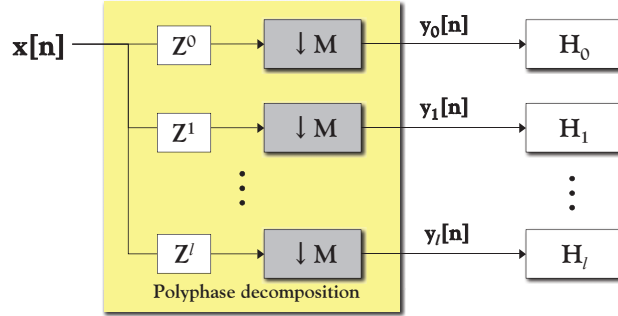
Figure C.2.: Implementation model of the polyphase decomposition combined with multiple parallel filters.

C.2. Expansion and Repetition Properties of DFT

The scaling properties of the DFT are important for understanding the time domain waveforms and range focusing in the proposed MIMO SAR concept. There is a sequence $x[n]$ with the length of N, defined in discrete time domain. When the sequence is expanded by a positive integer M_T as illustrated in Figure C.3 for $M_T = 2$, the resulting sequence $x_{(M_T)}[n]$ is described as:

$$x_{(M_T)}[n] = \begin{cases} x\left[\frac{n}{M_T}\right] & \text{for } \frac{n}{M_T} = \text{integer} \\ 0 & \text{otherwise} \end{cases} \tag{C.2}$$

where the subscript denotes the integer factor of the expansion. It must be noted that the discrete time domain sampling interval is unchanged in (C.2). Fourier transform of $x_{(M_T)}[n]$ is given by

$$X_{(M_T)}[p] = \sum_{n=0}^{N-1} x_{(M_T)}[n] \cdot \exp(-j\frac{2\pi}{N}np). \tag{C.3}$$

Substituting $\bar{n}$ for $\frac{n}{M_T}$, (C.3) is modified with respect to $M_T\bar{n} = n$, and (C.3) is rewritten as

$$X_{(M_T)}[p] = \sum_{n=0}^{N-1} x[\bar{n}] \cdot \exp(-j\frac{2\pi M_T}{N}\bar{n}p). \tag{C.4}$$

---

[1]Here, the same symbol H for the channel transfer function is used to describe the parallel filter bank, since the parallel channel transfer functions will follow the decimators in the MIMO SAR scenario.

It is found out that, during the expansion in time domain by a factor of M_T, its Fourier transform pair is compressed as M_T. The compressed spectrum is repeated within the range of sampling frequency [97]. Ignoring the envelope of the sequence and spectrum for simplicity, Figure C.3 illustrates this relationship for $M_T = 2$.
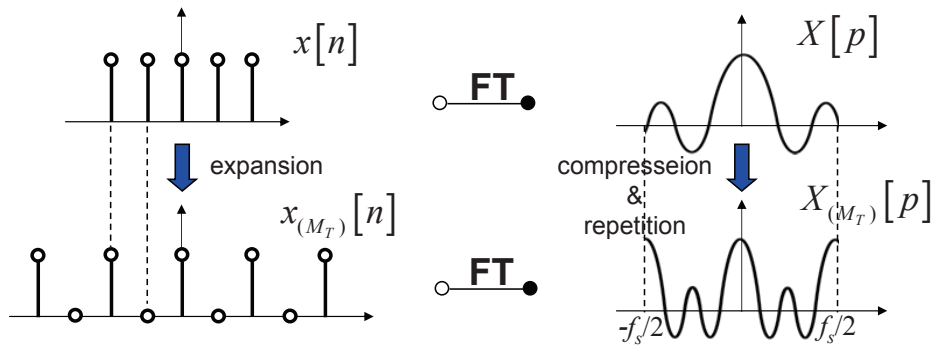
Figure C.3.: Time domain expansion and repetition in its Fourier transform by the factor of 2 ($M_T = 2$).

In practice, this property should be interpreted, taking the sampling rate into consideration. Since the discrete signal is denoted only by the discrete time index n, any change of sampling interval is not presented. For example, assume that a continuous time signal is sampled at every T_s interval. The sampled signal is denoted by $x[nT_s]$ where $n = 0, 1, 2, \cdots$. Now this signal is interleaved by zeros. Following this, the sampling rate becomes double that of the first case, i.e. the sampling interval becomes $T_s/2$. As shown in Figure C.4, M_T zeros between successive values of the sequence $x[n]$ are inserted.
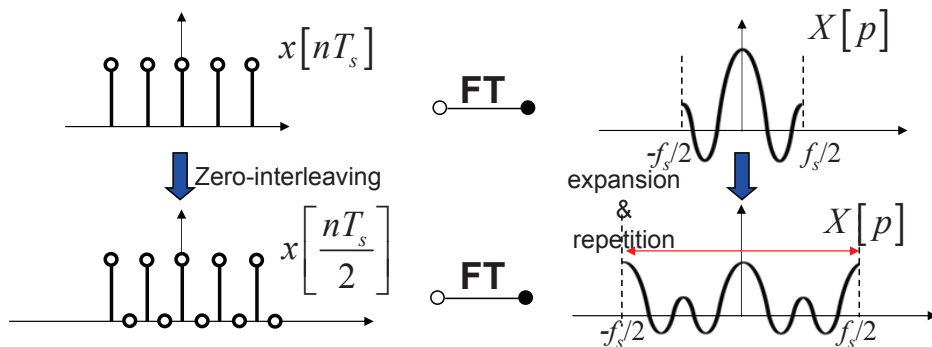
Figure C.4.: Comparison of time domain interleaving with zeros and its Fourier transform pair by a factor of 2 ($M_T = 2$).

In this case, the sampling interval is shortened by a factor of M_T, so that it yields the wider visible range in spectrum. The envelope of the spectrum is reduced by $1/\sqrt{M_T}$, since the total power of both spectra must be same according to Parseval's theorem [97].

D. Phase Gradient Autofocus Method

The *Phase Gradient Autofocus* (PGA) algorithm is a robust tool used to correct the phase error in high resolution spotlight SAR [125]. A focused SAR image is reconstructed using 2-dimensional matched filtering, which removes the quadrature phase term from the chirp waveform by multiplying a complex conjugate of the transmitted chirp waveform, and consequently the phase remains linear [113]. The slope of linear phase terms depends on the target position, and its Fourier transform appears at a corresponding position in a SAR image. The PGA algorithm exploits the gradient property of an exponential function in order to estimate a higher order phase term. After taking the gradient, the higher order term remains as a function of the azimuth position, whereas the linear phase term becomes a constant.
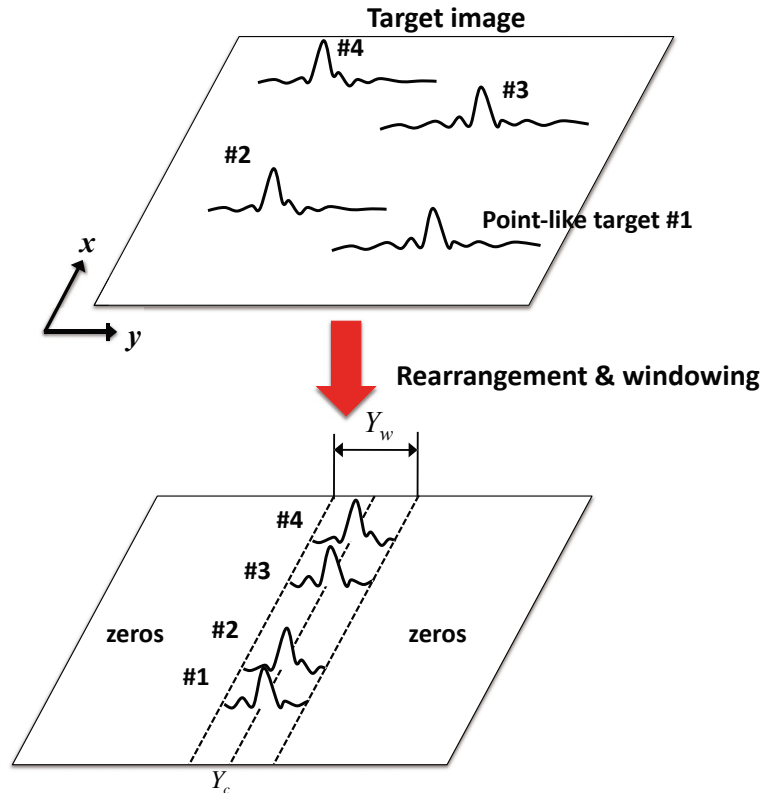
Figure D.1.: Selection of several point-like targets, rearrangement at the center of azimuth, and windowing with the length Y_w.

The first step in the PGA algorithm is to select point-like targets in a SAR image. In practice, systematic higher order phase errors can be estimated from a calibration site, encompassed by some dominant scatterers in distributed target. The selected peak blurs are circularly shifted to the azimuth center Y_c for every range bin. The circular shift of the peaks in each range bin transforms the linear phase variation into a constant phase in the case of a zero-squint SAR

geometry [125]. Furthermore, to maximize SNR, all point targets are summed up over the range. The selected peaks are windowed and the outside of the window region is zero-padded to maintain the same number of pixels. All of the above procedures are illustrated in Figure D.1. Regarding the SAR image as a function of target coordinate x and y, the image is denoted by $f(x, y)$ and its windowed and integrated version, $f_w(y)$, is given by

$$f_w(y) = \int \left(f(x, y - Y_c) \cdot \text{rect} \left[x, \frac{y - Y_c}{Y_w} \right] \right) \cdot \mathrm{d}x \tag{D.1}$$

where Y_w is the window size. The size of the window plays an important role in the PGA. In [125], 10dB threshold of the window is recommended. If a peak blur is surrounded by strong clutters, a wide window will include the clutter responses, so that the selected peak is affected by the phase of the clutters. This means the estimation will be perturbed by the clutter noise. Therefore the window size should be carefully determined. Further steps are carried out in frequency domain. The Fourier transform of the complex image function $F_w(k_a)$ is described in complex form as

$$F_w = |F_w| \exp\left(j\Psi(k_a) + j\Psi_e(k_a) \right) \tag{D.2}$$

where the phase term is a superposition of the desired linear phase Ψ and the non-linear phase error Ψ_e. Taking the gradient of this, the phase error terms can be estimated by means of removing the linear trend:

$$\nabla F_w(k_a) = j\left(\Psi' + \Psi_e' \right) |F_w| \exp\left(j\Psi(k_a) + j\Psi_e(k_a) \right) \tag{D.3}$$

where ∇ denotes the gradient operator. In (D.3), the derivative of the desired phase term must be minimized in order to estimate the *true* phase error from the derivative of the total phase. As mentioned above, the linear phase of target response, depending on the target azimuth position, is removed by the circular shift. Hence the phase of the selected point-like target responses are constants. The derivative of the phase error is extracted as follows:

$$\nabla\widetilde{\Psi}_e = \frac{\sum\limits^{N} \text{Im}\{\nabla F_w(k_a) \cdot F_w^*(k_a)\}}{\sum\limits^{N} F_w(k_a) \cdot F_w^*(k_a)} \tag{D.4}$$

where the upper asterisk denotes the complex conjugate, and Im· denotes the imaginary part of a complex number. The optimum estimation is accomplished by several iterations of the whole procedures. It is noted that the initial output of the PGA is the gradient of an estimated phase error. Therefore the output must be integrated over the range, before determining the phase error in our interest. Figure D.2 shows the signal flow chart of the PGA algorithm implemented for the side-looking SAR experiment in Chapter 7.

Generally, the PGA works properly in the case that the phase errors are identical over the target scene. That is a typical situation in the spotlight SAR mode, therefore the method is popularly used in the spotlight SAR data. However in the stripmap SAR mode, the phase error caused by a non-linear motion of the platform depends on target positions, as illustrated in Figure D.3. In the target area, two selected targets are focused from different synthetic aperture 1 and 2 as an example. Therefore their phase errors estimated by the PGA algorithm will be wrong, since those errors are caused by two different non-linear flight trajectories.
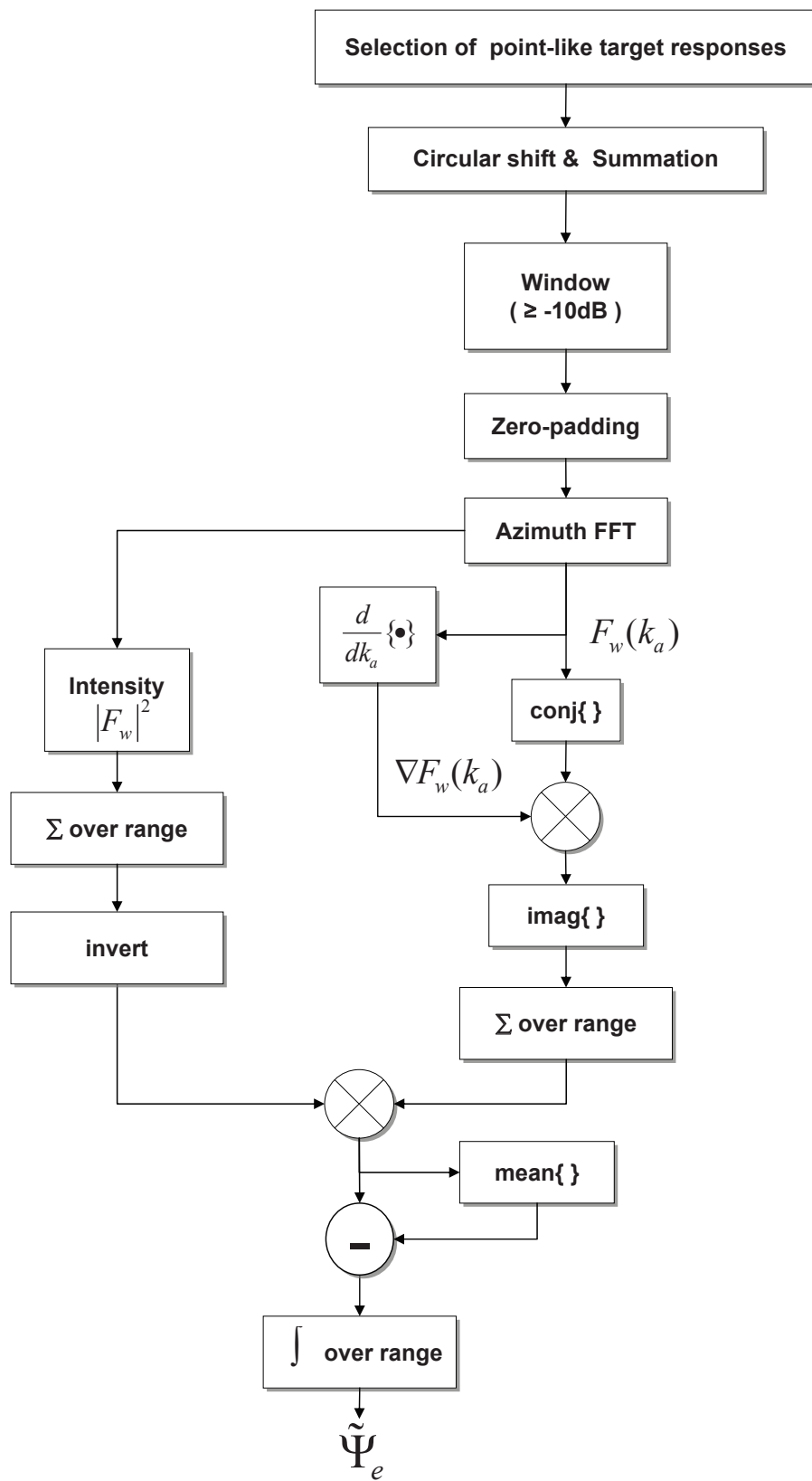
Figure D.2.: Signal flow chart of the implemented PGA algorithm.
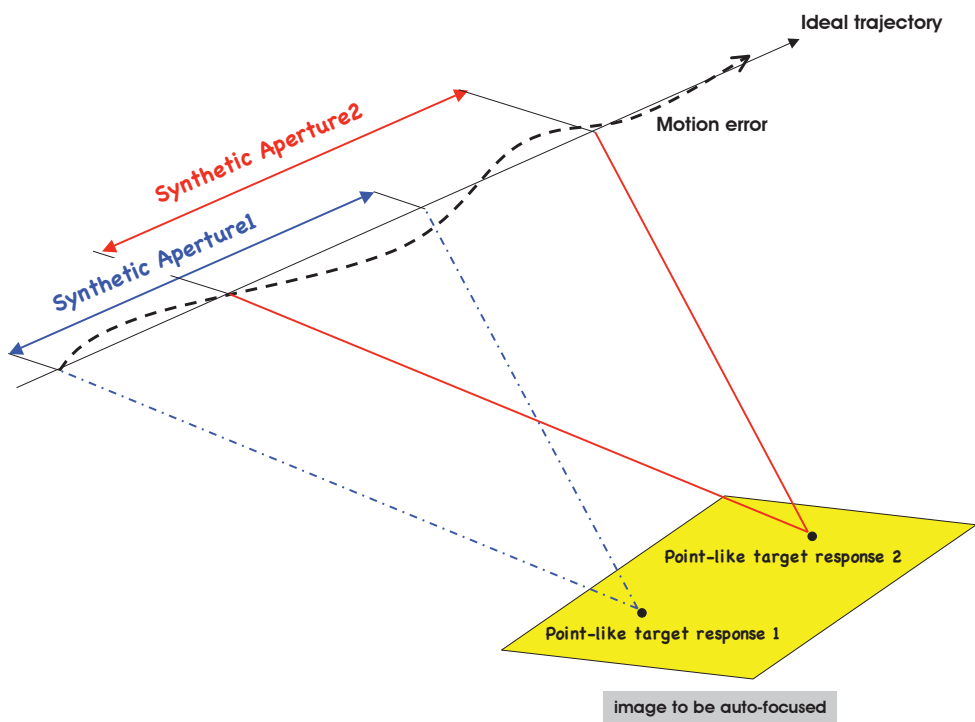
Figure D.3.: Motion error depending on the target position in the stripmap SAR mode.

E. Timing Diagram

A proper PRF range of spaceborne SAR systems can be efficiently determined by using a timing diagram for echo signals. The time diagram indicates incident angles where the echo can be correctly received without overlapping transmission events and nadir echo arrival times over various PRF [35]. Under the assumption of flat terrain over a target scene, a round-trip time delay, dependent of the incident angle can be approximated as follows:

$$\tau = \frac{2h_o}{c_o \cdot \cos \theta_{inc}} \tag{E.1}$$

where h_o denotes the orbital height of the SAR sensor, and θ_{inc} is the incident angle. When the echo arrival time coincides with the transmission events, the signal reception fails in the case of the monostatic systems. However, the present MIMO SAR system is equipped with independent Tx and Rx channels, so that the transmission and reception can be carried out at the same time. Consequently the echo delay arrival time should meet the condition of

$$\frac{m'}{PRF} < \tau < \frac{m'+1}{PRF} - T_p \tag{E.2}$$

where m' is the order of the pulse transmission events. In the other words, the delay echo shouldn't arrive at the receiver within the time range of

$$\frac{m'}{PRF} - T_p < \tau < \frac{m'}{PRF}. \tag{E.3}$$

Using the relation in (E.1), the time range can be converted into the incident angle. Then the angular range θ_{un} where unambiguous signals can be received is described as

$$\theta_{un} \in \left[\cos^{-1}\left(\frac{2h_o \cdot PRF}{c_o \cdot m'}\right), \quad \cos^{-1}\left(\frac{2h_o \cdot PRF}{c_o \cdot (m' - T_p \cdot PRF)}\right) \right]. \tag{E.4}$$

In addition, the acquisition time should avoid overlapping with the nadir echo arrival instant. The nadir echo arrival time is given by

$$\frac{2h_o}{c_o} + \frac{m}{PRF} < \tau_n < \frac{2h_o}{c_o} + \frac{m}{PRF} + T_p \tag{E.5}$$

where m is also the order of PRF. It is noted that the order m and m' are integers but indicate different transmission events. For example, the first pulse will return after the fourth pulse transmission event from the nadir, but return after the sixth event from the targets of interest,

due to the high altitude. The nadir echo arrival time range is converted into an unobservable incident angle range:

$$\theta_{na} \in \left[\cos^{-1}\left(\frac{2h_o \cdot PRF}{2h_o \cdot PRF + c_o \cdot m} \right), \quad \cos^{-1}\left(\frac{2h_o \cdot PRF}{2h_o \cdot PRF + c_o \cdot (m + T_p \cdot PRF)} \right) \right]. \tag{E.6}$$

A reasonable assumption would be that the nadir echo is separated by the range compression since the nadir echo is focused away from the targets of interest. Assuming five degrees near to the nadir affect the timing diagram, (E.5) can be replaced by

$$\frac{2h_o}{c_o} + \frac{m}{PRF} < \tau_n < \frac{2h_o}{c_o \cdot \cos(5°)} + \frac{m}{PRF}, \tag{E.7}$$

and the nadir angle is changed as follows:

$$\theta_{na} \in \left[\cos^{-1}\left(\frac{2h_o \cdot PRF}{2h_o \cdot PRF + c_o \cdot m} \right), \quad \cos^{-1}\left(\frac{2h_o \cdot PRF \cdot \cos(5°)}{2h_o \cdot PRF + c_o \cdot m \cdot \cos(5°)} \right) \right]. \tag{E.8}$$

F. Low-IF Topology: Image Rejection Principle

This appendix deals with detailed principles of the Low-IF topology used in the receiver of GB SAR demonstrator. The main feature of it is found in the image band rejection. There are two approaches regarding the implementation of this receiver topology. One is to directly use polyphase IF band pass filters and the other is to use successive I-Q demodulations, combined with real band pass filters. In the former approach, after the first I-Q demodulation, only the desired IF band signal is selected by the polyphase filters. Therefore the final baseband conversion does not produce the image band signal. In the latter approach, the real band pass filters are employed instead of the polyphase filters, and a cascade I-Q demodulator removes the image band during the down-conversion. In the demonstrator, the latter method was chosen since the receiver could be realized with commercial filter products at the desired IF band (50-350MHz). Additionally, the second I-Q demodulation is easily implemented by software.

F.1. Image Rejection Principle

This section describes the principles of image rejection in detail for the second approach. First, a real RF signal $s(t)$ is fed to the second type of Low-IF receiver and is given by

$$s(t) = s_d(t) \cdot \cos\left(2\pi \cdot f_c \cdot t\right) + i(t) \cdot \cos\left(2\pi \cdot (f_c - 2f_{IF}) \cdot t\right) \tag{F.1}$$

where $s_d(t)$ and $i(t)$ denote the desired baseband signal and the image band signal that are carried at frequency f_c respectively. In the frequency domain, the RF signal is depicted as the upper plots in Figure F.1 and F.2. Without any image rejection filter at the RF stage, the spectrum of the RF signal contains the desired band and the image band originated from the transmitter. However, if the RF antenna plays a role as a preliminary band pass filter, the amplitude of the image band is weaker than the desired band signal. This RF signal is mixed with a complex local signal by the first I-Q demodulator and converted into a *low* intermediate frequency. The IF band is chosen in regard to the performance of available IF band pass filters and ADCs (sampling frequency). In reality, one should consider the quantization effect as well, but in this section an ideal ADC is assumed for both I- and Q-channels. The I-channel signal is multiplied by a cosine LO signal, and the Q-channel is multiplied by a sine LO signal. Then the IF signal of each channel is given by:

$$I(t) = s(t) \cdot \cos(2\pi \cdot f_{LO} \cdot t) = \frac{1}{2} \left(s_d(t) \cdot \cos(2\pi \cdot f_{IF} \cdot t) + i(t) \cdot \cos(2\pi \cdot f_{IF} \cdot t)\right), \tag{F.2}$$

$$Q(t) = s(t) \cdot \sin(2\pi \cdot f_{LO} \cdot t) = \frac{1}{2} \left(-s_d(t) \cdot \sin(2\pi \cdot f_{IF} \cdot t) + i(t) \cdot \sin(2\pi \cdot f_{IF} \cdot t)\right). \tag{F.3}$$

Each channel output is given as a superposition of the desired signal and the image signal, due to the absence of the image rejection filter in this topology up to this point. The lower parts of Figure F.1 and F.2 show the low IF signal spectra of the respective channels, which result
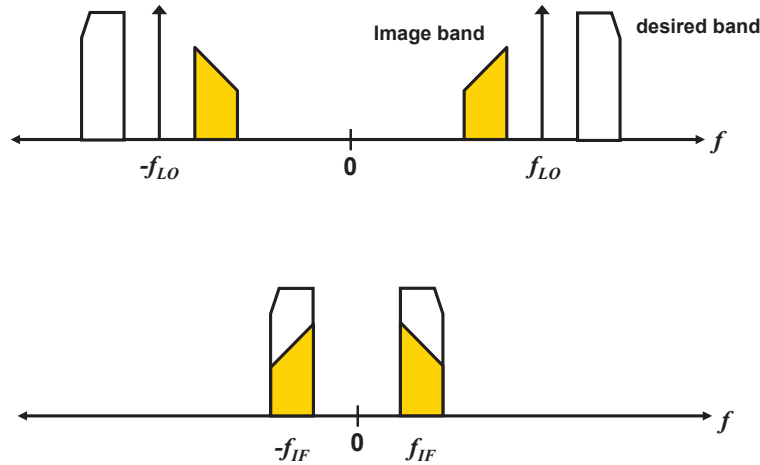
Figure F.1.: Spectrum of I-channel at the RF band (top) and the low intermediate frequency (bottom).
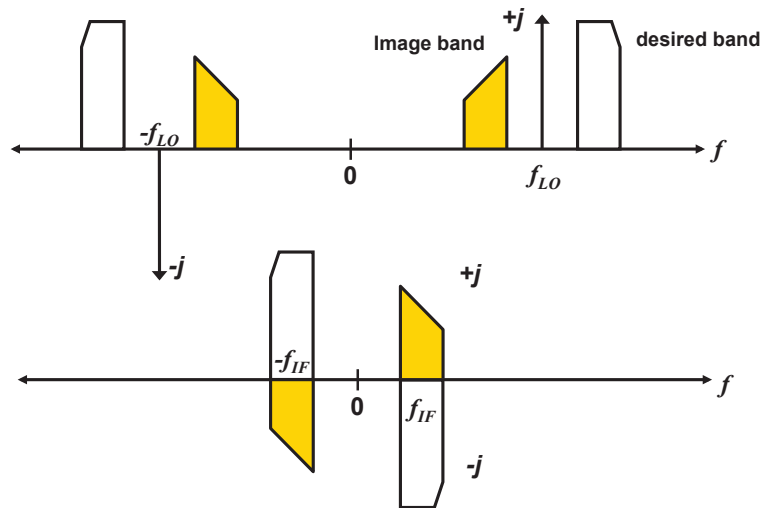
Figure F.2.: Spectrum of Q-channel at the RF band (top) and the low intermediate frequency (bottom).

from the real band pass filters. Hence both positive and negative frequency bands remain after filtering. For simplicity, a constant spectrum amplitude is assumed.

As the digital IF topology, those signals are digitized at the IF stage and multiplied by the second local signal in order to convert them to the baseband. At this procedure, the image bands will be rejected. As explained in section 6.4.2, this final conversion is accomplished by four parallel complex down-conversions. Firstly, the ADC of the each channel digitizes the IF signal, so that all signals are treated by digital processors. Since $s_{IF}(t) = I(t) + jQ(t)$, the baseband signal $s_b(t)$ is obtained:

$$s_b(t) = I(t) \cdot e^{j2\pi f_{IF}t} + jQ(t) \cdot e^{j2\pi f_{IF}t}. \tag{F.4}$$

Using Euler's formula, it is decomposed as follows:

$$s_b(t) = \underbrace{I(t)\cdot\cos(2\pi\cdot f_{IF}\cdot t) - Q(t)\cdot\sin(2\pi\cdot f_{IF}\cdot t)}_{I_b(t)} \tag{F.5}$$

$$+ j\underbrace{(I(t)\cdot\sin(2\pi\cdot f_{IF}\cdot t) + Q(t)\cdot\cos(2\pi\cdot f_{IF}\cdot t))}_{Q_b(t)}.$$

The first term of (F.5) is the in-phase component $I_b(t)$, and the second term is the quadrature component $Q_b(t)$ of the baseband signal. The second I-Q demodulator is directly implemented according to (F.5). The four parallel mixers realize the parallel I-Q demodulations of the decomposed signals in (F.5), and the following real low pass filters suppress higher frequency products of the I-Q demodulators. Following this, one obtains the ideal complex baseband signal, which means that the image signal is removed during this final down-conversion, as depicted in Figure F.3.

F.2. Effect of I-Q Channel Imbalance

The second down-conversion performed in the digital domain improves the image rejection performance. However, the first I-Q demodulation is carried out by the analog mixer around the carrier frequency band. Hence possible errors within the analog mixer or RF devices affect the image rejection performance. In particular, an imbalance between the I- and Q-channel will degrade the performance significantly. This section derives a mathematical model of the channel imbalance in amplitude and phase, referred to [133]. The RF signal given in (F.1) is rewritten using Euler's formula as follows:

$$s(t) = s_d(t)\left(\frac{e^{j2\pi f_c t} + e^{-j2\pi f_c t}}{2}\right) + i(t)\left(\frac{e^{j2\pi(f_c - 2f_{IF})t} + e^{-j2\pi(f_c - 2f_{IF})t}}{2}\right). \tag{F.6}$$

Here, the amplitude and the phase imbalance between the I- and Q-channel, ΔA and $\Delta\phi$, are introduced in the local signal, $x_{LO}(t)$. The amplitude imbalance ΔA is defined as a normalized amplitude by the I-channel (reference), and $\Delta\phi$ is the phase difference between the I- and Q-channels. The local signal with the I-Q imbalance is described as

$$x_{LO}(t) = \cos(2\pi\cdot f_{LO}\cdot t) + j\Delta A\cdot\sin(2\pi\cdot f_{LO}\cdot t + \Delta\phi). \tag{F.7}$$

The local signal can be described by a complex exponential form based on the Euler's formula as follows:

$$x_{LO}(t) = \frac{e^{j2\pi f_{LO}t} + e^{-j2\pi f_{LO}t}}{2} + j\Delta A\cdot\frac{e^{j2\pi f_{LO}t + \Delta\phi} - e^{-j2\pi f_{LO}t - \Delta\phi}}{2j}. \tag{F.8}$$

Rearranging (F.8) with respect to the exponentials, (F.8) is simplified

$$x_{LO}(t) = K_1\cdot e^{j2\pi f_{LO}t} + K_2\cdot e^{-j2\pi f_{LO}t} \tag{F.9}$$

Figure F.3.: Digital baseband down-conversion and the image rejection through the complex local signal, implemented with the real band pass filters

where K_1 and K_2 are the imbalance factors [133], which are defined by

$$K_1 = \frac{1 + \Delta A \cdot e^{j\Delta\phi}}{2} \tag{F.10}$$

$$K_2 = \frac{1 - \Delta A \cdot e^{-j\Delta\phi}}{2} \tag{F.11}$$

The IF signal is obtained by multiplying the local signal with the RF signal ($s_{IF}(t) = s(t)x_{LO}(t)$). The real low pass filters after the demodulation reject the high frequency products. Thus, the filtered IF signal is written by

$$s_{IF}(t) = \frac{1}{2}\left[s_d(t)\cdot\left(K_1\cdot e^{-j2\pi f_{IF}t} + K_2\cdot e^{j2\pi f_{IF}t}\right) + i(t)\cdot\left(K_1\cdot e^{j2\pi f_{IF}t} + K_2\cdot e^{-j2\pi f_{IF}t}\right)\right] \tag{F.12}$$

Digitization and quantization are skipped for simplicity in this formulation. The final baseband conversion is now the complex multiplication of the IF and the second local signals, and consequently the baseband signal of each channel is filtered by the final low pass filter:

$$s_b(t) = s_{IF}(t)e^{j2\pi f_{IF}t} = \frac{1}{2}\left(K_1 s_d(t) + K_2 i(t)\right) \tag{F.13}$$

(F.13) implies that the image signal, $i(t)$, remains in the baseband with the desired signal, $s_d(t)$. If there is no channel imbalance in amplitude and phase ($\Delta A = 1, \Delta\phi = 0$), then K_1 is equal to

one and K_2 becomes zero. The degradation of image rejection performance can be estimated by measuring the *Signal-to-Interference (Image) Ratio* (SIR) defined as

$$\text{SIR} = \left| \frac{K_2}{K_1} \right| = \left| \frac{1 - \Delta A \cdot e^{-j\Delta\phi}}{1 + \Delta A \cdot e^{j\Delta\phi}} \right|. \tag{F.14}$$

Figure F.4 presents the calculated SIR over the amplitude imbalance, and the phase imbalance varies from 0.5 to 4.5 degrees.
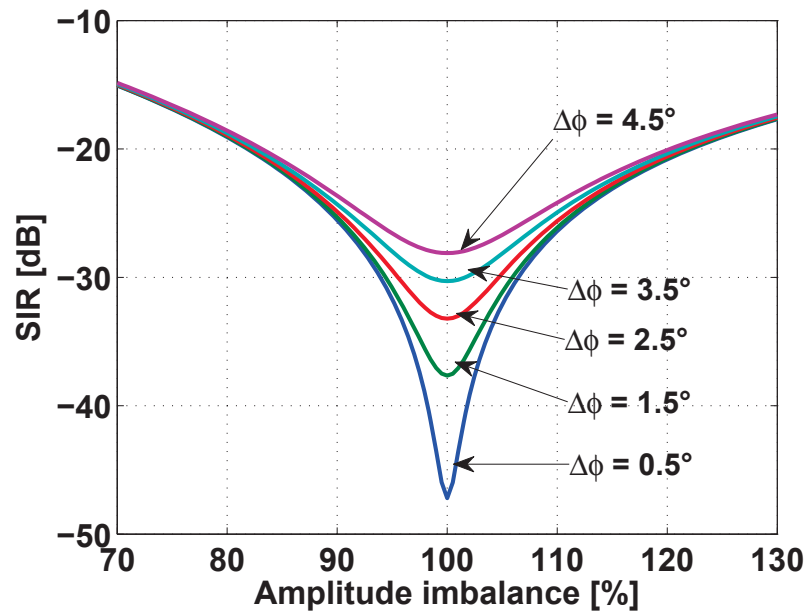
Figure F.4.: SIR over the amplitude and phase imbalance in decibel

This plot shows that the phase imbalance has the dominant affect when the amplitude imbalance varies within a $\pm 10\%$ range from the optimum point (100%). However, if the amplitude imbalance becomes more significant, then the phase imbalance effect becomes negligible, and the image rejection performance depends on the amplitude imbalance.

Lebenslauf

Persönliche Daten

Name	Jung-Hyo Kim
Geburtsdatum	23. Mai 1972
Geburtsort	Seoul, Republik Korea (Südkorea)
Staatsangehörigkeit	südkoreanisch
Familienstand	verheiratet

Wehrdienst

1994 − 1997	Militärpolizei der Koreanische Luftwaffe

Studium und Berufsweg

seit 2009	Gastwissenschaftler am Institut für Hochfrequenztechnik und Radarsysteme des Deutschen Zentrums für Luft- und Raumfahrt
seit 2006	Wissenschaftlicher Mitarbeiter am Institut für Hochfrequenztechnik und Elektronik an der Universität Karlsruhe (TH)
2004 − 2005	Gastwissenschaftler am Institut für Hochfrequenztechnik und Elektronik an der Universität Karlsruhe (TH)
2001 − 2003	Forschungs- und Entwicklungs-Ingenieur bei LG Electronics, CDMA Laboratory, New Techniques Group, Korea
1999 − 2001	Masterstudium der Elektrotechnik an der Yonsei Universität, Korea Schwerpunkt: Hochfrequenztechnik und Telekommunikation
1992 − 1999	Bachelorstudium an der Kyunghee Universität, Korea Schwerpunkt: Astronomie und Elektrotechnik